



Mixed Elastohydrodynamic Lubrication and Fatigue Calculation for Rough Surface Contacts Using a Synthesised Running-in Model

by

Hassneen AL - Asadi

Thesis submitted in candidature for the degree of
Doctor of Philosophy at Cardiff University

Tribology and Contact Mechanics Research Group
Institute of Mechanics and Advanced Material
School of Engineering
Cardiff University

February, 2020

Declaration

This work has not previously been accepted in substance for any degree and is not Concurrently submitted in candidature for any degree.

Signed (Hassneen AL-Asadi) Date

STATEMENT 1

This thesis is being submitted in partial fulfilment of the requirements for the degree of PhD

Signed (Hassneen AL-Asadi) Date

STATEMENT 2

This thesis is the result of my own work/investigation, except where otherwise stated. Other sources are acknowledged by explicit references.

Signed(Hassneen AL-Asadi) Date

STATEMENT 3

I hereby give consent for my thesis, if accepted, to be available for photocopying and for inter-library loan, and for the title and summary to be made available to outside Organisations.

Signed(Hassneen AL-Asadi) Date

STATEMENT 4

I hereby give consent for my thesis, if accepted, to be available for photocopying and for inter-library loans after the expiry of a bar on access previously approved by the Graduate Development Committee.

Signed(Hassneen AL-Asadi) Date

Acknowledgments

First of all, I would like to praise and thank God for helping me to complete this thesis.

I would like to express my gratitude and thank my three supervisors: Prof. H.P. Evans, Dr. K.J. Sharif and Dr Alastair Clarke for their encouragement, thoughtful advice and support throughout my study.

Most especially I would like to thank Prof. H.P. Evans for providing guidance and invaluable experience to develop my skills as a researcher and also for dealing with me as a colleague more than a student.

The work presented in this thesis would not have been possible without the financial support of the Iraqi Ministry of Oil and the Higher Committee for Education Development.

I would particularly like to thank the Peter Jost Travel Fund, which supported the presentation of this work at a conference of STLE 2019.

Thanks are also due to my friends in the Tribology research group, in particular: Dr Maasi AL-Mayali, Dr. Simon Hutt and William Britton for their help and support.

Last but not least, my deepest gratitude goes to my wife, and I am also thankful for the endless support of parents. My parents have given me love and support throughout my life, and without them I would not be where I am today. I am eternally grateful for everything they have given me, and am forever indebted to them.

Summary

This thesis presents a method to investigate the contact and deformation of rough surfaces such as those found on the teeth of gears. As-manufactured rough surfaces undergo a process known as “running-in”, in which the geometry of the surface is changed by interaction with the counterface when they are first loaded together.

The process of surface roughness modification in machine elements when loads are applied was studied. This is a plastic deformation that modifies the roughness asperities to form the surface finish that characterises the components during their useful life. Protection of heavily loaded machine element surfaces is provided by mixed elastohydrodynamic lubrication (EHL) which depends critically on the component surface roughness.

A procedure was developed to synthesise the running-in process based on real as-manufactured profiles. Surface roughness profiles obtained from transverse ground test disks were used to simulate asperity modification during running-in under load. This simulation is based on a detailed analysis of the way in which the surface roughness asperity tips change shape during running-in. Information on these changes was extracted by measuring surface roughness profiles before and after running-in and quantifying the statistical changes seen in the asperity tip radii of curvature. The surfaces were run against each other in mixed EHL analyses and the radius of curvature of asperity peaks subjected to extreme loading was increased in a controlled fashion to synthesise plastic deformation.

The process was developed by comparison with the corresponding run-in profiles and with observed changes in asperity peak radii of curvature. Simulations were conducted for a range of different surface roughness pairs with various operating conditions.

The synthesised and measured run-in surfaces were compared in various ways. Their geometry was examined in terms of form and asperity peak radii of curvature. Rolling / sliding EHL contact analyses were performed and their behaviour in terms of peak asperity pressure and direct asperity contact was assessed. The transient mixed EHL analysis results were used to apply surface loading to the rough profiles to obtain stress histories, which were the basis of the fatigue modelling then carried out. Finally, experimental work was implemented to detect the micropits developing on the rough

surfaces using surface measurements taken during endurance tests, and a good agreement was found when compared with numerical fatigue model.

Table of Contents

1. Chapter 1: Introduction and literature review	1
1.1 Definition and History of Tribology	1
1.2 Lubrication mechanisms	4
1.2.1 Full film regime	5
1.2.2 Micro-EHL regime	5
1.2.3 Mixed EHL lubrication regime	5
1.2.4 Boundary lubrication regime	6
1.3 Elastohydrodynamic lubrication	7
1.4 Surface roughness	13
1.5 Surface Fatigue Failures.....	14
1.6 Scuffing failure.....	15
1.7 Pitting failure.....	17
1.8 Micropitting failure	18
1.9 Running-in	25
1.9.1 The effect of different operating conditions on running-in	25
1.9.2 Effect of hardness on running-in surfaces	27
1.9.3 The influence of surface topography on efficiency	28
1.9.4 The effect of the plastic deflection on residual stresses	30
1.9.5 Effect of surfaces statistics during running-in process.....	32
1.10 Thesis aims and structure	39
2. Chapter 2: Transient EHL analysis	41
2.1 Introduction	41
2.2 Development of EHL line contact problems.....	42
2.3 The viscosity equation.....	43
2.4 The density equation	44
2.5 The load equation	44
2.6 Elastic Film Thickness equation	45
2.7 The Reynolds equation.....	46

2.8	Differential deflection method	48
2.9	The coupled EHL Solution method.....	50
2.10	Surface Asperity Modification Process	54
2.10.1	Profile Set One.....	54
2.11	Numerical Results	56
2.12	Arbitrary surface modification	60
2.13	The First Attempt	63
2.14	The Second Attempt.....	64
2.15	The Third Attempt.....	66
2.16	An investigation in radii of curvature for both fast and slow surfaces.....	68
2.17	Conclusion.....	71
3.	Chapter 3: Simulating running-in	72
3.1	Introduction	72
3.2	Development Stages of coding the plastic deformation synthesis in Fortran 90	73
3.3	Stage One	75
3.4	Stage Two.....	77
3.5	Stage Three.....	82
3.6	Stage Four.....	84
3.7	Stage Five	86
3.8	Profile Sets Two and Three	94
3.9	Lowest Penetration Surfaces	97
3.10	Highest Penetration Surfaces.....	108
3.11	Conclusion.....	123
4.	Chapter 4: Fatigue.....	124
4.1	Introduction	124
4.2	Variable Amplitude Multiaxial Fatigue	125
4.3	Rain-Flow Counting Method.....	125
4.4	Cumulative damage.....	127

4.5	Critical Plane Approach	128
4.6	Multiaxial Models based on the critical plane	129
4.7	Numerical Procedure.....	130
4.8	Weibull Cumulative Density Function (<i>CDF</i>).....	134
4.9	Conclusion	135
5.	Chapter 5: Experiment	136
5.1	Introduction	136
5.2	Twin-Disk Test Rig.....	137
5.3	Load Application.....	137
5.4	Load Calibration.....	138
5.5	Description of Drive to Test Rig.....	139
5.6	The slide/roll ratio (SRR).....	141
5.7	The Disks Geometry and Properties	142
5.8	Surface Orientation and Grinding Process	143
5.9	In Situ Talysurf Measurements	145
5.10	Filtering the raw profile	149
5.11	Realignment of run-in surfaces	151
5.12	Vertical alignment of the deepest common features	152
5.13	Experimental Procedure	155
6.	Chapter 6: Results	158
6.1	Introduction	158
6.2	Comparison of Model and Experimental Micropitting Results	159
6.3	High Roughness Gears (Process A)	165
6.3.1	Profile Set Four	165
6.3.2	Profile Set Five	168
6.4	Low Roughness Gears.....	171
6.4.1	Profile Set Six.....	171
6.4.2	Profile Set Seven	173

6.5	Profile Set Eight	176
6.6	Surface and near surface fatigue analysis.....	178
6.7	Comparison between the predicted damage for the synthesised and measured surfaces	181
6.8	Comparison between the high and small roughnesses for gear profiles ...	194
6.9	Comparison with disk tests where micropitting occurred	198
6.10	Comparison between the highest and the lowest penetration disk surfaces.	216
6.11	Comparison with gear micropitting experiments	219
6.12	Sensitivity of calculated fatigue to counter face orientation	219
7.	Chapter 7: Conclusions and Future Work	229
7.1	Conclusion.....	229
7.2	Future work	232
	References	233
	Appendix	251

Nomenclature

Symbol	Description	Units
a	Hertzian semi-contact dimension	m
b_o	Fatigue strength exponent	-
c_o	Fatigue ductility exponent	-
D	accumulated damage fraction	-
E	elastic modulus	Pa
E'	Effective elastic modulus	Pa
$E1, E2$	Elastic modulus, surface 1 and 2	Pa
f	Weighting function used in the differential deflection equation	m
g	Weighting function used in the deflection equation	m
G	Shear modulus	Pa
G_m	Materials parameter	-
h	Film thickness	m
h_{min}	Minimum film thickness	m
h_c	Central film thickness	m
K	Material constant with the range, $0.6 < k < 1.0$.	-
MTP	Maximum transient pressure	Pa
N_f	Fatigue lifetime (cycle to fatigue failure)	-
p_o	Hertzian contact pressure	Pa
p_g	Yield pressure	Pa
Ra	Roughness average parameter	m
$R1, R2$	Radius of curvature, surface 1 and 2	m
S	Non-Newtonian flow factor	-
U_1, U_2	Velocity of surface 1 and 2	m/s

\bar{u}	Mean velocity	m/s
w'	Load per unit length	N/m
α	Viscosity pressure coefficient	-
ν_1, ν_2	Poisson's ratio for surface 1 and 2	-
ζ	Slide roll ratio (SRR)	-
ρ	Density	Kgm ⁻³
ρ_o	Density at reference pressure	Kgm ⁻³
η	Viscosity	Pa.s
η_o	Viscosity at reference temperature and pressure	Pa.s
τ	Shear stress	Pa
τ_o	Eyring shear stress	Pa
τ_f'	Shear fatigue strength coefficient	Pa
σ_γ	Yield strength for the cyclic stress-strain curve	Pa
σ_n^{\max}	Maximum tensile stress normal to the critical plane	Pa
$\sigma_{xx}, \sigma_{zz}, \tau_{xz}$	material stress components	Pa
ϵ_f'	Fatigue ductility coefficient	-
$\dot{\gamma}$	Shear strain rate	s ⁻¹
γ_f'	Shear fatigue ductility coefficient	-
N.B. Other symbols are defined in the text when their use is local to the section concerned.		

Chapter 1: Introduction and literature review

1.1 Definition and History of Tribology

Tribology is defined as the study of friction, lubrication and wear of contacting surfaces in relative motion and of related subjects and practices, such as rotating parts that are subjected to large contact forces with a thin lubricant film (Bhushan, 1998) which are the subject of this thesis. Tribology as a science and the word was first introduced by the UK Department of Education and Science (Jost, 1966). The word tribology comes from the Greek word, “tribos”, meaning “rubbing” or “to rub”, so the literal translation would be “the science of rubbing.” Its popular English language equivalent is lubrication, friction and wear, or lubrication science.

Although Tribology was given a name and definition in 1966, the principles of tribology are not new and have been applied in many cases since the beginning of recorded history. Dowson (1979) provided a comprehensive description of the history and development of human activities related to tribology. Looking as far back as 200,000 years ago, early man started to generate fire in the Palaeolithic period. The idea of using friction to generate fire by the percussion of flint stones and the rubbing of wood-on-wood can be considered the first evidence of man’s application of the practical use of frictional heating (James et al., 1989).

Other tribological ideas followed through the expansion of humanity and the emergence of the first civilisations. Bearings were the first tribological systems, used about 7000 years ago, in the Neolithic period, where wood, bones, stone and antlers were used in plain rotary drills and door hinges (Singer et al., 1954). The invention of the potter’s wheel marked the usage of lubricants and an appreciation of the purpose of lubrication has been found as far back as 3250 BC.

As early as 2400 B.C., the Ancient Egyptians invented wheeled vehicles and potter's wheels that used bearings, and grease-like substances, while bitumen and water were used as lubricants to reduce sliding friction. In a painted wall relief of an Egyptian Pharaoh's tomb dated to around 2400 B.C., a worker is seen pouring lubricant in front of a sledge for moving statues, as shown in Figure 1.1. Furthermore, olive oil was apparently a lubricant of choice; the tomb of Egyptian king Tehut-Hetep (circa 1650 B.C.) was found to include a description of the application of olive oil to wooden planks to move large stones.



Figure 1.1 The first recorded tribologist – pouring lubricant in front of the sledge in the transport of the statue of Ti.

In the Greek islands, the earliest evidence on the use of gears was found to date back to 87 BC where they were seen in the Antikythera mechanism, which was excavated from a sunken ship in 1900. The mechanism was a Greek astronomical calculator, and contained a complex clockwork mechanism composed of at least 30 epicyclic differential bronze gears (Freeth et al., 2006). The remains of the Antikythera mechanism can be seen in Figure 1.2.



Figure 1.2 The remains of the Antikythera mechanism.

Roman civilisation brought new technologies and materials as well as scientific research into tribological matters. They used rolling elements and bronze to reduce friction, which became a common practice during that period. Evidence of tapered rolling element bearings has been found in Roman ships from approximately 50 A.D. (Hamrock and Anderson 1983).

During the Middle Ages, many significant developments of lubricants and structural materials occurred. Leonardo da Vinci (1452-1519) conducted studies of a number of the concepts and principles that are now considered as tribological, such as friction, wear, and bearings (Dowson, 1977). DaVinci was the first to discover laws of friction and deduced the rules governing the motion of a rectangular block sliding over a flat surface. He introduced the concept of the coefficient of friction as the ratio of the friction force to normal load. He also investigated wear patterns and designed bush and rolling element bearings, including the necessity of a cage to separate the rolling elements.

In 1699 Amontons verified da Vinci's laws of friction after he studied dry sliding between two flat surfaces and these laws are still recognisable today. First the friction force is directly proportional to the normal load applied in sliding. The friction force is independent of the projected contact area. This finding was verified by the French Physicist Coulomb (1736-1806), who was one of many who questioned Amontons'

work due to scepticism over his second law. He added a third law that kinetic friction is nearly independent of the speed of sliding. Coulomb defined friction formulas based on his own experimental studies.

Lubrication involves fluid motion and the basics of fluid mechanics were formulated by Euler, Bernoulli, Couette, Poiseuille etc. Newton's law of flowing fluids was developed by Navier by including the viscous terms. At the same time Stokes defined the basics of viscous flow. Subsequently, the equations formulated in this way became known as the Navier-Stokes equations. The first distillation of mineral-oil based lubricant was conducted in Prague in 1812 and the first graphite-containing lubricant was patented in the United Kingdom in 1835 (Bhushan, 2013).

During the Second Industrial Revolution, the cornerstone of tribological study was laid by numerous scientists, including: studies of rolling friction by Reynolds (1875) and Hertz's analysis of contact between elastic materials (1881); (Mang et al., 2011). Moreover, rapid and impressive development of machinery was seen in industrial production. The use of steam power following the development of the railways in the 1830s, vehicles in the early 1900s and aircraft in the 1940s all led to the demand for a better understanding of tribology. In the earlier part of the twentieth century, tremendous industrial growth fuelled the demand for better understanding and application of tribology, so that knowledge in all areas of tribology expanded massively as a result.

1.2 Lubrication mechanisms

Lubrication is an effective interposition of a solid, liquid or gas between two bodies to reduce friction and/or wear as a body moves over the other (Stachowiak Batchelor, 2013). The lubrication regime in which the machine element operates depends on many factors which are:

- 1- Operating conditions such as, load, temperature and speed.
- 2- Surface and material properties.
- 3- Lubricant properties.

There are three main classifications of lubrication regimes which are Micro-EHL, Mixed lubrication and Boundary lubrication.

1.2.1 Full film regime

This is the regime for smooth surfaces and also for rough surfaces where the film thickness is at least three times bigger than the composite surface roughness, as represented in Figure 1.3 (a).

1.2.2 Micro-EHL regime

This regime is shown schematically in Figure 1.3(b) where the surfaces are completely separated by a continuous full film lubricant which is thick enough to avoid direct contacts of surfaces. No metal to metal contact takes place, while the friction is only caused by shear stress in the viscous lubricant but the roughness features have a significant influence on the pressure distribution (Hamrock et al., 2004).

1.2.3 Mixed EHL lubrication regime

Mixed lubrication, is a regime governed by a mixture of hydrodynamic and boundary lubrication. In other words, there are areas in the contact interface which are fully separated by lubricant film and other areas in which direct asperity interactions take place without the help of a hydrodynamic film. This is depicted schematically in Figure 1.3 (c). The lubricant film is present but the transient micro-EHL effects are insufficient to separate the surfaces effectively, resulting in direct asperity contact (Evans et al., 2009). Typically, the surfaces are separated by a thin lubricant film with a mean thickness of between (0.05 - 1 μ m) in this regime. Reduced lubricant film coincides with increased contacting load and direct asperity contact pressures if the other parameters are kept constant. Accordingly, the mixed EHL regime plays a vital role in the occurrence of surface failures of gears, such as pitting, micropitting and various other types of surface distress in which the asperities on the two surfaces come into contact (Johnson, 1989).

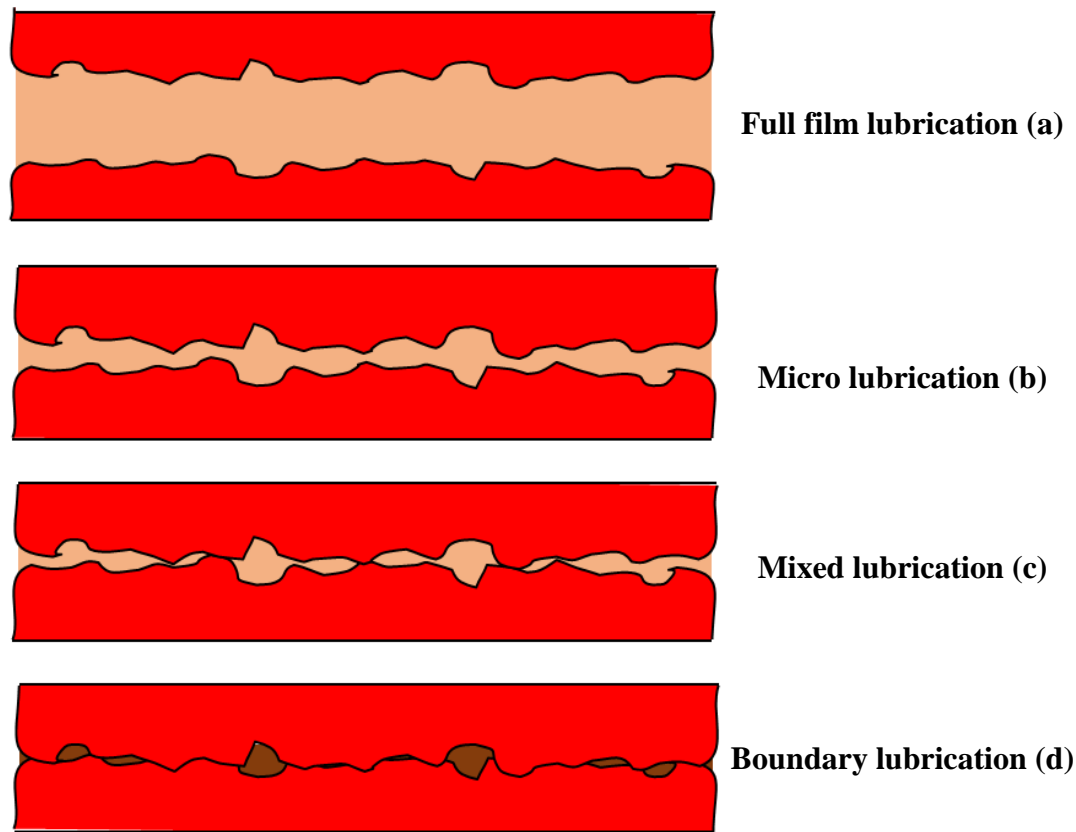


Figure 1.3 Lubrication regimes: (a) full fluid film lubrication, (b) micro lubrication , (c) mixed lubrication , and (d) boundary lubrication.

1.2.4 Boundary lubrication regime

In this regime, the average surface roughness is greater than the average lubricant film thickness (Stachowiak and Batchelor, 2013). As a result, the lubricant film, which is in the range of (5-100 μm) in boundary conditions, cannot develop sufficient pressure to contribute to load support. The load is carried by direct contact of asperities as shown in Figure 1.3 (d). Under this regime, the friction behaviour is controlled by an extremely thin film of lubricant and the boundary film can be attached to the surface of one or both of the contacting bodies. The friction coefficient is high, where the mechanical properties and nature of the junctions are the defining criteria for the friction coefficient. The collisions between the asperities of the two surfaces in contact produce friction, heat and wear. Any reduction of friction and wear in this regime depends on the lubricant chemistry, while the fluid film has no effect (Korres, 2013).

1.3 Elastohydrodynamic lubrication

The form of lubrication that is the subject of this thesis is elastohydrodynamic lubrication (EHL). This is a type of hydrodynamic lubrication in which elastic deformation occurs in the contacting surfaces which causes a significant change in their shape and enables them to be separated by a thin lubricant film. In particular, EHL refers to the typical type of lubrication that occurs between non-conforming contacting surfaces when lubricant film pressure is high enough to significantly influence the shape of the film thickness profile through elastic deflection. It can be found in several examples: gearboxes, rolling element bearings, cams and tappets, and some other heavily loaded non-conformal contacts. For instance, Figure 1.4 shows EHL in a rolling-sliding gear contact in which a contact force is transmitted over a very small area (of width $2b$) which implies a high contact pressure, i.e. typically 1 - 3 GPa. Despite this very thin layer of lubricant, it is probably sufficient to prevent metal to metal contact between the interacting surfaces provided that the surface finish is carefully controlled. Contacts of this type are called Hertzian contacts because their thin film area corresponds to the dry contact area.

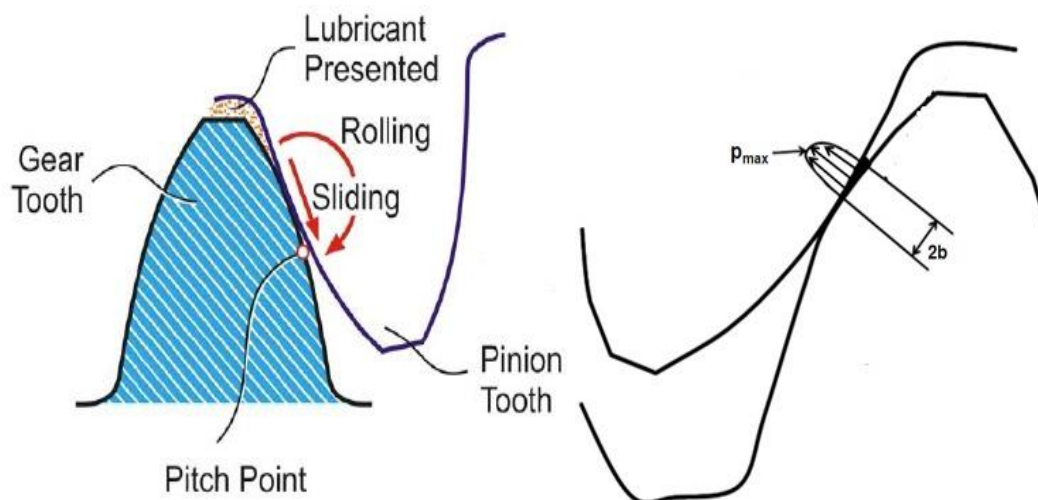


Figure 1.4 Non-conformal contacts (Stadtfeld and Saewe 2015).

Beauchamp Tower and Petrov (1883) examined lubricated bearings experimentally. Petrov found that viscosity was a vital lubricant property, in addition to the relationship between frictional force and bearing area and clearance as well as sliding speed. Meanwhile, experimentation by Tower proved for the first time that lubricant

could completely separate surfaces moving relative to one another, i.e. full-film hydrodynamic lubrication. A year later, Reynolds used the Navier-Stokes equation to provide the theory behind the experimental findings (Reynolds, 1886).

Reynolds found that when the velocity of the contact surface increases, the liquid flow velocity also increases and produces a liquid with a pressure sufficient to keep the two surfaces separated. The speed and viscosity are the most significant factors governing hydrodynamic lubrication. The higher the viscosity, the higher the friction coefficient. High friction generates heat, which will decrease viscosity. While such work in lubricated contacts was evolving, Hertz, perhaps more widely known for his research on electromagnetic waves, developed the first analytical solution for frictionless dry non-conformal contact of smooth surfaces Hertz (1882). His work is based on several assumptions; that the contact area is small compared to the radius of relative curvature, and the size of the contacting bodies, and that the contact is frictionless. The results of his research still provide the basis for studies on non-conforming contacts today.

Elastohydrodynamic lubrication has characteristic features, such as constant film thickness and near Hertzian contact pressure profile within the Hertzian contact zone. The film thickness is one of the primary properties of EHL since it describes how well surfaces are separated and thus how well the lubricant film protects them from wear and high friction, as illustrated schematically in Figure 1.5. These features have been widely used in the construction of approximate solutions of EHL theory.

Extreme operating conditions may play a significant role in the breakdown of the EHL mechanism which reduces friction and wear between contacting surfaces. The earliest studies and understanding of EHL can be traced back to the beginning of the 20th century.

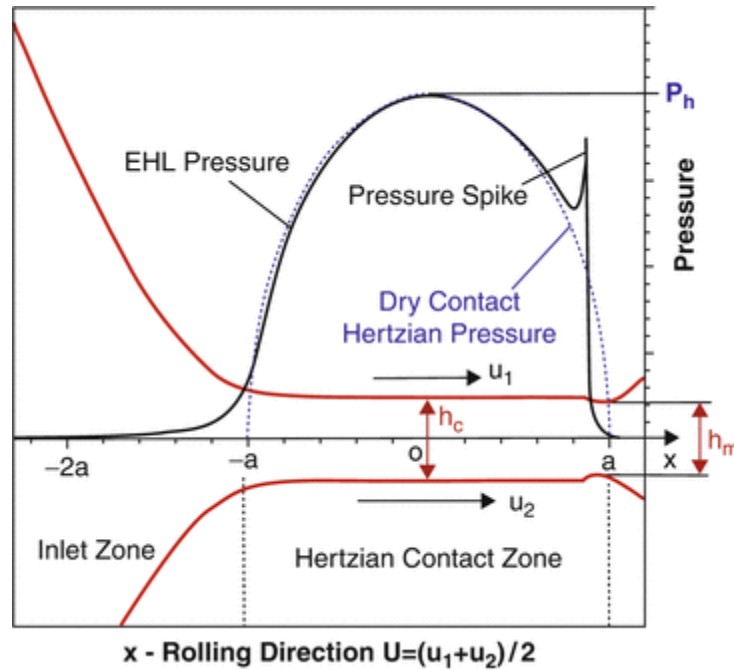


Figure 1.5 Hertz Contact Pressure Vs. Elastohydrodynamic Pressure line contact (Pflumm and Botchan 2001).

Martin (1916) was the first person who attempted to calculate the lubricant film thickness by solving the Reynolds equation for line contact spur gears, with the assumption that the lubrication fluid is isoviscous and Newtonian. Martin's analysis enabled him to establish a formula for the predicted film thickness within the contact as:

$$h_{\min} = h_c = 4.9UW_L^{-1} \quad (1.1)$$

where h_{\min} is the minimum film thickness, h_c is the central film thickness, U is the speed parameter given by equation:

$$U = \frac{\eta_0 u}{E' R_e} \quad (1.2)$$

R_e is the equivalent radius of curvature, E' is the elastic contact modulus, η_0 is the viscosity, W_L is the dimensionless load parameter given by the following equation:

$$W_L = \frac{w}{LE' R_e} \quad (1.3)$$

Where w is the load, L the width of the line contact. u is the entraining velocity described by

$$u = \frac{u_1 + u_2}{2} \quad (1.4)$$

Where u_1, u_2 are the velocities of the two surfaces relative to the contact.

The film thickness predicted by Martin's equation was very small, and is much smaller than the average surface roughness of ordinary gears, therefore his theory failed to explain the lubrication of gear teeth.

Ertel was the author who found an innovative solution to the problem of EHL by including the effects of elastic deformation of the bodies in contact as well as the dependency of the lubricant's viscosity on pressure and temperature. Hence, he opened new doors for further development and consideration of EHL in tribology. In the first assumption of Ertel's method, he considered the lubricant variation in a very narrow gap. Later, he expanded the gap of lubricant using Taylor series as explained by Popova and Popov (2015). This section briefly sketches the central concepts of Ertel's method of elastohydrodynamic. The following two factors can be defined as the core of Ertel's novelty to elastohydrodynamic (Ertel 1945):

1. Pressure dependence of viscosity.
2. Elasticity under high loading.

Ertel assumes that the viscosity is pressure sensitive based on Barus' law (1893)

$$\eta = \eta_0 e^{\alpha p} \quad (1.5)$$

Where p is the pressure, α is a pressure viscosity coefficient of the lubricant, and η_0 is the dynamic viscosity under atmospheric conditions

After the discovery of Ertel, many studies have been conducted to address the problem of Elastohydrodynamic lubrication. Grubin and Vinogradova (1949), developed a theory based on Ertel's (1939) experimental results that integrated the effect of the deformation of surfaces and the viscous response on the pressure with respect to time. Grubin numerically integrated a simplified Reynolds equation over the inlet zone to

the Hertzian contact area. This was done in terms of the reduced pressure, q , where for the Barus viscosity formula

$$q = \frac{1 - e^{-\alpha p}}{\alpha} \quad \text{and} \quad p = -\frac{1}{\alpha} \ln(1 - \alpha q) \quad (1.6)$$

This change of variables simplifies the Reynolds equation given as equation (2.8) in the next chapter for steady state incompressible case. Under these conditions it becomes

$$\frac{\partial}{\partial x} \left(\frac{\partial q}{\partial x} \right) = 12\bar{u} \eta_o \frac{\partial h}{\partial x}$$

When q reaches a value of $1/\alpha$ the corresponding pressure becomes infinite. The Reynolds equation, discussed in chapter 2, and the calculation was organised to identify the film thickness, h_c , that achieved this condition at the inlet to the Hertzian contact zone. This theory led to the well-known film thickness formula:

$$h_c = 1.95U^{8/11}G^{8/11}W_L^{-1/11} \quad (1.7)$$

Where: G is a dimensionless materials parameter.

$$G = \alpha E' \quad (1.8)$$

Predicted film thicknesses calculated by Grubin were two orders of magnitude greater than those predicted by Martin's theory, and comparable to the surface roughness of gears.

Further attempts, between 1950 to 1990, were undertaken to predict a minimum film thickness. Several studies investigated the minimum and central film thickness for the lubricated line contact between smooth surfaces operating in the EHL regime.

A new algorithm for the numerical solution of the Reynolds equation and the elastic deflection due to the pressure was presented by Dowson and Higginson (1959) to obtain the solution to the EHL problem in an iterative numerical method. The method presented two different film thickness curves for a given approximation to the pressure distribution. The first curve is the solution to the elastic deflection equation for the given pressure approximation. The second curve is the inverse solution to the Reynolds equation, i.e. the film thickness curve that results from introducing the

approximate pressure distribution into the Reynolds equation. The authors modified the approximate pressure distribution to reduce the difference between these two curves and so provide the solution after a finite number of iterations. This modification process involved manual adjustments of the pressure distribution in the first published solutions, reflecting the low level of computational power available, but was subsequently developed by introducing an automatic algorithm in the later more complete solutions presented in Dowson, Higginson and Whitaker (1962).

Dowson and Higginson developed a minimum film thickness formula for lubricated line contacts (Dowson & Higginson, 1959) for predicting the film thickness and found that the film thickness can be expressed as follows:

$$h_{\min} = 2.65G_m^{0.54}U^{0.7}W_L^{-0.13}R \quad (1.9)$$

Where G_m is the materials parameter,

Later, central film thickness h_c formulae were also derived based on full numerical solutions. The following is one by Dowson and Toyoda (1978):

$$h_c = 3.06G_m^{0.56}U^{0.69}W_L^{-0.10}R \quad (1.10)$$

Otto (2009) investigated the influence of minimised dip lubrication on the flank load carrying capacity of gears. The results of his research showed a dramatic risk of scuffing, as well as higher bulk temperatures in response to the decrease in oil volume.

A study was carried out by (Ebner et al. 2018) to investigate the impact of starved lubrication of different surface structures on the operating behaviour of highly-loaded EHL line contacts. This was achieved by measuring the friction behaviour in an FZG twin-disk test rig. In addition, the gap fill factors for initial oil volumes were calculated analytically and assigned to the experiments. It has been shown that under dry lubrication, the minimal amount of lubricant is essential to ensure the functionality of highly-loaded EHL contacts. Furthermore, a very small volume of initial oil is sufficient for lubrication and varying the initial oil volume has little effect on the friction. For the surface structures investigated, the area of damage is proportional to the initial volume of oil.

1.4 Surface roughness

The surface of a solid contains many flaws and imperfections. An ideal surface is defined as a perfectly smooth surface and referred to as the nominal surface. In reality, there are no ideally smooth surfaces because the real surface deviates from the nominal surface as a result of the manufacturing process used to create the surface.

The real surface contains peaks and valleys. A peak is specified as a point higher than its two neighbouring points. A valley is a point lower than its two neighbouring points, as shown in Figure 1.6. The irregular spacing forms a pattern or texture on the surface. The surface finish process can affect the surface features depending on the tools used.

The topography of a surface consists of certain components. Surface roughness represents the high frequency irregularities caused by the interaction of the material and the cutting tools. Roughness is characterised by asperities. The real area of contact between two surfaces under load is the combined area of the contacts that occur between asperities. Surface waviness is defined as the medium frequency irregularities on the surface on which the surface roughness is superimposed. The lay is the predominant direction of the surface pattern, normally determined by the production method used.

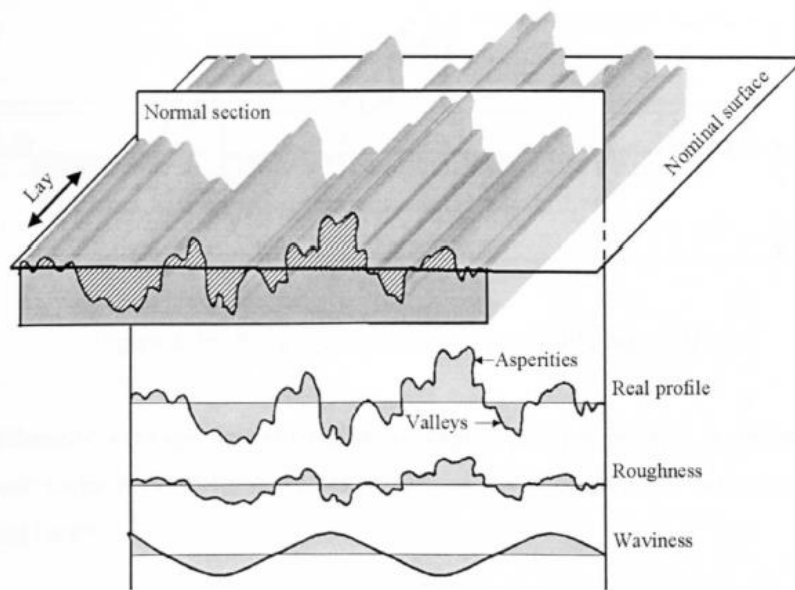


Figure 1.6 Surface texture characterisation (Greenwood 1992).

The measurable surface deviations are known as surface texture. The surface texture is of crucial importance because it affects the real area of contact, friction, wear and lubrication. Gear manufacturing processes leave relatively rough surfaces; typical high quality ground gears used in the aerospace industry have a surface roughness of R_a about $0.4 \mu\text{m}$. (Britton et al., 2000). R_a is the roughness average amplitude parameter which is the most common parameter for measuring the mean height of the roughness profile. R_a can be described by the equation:

$$R_a = \frac{1}{L} \int |y(x)| dx \quad (1.11)$$

where $y(x)$ is the height the surface measured from the mean surface height profile. L is the sampling length.

1.5 Surface Fatigue Failures

Surface fatigue is the failure of surface and near surface material during rolling contact of components as a result of repeated surface loading so that the cyclic sub-surface stresses exceed the endurance limit of the material. The most common modes of failure of surfaces in rolling contact include plastic deformation, wear, contact fatigue,

scuffing, pitting and micropitting (Johnson, 1989). Micropitting can be viewed as the end result of contact fatigue which leads to the initial crack formation at the contact surface or immediately below the surface, and growth of the initial crack may subsequently lead to damage varying in extent from microscopic pitting to larger macro-pits and eventual surface fracture. This work concentrates on conditions that lead to surface failure of surfaces operating in the micro-EHL or mixed lubrication regime caused by rolling contact fatigue and are discussed in the following sections.

1.6 Scuffing failure

Scuffing is the sudden failure of the lubricant film during operating conditions, usually occurring under severe conditions of relatively high sliding velocities and applied load due to localised welding between meshing teeth. It occurs in sliding environments on components such as gears and bearings. Scuffing is characterised by rapid wear and a high coefficient of friction (Hutchings, 1992). It can be seen in gear surfaces as rough-edged scratches, usually at the extreme ends of the contact path where sliding is at a maximum, as shown in Figure 1.7.



Figure 1.7 Scuffing failure in helical gear teeth at their tips. Source: Courtesy of Design Unit, Newcastle University.

There are many suggested theories as to why scuffing occurs, but the most commonly accepted line of thought is that it is related to critical lubricant temperature. This concept was first proposed by Blok (1937). It is seen that scuffing is linked to the bulk

temperature of the component and the instantaneous flash temperature rise, which occurs as the surfaces pass through the contact zone.

Many studies have been conducted investigating different parameters that influence scuffing. Snidle et al. (2008) examined the scuffing resistance performance of a hard coating. It was seen that the hard coating effectively reduced the friction and prevented scuffing from occurring for the relatively rough ground specimens within the operating conditions considered.

Other researchers such as Kobori (1992) and Jackson. et al. (1994) examined the effects of lubricant additives on scuffing failure. Using a twin-disk test, Kobori (1992) found that the scuffing resistance of steel could be improved by introducing additives to form a film with the characteristics of either electrical insulating and high friction or conductive and low friction. The experimental studies of Patching et al. (1995) Nakatsuji and Mori (1998); Li (2015) examined the impact of surface roughness amplitude on scuffing failure, showing smoother surfaces can survive a higher load under the same slide/roll ratio without scuffing. Additionally, the simulation work conducted by Holmes et al. (2005) found that results of the scuffing tests carried out by Patching et al. (1996) where the scuffing location of the axially ground disks was found to be at the transverse boundary of the contact area were consistent with the result from the numerical EHL analysis that showed a higher incidence of asperity contact also occurred at the transverse edge of the Hertzian zone. This was associated with lubricant side-leakage occurring due to the unsealed valley features in a transverse ground surface.

The roughness orientation plays an essential role in determining the contact behaviour. The roughness lay direction and its relation to the scuffing failure for the ball on disk contact was studied by Li (2013) using a scuffing model developed by Li and Kahraman (2013). It was found that the scuffing performance was substantially affected by the roughness lay direction where scuffing resistance was found to be inversely proportion to the difference between the angles of orientation of the lays on the two surfaces.

Contacting surfaces can be protected from scuffing failure by using special additives to improve lubricant properties under severe conditions of high pressure and

temperature (EP additives). Also, protection can be achieved by reducing the roughness of the surface by pre-running of the gears at slowly increased increments of load and speed or by “superfinishing”.

1.7 Pitting failure

Pitting is the formation of microscopic surface notches and cavities caused by rolling and sliding contact fatigue. Unlike scuffing, it does not necessarily occur early in the component’s life. Pits occur at high points on the surface which are subjected to high stresses. These points are sheared due to the interaction with the counter-face creating residual stresses as a result of the shearing which tends to promote cracks which propagate thus removing the high points in an erosive fashion (Chue and Chung 2000). If full EHL film conditions are achieved, and friction at the surface is comparably low, pitting can build up below the surface, primarily in the zone of highest subsurface stress due to the Hertzian contact pressure. An example of pitting in gear contacts is shown in Figure 1.8. It is seen from this figure that the fracture surfaces of the pitting failures have irregular morphology. The progressive form of pitting is likely to be found on the tooth dedendum but it may spread further to the pitch line area.

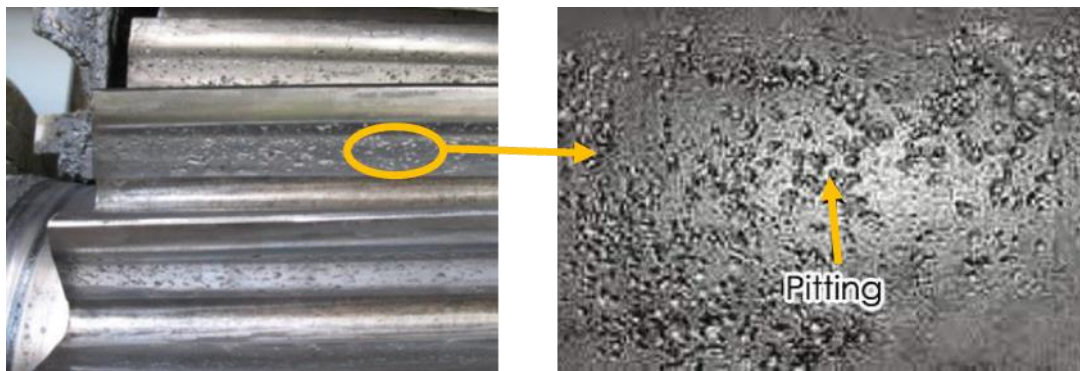


Figure 1.8 Pitting failure of spur gear teeth (Novex.com 2018).

It is worth mentioning that mild wear can continue to remove material at the rolling/sliding asperity encounters even when gears operate under conditions that may not be severe enough to cause pitting or scuffing failure. Also, the edges of pits can break and form large irregular shapes that can adjoin one another. Thus, gear materials are generally subjected to heat treatment to prevent surface fatigue failures such as pitting or spalling.

1.8 Micropitting failure

Micropitting is a near-surface fatigue response to the very complex tribological behaviour of lubricated rough surface contacts. It is also known as grey staining or micro spalling. It appears in the form of progressive material removal through rolling contact fatigue (Clarke et al., 2015). Micron-sized pits are commonly seen on the surfaces of rolling mechanical elements such as bearings and gears that operate under mixed elastohydrodynamic lubrication (mixed EHL) or boundary lubrication conditions.

Micropitting can sometimes be seen by the naked eye and the size of usual pits are of the scale of the roughness and often associated with plastic deformation due to the running in the process. Micropitting is of the scale of the asperities, and their diameters tend to measure the order of microns (Aslantaş and Taşgetiren, 2004; Snidle et al., 2004). The experimental study of Aslantaş and Taşgetiren (2004) on ductile iron gears suggested that there is an opposed relation between pitting and temperature, as when the temperature decreases, pitting formation life increases. So the pitting resistance of the surfaces is affected by temperature and time.

Research on micropitting may be divided into experimental and theoretical areas. Experimental work has concentrated on the development of test rigs and test procedures in order to reproduce micropitting under controlled conditions. Generally, these tests have provided a better understanding of micropitting behaviour and enabled the identification of those parameters which influence the problem. The theoretical approach is to study the possible mechanism of micropitting predominately by calculating pressures and tractions in rough surface contacts operating in the mixed lubrication regime. A further avenue for modelling is the hypothesis that pits grow in response to internal lubricant pressure when the crack mouth is sealed by elastic deflection as the crack moves into the Hertzian contact zone.

The micropitting tests reported in the literature have been undertaken either on gear test rigs or on disk machines. Disk machines have been widely used and have proved to be a repeatable way of producing micropitting under controlled conditions. Examples of the use of disk machines are found in various studies (Zhou et al. 1989; Webster and Norbart 2008; Li and Kahraman 2013; Evans et al. 2013; Clarke et al.

2016; Hutt et al. 2018) and others. Examples of the use of gear tests are found in studies by Winter and Oster (1990); Bull et al. (1999); Oila et al. (2005) and others.

For many years, it has been a matter of controversy as to whether or not the propagation of cracks in rolling contact fatigue is influenced by, or is even dependent upon, the presence of a fluid, such as a liquid lubricant. In Way's 1935 experiment (Way, 1935) rolling fatigue only occurred when a liquid was present, perhaps because the fluid entered the crack and created an opening displacement, despite the predominantly compressive field of stresses.

Theoretical studies (Bower, 1988; K. Matsuda et al., 1997) have addressed the possible mechanisms of micropitting. It has been proposed that the fluid may act in one of two ways: either the fluid pressure acts directly on the crack entrance (fluid pressurisation) as a result of the high elastic pressure in the region of contact or, alternatively, fluid becomes entrapped in the crack and a region near the tip is pressurised by the motion of the area of contact across the surface (fluid entrapment). The observations made from experimental studies have further helped the understanding of micropitting. Micropits occur at the tips of asperities, particularly near the roots of the teeth, and this damage manifests itself without necessarily affecting the corresponding contacting part of the tooth on the meshing gear. Damage starts in the form of small surface pits typically 10–30 μm in diameter and 5–10 μm in depth (Evans et al., 2012). Figure 1.9 shows micropitting damage on the teeth of a helical gear used in a testing programme at the Design Unit of Newcastle University.



Figure 1.9 Micropitting predominantly in the dedendum region of a helical test gear tooth.

The term ‘grey staining’ is widely used to describe the dull appearance of micropitting on the gear flank. Micropitting seems to be due to surface contact fatigue and plastic deformation on the scale of roughness asperities (Evans et al., 2012).

In the initial stages of growth, the cracks which give rise to micropitting or pitting are usually inclined at a shallow angle to the surface, as shown in the damaged surface sections of gear teeth in Figure 1.10 which suggests that surface cracking can lead to crack-branching which, in turn, can develop into the large-scale (macro) pitting and eventual tooth fracture.

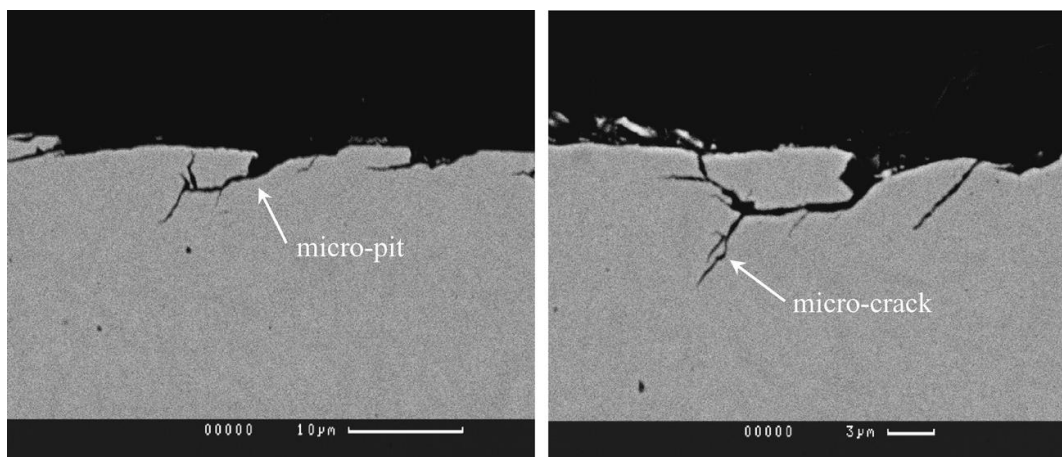


Figure 1.10 Sections through micropits showing crack growth (Evans et al., 2012).

The factors that influence the micropitting nucleation are diverse, including operating conditions, lubricant properties, material properties, surface roughness, etc.

Investigations by (Berthe et al.,1980) suggested that surface roughness was the driving force for the phenomenon and this is now generally accepted. Spikes et al. (1986) also showed that there was plastic deformation and that fatigue cracking occurred during the damage process. The importance of surface roughness has also been experimentally observed by other researchers, including Tokuda (1982); Maeda et al. (1980) and Cheng and Cheng (1995), using a two-disk contact setup. Thus, the surface finish appears to have a significant influence on the micropitting life, as higher roughness leads to wider micropitting areas (Zhu et al., 2009; Predki et al., 2011 and Gould and Greco, 2016).

Besides the surface roughness, many other factors that influence micropitting have been investigated. Some works examined the effects of normal load (Tokuda, 1982; Oila and Bull, 2005; Li and Kahraman, 2013; Mallipeddi et al. 2018) pointing to its significant role in micropitting, i.e., higher load results in more micropits.

Some studies focused on the direction of sliding. The theoretical work by Aslantaş and Taşgetiren (2004) suggested that the direction of micro crack changes depending on the presence of nodules near the crack tip and the shapes of micropitting do not depend on rolling direction. However, this assumption was disproved by the work of Oila (2003); Brimble et al. (2001); Cen et al. (2018) which showed that the prorogation of micropits is opposite to the sliding direction. Micropitting cracks characteristically grow in a direction which is opposite to the direction in which the sliding frictional traction acts on the affected surface, i.e. towards the pitch point on the driver's tooth, and away from the pitch point on the driven tooth as illustrated schematically in Figure 1.11. The early damage occurs at the tips of surface asperities, particularly in the root (dedendum) parts of both the driver and driven gears (Clarke et al., 2015). However, the shallow surface cracks may grow and lead to deeper crack branching, which in turn can develop into the larger scale (macro) pitting (Brimble et al., 2001; Morales and Gabelli, 2018).

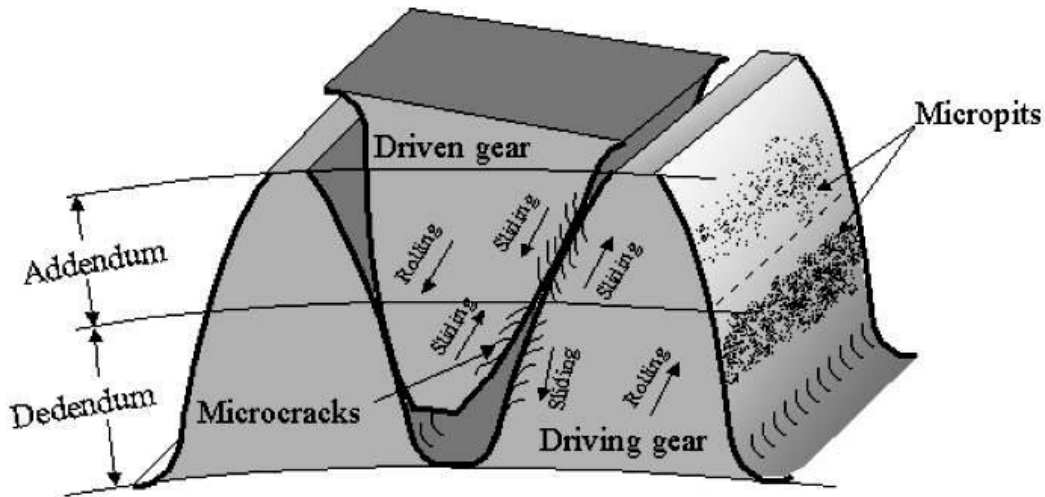


Figure 1.11 Illustration of the observed direction of the growth of micro-cracks, rolling (R) and sliding (S) velocities on the wheel and pinion gear teeth (Oila 2003).

Following experiments conducted by Oila and Bull (2005) assessing the effect of different parameters on micropitting, Oila et al. (2005) concluded that an appropriate choice of steel was the most significant factor in reducing martensite decay. The influence of temperature was also found to be significant. It was also proposed that the heat generated by plastically deforming asperities might play a role in promoting martensite decay in isolated regions. Contact pressure was also found to be influential in the initiation of micropitting, whereas sliding speed was found to be most significant in micropitting propagation (Oila and Bull, 2005).

The experimental work of Kadiric and Rycerz (2016) showed that under controlled conditions of a triple-disc micropitting rig, an increase in slide-roll ratio results in increased levels of micro pitting as a result of the increase in the number of stress cycles on a single asperity on the contact body during the contact passage.

The propensity for interactions is typically indicated by the Lambda ratio, (also known as the specific film thickness). First proposed by Tallian (1967), this is defined as:

$$\Lambda = \frac{h}{R_c} = \frac{h}{(R_{q1}^2 + R_{q2}^2)^{1/2}}$$

where h is the film thickness of an equivalent contact with smooth surfaces, and R_c is the composite roughness. R_c is composed of R_{q1} and R_{q2} , which are the R_q (RMS roughness) of the two surfaces. Λ is a measure of the inherent film-forming capability

of the lubrication mechanism taking into account load and temperature variation, with decreasing λ values indicating decreasing film-forming capability. λ is a widely used parameter in the tribological consideration of rough surfaces and has been shown to correlate with gear and bearing fatigue.

Another group of studies focused on the effects of the lambda ratio and the hardness. Increasing the lambda ratio, either by increasing the film thickness or reducing the surface roughness, could reduce or prevent micropitting. The difference in hardness between the two rough surfaces might considerably affect the rate of micropitting, the softer surface being much more prone to micropitting. For equally hard surfaces, when the faster surface is rougher than the smoother slower one, a higher number of fatigue micro-cycles are imposed on the smoother slower surface (Spikes et al., 1986; Webster and Norbart, 1995 and Brechot et al., 2000; Lainé et al., 2008; Morales-Espejel et al., 2018 and Vrček et al., 2019). These studies are essential because they show that contact fatigue is not only related to metal-to-metal contact but could be a result of pressures transmitted by the fluid film.

Surfaces of a similar hardness exhibit far less wear, maintaining finer features as they run in. However, under moderate conditions after sustained loading, the mechanism of deterioration appears to be much more akin to micropitting with the plastically deformed asperity peaks, which have been associated with regions of high residual tensile stress as seen by Bryant et al. (2012), giving way to new valley features. This failure mechanism has in the past been associated with the roughness features of the surface as seen by (Tao et al., 2003).

Micropitting appeared to form at the position of asperity features which were prominent in the original, as manufactured, surface and experienced significant plastic deformation during the running-in process (Oila et al., 2005; Clarke et al., 2016; Mallipeddi et al., 2018). It has also been verified that where micropitting is seen to occur, a higher amount of modification will be present on the slower surface, despite it undergoing fewer load cycles. The reason for this is considered to be related to the load cycling encountered by asperity features as they traverse the contact zone (Sharif et al., 2012).

The experimental work of Lainé et al. (2008) using disk machine tests suggested that there is a very strong relationship between roughness, film thickness and micropitting wear. It was found that there was an almost inverse correlation between the micropitting damage in the disk test rig and the mild wear in the reciprocating sliding test. This observation was referred to the tendency of anti-wear additives to prevent running-in of the rough surface.

Mallipeddi et al. (2019) compared the micropitting resistance of gears processed by grinding, honing and superfinishing. They concluded that the surface asperities could have a enormous influence on the surface-initiated fatigue such as micropitting. The micropitting initiation could be significantly affected by the running-in load level, but only for rough surfaces.

An interesting study by Morales-Espejel et al. (2018) using numerical simulations points out that some initial mild wear can be beneficial. Ideally, some mild wear at the beginning of gear pair operation can be sufficient to reduce subsequent micro pitting, leading to zero or very small amounts of wear for the rest of the gear pair life. If no wear was present, micropitting damage increases with decreasing film thickness as may be expected, but when some wear is present micropitting damage may reduce as the film thickness is lowered to the point where wear takes over and removes the asperity peaks and hence reduces asperity interactions.

The rate of pit formation and growth was investigated by Hutt et al. (2018) who considered how the average surface heights in the pitting locations were modified during the test. It was found that the pit locations were at relatively high elevations at the beginning of the test and their mean height was changed significantly as a result of the running-in process. However, it is important to note that the majority of the pitting occurred in the early stages of the fatigue test.

Mayali et al. (2018) examined the micropitting initiation theoretically and experimentally based on the real surface topography contacting under the mixed-EHL regime. The experimental results showed that the first micropits formed within 100,000 cycles of operation, which is in broad agreement with the model predictions where the most heavily damaged asperities failed in the first 30,000–100,000 cycles of operation.

1.9 Running-in

Running-in is a process that most contacting surfaces of machine elements undergo at the first time they are loaded together during their operating life. They have an initial settling period, where the prominent surface roughness asperity peaks are significantly modified or removed. When two surfaces are pressed together, the first contact takes place at the peak points of the highest asperities, which deform plastically or elastically under the load so that more asperities will be brought into contact. Therefore, the real contact area may be only about 10 % of the surface area predicted by Hertzian theory (Holmberg and Matthews, 2009).

The running-in phenomenon is specified as a series of processes during which the parameters of friction and wear for contacting bodies stabilise (Hutchings, 2003). These parameters are governed by changes in the rough surface features due to plastic deformation and mild wear. Furthermore, chemical changes that occur in the lubricant and tribo-films that form on the contacting surfaces also affect friction and the wear rate. During their initial running the most aggressive asperities are subject to combinations of normal and tractive loadings that exceed the elastic limit. This loading results in surface topography modification by what is reported to be a combination of wear and plastic deformation (Teer and Arnell, 1975; Akbarzadeh and Khonsari, 2010; Kumar et al., 2002 and Zhang et al., 2018).

1.9.1 The effect of different operating conditions on running-in

Running-in of gears performed under controlled conditions has a major impact on durability and mesh efficiency. The effectiveness of running-in depends on different operating conditions such as load, speed, physico-mechanical properties of material and lubrication medium (Kragelsky et al., 1982). Akbarzadeh and Khonsari (2013) modelled the effect of different operating conditions during running-in on the steady-state surface roughness of an EHL line contact problem. The model was a smooth rigid interacting with rough surface where the asperity heights have a Gaussian distribution. They observed that corresponding to each applied load, there is a value of speed which results in a minimum value of the average of asperity heights Ra at the end of running-in period. Previous to this study, Akbarzadeh and Khonsari (2010) reported that after the running-in process, the portion of the load carried by the asperities decreases, while

the portion of the load carried by the fluid film increases. Hence, the friction coefficient decreases during the running-in process.

It is usual that running-in is implemented at lower loads and sometimes lower speeds which result in reduced friction between the contacting components. The load and speed are then slowly built up to the operating conditions in stages, as shown by Ostvik and Christensen (1968). In the case of concentrated contacts which is the main interest of this research, during the process of running-in when load is applied, high pressures will be generated in the contact regions. As the surfaces possess a surface roughness from the manufacturing process the concentrated contacts will include many micro-contacts between surface roughness asperities. The surface asperities will deform until the increased bearing area is sufficient to support the applied load. Ostvik and Christensen also showed that the load carrying capacity of a contact operating in the regime of elastohydrodynamic lubrication (EHL) became significantly improved by running-in, and that surfaces subsequently scuffed at higher loads. Similar observations have been reported by Akbarzadeh and Khonsari (2011) during a running-in test performed on a gear test rig. They also noticed that when the surfaces became run-in, the contact of asperities became less frequent due to removing or flattening of the highest surface features. It is seen from comparison of profilometry results that finer features are subsequently removed as a result of wear processes.

Sjöberg et al. (2016) showed that a higher running-in load yields higher gear mesh efficiency and has greater effect on surface roughness parameters than a lower running-in load. Cavatorta and Cusano (2000) and Kragelsky et al. (1982) also showed that increased load significantly increased the amount of asperity deformation.

Work by Morag and Etsion (2007) described a revised elastic–plastic contact model of a single fractal asperity. They found that the critical contact area is scale dependent, as the applied load increases, the contact area increases as well, and a transition from elastic to plastic contact mode takes place in this order.

Wagner et al. (2017) studied the effect of maximum Hertzian contact pressures of 1 and 2 GPa and of surface texture on the running-in behavior of carburized steel under boundary lubrication. The tests were performed on a micropitting rig under a slide-to-roll ratio value of 0.2. This work reported the variation of roughness parameter (R_a ,

Rz) with the increase in running-in time from 0 min to 150 min and also observed a stable surface roughness within 5 minutes.

Bosman et al. (2011) conducted an analysis of the running-in process, where an elastic-plastic contact solver and a friction model were used in their semi-analytical method to explain the running-in process. However, this study's model is based upon the assumption that the plastic deformations are small, and so the results of the elastic-plastic model are unrealistic for large plastic strains.

1.9.2 Effect of hardness on running-in surfaces

Wagner et al. (2017) showed evidence of hardness gains within the contact region following approximately 110,000 load cycles. It was shown that running-in occurs at a relatively low number of contact cycles and hardness gains are present in this time frame as well, and it was proposed that work hardening develops early on within the same number of cycles.

Other studies have also observed an increase in hardness following rolling contact fatigue tests. (Burbank and Woydt, 2016) work hardened steel run-in at a contact pressure of 3.8 GPa for 10,000 cycles. It was found that there are significant increases in material hardness in the contact zone, as well as the introduction of beneficial compressive residual stresses close to the surface.

A previous study by Kang et al. (2014) saw an increase in hardness after 10^7 cycles under a contact pressure of 3.7–5.6 GPa, but this may have occurred in earlier cycles. Residual stresses are induced during running-in, due to work hardening and the transformation of retained austenite to martensite (Turteltaub and Suiker, 2005). The concentration of residual stress due to the phase transformation aids in the accumulation of strain in the material which can result in an increase in material hardness.

Jenson et al. (2018) investigated the evolution of hardness and tribofilm growth during the running-in of steel components with a range of contact pressures and initial composite roughness conditions. He found that tribofilm growth had no significant effect on the measured hardness increase. Also, the results showed that a higher initial composite roughness produced greater gains in hardness than increasing the contact pressure during the running-in process. After increasing the hardness during the run-in period, hardness appeared to stabilise almost immediately.

During the running-in of surfaces, it is understood work hardening can occur as a result of plastic deformation, contributing to the increases in hardness observed (Blau, 2008).

Bishop and Snidle (1982) conducted experimental tests that examined the scuffing limit as well as the running-in process for circumferentially ground steel disks when they were loaded together under EHL conditions. Their experiments revealed that the roughness features of the less hard disk were modified significantly, but that the harder disk was virtually unaffected by the running-in process at the same load. The most noticeable result to emerge from this work is that the running-in process is very quick and that there is also a rapid increase in radius of curvature of asperities as they deform. Under EHL operating conditions, the modification allows for more effective lubrication due to the less severe pressure spikes experienced at each ‘micro-contact’ due to improved conformity as the shape of asperities become more rounded. The shape of valley features remained unchanged and it was concluded that this was because they were not subject to the same high contact pressures or degree of interaction as the asperities.

For two disks in contact that have different hardness values, the plastic deformation during running-in happens on the surface with lower hardness. The same observation was seen in the experimental work of Akbarzadeh and Khonsari (2011). This observation also supports the conclusion that the process is one of plastic deformation. It is also found that micro pits occur at the position of asperity features which were prominent in the original, un-run surface and experienced considerable plastic deformation during running-in.

1.9.3 The influence of surface topography on efficiency

Other authors (Xiao et al., 2003; Larsson et al., 2011; Bergseth et al., 2012) have studied the influence of surface topography on efficiency (e.g. friction and lubricated contact) of polished and ground surfaces in twin disc and mini traction machines and have all found an overall higher efficiency in polished surfaces. An important factor in any lubricated contact is the film thickness ratio (Λ) parameter which relates the minimum film thickness to the RMS of the combined surface roughness necessary to separate the surfaces. When dealing with low roughness surfaces, Stanley et al. (1990) showed that these surfaces exhibited an increase in adhesion force if film thickness was below a certain threshold when compared to roughness profiles.

Andersson et al. (2016) investigated the effect of running-in on superfinished gears by using a FZG gear test rig. They found that when the as-manufactured surface has a small value of Ra ($0.08 \mu\text{m}$), the effect of running-in on this surface decreased (small changes to the surface topography happened). Superfinished gears showed an overall higher efficiency.

Mallipeddi et al. (2018) conducted running-in and efficiency tests on ground spur gears using an FZG gear test rig. They observed that surface asperities were smoothed through plastic deformation during running-in and micropitting which occurred after running-in.

Blau (2008) claimed that the initial period of plastic deformation can also modify the subsurface microstructure of the contacting components, causing a degree of work-hardening. However, most studies have concentrated on the geometric changes in the surface roughness features as this has the most direct implications for the hydrodynamic performance of the interface. Jeng et al. (2004) provided little explanation of running-in as a result of plastic deformation. Early experimental examinations have focused on the significance of considering the running-in process of lubricated surfaces because during this process the roughness profiles are modified considerably due to a smoothing of the asperities by plastic deflection (Wang et al., 2000; Nogueira et al., 2002; Zhu et al., 2007; Evans et al., 2013).

Sosa et al. (2017) conducted in situ surface measurements during running-in cycles. They conclude that the most significant changes in roughness surface and friction occurred during the first initial cycles at high load. The valleys stay unchanged while the asperity peaks become flatter. As a consequence of modification in topography, the friction tends to reach a steady state condition with respect to contact pressure, surface roughness, surface microstructure and the establishment of effective lubricating film at their interface (Tripathi et al. 2017).

Horng et al. (2002) conducted experimental disk on block tests in line contact by using a range of loads and surface finishes. Running-in is still mainly referred to as a wear process by the authors who also make some reference to plastic deformation. The effect of different loads on the same surface finish are shown in Figure 1.12. It was found that a higher applied load results in a larger modification in surface shape, while

also reaching a steady state after a short operating time. The disk, or upper specimen, was finished to a considerably smaller average roughness and was then observed to bear little or no modification in surface shape. With a longer period of running-in, the contact width and real contact area were observed to increase.

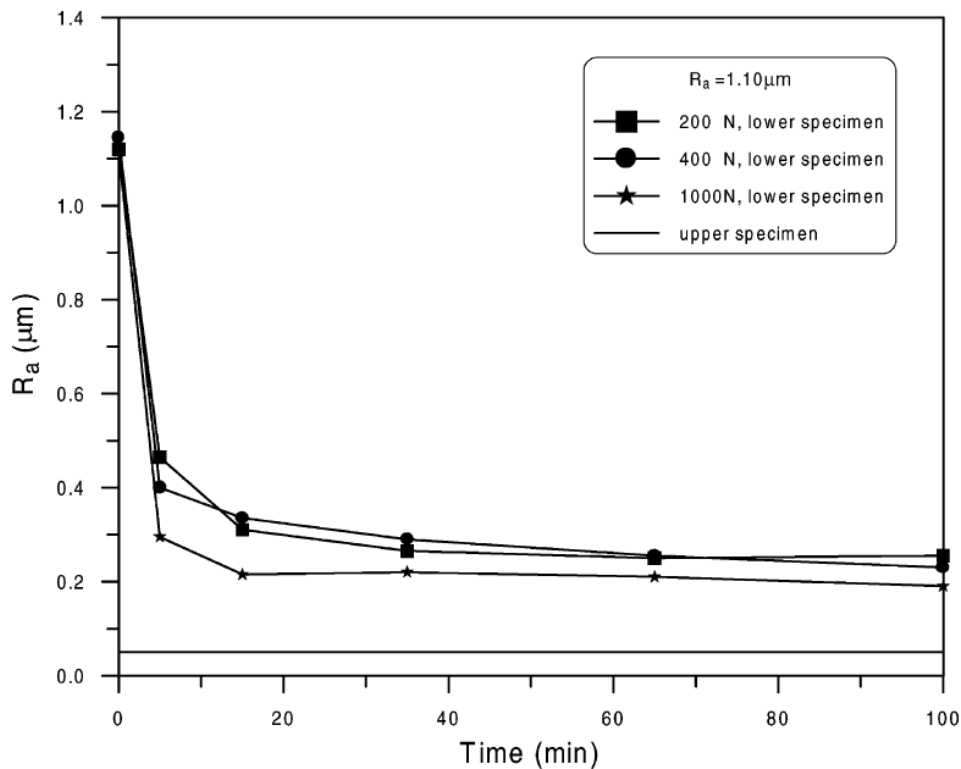


Figure 1.12 Difference of average roughness value of specimens at initial roughness of $1.10 \mu\text{m}$ with different applied loads (Horng et al., 2002).

1.9.4 The effect of the plastic deflection on residual stresses

Bryant et al. (2012) used finite element modelling to investigate the plastic deflection of surface roughness in line contacts using a plane strain contact model. One of their observations drew attention to residual tensile stresses caused by the plastic deformation during loading. Examples of these can be seen in Figure 1.13. When the load is removed, high residual stresses can be seen at the subsurface aligned with the asperities. The authors also showed that the residual surface roughness deformation only affects the asperity peaks and does not extend to the valley features.

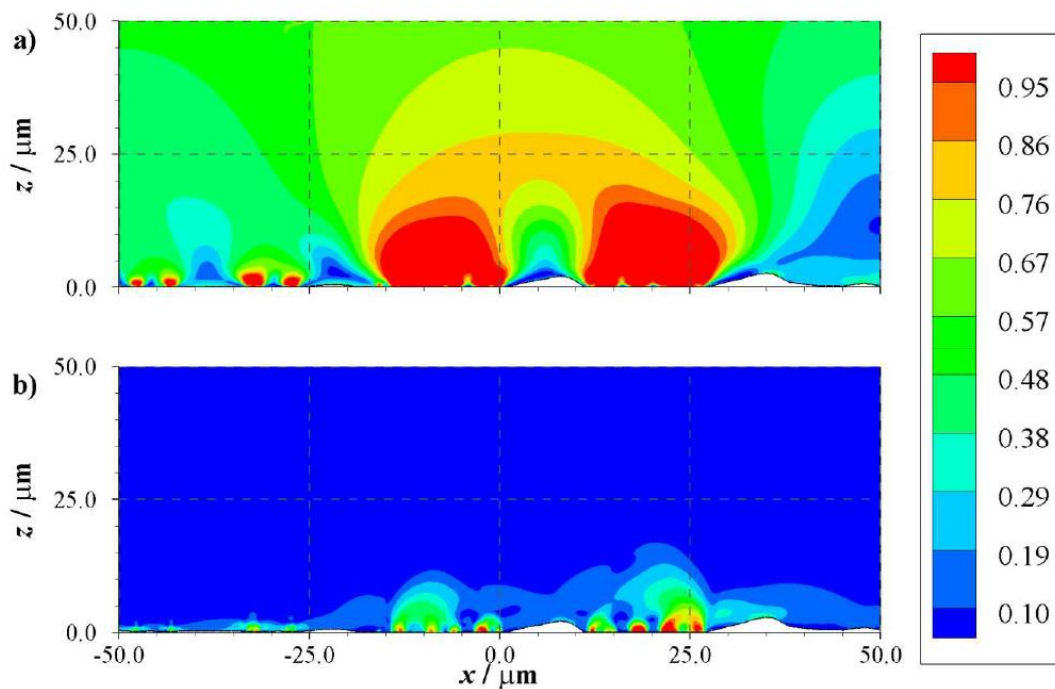


Figure 1.13 Stress contours for the line contact of surface roughness which have been normalised for a yield stress of 1.62GPa, (a) Loaded , (b) residual von Mises stress contours (Bryant et al., 2012).

In work by Al-Mayali et al. (2017), the running-in process was seen to cause significant residual stress at, or near, the surface due to the plastic deflection. This can be an important factor in fatigue damage estimation and, thereby, affect the fatigue life of the contacting components of real rough surfaces in the micro-EHL regime. Al-Mayali calculated the elastic/plastic deflection of the rough surface with a commercial finite element software (ABAQUS) using the observed asperity shape change to infer the appropriate asperity load. He was then able to incorporate the resulting residual stress developed during the early stage of running-in of gears into fatigue simulations based on a full mixed EHL solver. Having examined the results, it was observed that the residual rough surface deformation only affects the asperity tips and does not extend to the valley features.

Recently, more research has been focused toward the consequences of running-in in its effect on surface fatigue failure, due to substantial change in surface topography during running-in. A study of Mallipeddi et al. (2018) also reported that the surface stresses increased after running-in process.

1.9.5 Effect of surfaces statistics during running-in process

Greenwood and Williamson (1966) presented pioneering work on statistical description of rough surface contact to predict the real contact area and separation between a rough surface and a flat when load and nominal contact area are given. The rough surface was assumed to be isotropic in which asperity heights followed a statistical distribution and asperity tips shape are spherical. Using these approximations, the constant radius of curvature (mean asperity radius) was used to determine the contact parameters. Whitehouse and Archard (1970) quantified the surface roughness using several statistical parameters that had not been employed before as descriptors of surface topography. Whitehouse and Archard considered the mean radius of curvature of the asperity peaks to be a significant descriptor of a surface measurement. The geometric modification in the surface asperity peak shape during the running-in process is most frequently described by the use of the arithmetic average roughness parameter. The average roughness value (Ra) is used as a descriptor of the surface height deviations from the mean line. Despite the fact that Ra is in common use, it does not give any information concerning the shapes of the surface asperities (Arnell, 1976 and Bhushan, 2013).

Barber et al. (1987) investigated contact between piston ring and cylinder materials for a range of honed surface finish qualities experimentally. It was found that when subjected to constant loading, all materials reached a condition of nominally steady state wear quite rapidly. The majority of the surface roughness modification occurred within the first 10 minutes of loading. During this time the roughness height decreased and the skew of the surface height distributions increased. The observed changes in the Ra value are shown in Figure 1.14. It was also found that the initial surface finish had an effect on the scuffing load. When the initial Ra was greater than a threshold of approximately $0.2\mu\text{m}$ the scuffing load was found to reduce with increasing surface roughness. It was proposed that the proportion of the surface undergoing further plastic behaviour reduced during running time. The biggest reduction was found to occur quite early in the operating period as shown in Figure 1.14. It is important to see that the ten-minute period required to achieve steady state will depend in part on the time taken to reach steady state temperature in the test. This does not conflict with the observation that running-in is a very rapid process. However, in an endurance

experiment there will be a varying oil film thickness as the test component temperature changes and further asperity plastic deformation will occur as a result.

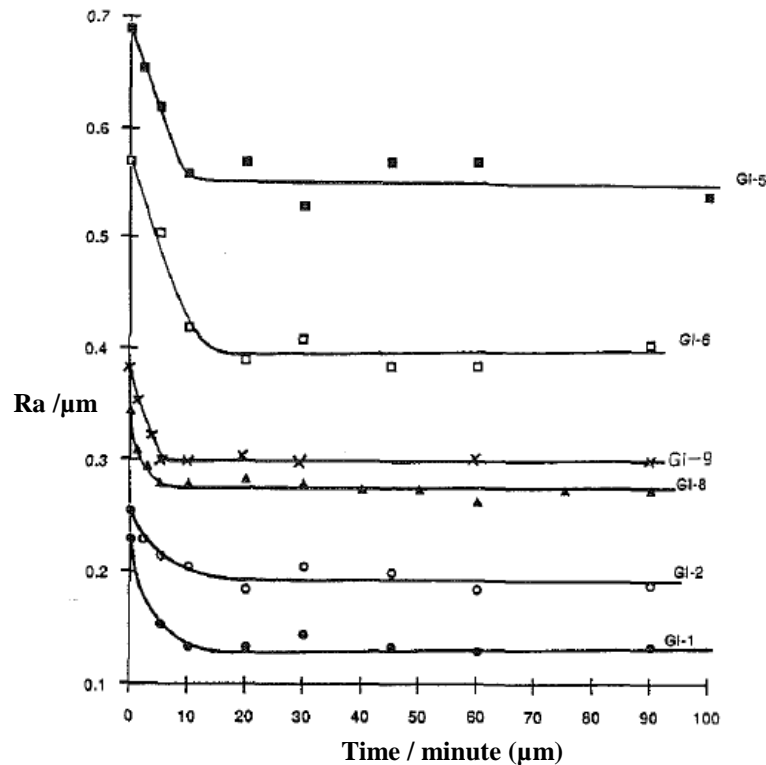


Figure 1.14 Average roughness parameter on cylinder liners versus time for a range of different grey iron surface finishes (Barber et al., 1987).

Clarke et al. (2016) measured the range of surface roughness heights present on transverse ground hardened steel surfaces in their as-manufactured form and then after running them under mixed lubrication conditions using in-situ profilometry. They also observed that the running-in is a quick process, where the peaks of the most prominent asperities are plastically deformed during the early loading stages. In these tests the surface roughness lay was perpendicular to the rolling / sliding direction so that asperity interactions were transient in nature rather than steady state as in the case of the circumferentially ground disks used by Bishop and Snidle (1982). The resulting finish also showed a considerably skewed height distribution, with valley features retained and asperity peaks that are less prominent and more flattened. Clarke et al. (2016) evaluated the radius of curvature of asperity tips for the un-run surface and for the surfaces after running-in and found that the mean asperity tip radii had increased

by a factor of four after running-in. The expansion in bearing area happens as the asperities supporting the load deform plastically and their height reduces. This brings further roughness features into the contact which share in supporting the load.

Prajapati and Tiwari (2019) performed a simulation on 3D rough surfaces having different skewness and kurtosis. They showed that the surface topography parameters vary during the running-in and wear processes. The mean summit radius and individual asperity summit radius were seen to be important parameters, which decide the real contact area, mean contact pressure and significantly change during the wear process. It was also found that after running-in, the surface became flattened resulting in an increase in the summit radius. This observation is also seen in the experimental work of Leighton et al. (2016). They found that during running-in, surface measurements show a rapid increase in the radius of curvature of asperity peaks whilst the height of these is reduced and asperity geometry becomes flatter with the running-in process.

Pogacnik and Kalin (2013) investigated the asperity-peak properties for five different real surface roughnesses after running-in in the broad engineering range from $R_a=0.003 \mu\text{m}$ to $R_a=0.70 \mu\text{m}$. The asperity peak was analysed by considering three criteria that take into account the number of neighbouring points used to define an asperity. They chose to do this using 3, 5 and 7 points referring to the criteria as 3PP, 5PP and 7PP. The radius of curvature for each asperity-peak was calculated for each criteria. They concluded that the asperity-peak radii decrease with the increasing surface roughness for all the three criteria as shown in Figure 1.15.

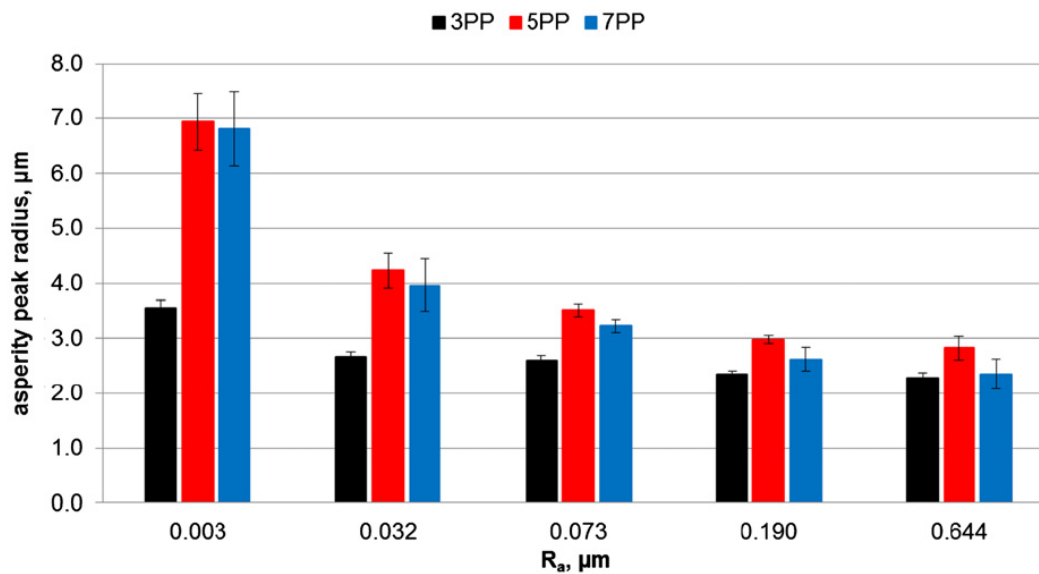


Figure 1.15 Asperity-peak radii in relation to the roughness parameter R_a for the three criteria of 3PP, 5PP and 7PP (Pogacnik and Kalin 2013).

Prajapati and Tiwari (2019) studied the evolution of roughness topography parameters during running-in and a subsequent rolling contact fatigue experiment. They also found that running-in is a fast process where substantial change in surface topography occurs due to plastic deformation of most prominent roughness peaks. The transition from boundary to mixed-lubrication regime is observed during the running-in test. The roughness parameters such as average roughness, root-mean-square roughness and the peak-to valley height changed significantly after running-in and the surface features became more flattened.

It has become clear in these works that the essential factor in the running-in process is the changes that occur to the asperity peak shapes and the consequent enhancement in hydrodynamic performance. Pang et al. (2009) studied the evolution of the autocorrelation function of rough surfaces during running-in, and they found that the shape of the autocorrelation function becomes smoother reflecting the local polishing.

Hutt et al. (2018) conducted experimental tests to study the running-in and subsequent micropitting of a pair of hardened steel surfaces with a slide / roll ratio equal to 0.5 under mixed lubrication conditions at a load of 1.2 GPa. It was found that there was a large reduction in the surface roughness after the first loading stage at the start of the running-in process. In the following load stage of 6000 revolutions, there was a

negligible decrease in surface roughness compared to that observed in the first stage. Detailed measurements of the evolution of surface features have shown that running-in is a quick process whereby the numerous asperities become flattened and rounded during the first few cycles of operation. This is shown in Figure 1.16. Most of the changes observed are due to plastic deformation. It can also be seen that there is very close agreement between profiles taken after the running-in stage and those obtained at the end of the test.

This confirms that running-in happened extremely rapidly at the beginning of the test, which is in agreement with previous work which concluded that early running-in is predominantly a process of plastic-deflection (Clarke et al., 2016). Subsequent changing of the surface shape is predominantly due to micropitting and wear rather than further running-in. Nevertheless, for the most aggressive asperities the local material volume appears to reduce which implies some material removal as well as pit creation. An example of the apparent pits can be seen in Figure 1.16 at positions of A, B, C and D.

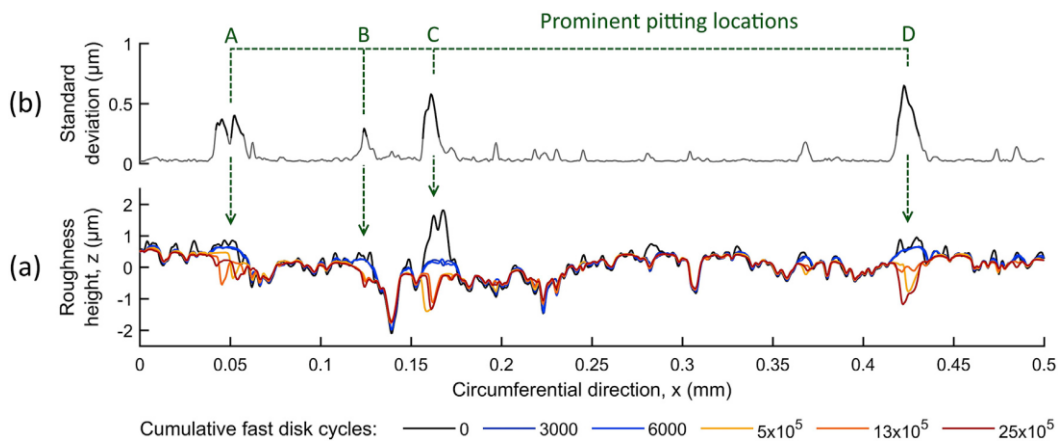


Figure 1.16 An example of micro-pitting identification using a 0.5 mm profile length from the fast disk centre-line. (a) A selection of realigned profiles showing the surface in the following conditions: un-run (black), run-in (blue), and pitted (yellow to red). (b) The standard deviation of realigned profiles measured between 6000 and 25×10^5 fast disk cycles is shown above (Hutt et al., 2018).

Hutt et al. (2018) also revealed that the acoustic emission (AE) at the contact was highly sensitive and strongly related to changes in asperity interaction under mixed

lubrication conditions due to running-in process as shown in Figure 1.17. This figure shows that when the disks were first loaded at the start of the running-in, there was an extremely short transient peak in the mean AE signal to above 1.5 mV. After this it remains at a comparatively steady state of approximately 0.9 mV until the end of the first stage. As it is known that there was a large reduction in the surface roughness during this period so a large reduction in AE is also expected.

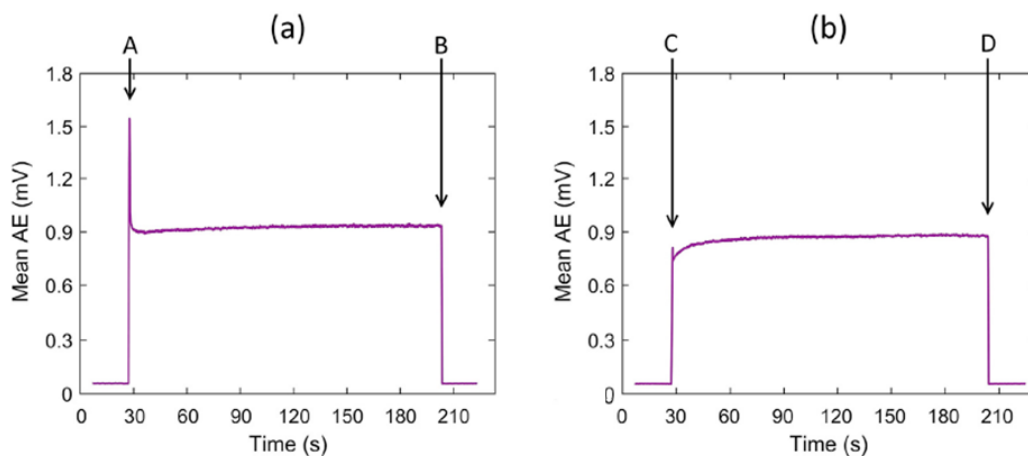


Figure 1.17 Acoustic emission data for (a) the first test stage, 0–3000 fast disk cycles and (b) the second test stage 3000–6000 fast disk cycles. Data for the unloaded periods preceding and following the test are also shown, with arrows A and C indicating the points of loading and B and D the points of unloading (Hutt et al. 2018).

Zhang et al. (2018) studied the evolution of roughness parameters numerically in order to investigate the behaviour of surface topography during the running-in mixed lubrication regime. The simulation was for a smooth stationary plate and a sliding rough cylinder. The roughness parameters of skewness and kurtosis were selected to describe the changes of the surface roughness. They found that “the skewness of rough surface decreases during the running-in process”. This statement is probably misleading as skewness = 0 for a symmetric distribution and if the skewness value is negative, increased skewness will correspond to a more negative value, i.e. a reduction. Zhuravlev (1940) investigated the simulation model of surface roughness as a distribution of micro-contacts with spherical summits to produce a factor that might express the tendency for a contact to plastically deform.

Ghosh and Sadeghi (2015) proposed a novel approach to simulate the running-in and steady wear stages. They performed simulation on rough surfaces over a widerange of RMS roughness, skewness and kurtosis in contact with a rigid plane surface. The method was applied to a linear elastic material. This investigation highlights the importance of studying the effects of surface parameters on wear rate. The plastic deformation component of asperities was also studied in situ by Berthe et al. (2014) in rolling contact for the first 20 cycles, and it was shown that the running-in process stabilized after 10 cycles.

The aim of this study is to develop a method to synthesise the surface geometry changed experienced by the as-manufactured surface during running-in using a mixed EHL analysis. The synthesised and measured run-in surfaces will be compared in various ways. Firstly, their geometry will be examined in terms of shape and asperity peak radii of curvature. Secondly, rolling sliding EHL contact analyses will run under the real operating conditions and their behaviour in terms of peak asperity pressure and direct contact will be assessed. Finally, the transient mixed EHL analysis results will be used to apply surface loading to the rough profiles to obtain stress histories to be used for fatigue modelling of the surfaces, and for comparing the predicted growth of micropitting with results obtained from a parallel experimental study.

1.10 Thesis aims and structure

The main aim of the thesis was to develop a procedure to synthesise the running-in process based on the way that real as-manufactured surface roughness profiles run-in during experimental tests. The objective was to create a numerical simulation model of the asperity modification that is similar to the real case for transverse ground surfaces and to compare the way in which the synthesised run-in surfaces behave in mixed-EHL conditions with corresponding results based on the measured run-in profiles.

A further goal was to use the synthesised and measured run-in surfaces to conduct surface layer fatigue analyses of the mixed-EHL contacts and to compare the way in which the predicted growth in fatigue damage was related to micropit development in endurance testing of the rough surfaces in rolling sliding disk tests.

This thesis contains seven chapters, and the following is a brief description of the remaining chapters.

Chapter 2 gives a brief description and introduction to the main equations that govern the mixed-EHL line contact problem, with some related equations and explanation of the solution methods adopted. The initial arbitrary method of modifying the geometry of the surfaces and an investigation of the radii of curvature of un-run and corresponding run-in profiles are presented in this chapter.

Chapter 3 describes the development of the techniques employed in the numerical transient EHL solution for modifying roughness surfaces stage by stage to synthesise the running-in process. The results of numerical simulations are presented and compared with measured results for the corresponding test disks.

Chapter 4 provides an overview of the concepts and theories of fatigue, which are developed for rolling contact fatigue. A shear strain based model that incorporates cumulative damage analysis was used.

Chapter 5 describes the test rig used for the experimental work undertaken and explains the roughness profile measurements taken and how they are processed to identify the asperity changes and detect the evolution of micropitting.

Chapter 6 presents a detailed analysis and comparison of the synthesised and experimental results of the EHL and fatigue-life analyses of all sets of profiles considered in the research. The results of experimental observations of the micropitting test are compared with the numerical fatigue model.

Chapter 7 concludes the thesis with a summary of the main findings, and also suggests some ideas for future work.

Chapter 2: Transient EHL analysis

2.1 Introduction

The elastohydrodynamic (EHL) problem is described by two fundamental equations which deal with the elastic deflection of the contacting bodies and the flow of lubricant in the interface between their surfaces. These are the equations for elastic deflection of semi-infinite bodies and the Reynolds hydrodynamic equation. This chapter covers these main equations for the case of the line contact problem together with some related further equations. A characteristic feature of EHL is that a heavy load is applied over a small contact area, and this creates pressures that are high enough to cause significant elastic deformation of both rough surfaces as well as to change the oil's properties as it flows through the contact. More details and a full description of the line contact problem can be found in (Davis, 2005; Khaustov, 2016). The line contact model is adopted for this work because the surface roughness has a lay direction that is nearly perpendicular to the rolling sliding direction of the surfaces.

The EHL numerical analyses implemented in this chapter are for two as-manufactured real rough surfaces to start modifying surface geometry to develop a plastic deflection approach. Running as manufactured profiles in an EHL analysis at the operating conditions leads to excessive pressure levels. In the real contact, this would cause plastic deformation in order to develop the modification process initially, high viscosity and high speeds were used to limit the extreme pressures.

The realization of changing the height of asperities that led to focus on the changing in asperity radii of curvature and not just asperity height. An investigation of the changes in surface asperity radii of curvature during running in was carried out to establish the changes that the simulation method would need to replicate.

2.2 Development of EHL line contact problems

The EHL problem is defined by two basic equations: the hydrodynamic equation and the surface elastic deformation equation. This pair of equations presents a highly non-linear system and thus has led researchers to develop ingenious numerical solution models during the last six decades to obtain solutions to this difficult problem. EHL problems are usually solved using either a line contact or point contact approach depending on the shape of the contact area under load. Line contacts are present in roller bearings and spur and helical gears, and point contacts occur in ball bearings and certain types of crossed-axis gears. Dowson and Higginson (1966) provided the first numerical solutions to EHL problem for smooth surfaces, which is considered the normal film creation mechanism in gear tooth contact analysis.

The solution method used in the software developed and adopted for this research was first created by Elcoate et al. (1997). It can be described as a simultaneous solution of the Reynolds hydrodynamic equation and the elastic deflection equation formulated as a differential equation. The elastic deflection was formulated in this form by Hughes et al., (2000) for both line and point contacts. Both equations are functions of pressure and surface separation. The film thickness equation incorporates density and viscosity terms that are dependant and strongly dependent on pressure, respectively. This system exhibits strong nonlinear behaviour predominantly due to the elastic deformation and the near exponential rise of viscosity with pressure at the high pressures encountered in realistic concentrated contacts. Further development was performed by Holmes (2002) and Sharif et al. (2001). The Johnson and Tevaarwerk (1977) shear thinning rheological model was used to incorporate the non-Newtonian effect into the formulation of the problem.

This work is based on numerical analysis of EHL contacts using the differential deflection method formulation (Hughes et al., 2000; Elcoate et al., 2001; Holmes et al., 2003a, 2003b, and 2005) that successfully models the mixed-EHL transient problem in which the mean asperity height was at least an order of magnitude greater than the minimum lubricant film thickness.

2.3 The viscosity equation

The equation which relates the lubricant viscosity to its pressure, is called the viscosity equation. There are two equations that are commonly used to take account of this behaviour. Firstly, the Barus equation which was developed by Barus (1893), defined in equation (1.5) and given here for convenience

$$\eta = \eta_0 e^{\alpha p}$$

Within the contact the pressure increases to the order of 1GPa and the viscosity of the oil increases by several orders of magnitude. The Barus equation is only accurate up to pressures of around 1GPa, above this pressure it tends to overestimate the viscosity. It has been widely used to determine the film forming effects of EHL because the film is formed at low pressures in the inlet.

Secondly, the Roelands equation is considered a more realistic equation for high pressure conditions. This equation is derived from dimensionless correlations given by Roelands (1966) and is adopted in the form (Clarke et al. 2006):

$$\eta = \eta_0 \exp\left\{\ln(\eta_0 / \kappa)[(1 + \chi p)^Z - 1]\right\} \quad (2.1)$$

Where κ and χ are constants, Z is the Roelands parameter that determines pressure viscosity behaviour, and p and η_0 are in units of Pa and Pas respectively. To ensure that the two equations of Barus and Roelands give similar behaviour at low pressure, the constant Z can be related to the viscosity pressure coefficient, α . This can be achieved by equating the slopes of $\ln(\eta)$ with pressure as p approaches zero, which results in equation (2.2):

$$Z = \frac{\alpha}{\chi \ln(\eta_0 / \kappa)} \quad (2.2)$$

2.4 The density equation

In addition to the viscosity, the density of the fluid changes due to the pressure increase experienced within the contact. The relationship that is commonly used to describe this behaviour is given by the Dowson and Higginson (1966) formula which takes the following form:

$$\rho = \rho_0 \frac{1 + \gamma p}{1 + \lambda p} \quad (2.3)$$

Where γ and λ are the pressure coefficients of compressibility.

2.5 The load equation

The load carried by the EHL film is the integral of the pressure distribution, and the load per unit length in the y direction can be expressed as:

$$w' = \int_{p>0} p(x) dx \quad (2.4)$$

2.6 Elastic Film Thickness equation

A typical centreline section of film thickness in the entrainment direction for the EHL contact problem is shown in Figure 2.1.

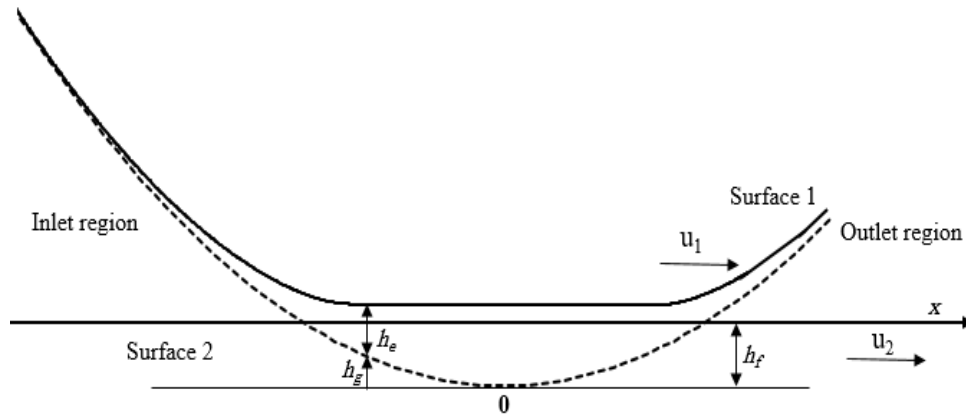


Figure 2.1 Lubricant film geometry centreline section at $x = 0$.

The elastic film thickness that is linked with the hydrodynamic equation consists of the expression given in equation (2.5). $\phi(x, t)$ is the measured roughness at x taken from profilometer measurements for the fast and slow rough disks, h_g is the undeformed gap between the contacting surfaces under zero load that is assumed to be a parabola, h_e is the elastic deformation of the contacting surfaces due to pressure distribution p , and h_f is a constant and its value controls the separation of the surfaces, and thus the load supported.

$$h(x, t) = \phi(x, t) + h_g(x) + h_e(x, t) - h_f \quad (2.5)$$

It is assumed that the contacting bodies behave as semi-infinite bodies, as the size of the contact is usually small compared to the remainder of the solid body.

Considering a parabolic curve, the undeformed geometry h_g can be determined as:

$$h_g = \frac{x^2}{2R'}$$

The deflection equation used is based on the deflection of a semi-infinite body as given by Johnson (1985):

$$h_e(x,t) = -\frac{4}{\pi E'} \int p(s,t) \ln|x-s| ds + Const \quad (2.6)$$

Substituting in equation (2.5) and incorporating the constant of integration in h_f gives:

$$h(x,t) = \phi(x,t) + \frac{x^2}{2R'} - \frac{4}{\pi E'} \int p(s,t) \ln|x-s| ds - h_f \quad (2.7)$$

2.7 The Reynolds equation

The Reynolds equation is the well-known hydrodynamic equation which governs the pressure and film thickness distributions in lubricant film. This equation was first proposed by Reynolds in 1886. It can be derived from two physical principles; the full Navier-Stokes equations for the motion of a viscous fluid (conservation of momentum), and the continuity equation (conservation of mass) with simplifying assumptions, as used by Dowson (1962).

Reynolds introduced several assumptions to simplify the complexity of the nature of the problem.

- 1- The body forces can be neglected.
- 2- The pressure, viscosity and density, are constant through the thickness of the film
- 3- No slip at the solid/lubricant boundaries.
- 4- The fluid is Newtonian so that shear stress is proportional to the shear strain rate.
- 5- The film thickness is much smaller than the Radius of Relative Curvature of the lubricated contact.
- 6- Flow is laminar.
- 7- The inertia (rates of change of momentum) for the fluid is neglected.

The form of Reynolds equation for the 1D of the line contact problem is:

$$\frac{\partial}{\partial x} \left(\frac{\rho h^3}{12\eta} S \frac{\partial p}{\partial x} \right) - \frac{\partial}{\partial x} (\rho \bar{u} h) - \frac{\partial}{\partial t} (\rho h) = 0 \quad (2.8)$$

where \bar{u} is a mean velocity:

$$\bar{u} = \frac{u_1 + u_2}{2}$$

Where u_1, u_2 for the fast and the slow surfaces, respectively.

This equation is the transient Reynolds equation and factor S quantifies any non-Newtonian effects. The rheological model of the Eyring fluid (Kim et al., 2001), that relates shear stress to shear strain rate was used to incorporate the non-Newtonian effect into the formulation of the problem. Neglecting the elastic shear term, this is

$$\dot{\gamma} = \frac{\tau_0}{\eta} \sinh \left(\frac{\tau}{\tau_0} \right) \quad (2.9)$$

where $\dot{\gamma}$ is the shear strain rate, τ_0 is the non-Newtonian parameter referred to as the Eyring shear stress.

Term S is the non-Newtonian factor which depends on pressure, film thickness, sliding speed and pressure gradient. Considering shear thinning using the Eyring model, the S factor is available in closed form taken from Conry et al. (1987) as follows:

$$S = \frac{3(\Sigma \cosh \Sigma - \sinh \Sigma)}{\Sigma^3} \sqrt{1 + \frac{\eta^2 (u_2 - u_1)^2}{\tau_0^2 h^2} \frac{\Sigma^2}{\sinh^2 \Sigma}} \quad (2.10)$$

Where
$$\Sigma = \frac{h}{2\tau_0} \frac{\partial p}{\partial x}$$

The representative stress, τ_0 , for the current thesis is taken as constant although it is known to be weakly dependent on the pressure. As τ_0 approaches infinity so Σ approaches zero and it can be shown that $S(x)$ approaches unity, therefore returning equation (2.9) to the Newtonian fluid formulation. The last term in equation (2.9), which is the only time dependent term, is called the squeeze film term. This terminology arises from squeeze film dampers where the pressure is generated by the movement of parallel solid surfaces towards each other when the gap in between is filled with damping fluid.

An important parameter for contacts where $u_1 \neq u_2$ is the slide roll ratio SRR defined as:

$$\xi = \frac{|u_1 - u_2|}{\bar{u}} = \frac{2|u_1 - u_2|}{u_1 + u_2} \quad (2.11)$$

2.8 Differential deflection method

The deflection solution method that is implemented is the differential deflection method. This method originated from Okamura's (1982) first order full coupled formulation, presented by Houpert and Hamrock (1986) and further developed by Elcoate (1996) and Hughes et al. (2000) for the line contact problem and by Holmes et al. (2003) for point contacts.

The elastic deflection given in Equation (2.7) is the convolution integration of pressure with the appropriate weighting function. The numerical calculation of deflection at a point can be reduced to a simple quadrature by summation of influence coefficients multiplied by the pressure value at all points of the solution domain (Evans and Hughes 2000), which is given by the following expression:

$$u(x_i) = \sum_k g_{k-i} p_k \quad (2.12)$$

Here the weighting function g_{k-i} depends on the surface geometry and material properties, and the quadrature form used for the pressure. Evans and Hughes (2000) developed an alternative differential formulation of the relative elastic deflection. It can be seen that the effect of the pressure at the point is more dependent on the slope of the deflection than on its value (Johnson, 1985). The advantage of this method is that pressure has an extremely localised effect on the second derivative of deflection which allows the use of a limited bandwidth matrix in solving the coupled EHL governing equations simultaneously and to increase stability under heavy loading conditions.

The quadrature formula of the ordinary differential equation obtained by differentiating equation (2.12) twice has a weighting function that decays rapidly with increasing distance from the evaluation point. The differential form of the deflection is written as:

$$\frac{\partial^2 u(x_i)}{\partial x^2} = \sum_k f_{k-i} p_k \quad (2.13)$$

Where f_{k-i} are the differential influence coefficients. The influence coefficients in this quadrature formula are available in closed form in Evans and Hughes (2000). The advantage of such a modification can be seen by comparing the differential influence coefficients (g and f), where the f coefficients decay significantly faster than the g coefficients, as shown in Figure 2.2. For a line contact equation (2.12) gives the deflection relative to the deflection at a reference position, $x = r$. The three curves for the g_i weighting functions correspond to the different reference positions specified.

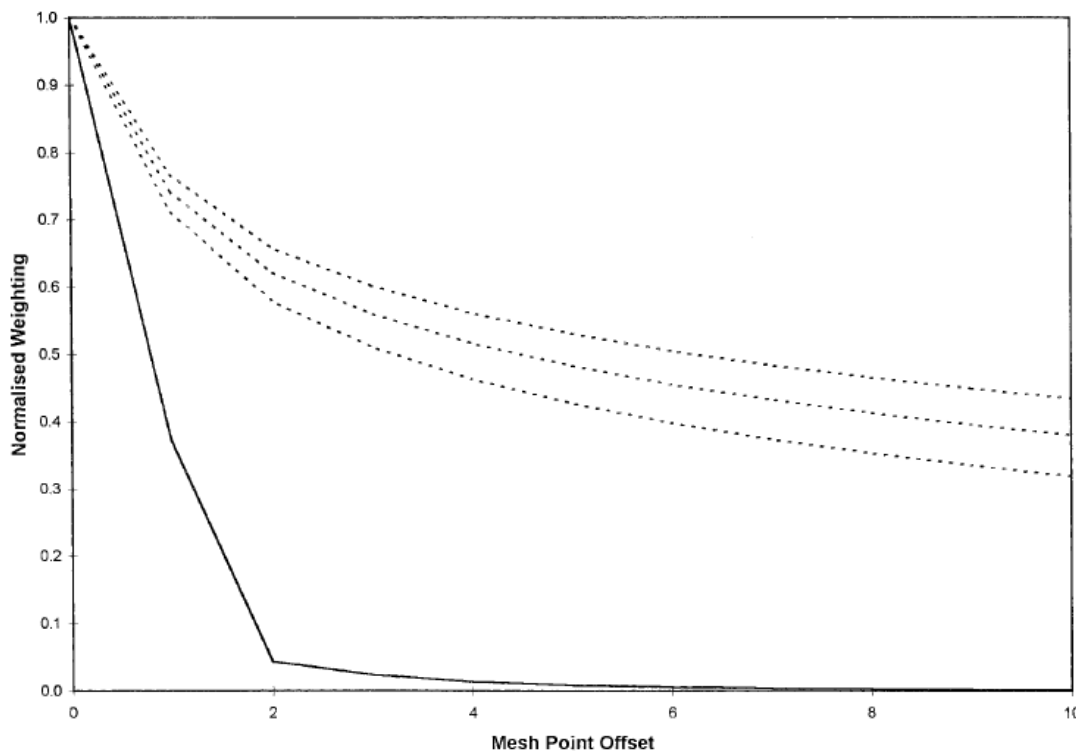


Figure 2.2 Normalized decay of f_i weighting coefficients (solid line) and g_i weighting coefficients (dotted line). Three g_i curves are shown with $x - r = 50\Delta$ (lower curve), $x - r = 100\Delta$ (middle curve) and $x - r = 200\Delta$ (upper curve) (Evans and Hughes, 2000).

With the differential deflection technique, the film thickness equation (2.8) can be written in the following differential form:

$$\frac{\partial^2 h}{\partial x^2} = \frac{\partial^2 \phi}{\partial x^2} + \frac{1}{R'} + \sum_k f_{k-i} p_k \quad (2.14)$$

2.9 The coupled EHL Solution method

The flow chart describing the coupled method for solving the EHL line contact problem is shown in Figure 2.3. The two governing equations, the Reynolds and the film thickness equations are discretised on a uniformly spaced mesh. Discretisation is by central differences for equation 2.14 and by either finite difference or finite element approaches for equation (2.8). The equations are expressed as a summation of mesh point pressure and film thickness values multiplied by coefficients according to the discretisation method adopted. These are linearised in equations (2.15) for the Reynolds equation and equation (2.16) for the elastic equation by selecting the n_c closest mesh points to the point of interest and moving the contributions of the other mesh points to the right hand side of the equations.

$$\sum_{k=0}^{n_c} A_k p_k + \sum_{k=0}^{n_c} B_k h_k = R_i \quad (2.15)$$

$$\sum_{k=0}^{n_c} C_k p_k + \sum_{k=0}^{n_c} D_k h_k = E_i \quad (2.16)$$

Variables p_0 and h_0 are the values of pressure and film thickness at the point of interest, and p_k and h_k are the values at the neighbouring mesh points. A_k and B_k are the pressure and film thickness coefficients for the hydrodynamic Reynolds equation. For the transient problem an implicit Crank-Nicolson formulation is used so that R_i includes the values from the previous time step. A_k and B_k are dependent on the density and viscosity at the mesh points in accordance with the discretisation method adopted. C_k and D_k are the coefficients for the pressure and film thickness determined from the differential deflection approach and E_i includes the influence of the other pressures in the mesh. Parameter n_c is the number of nodes involved in the formulation which is determined from the ‘local’ points in the elastic film thickness equation.

The two key variables, pressure and film thickness are determined by solving this pair of equations simultaneously through the contact for each nodal value pair. Coefficients A_k and B_k involve ρ , η and S in equation (2.10) and as the value of viscosity is highly pressure dependent and to solve the equations the fluid properties are obtained at each

mesh point using pressure and film thickness distribution for an outer loop. Equation (2.15) and (2.16) are set up using the current outer loop values to determine the A_k and B_k values.

The discretised equations which are defined by the Reynolds and elastic film thickness can be then written in terms of the two key variables, pressure and film thickness, as a pair of simultaneous equations in the variables P_o and h_o in the form :

$$A_0 p_0 + B_0 h_0 = \hat{R}_i \quad (2.17)$$

$$C_0 p_0 + D_0 h_0 = \hat{E}_i \quad (2.18)$$

In these equations $\hat{R}_i = R_i - \sum_{k=1}^{n_c} A_k p_k - \sum_{k=1}^{n_c} B_k h_k$ and $\hat{E}_i = E_i - \sum_{k=1}^{n_c} C_k p_k - \sum_{k=1}^{n_c} D_k h_k$.

The coupled solution method solves this pair of equations simultaneously for each node in the computational mesh. In the current research equations (2.17) and (2.18) are expressed in the form,

$$p_0^{new} = \frac{\hat{R}_i D_0 - \hat{E}_i B_0}{A_0 D_0 - B_0 C_0} \quad (2.19)$$

$$h_0^{new} = \frac{\hat{E}_i A_0 - \hat{R}_i C_0}{A_0 D_0 - B_0 C_0} \quad (2.20)$$

and are solved using a pairwise iteration in a Gauss Seidel approach.

In some contact situations in the iterative time step scheme the value of h_0^{new} obtained from equation (2.20) is negative at some mesh points, when this occurs the fluid film is unable to separate the surfaces. The film thickness then has its value set to zero and equations (2.19) and (2.20) can be modified to:

$$p_0^{new} = \hat{E}_i / C_0 \quad \text{and} \quad h_0^{new} = 0 \quad (2.21)$$

This effectively sets a new boundary condition, $h = 0$ at the point and applies the deflection equation subject to that boundary condition. In this way the method determines where asperity contacts occur dynamically at each mesh point and in each time step. This technique is considered as a further advantage of the application of the coupled differential deflection approach. Every mesh point through each iterative sweep is assumed to be in a full film condition at each time step unless the iterating

equations (2.19) and (2.20) result in a negative value for h_0^{new} at that mesh point. The approach of the coupled iterative scheme is able to deal with the difficulties in simulation of EHL contact problems between surfaces that have aggressive asperity features.

When the equations (2.15) and (2.16) have been solved in this way the outer loop pressure and film thickness distribution are updated using a relaxation process. The A_k and B_k terms are then re-calculated and the equations are solved once more.

This sequence of operations is repeated until the outer loop pressure has converged, which means that the solution for the current time step has been obtained. The outer loop pressure and film thickness distributions then become the first outer loop value for the next time step. The right hand side of equation (2.15) is calculated for the newly converged time step and the procedure to solve the next-time step then starts.

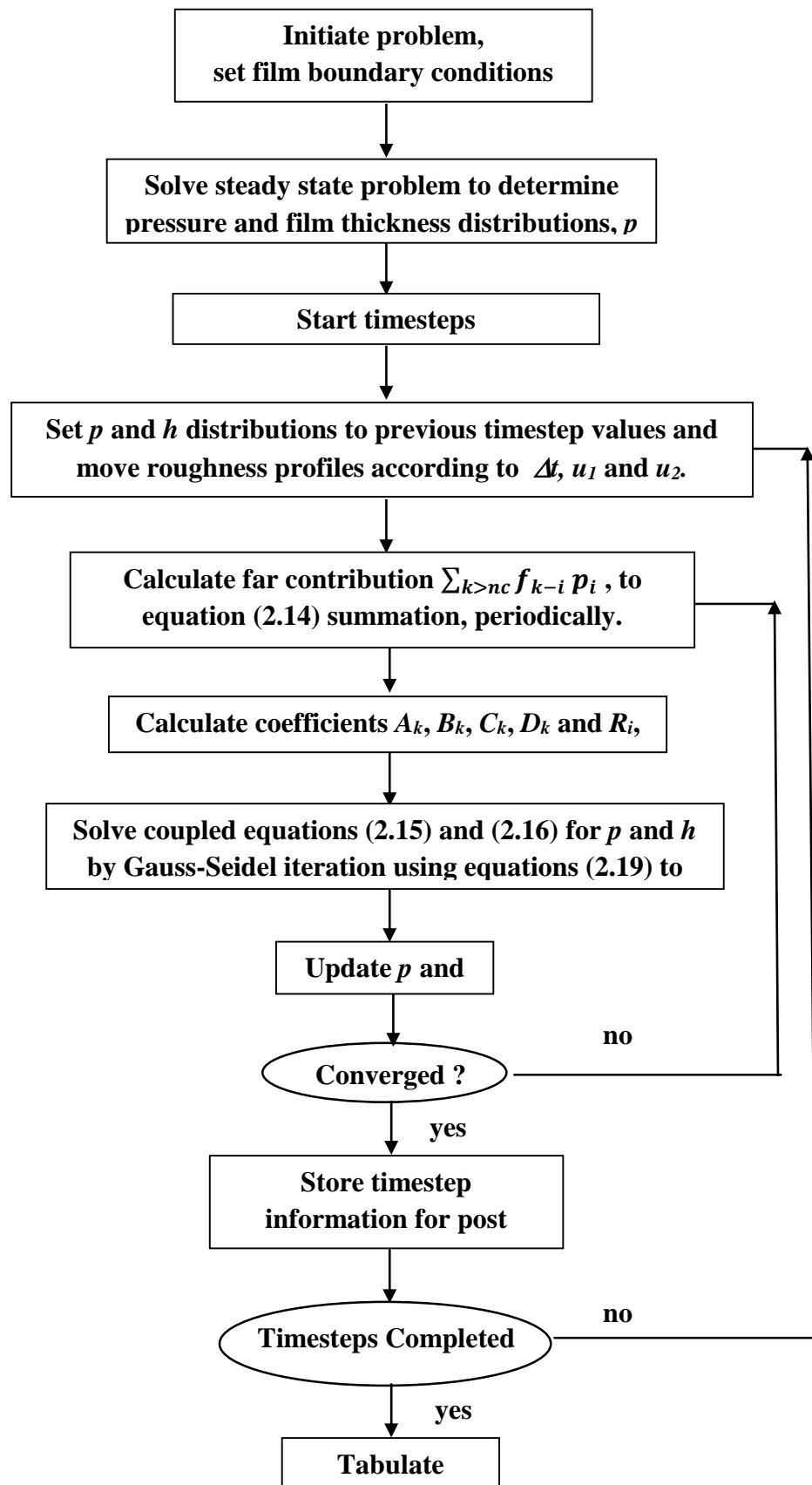


Figure 2.3 Flow chart describing the coupled EHL transient analysis.

2.10 Surface Asperity Modification Process

2.10.1 Profile Set One

This procedure was developed using two surface roughness profiles that were obtained from experimental results obtained by (Weeks 2015) as a first attempt to create a simulation model of the asperity modification that is similar to the real case and to compare with experimental results. These profiles were taken from the fast disk (FD) and the slow disk (SD) in an endurance test. The disk radius was 38.1 mm for each. The disks had equal hardness and ran in rolling/sliding contact with a slide roll ratio of 0.5. Their roughness profiles were measured in-situ in the test rig using a portable Talysurf Ultra profilometer. The profiles were taken in the circumferential direction perpendicular to the roughness lay and parallel to the disk face. A Gaussian filter with a cut off of 0.25 mm was used to remove the circular form and the waviness from the surface roughness profile which was retained for analysis. Before the test, 8mm long profiles were taken at particular marked locations on the disk circumference in the as-manufactured condition. The test was then started for a short period. The disks were loaded against each other in rolling sliding contact with a nominal maximum contact pressure of 1.4 GPa. The profiles were taken again at the same specific circumferential locations of the disk. This method was used by Weeks to detect the changes occurring at roughness asperity features. The run-in surfaces were relocated by shifting the profile along with a selected value of offset in the profile direction to align the profiles with regard to the unchanging valley profiles. This is necessary because the second measurement taken after loading is not at exactly at the same position. The experiment and profile processing procedures are explained in detail at sections 5.9 and 5.10.

Sections of the profiles about 1mm long were selected which are approximately equal to $2a$ where a represents the Hertz contact dimension.

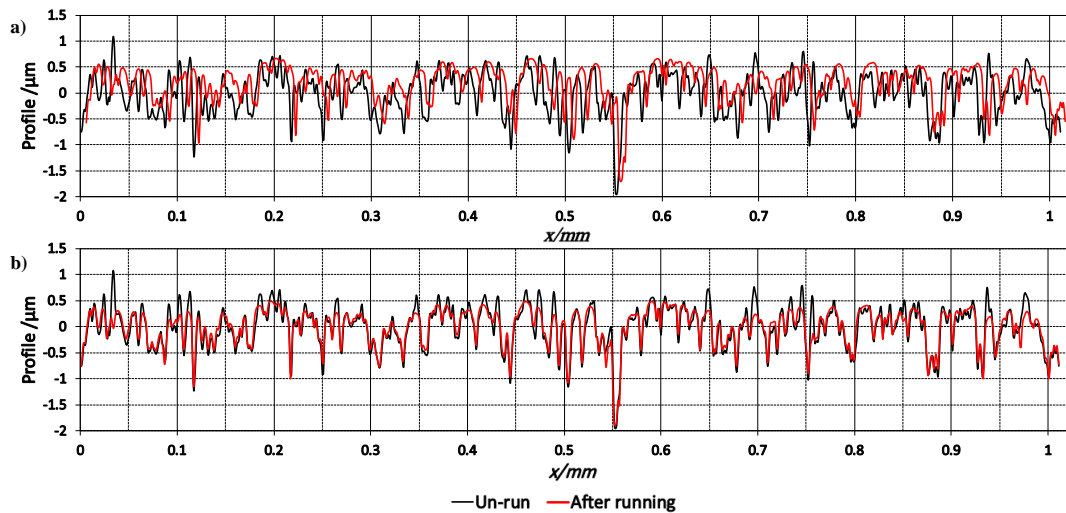


Figure 2.4 Profiles taken from 1mm section of the fast disk for un-run and after loading a) before Alignment b) after Alignment.

Figure 2.4a shows the two profiles for the fast disk in their nominal measured form. The offset and surface height values were adjusted so that the deep valley features were aligned. This is shown in Figure 2.4b. It can be seen that a significant amount of plastic deformation occurs during the running-in of the surfaces. Asperity features have become curved load bearing lands. Comparison of the profiles shows that the valley features remain undisturbed throughout the loading process even though significant deformation is occurring on the peaks of the surface. The radii of curvature of asperities became larger through this plastic deflection. Bryant et al. (2012) carried out detailed FE analyses of dry contact of such surfaces and demonstrated that the residual rough surface deformation only affects the asperity peaks and does not extend to the valley features. The valley features remain relatively unchanged as high-localised loads occur predominantly between interacting asperities (Holmes et al., 2005b).

2.11 Numerical Results

The numerical results are presented for the two rough profiles that were obtained from experimental test disks and then incorporated into the EHL line contact analysis procedure, i.e. the coupled solution method with differential deflection technique. The operating conditions in the test experiment and lubricant parameters adopted for EHL analysis are specified in Table 2.1.

Table 2.1 Parameters used for transient EHL line contact analysis

w'	1030 kN/m	SRR	0.5
a	0.468 mm	α	23.5 GPa ⁻¹
p_0	1.4 GPa	η_0	0.0651 Pa.s
E_1, E_2	207 GPa	ρ	846
v_1, v_2	0.3	U_1	11.8742 m/s
R_1, R_2	38.1 mm	U_2	6.05474 m/s

The representative profiles were copied to provide *multi-profiles* which repeat the selected profile with the joins made at valley features so as not to introduce new asperity features. In the EHL model, the two rough multi-profiles were superimposed on the smooth disk surfaces and simulated in “rough on rough” contact conditions. The two disks rotate at different speeds and these were applied to the surfaces in the model, their values give a mean velocity $\hat{u} = 8.96$ m/s.

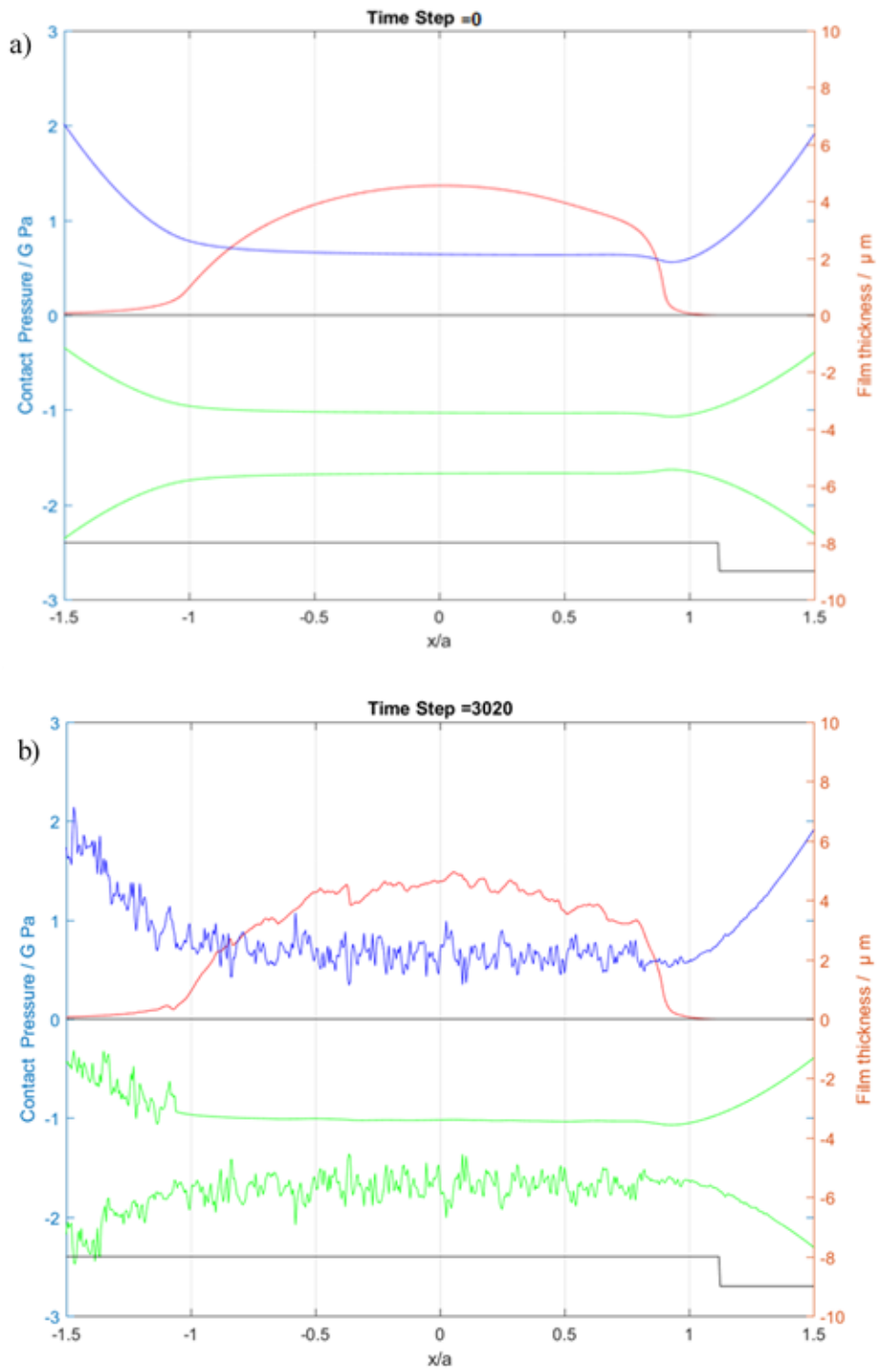
Analyses started from the corresponding smooth surface steady state solution, and the rough surfaces were then allowed to migrate from the entry boundary located at $x/a = -2.5$ to the exit boundary at $x/a = 1.5$. Pressure and film thickness outputs in the contact area at different timesteps are presented in Figure 2.5 which illustrates the initial smooth surface solution and three timesteps from the transient analysis. The pressure and film thickness distributions are shown in the upper part of the figures and the two rough surfaces are shown in their current contact conditions in the lower part with a

negative offset of $6\mu\text{m}$ for two clarity. The lower curve indicates whether each mesh point has a full film (-8), is in direct asperity contact (-7) or is cavitated (-9).

At the timestep shown in Figure 2.4(b) the initial roughness of the slower moving surface has already passed beyond the exit boundary and the fast surface roughness is moving into the Hertzian contact area. For figures 2.4(c) and (d) both surfaces are fully rough. The mesh size adopted in the figures is $\Delta x = a/200$, where a is the Hertzian contact semi-dimension. Using different mesh spacing such as $\Delta x = a/400$, $a/200$ and $a/100$, the results obtained show that there is no significant difference in the predicted pressure and film thickness profiles as the mesh is varied (Qiao, 2005).

It can be clearly seen that from Figure 2.5(a) at the timestep 0 that the two surfaces are smooth. At timestep 3020 in Figure 2.5 (b) the slow surface has become rough and the fast profile is approaching the inlet to the Hertzian zone. There are small changes to the pressure and film thickness distributions due to the roughness. The first $0.5a$ length of the multi-profiles are attenuated linearly to have height zero at the first profile point. This is necessary to avoid a fictitious impact loading which will otherwise occur. Note that the slower surface roughness profile is fed into the contact at $x = -2.5a$ from the first timestep and the fast profile is delayed so that the un attenuated parts of both profiles reach the exit at the same timestep.

Figure 2.5 (c) and (d) show timesteps 5000 and 12000 where the two surfaces have become fully rough. The pressure distribution is greatly changed in comparison with the smooth surface case with high localised peaks as large as 3 GPa. There are occurrences of asperity contact and cavitation at some mesh points so that the conditions contain these features of mixed lubrication.



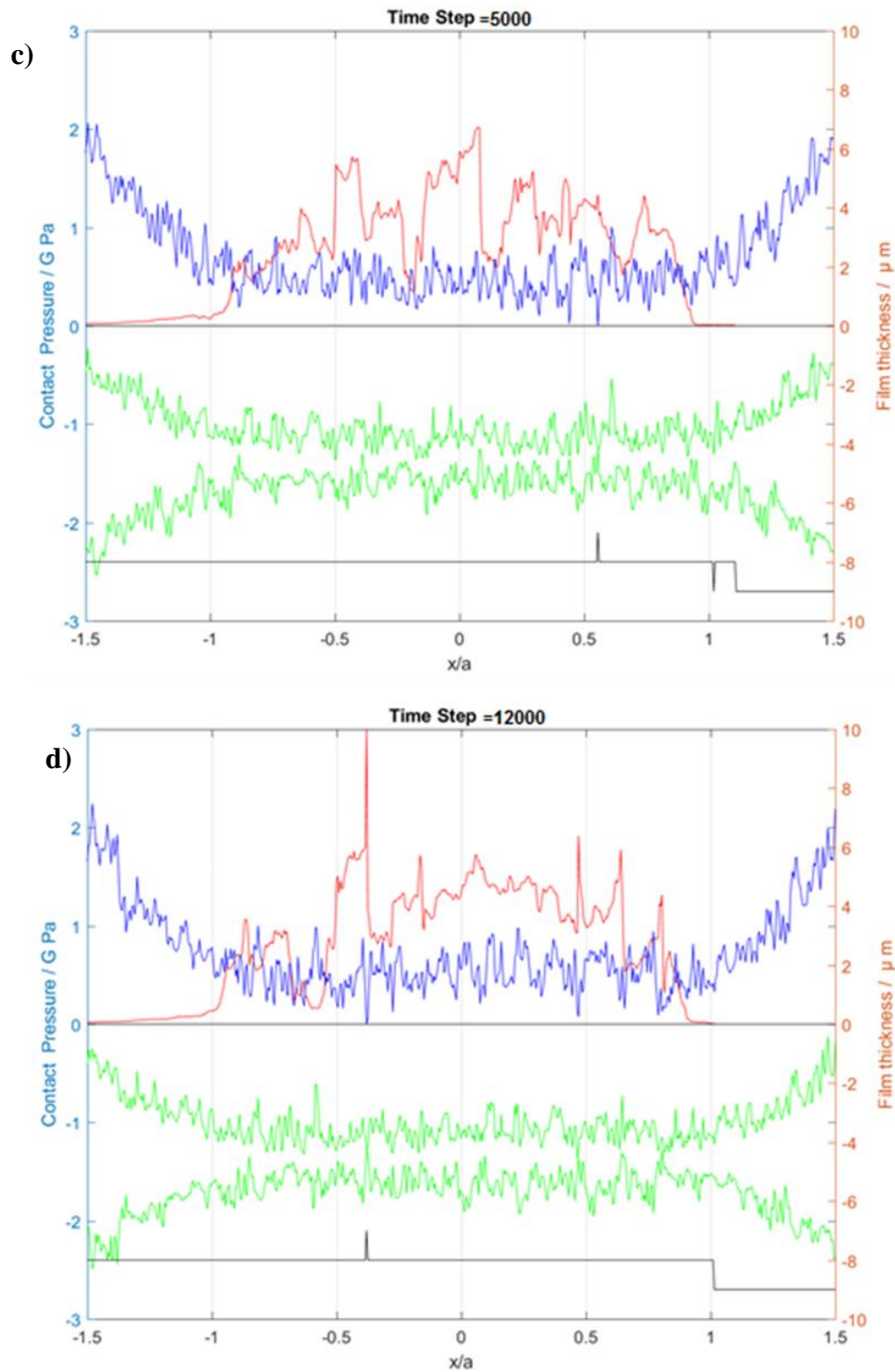


Figure 2.5 Pressure(Red ,upper curve) and film thickness distribution (Blue) for the contact between two rough surfaces .The two rough surfaces(Green) are shown below with a negative offset of $6\mu\text{m}$ for clarity, the upper curve is the Fast surface and the lower is the Slow surface. Film condition is indicated below the rough surfaces (Black). Results shown (a) at 0 timesteps, (b) at 3020 timesteps, (c) at 5000 timesteps, (d) at 12000 timesteps.

2.12 Arbitrary surface modification

Fortran programming was used to begin conducting EHL numerical analyses of the un-run rough surfaces by applying the load giving a maximum smooth surface contact pressure of 1.4 GPa with a high value of viscosity to start to develop a plastic deflection approach. Representative sections from the two profiles were selected that were about $2a$ long. For the experiment considered the Hertz dimension $a=0.468$ mm. The representative profiles chosen were 1.011 and 1.008 mm long for the fast and slow surfaces respectively. Each representative profile contains many asperities and they experienced considerable shape changes during running-in. They are illustrated in Figure 2.6.

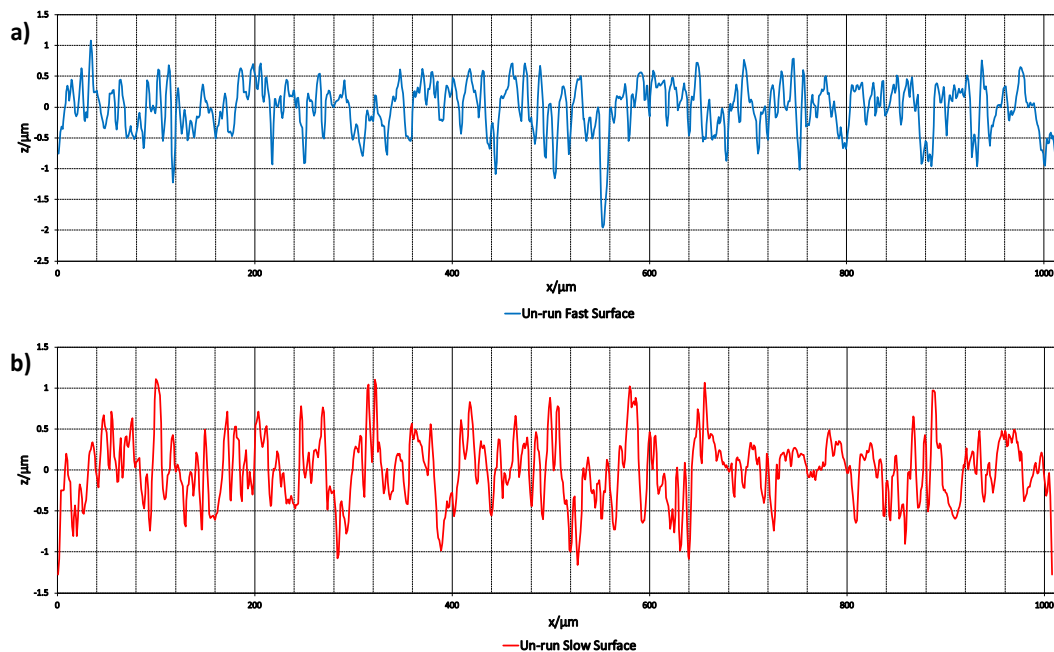


Figure 2.6 Shows the two surface roughness profiles used for analyses. (a) Fast surface, (b) Slow surface.

Care was taken to ensure that the representative profiles finish at a valley feature at each end. The profiles were then replicated a number of times to form a *multiprofile* joined at these valley features. One of the profiles was reversed in order to ensure that the motion of the roughness features in the analysis replicated the experimental motion. (This was necessary as the slow disk profile is taken in the motion direction while the fast disk profile is taken in the reverse direction) 50 repeats were used for

the fast profile and 40 repeats for the slow profile. The analysis was then run for 20,000 timesteps with a 1 μm mesh spacing.

The results were obtained after running the EHL program and were represented as a drawing of the EHL timestep results and an animation movie by building code in Matlab to combine these frames.

After running the program and analysing the results, especially the pressure distribution, for the purpose of finding the general behaviour, it was noticed that both surfaces were periodically exposed to a series of high pressures of more than 2.5GPa.

The main emphasis of the current contribution is on the extent of direct contact experienced by the surfaces and on modelling the running-in process and results for the five analyses of the pressure profiles on the surface are considered.

High asperity pressures and transient contact events occur during the mixed EHL analyses and this is what leads to plastic deformation of the asperities. Since the roughness profile traverses repeatedly through the contact zone during the *multiprofile* surface analysis, pressure values for each traverse were obtained and associated with roughness section.

The pattern becomes clear in considering the data shown in Figure 2.7. In this figure the maximum transient pressure experienced by each point in the representative profile is plotted for each of the first five transits of the Hertzian zone. These are offset from each other (by 3GPa) for clarity and are aligned with the representative roughness section shown below the maximum pressure profiles. In this example the maximum pressures plotted are set to fixed values at positions where the maximum transient pressure is less than this value. This is for clarity as the purpose of the figure is to examine the repeating nature of the extreme pressures.

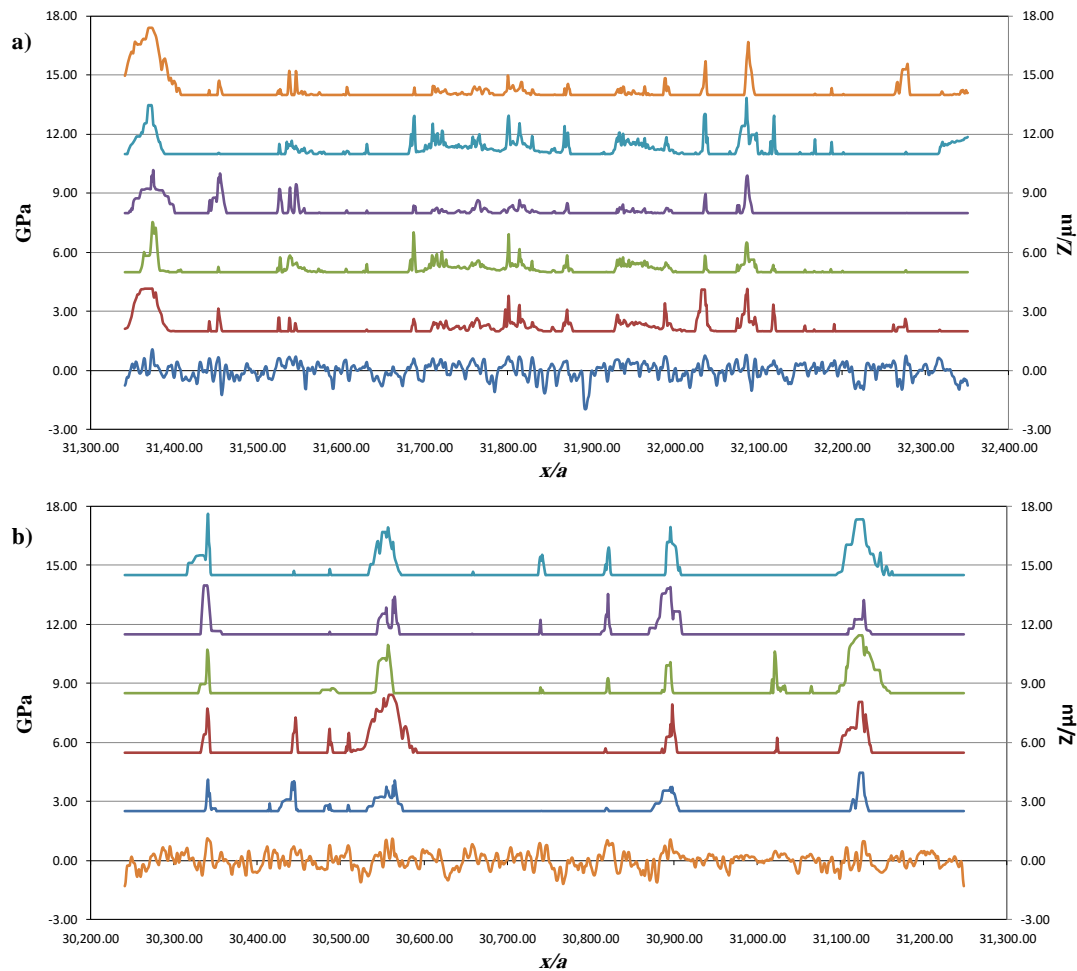


Figure 2.7 Shows the five maximum pressure distribution traverses together with the surface profile as the lower of the curves. (a) Fast profile, (b) Slow profile. Note that the curves are offset for comparison purposes.

It can be seen that during the traverses the same prominent asperities experience high pressure values greater than the yield pressure level of 2.5 GPa. It is to be expected that these asperities will be modified by plastic deformation during running. The research objective is then to try to simulate this process based on the observation that when the profiles have run-in the EHL pressures do not reach values that are much greater than the threshold. Initial attempts were made to implement gradual changes to the roughness profile to experiment with the results numerically.

2.13 The First Attempt

In the first attempt a plastic deflection was introduced to asperities that experienced maximum transient pressures (MTP) higher than 2.5GPa. These were the asperities identified as most overloaded from Figure 2.8. A reduction was made to the original peak surface height above the mean line of the filtered profile, h_o , by amount Δh where $\Delta h = k * h_o$, and k is a variable parameter as shown in Figure 2.8. A modification was made to these asperities in three steps and each asperity was represented by five points. The change was made to the asperity height by the value of $k=0.15$ for the peak point and $k = 0.1$ for the neighbouring points. The modified profiles for the fast and slow surfaces were used to create new *multiprofiles* which were then used in a new EHL analysis. The analysis of the results revealed that the MTP was still high.

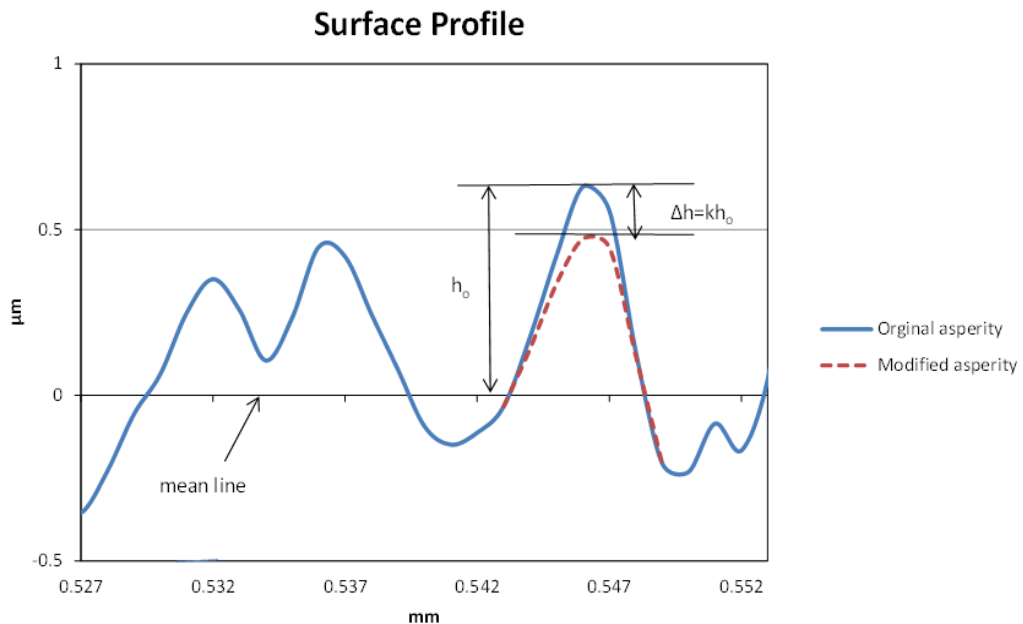


Figure 2.8 Shows the asperity height before and after modification.

2.14 The Second Attempt

In a second experiment asperities that experienced high MTP were modified according to the height above the mean line of each asperity but by a larger amount than in the first attempt. This was achieved using an Excel spreadsheet taking each asperity to be represented by five points and making a modification by reducing the highest point by a k value of 0.2 and the neighbours by $k = 0.15$. These modified *multiprofiles* were then used in the EHL analysis and it was found that the MTP was somewhat reduced as shown in Figure 2.9.

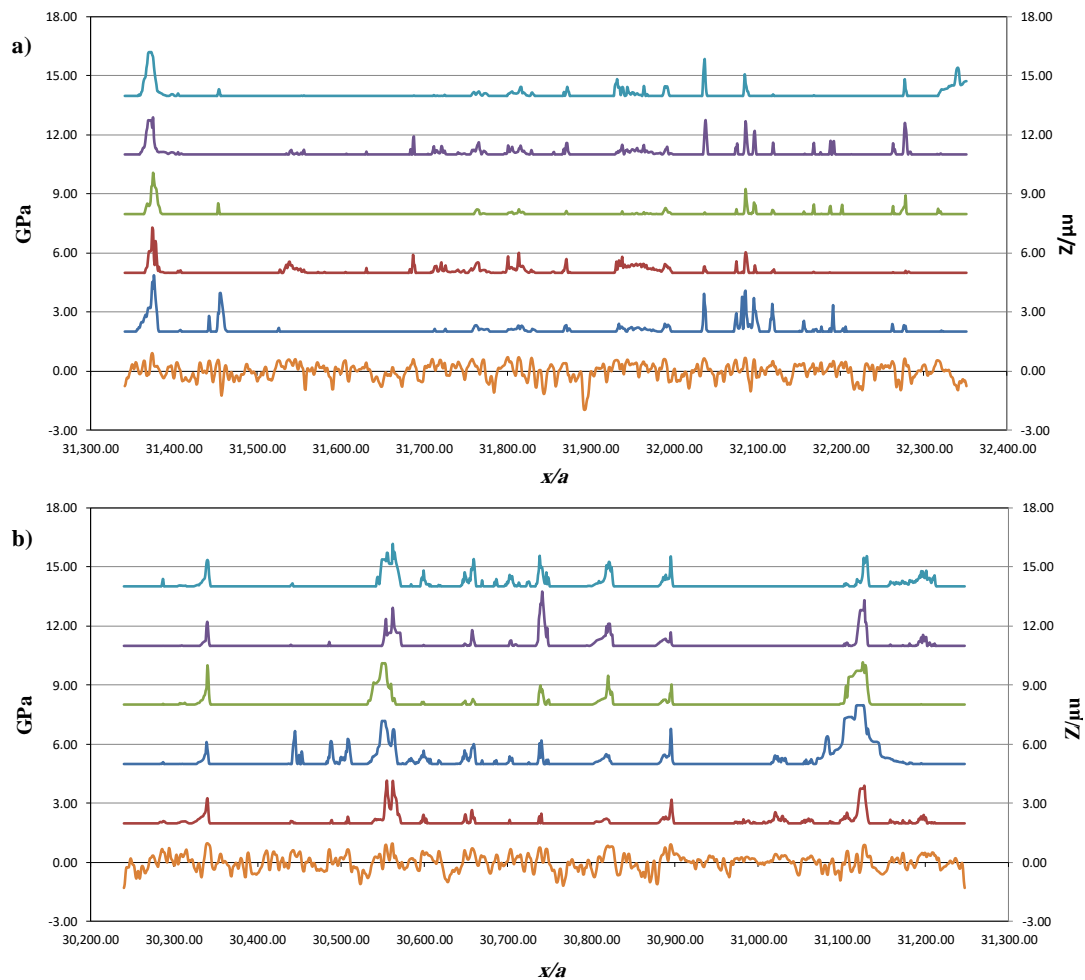


Figure 2.9 The five maximum pressure traverses after the first step modification together with the surface profile. (a) Fast profile, (b) Slow profile.

It is clear from Figure 2.9 that the events range became slimmer after the first modification in comparison with Figure 2.7.

A second step was to make a further modification for fast and slow profiles, with a k value of 0.25 and the neighbours by $k = 0.2$ and repeat the same process as the first step. It was found that the results became better than the first step and most asperities had MTP less than 2.5GPa as shown in Figure 2.9, but there were still some asperities that needed to be modified further.

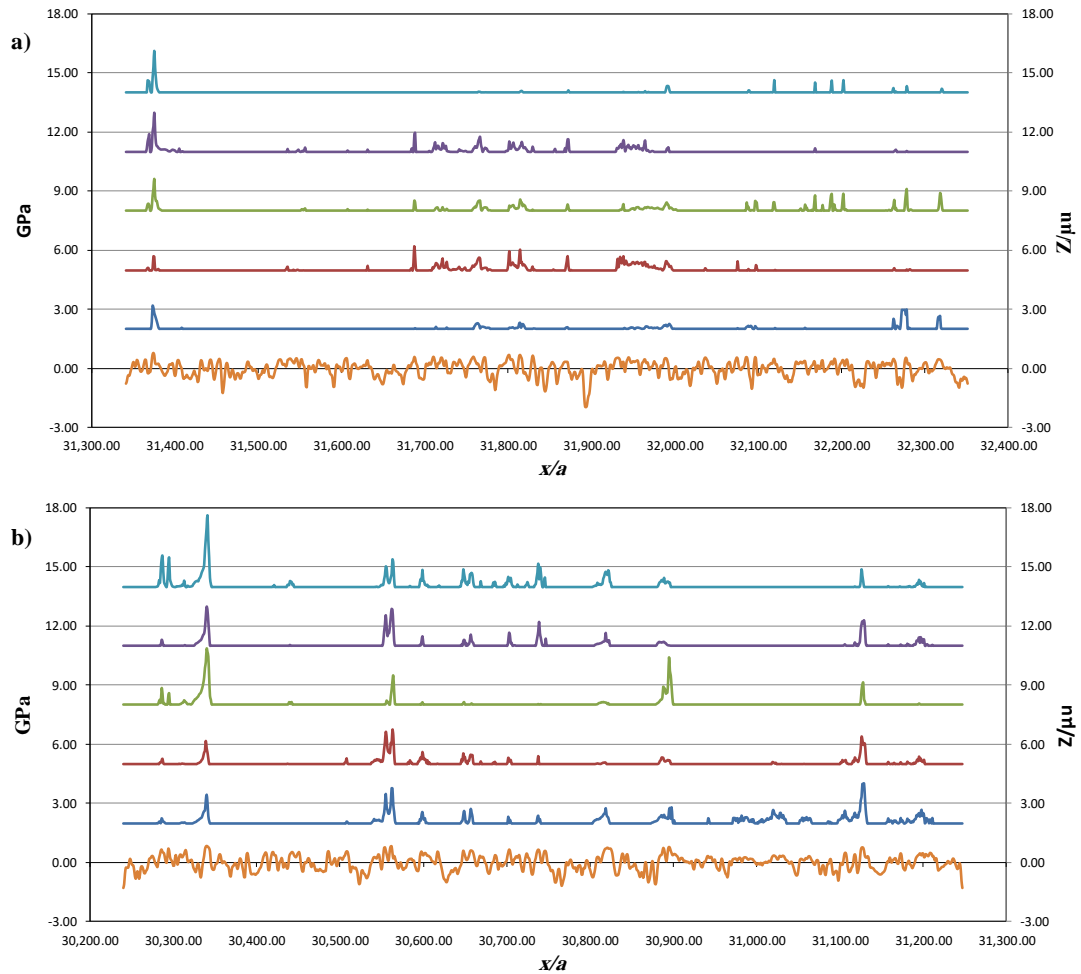


Figure 2.10 The five maximum pressure traverses after the second step modification together with the surface profile. (a) Fast profile, (b) Slow profile.

2.15 The Third Attempt

The third attempt made modifications to the remaining asperities that still had high pressure (k value of 0.3 to 0.4) and run the program again. This showed a significant effect for the fast surface where MTP values higher than 2.5GPa almost disappeared as shown in Figure 2.10.

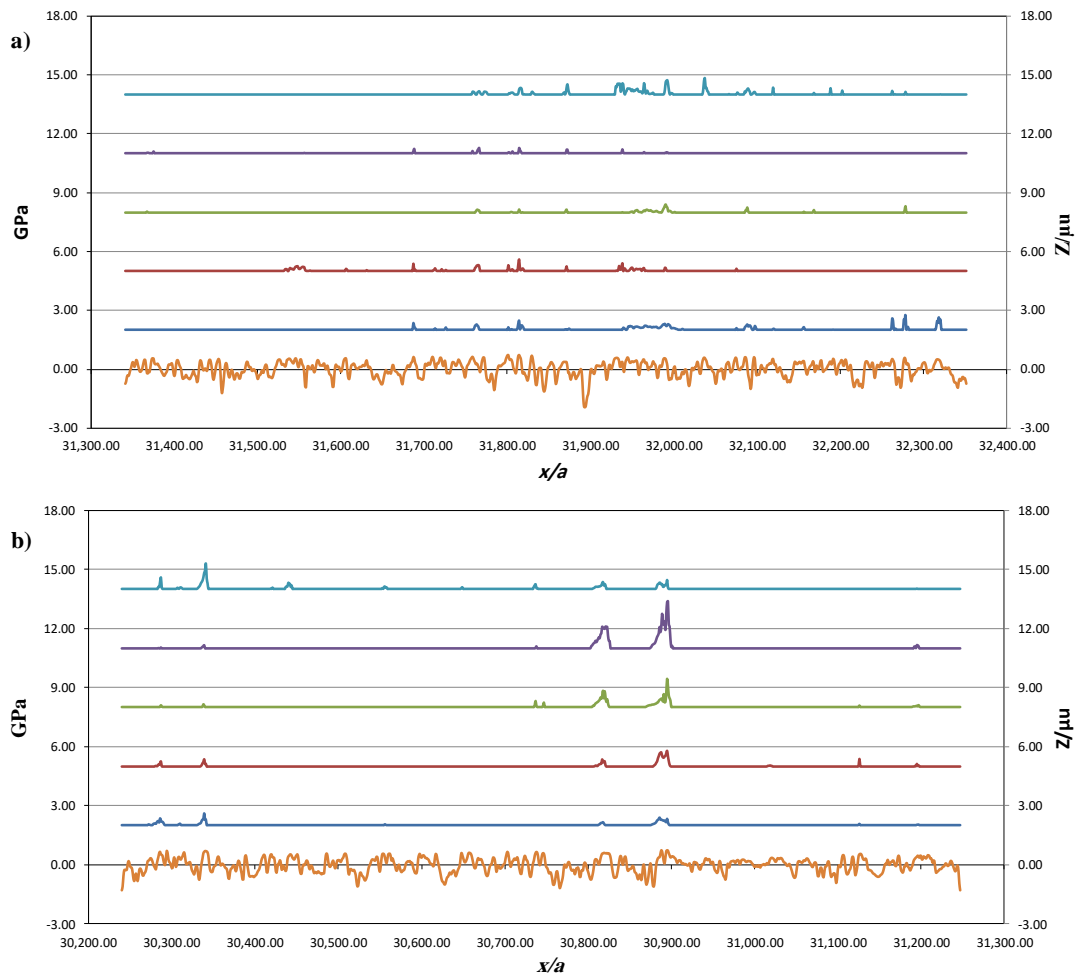


Figure 2.11 The maximum pressure traverses after the third step modification together with the surface profile. (a) Fast profile, (b) Slow profile.

However, from Figure 2.11, it is clear that a small number of asperities on the slow surface still have high MTP values and need further modification, and this gives an indication that the slow surface is more complicated than the fast one.

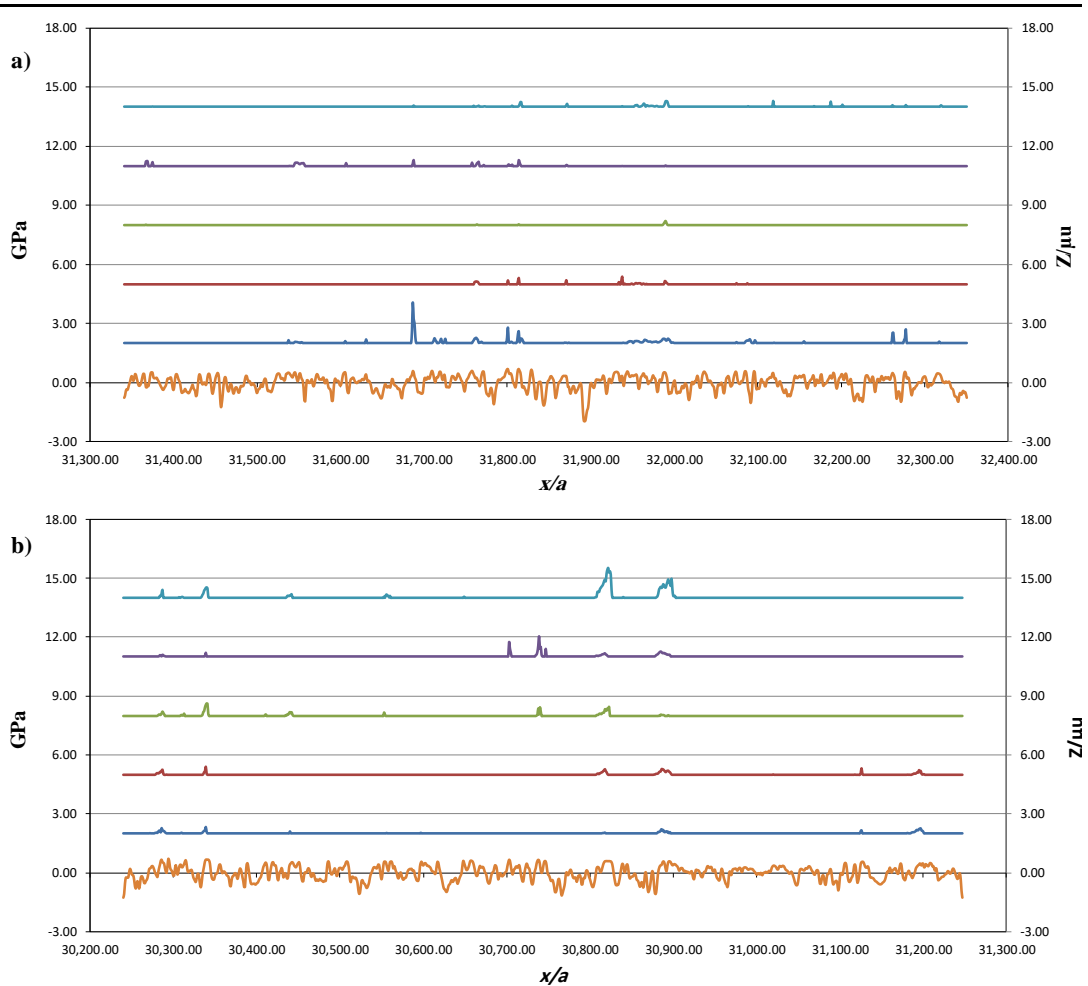


Figure 2.12 Shows the five pressure traverses after the last step modification to some asperities on the slow surface only, and the surface profile is demonstrated as the lower of the curves. (a) Fast profile, (b) Slow profile.

Figure 2.12 shows that most of the high MTP was eliminated and this gives an indication that the process has reached the right solution in replicating plastic deflection. However, manual intervention of this kind is not a solution to the problem as it is arbitrary and impractical, but the results are encouraging and led to considering how a more suitable process could be incorporated into the EHL analysis.

2.16 An investigation in radii of curvature for both fast and slow surfaces

A separate Fortran program was developed to consider all asperity peaks in a surface roughness trace and to evaluate their radii of curvature. This was used to obtain the radii of curvature for a roughness profile taken from a disk after manufacture and to compare with the results obtained for the same surface after running. Profiles were taken for both the fast and the slow disks before and after running-in for the earlier loading stages of the rig test.

Histograms of the radii of curvature of the peaks were generated using the program data for the four disks. These were scaled to produce the probability density functions (PDF) for asperity tip radius, which are presented in Figure 2.13. This shows the changes taking place and is a guide to what the plastic deformation simulation needs to achieve. Figure 2.14 presents the same results in the form of cumulative distributions.

It is interesting to note from these figures for the as-manufactured surfaces, 60% of the peaks have a radius that is smaller than 10 μm and there are no peaks with radii greater than 50 μm . During running-in the radius of curvature of peaks increases due to plastic deformation. After running-in only 20% of the peaks have radii below 10 μm . The peak value of each PDF is around 15 μm and there is a general shift of the curve towards higher radii.

As a result of these observations the decision was made to modify the surfaces by imposing changes on the radius of curvature of peaks. It is expected that peaks that have small R values will tend to carry pressures that are higher than the hardness. The changes made to the surfaces should make asperities become smoother through the increase of the radius of curvature for all asperity peaks bearing pressures higher than 2.5 GPa in the Hertz zone contact. This will lead to the height of asperities being reduced and becoming flattened into load bearing areas (referred to as “lands”), whilst leaving valley features unchanged. The aim of this investigation is to develop a process to achieve this objective.

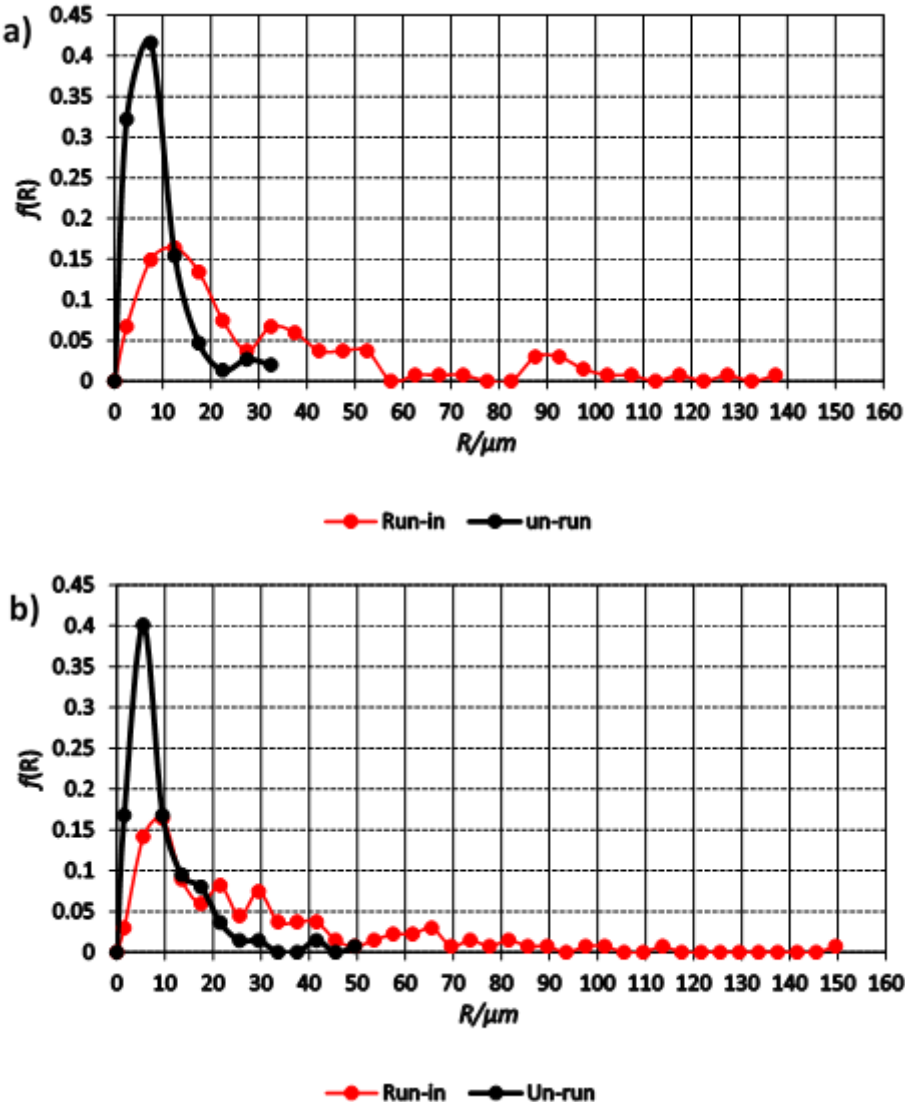


Figure 2.13 PDF of the radius of curvature at peaks in the profile for; a) the fast, b) the slow disk.

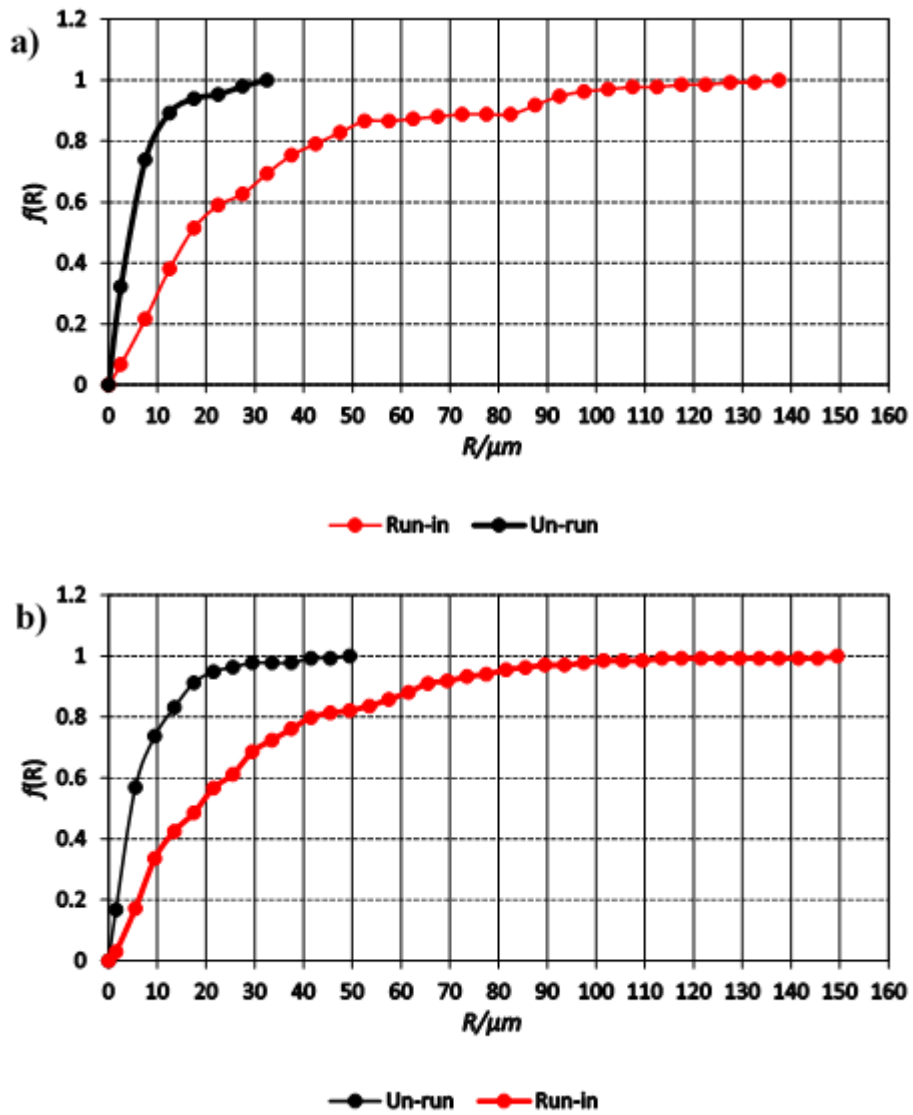


Figure 2.14 The cumulative density functions asperity peak radius of curvature of a) the fast disk, b) the slow disk.

2.17 Conclusion

The methods for asperity changes described in this chapter are the initial numerical experiments carried out in seeking to develop a running-in synthesis. Some of the changes made to the surfaces reported in this chapter are incorrect, impractical or somewhat arbitrary, but the results were an encouraging start and led to considerations of how the process could be incorporated into the EHL analysis and controlled effectively. As a result of evaluation of the asperity radii of curvature of the surfaces, the decision was made to modify the surfaces by imposing changes on the radius of curvature of asperity peaks that experienced extreme contact pressures in passing through the Hertzian contact. These asperities should experience a plastic deformation that increases their radius of curvature leading to asperities becoming flattened and more rounded with reduced heights.

Chapter 3: Simulating running-in

3.1 Introduction

The ways of modifying the surfaces summarised in Chapter 2 were considered in setting up the numerical mixed EHL model for real engineering conditions. The author had access to existing mixed EHL analysis software developed by the Tribology group at Cardiff University. This was in the form of a code to provide transient solutions to the rough surface line contact EHL problem including Non-Newtonian rheology to evaluate pressure distribution and film thickness between the rough surfaces.

For the current research new subroutines were developed and introduced to the EHL code to identify portions of the rough surface profile that carry high maximum transient pressures during their passage through the Hertzian contact. These portions are called high pressure events and consist of one or more asperities and changes were made to their peak geometries to obtain synthesised surfaces close to the experimental ones.

The Chapter describes the method used for modifying surface geometry through several stages. Three sets of rough surface profiles taken from experimental work within the research group were examined. Also, the results of the synthesised and measured run-in surfaces were compared in terms of their geometry and their mixed EHL behaviour using peak asperity pressure and direct contact occurrence as parameters.

3.2 Development Stages of coding the plastic deformation synthesis in Fortran 90

The first step to be taken was to modify the EHL analysis to obtain the Maximum Transient Pressure (MTP) experienced by all the rough surface points as they pass through the Hertzian zone. These are considered as the points leave the EHL analysis zone at the exit boundary, $x/a=1.5$. The modification process starts when the EHL analysis has become fully rough. The EHL pressures are distributed across the whole Hertzian contact zone and are not related to the roughness surface pressures at the same position. There is a difference in the mesh spacing for the analysis EHL zone and for the profile surface, which in this research were 2.25 and 1 μm , respectively. The pressure distribution obtained in each timestep is transferred by the interpolation to the *multiprofile* where the corresponding MTP profile is accumulated. A new subroutine was developed to detect high MTP (HMTP) events. An HMTP event is defined as a portion of the rough surface leaving the contact where each point has an MTP value greater than a set threshold, as shown in Figure 3.1 This is taken as a basic surface feature that will be modified by plastic deformation of the asperities that it contains. A code has been developed to implement these changes.

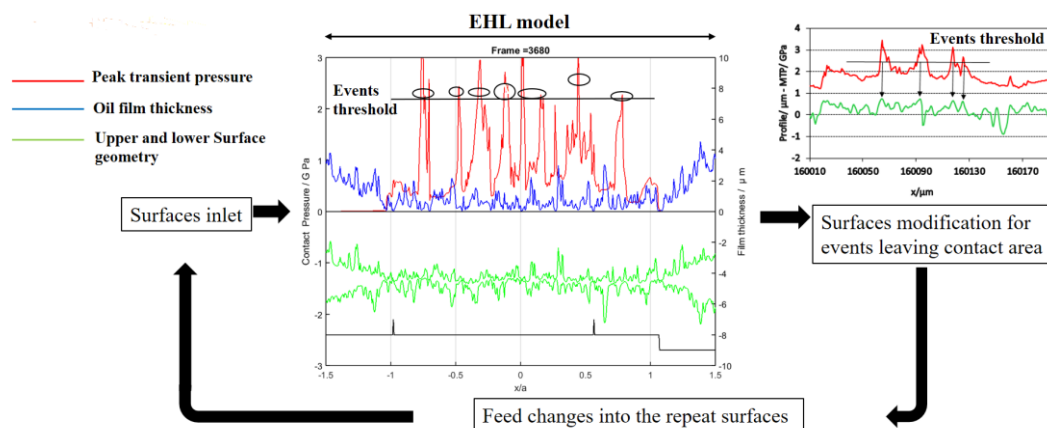


Figure 3.1 Process of surface modification.

Having identified all HMTP events for fast and slow surfaces it was clear that they might contain several asperity peaks and the code was developed so as to increase the radius of curvature of each asperity peak within the event. Subroutines were built to

make the changes to the asperities for the individual HMTP events. They modify the surface features by the increasing the radius of curvature for asperities to produce a new asperity geometry with curved load bearing lands. The way in which this works depends on the number of points in each asperity feature within the event that needs to be modified.

Initially each peak was regarded as a three-point feature and its peak point was reduced in height to increase the radius of curvature. When repeated this resulted in straight three point peaks and a process to expand the width of the modified area was required i.e. a mechanism whereby three point asperities become four point asperities, four point asperities become five point asperities, and so on. Following several numerical experiments this became a process where the new shape for an n point asperity maintains the height of end points and generates a new parabola for the other points to produce an increase in the radius of curvature from R to $R (1+m)$, where m is a parameter used to control the amount of radius of curvature increase.

To enable this to be achieved a new array (istatus) that represents the number of points in each asperity was introduced. This istatus value for each point is carried to each of its upstream positions in the whole *multiprofile*. In this way, the istatus array records the way in which asperities are modified and expanded. The value of parameter m controls the amount of radius of curvature increase for each asperity in each shape change stage was found to be best specified by the following equation:

$$m = \frac{P_{\max} - P_g}{P_g} * 0.1 \quad (3.1)$$

Where P_{\max} is the HMTP value for the n point asperity, P_g is the yield pressure and R is a radius of curvature for the n point asperity before modification. The profile change was calculated by fitting a least square parabola to the asperity points and changing its coefficients to obtain the required change in R . The theory used for this is given in the appendix. The different stages in the evolution of the process are illustrated in the following sections.

3.3 Stage One

The simulation method was first developed for the case of EHL contact between un-run real surfaces from test disks having a similar hardness at a slide to roll ratio of 0.5. The conditions were analysed at a nominal maximum Hertzian contact pressure of 1.4 GPa. Program tests were carried out with an oil meeting the OEP-80 specification at a temperature of 95°C. Other data are given in Table3.1 .

Table3.1 Operating Conditions.

Fast surface velocity	U_1	5.98 m/s
Slow surface velocity	U_2	3.59 m/s
Oil viscosity	η	0.0092 Pa.s
Oil pressure viscosity coefficient	α	$1.37 \cdot 10^{-8} \text{ GPa}^{-1}$
lambda ratio	λ	0.4

In the first stage program, peaks were regarded as three point peaks without expansion capability. Peaks with HMTP events were modified with a fixed value of m , which set at 0.1, 0.2 and 0.3 in turn. The asperity-peak radius R was calculated as the radius of the parabola through the peak point and its two closest neighbours. The new radius of curvature was then calculated according to the value of m described above and the modification was made to the peak point only and to all the upstream repeats of the point in the *multiprofile*.

The representative profiles were chosen for the *multiprofile* by joining repeats at their first and last valley features. 50 repeats were used for the fast profile and 40 repeats for the slow profile. The EHL analysis was run for 20,000 timesteps with a 1 μm mesh spacing, and the results used to assess the operation of the model are shown in Figure 3.2.

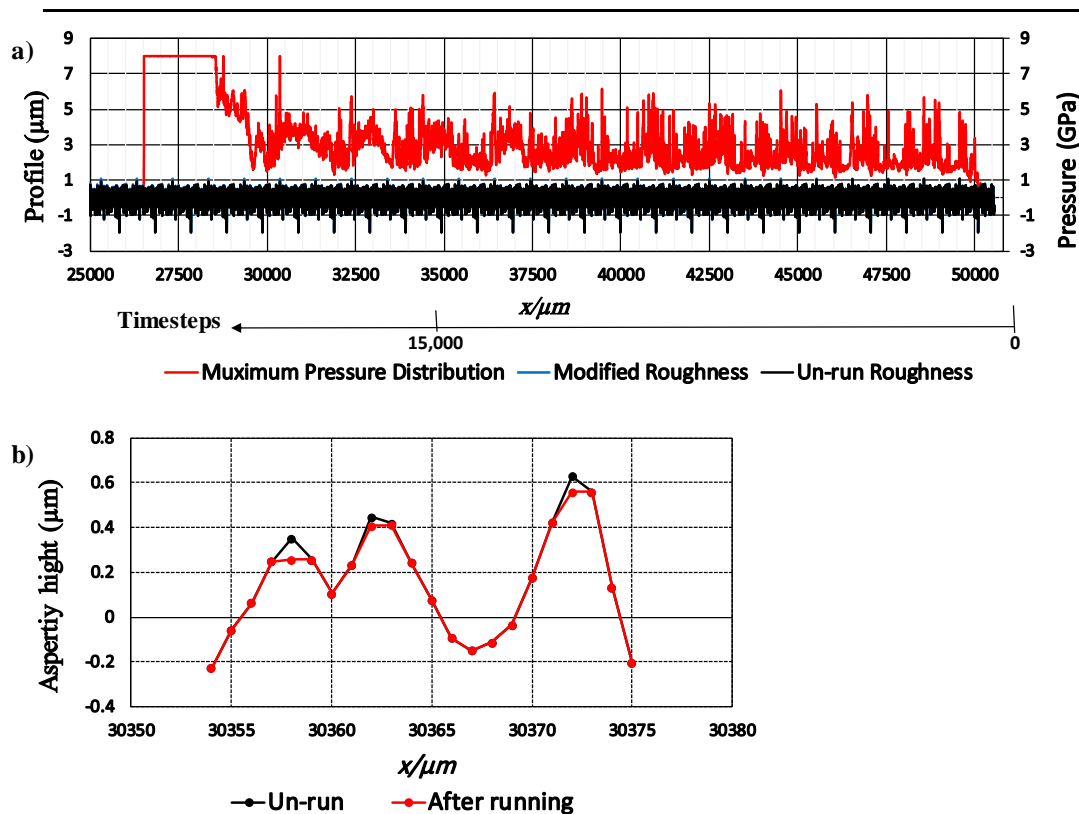


Figure 3.2 a) The MTP pressure distribution and surface heights for the multiprofile for 20,000 analysis timesteps for stage one, b) HMT event that includes three asperities showing their shape before and after modification for the fast disk.

Figure 3.2a shows the results of the full run in terms of the multiprofile. A detail of the multiprofile at the end of the run is shown in Figure 3.2b. It includes the modifications made as the run progressed but these are not apparent at the scale of Figure 3.2a. The upper curve shows the MTP value for each point in the multiprofile. In the analysis the multiprofile passes through the EHL mesh with high index first i.e. point 50000 is the first to reach the exit boundary. An indication of the timestep is given in the added scale below the figure. The objective is to find a model that will reduce the MTP value to the hardness level. This does not happen in this first example.

Figure 3.2b shows a short length of the multiprofile for an HMT event centred at index position 30365 in the as-manufactured and modified form on a scale that allows asperities to be seen.

It is clearly seen in from Figure 3.2a that the pressure distribution deteriorates during the run and reaches up to 8 GPa as the process of surface modification continues. This value of pressure is imposed as a maximum in the EHL analysis. This means the EHL

mechanism obtains higher and higher MTP but it is restricted to 8 GPa. This indicates that the asperity modification model is not working in the intended way.

A three asperity event has been chosen to illustrate the way in which this model modifies the peaks in Figure 3.2b. The three asperities have different shapes and were extracted from a specific position in the fast profile. The figure shows that the asperity tip shapes have been modified to produce a plane surface as the radius of curvature increases. This approach made the surface become more aggressive and caused it to generate very high pressures causing the EHL analysis to break down. It was concluded from this process that some asperities are modified until they become flat and do not produce a large pressure. This makes a local flat in the asperity shape rather than causing it to expand in width and become a load bearing land. It was concluded that the asperity modification areas need to be able to grow in width.

3.4 Stage Two

The results for stage one, show that the three-point process is not sufficient. The deforming asperity area needs to grow wider if modifying the peak does not lead to reduced HMTP values. The process of expansion adopted is shown in Figure 3.3. Points A and B represent the peak asperity boundary points. Dimensions h_1 and h_2 represent the height difference between the peak point and the neighbouring points on both sides.

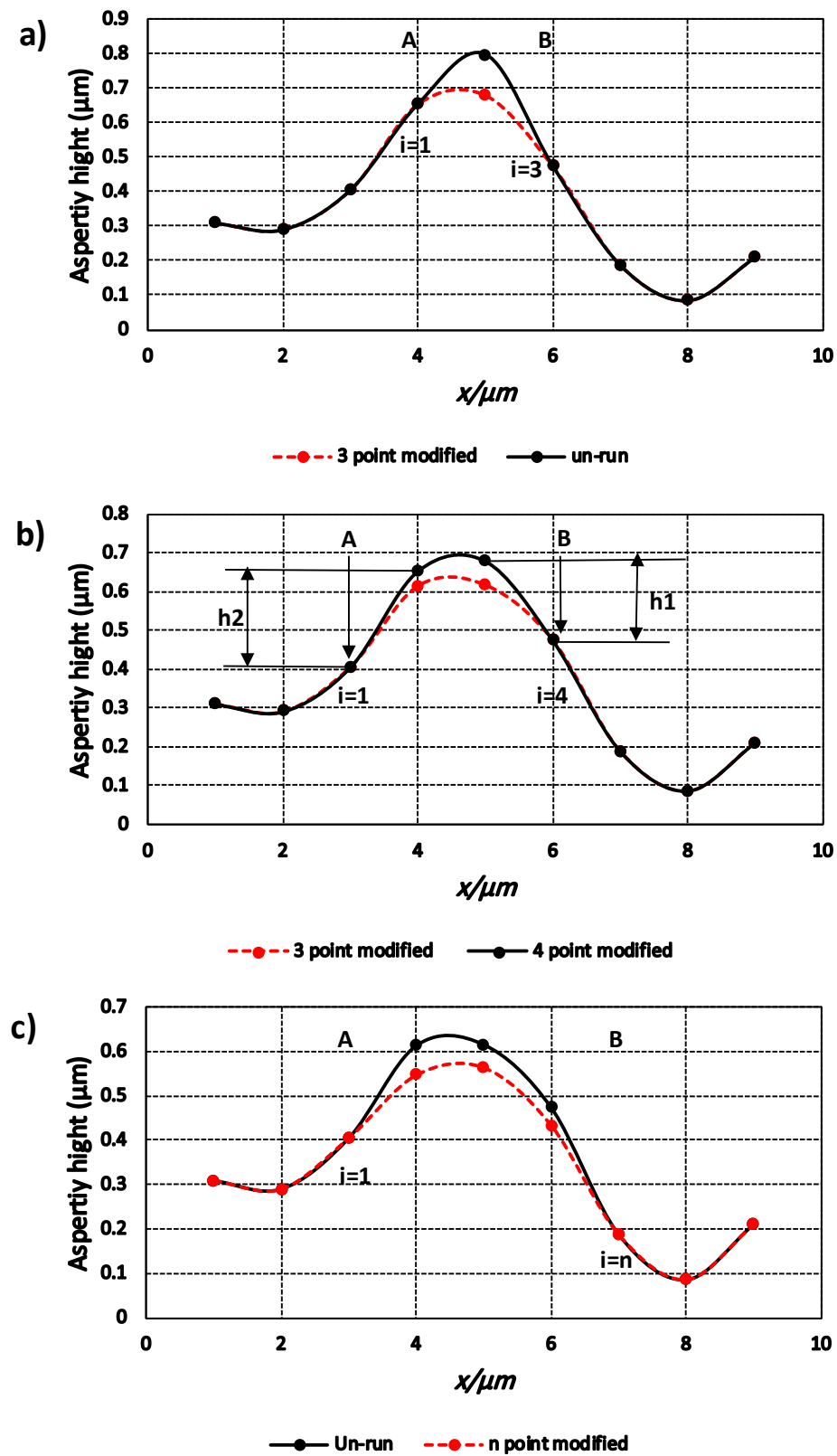


Figure 3.3 Criterion for expansion of asperity a) 3 point modification b) 4 point modification c) n point modification.

The criterion for expansion is represented by considering each asperity in the event as a three-point feature and reducing its peak point in height progressively to increase the radius of curvature. There is no change to the A and B boundary points until the three-point asperity is becoming near to planar. This situation could be linked to the increasing radius of curvature in terms of Figure 2.12 but was developed simply in terms of dimensions h_1 and h_2 .

When the value of h_1 becomes less than 10 % of h_2 , or vice versa, this is taken as the trigger to expand the three-point asperity to a four-point asperity. The expansion takes place on the side of the least of dimensions h_1 and h_2 giving new boundary points A and B where one point has been moved so as to expand the asperity. Least squares curve fitting is used to generate a new parabola passing through the new boundary points A and B with a minimised distance between it and the internal points. This has a radius of curvature R at its peak and the new modified shape is adjusted to be the parabola passing through the end points which has a radius of curvature $R(1+m)$ at its peak. Further expansion from four to five points (or generally from n to $n+1$) occurs when an internal modified point becomes smaller than a boundary point. Expansion is in the direction of that boundary point. When two asperities share a boundary point, the expansion process will cause the two asperities to merge. The process for changing the asperity height occurs step by step in many stages and asperities grow from three to n points by the expansion process as shown in Figure 3.4.

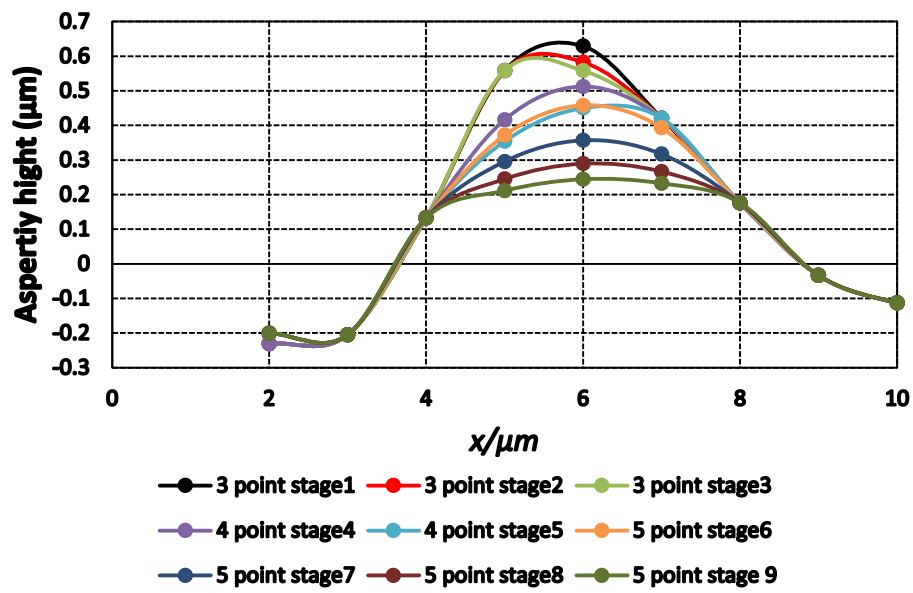


Figure 3.4 The process for the expansion of asperity in different stages starting from 3 points to n point modification.

The simulation test was implemented over 35,000 timesteps with the same conditions as stage one and the results are shown in Figure 3.5.

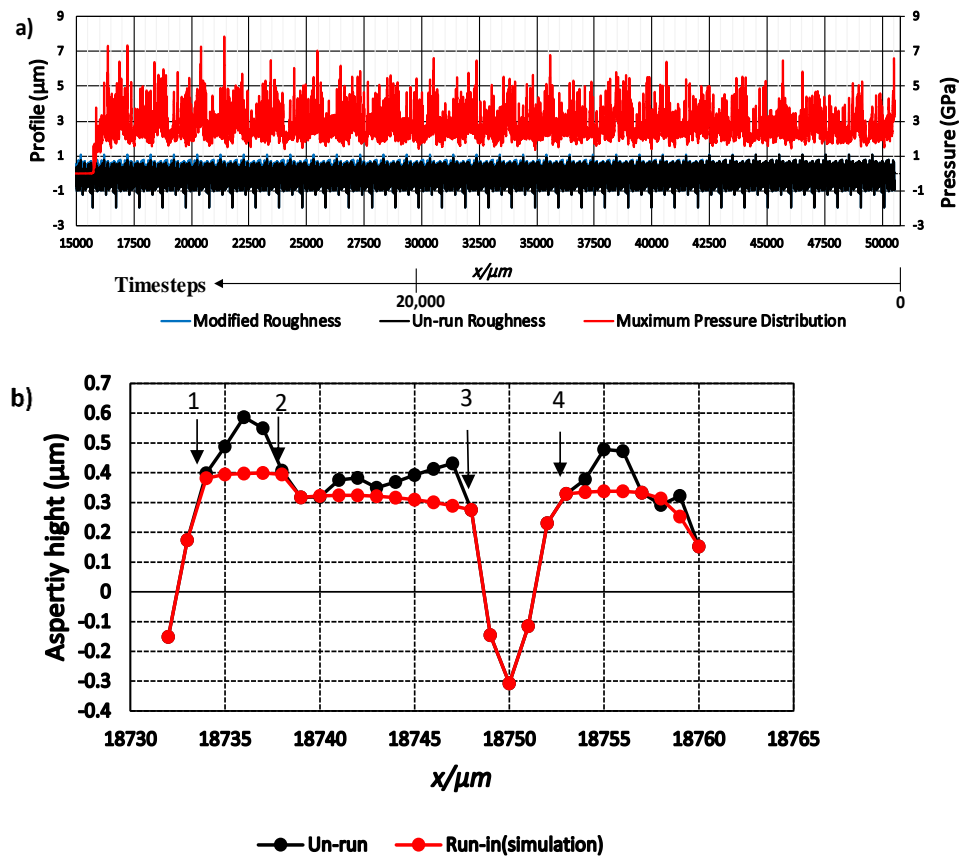


Figure 3.5 The MTP pressure distribution and surface heights for the multiprofile after 35,000 timesteps for stage two, b) HMTP Event that includes three asperities showing their shape before and after modification for the fast disk.

It is clear from Figure 3.5a that the surface still experiences HMTP values as high as 7.5 GPa. However, from the comparison between the results in Figure 3.2 and Figure 3.5 there is a big difference. It is clearly seen that there is an improvement in MTP distribution results. For instance, the maximum value of MTP in stage two does not exceed 7.5 GPa and the number of points in the profile that have an HMTP value of 7.5 GPa are very small in comparison with stage one. Furthermore, Figure 3.5a shows the points in the profile that have the lower value of MTP are down to the 2 GPa level whereas in stage one there was an increased to 8 GPa. These results indicate that the stage 2 approach still needs further improvement. Three asperities have been chosen from a fast profile for this investigation. It is important to notice from Figure 3.5b that the radius of curvature of asperity tips after modification becomes very large. In

addition, the corners for both sides of tip became very sharp and this is not realistic in comparison with the results from the laboratory tests, which have smooth curves with gentle corners. For example, at the peak asperity boundary points identified with numbers 1, 2, 3 and 4 in Figure 3.5b unrealistic corners have developed which do not become modified as the process continues. It is clear that high pressure is generated by these corners but the asperity expansion process does not bring them into the modification area.

3.5 Stage Three

After considering the results from stages one and two it was concluded that more factors need to be considered in the approach. Stage two produces plane lands with sharp corners. A plane land has very high peak radius of curvature but the statistics of run-in surfaces show that this is incorrect. Therefore, two further factors were added to the model to address this difficulty, R_{gm} and R_{co} . R_{gm} is the radius of curvature of the asperity and R_{co} is the smaller three-point radius of curvature at its corners. To prevent R from becoming too large R_{gm} is limited to a value of $120\mu\text{m}$. Similarly, to prevent very small corner radii, R_{co} is required to be at least $12\mu\text{m}$.

The values of these limits can be specified in the program and are chosen based on the observed statistics of the run-in surfaces. They are implemented as follows. If the R_{co} value is too small at the boundary point, the boundary height is reduced so that the corner three-point radius of curvature is maintained at $12\mu\text{m}$. The best-fit parabola is then recalculated based on the new boundary height and the process continues. If the, R_{gm} value is too large then the asperity grows by one point at its highest boundary. Again, this leads to a new best-fit parabola and the process continues.

The test was implemented with 200 repeats used for the fast profile and 160 repeats for the slow profile. The program was run for 175,000 timesteps. The value of m that controls the amount of radius of curvature increase for each asperity was used from the equation (3.1). The other operating conditions were the same as for stage two and the results are shown in Figure 3.6. The changes made to the asperities are now much more realistic but the pressures are not reduced to the set level. The pressure distribution gives better results than stage two. Its values are less than 7 GPa and decrease to below 5 GPa with continuing modification of the surfaces. Figure 3.6

shows the asperity peaks became rounded with gentler corners and the modification made to the shape was much improved in comparison with Figure 3.5b.

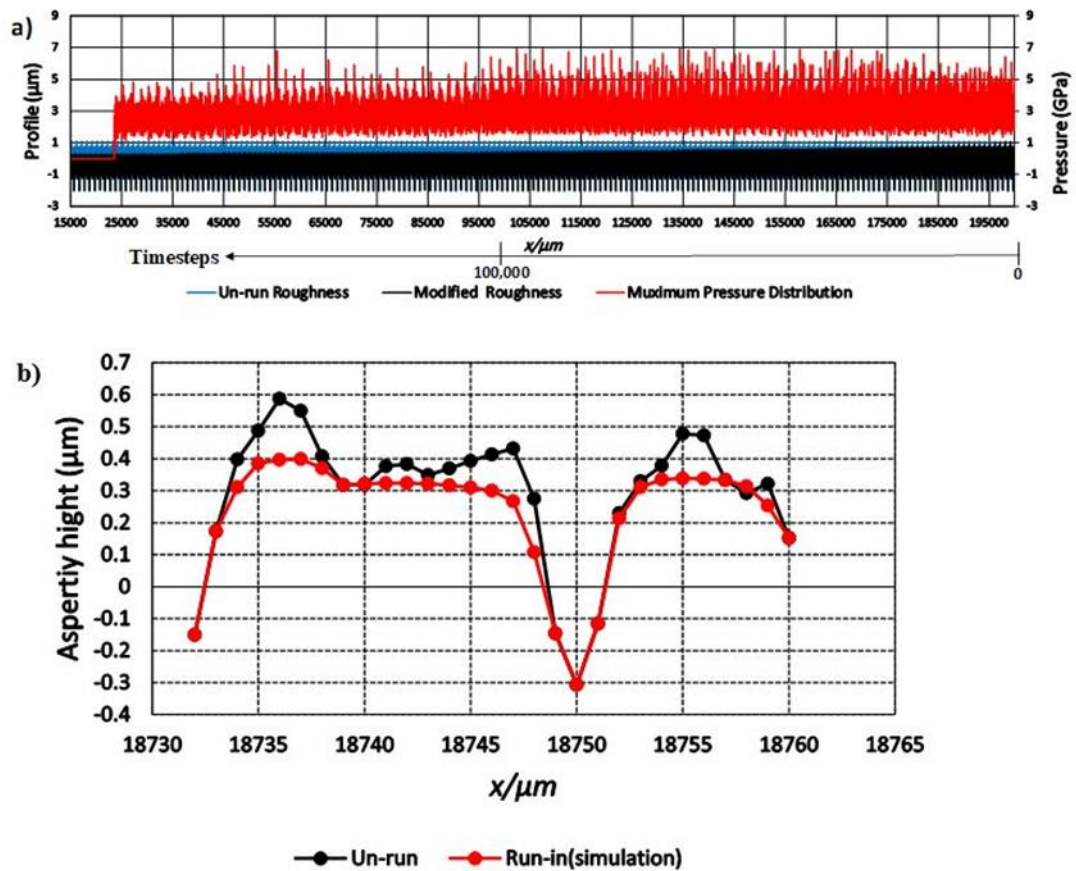


Figure 3.6 The MTP pressure distribution and surface heights for the multiprofile after 155,000 timesteps for stage three, b) HMTP Event that includes three asperities showing their shape before and after modification for the fast disk.

It was realised that the MTP at local peaks could now fall below the threshold, or close to it, and when that happened the algorithm does not find the peak. The profile shape is much improved but the model stabilises with high pressure remaining because the HMTP values do not then happen at the asperity peaks when the asperities have modified to the form of realistic asperity lands. The m formula for asperity modification is driven by the peak pressure at the highest point, but the actual highest pressure is not generated at the highest point. As the pressure at the highest point falls to be near to the threshold for action, the formula gives an m change value that is very low and essentially prevents further change to the asperity. The program detects all the events but does not actually implement changes because most of the events do not

have peaks. If the event does not have a peak in it, no further change is made even though the asperity has a high HMTP value. The asperity will plastically deform when it has high pressure at the peak point and otherwise it will not deform. This observation leads to the consideration of the maximum pressure at all asperity points for the next development stage.

3.6 Stage Four

Further investigation was made to the previous stages. It was found that the HMTP occurs not only on the asperity peaks but also on the asperity flanks. Moreover, as the modification progresses, a large number of events do not have peak points and this means that the event is not modified. The pressure is hydrodynamic and is generated in the oil film thickness according to the velocity of the surfaces.

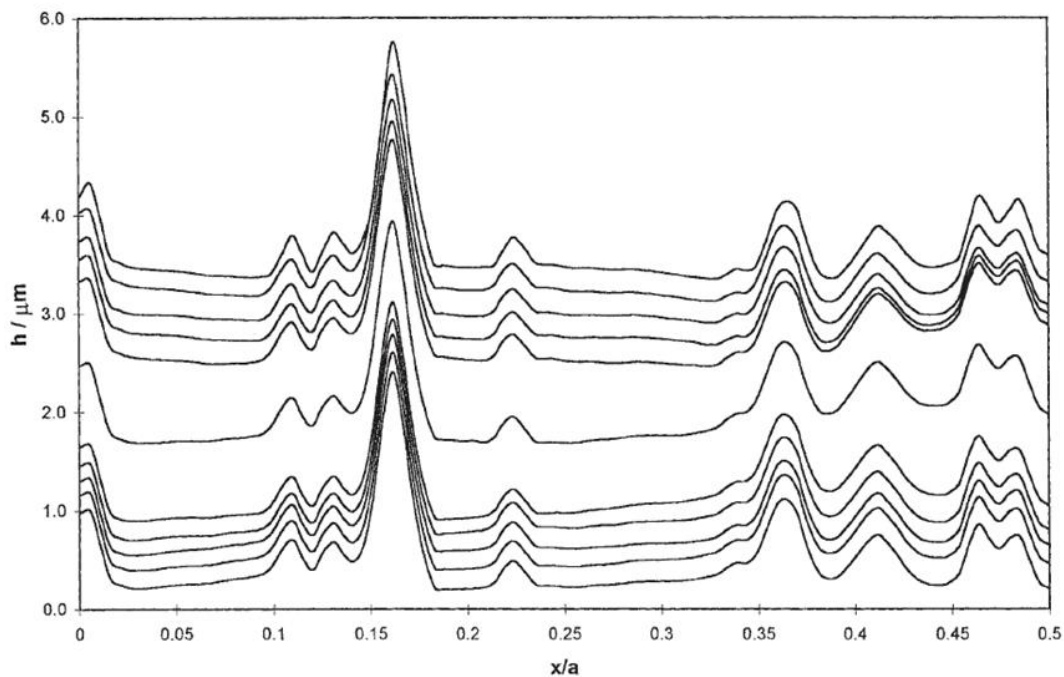


Figure 3.7 The effect of the different slide–roll ratios on the Film thickness for the roughness profile at the centre of the contact (Elcoate et al., 2001). Note that the curves are offset for comparison purposes.

Elcoate et al. (2001) consider the EHL contact of a rough and smooth surface over a range of sliding conditions. They draw attention to the film thickness distribution generated for a section of the roughness profiles according to the slide–roll ratios. Figure 3.7 illustrates the full range of slide–roll ratios with the film thickness of the

surface section at the same contact position. The film thickness distribution for each case is offset to make it clear for comparison with the others. The five upper curves represent the family of the negative slide–roll ratios (-1.2, -0.6, -0.3 and -0.15) respectively. In these cases, the profile deforms to generate an asperity film that is convergent from left to right. This is the direction of entrainment relative to the rough surface. The lowest five curves, which represent the positive slide–roll ratios, form another family of EHL responses with the film convergent from right to left. The curve in the middle is for case of pure rolling and is different, as it does not generate entrainment relative to the profile asperity within the interaction area. It is clear that the pressure generated is governed by the hydrodynamic action and will not be maximum at the highest point of the un deformed surface. The observations from stage three results and this study (Elcoate et al., 2001) were considered in developing the code. The process was designed to be driven by the maximum pressure in the event and not that at the local peak point. Moreover, when the event does not include an internal peak its width is increased so that the peak beyond the highest boundary is included together with two further points so that the boundary is beyond the peak. This process was carried out for a total of 175,000 timesteps with other operating conditions the same as for stage three.

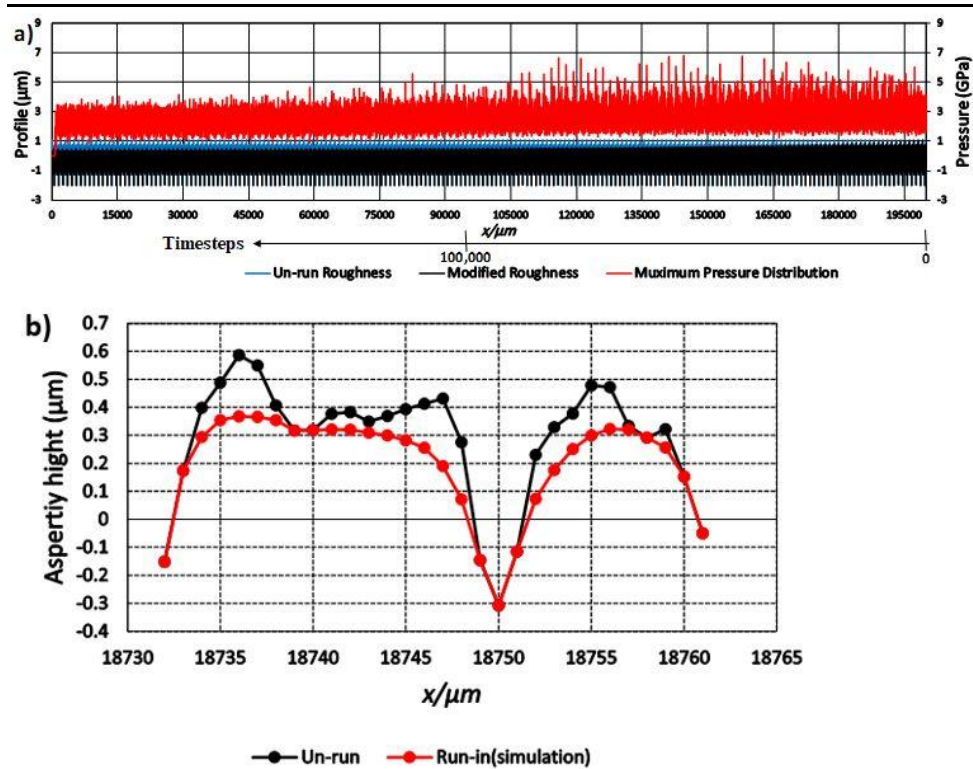


Figure 3.8 a) The MTP pressure distribution and surface heights for the *multiprofile* after 175,000 timesteps for stage four, b) HMTF Event that includes three asperities showing their shape before and after modification for the fast disk.

Figure 3.8 shows the result, which is the most promising result in comparison with the other stages. The pressure maximum value is reduced significantly, as the process of modification continues and becomes stabilised at a value of around 3.25 GPa after 70,000 timesteps. This change to maximum pressure occurs smoothly but comparison with the experimental results of running-in indicates that the shape of asperities need to be modified further in order to have good agreement with experimental ones.

3.7 Stage Five

Further development was made to the stage 4 code. The parameter $Pcount$, which is the count of the number of time steps where High Maximum Transient Pressure values $HMTF > 2.5$ GPa occurred was incorporated in the surface modification process. The modification to the surface asperities was suppressed for points with $Pcount$ less than four. This is because a low value of $Pcount$ indicates that the asperity is not itself the cause of its high maximum pressure, and that this results from contact with a particular counterface asperity that has not been modified sufficiently. These counterface

asperities will tend to have high *Pcount* values. In Figure 3.9, which shows one asperity event, for example, the stage four code makes a greater change to the wide central asperity than it does to the neighbouring narrower asperities. Because the process of surface modification in stage 4 is driven by the radius of curvature, its changes in height continue until its MTP value falls below the threshold for change.

It can be seen from Figure 3.9 that in their interaction with the counterface the case 4 synthesis made a significant change to the asperity with a large radius of curvature but a much smaller change to the sharp asperities for a specific value of parameter *m*. It is clear from the run-in profile that this process does not happen in the experimental case.

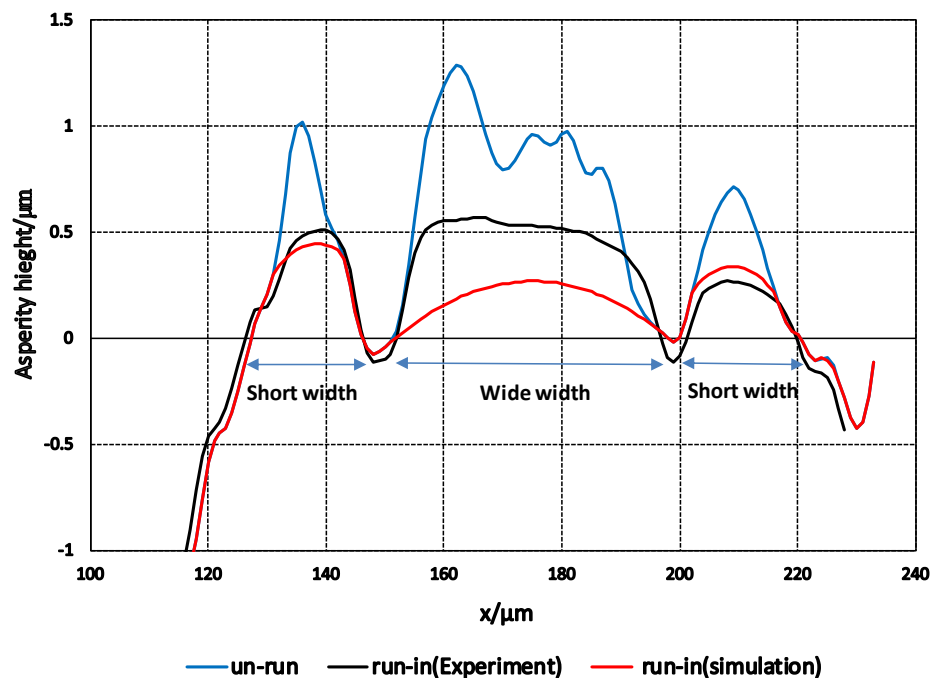


Figure 3.9 The shape of a group of three asperities for the as-manufactured, experimental and stage 4 model synthesis profiles.

Further changes to the process were developed at this stage to consider this issue by adding a new factor to the *m* equation (3.1) that introduces more control to the amount of change in radius of curvature and the height of the asperity. This factor (*f*) is specified by the following expression:

$$f = \frac{8}{NP_modified} * va \quad (3.2)$$

Where *NP-modified* represents the number of points in the asperity to be modified, and *va* is a variable value. The values of *m* obtained from this formula for a range of MTP and *NP-modified* values are presented in Figure 3.10.

The *m* formula is also modified to include a further factor *f*:

$$m = \frac{MTP - P_g}{P_g} * f \quad (3.3)$$

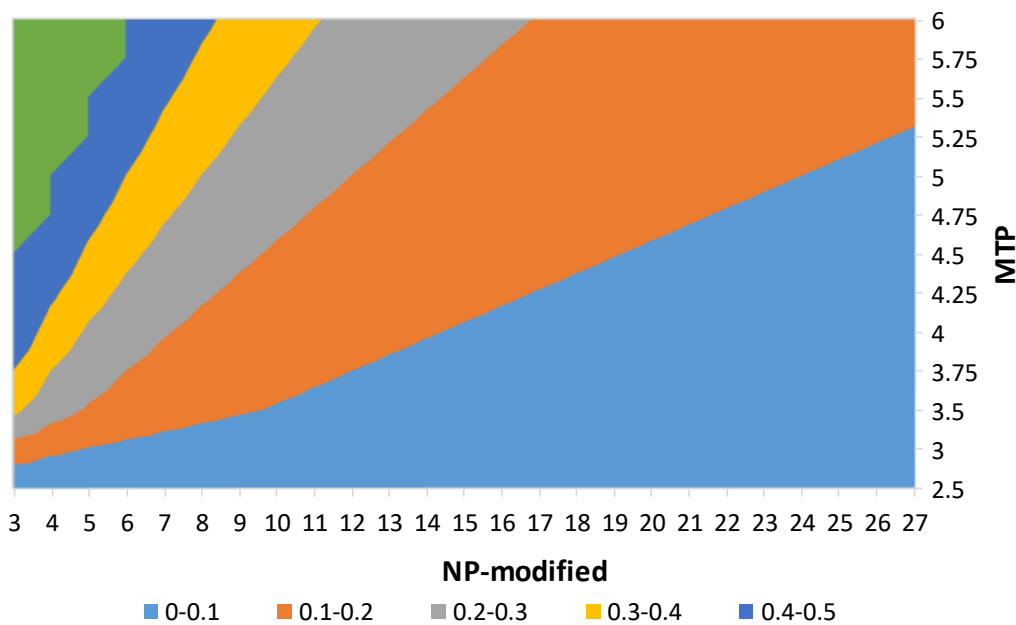


Figure 3.10 The values of *m* for different values of MTP and NP-modified for *va* = 0.2.

The mesh spacing for profile surfaces in the *x*-axis direction is uniform and equal to 0.5 μm . The height intervals between points are non-uniform. It was noticed that some asperities that have sharp valleys have large height intervals. The process of modification moves through each point of the profile included in the HMTP event individually. When an asperity boundary point has large height difference compared to the neighbouring point outside the asperity, the process for widening the asperity to include this neighbouring point was found to be aggressive and cause large changes. To counter this, when the value of this vertical spacing (*h*) in Figure 3.11 a was greater than 0.04 μm at the boundary the widening process was replaced by reducing the endpoint height by 0.04 μm . This result of this change process is shown in Figure 3.11.

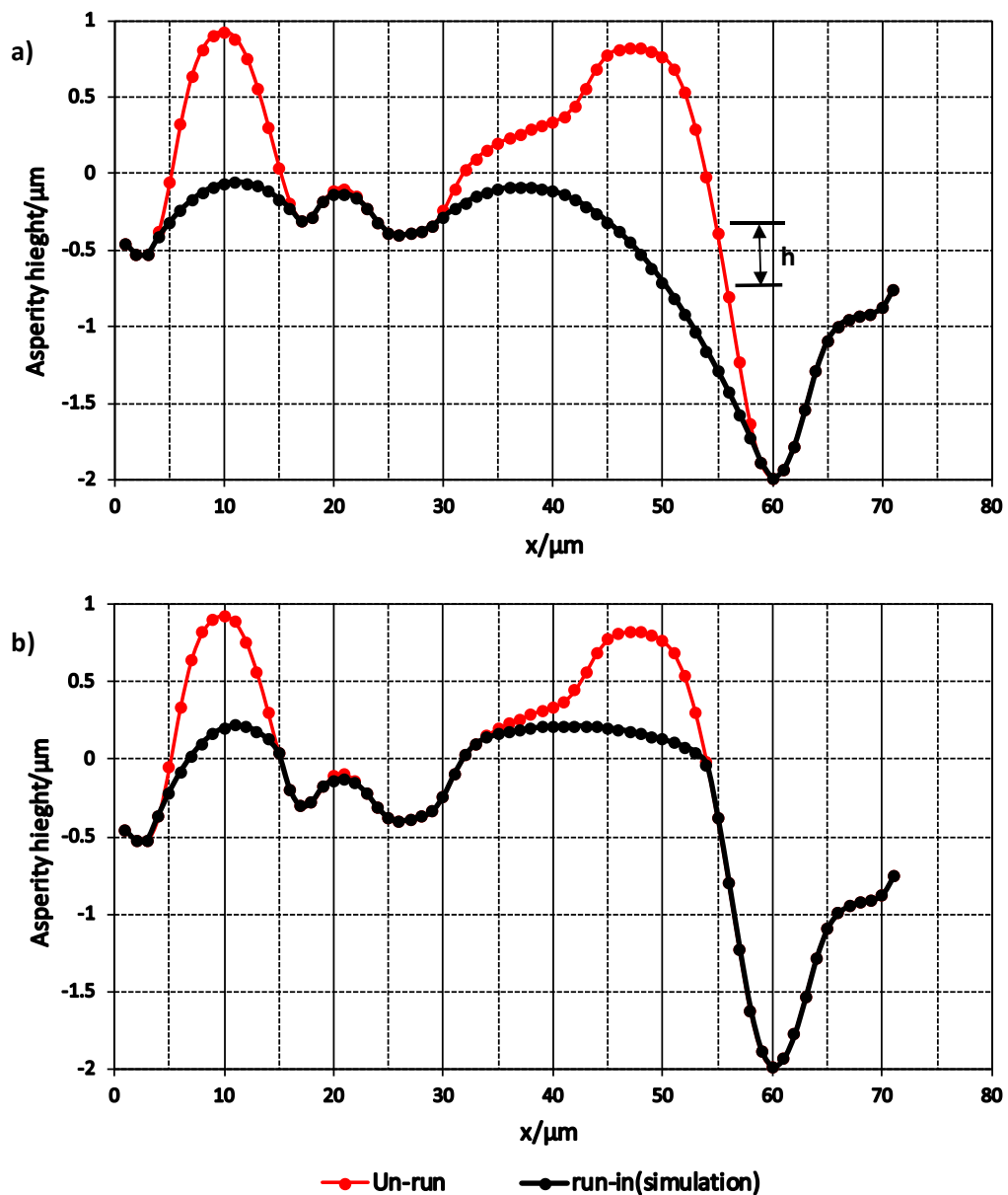


Figure 3.11 The process of expansion to include large vertical height differences at asperity boundaries a) before introducing improvements b) after improvement.

Because the surfaces run in rolling/sliding contact and with a slide roll ratio of 0.5, the m parameter equation of the slow surface was multiplied by two. This was introduced in response to observing that asperities on the fast surface were seen to be modified more quickly than those of the slow surface, which was counterproductive.

The form of the running-in synthesis formula was developed by conducting tests using a range of values of parameter va , as listed in Table 3.2.

Table 3.2 The values of νa that were tested.

0.2	0.09
0.15	0.085
0.13	0.08
0.12	0.075
0.1	0.07

After implementing the program with the values of νa given in Table 3.2, it was found that the best results were obtained with $\nu a = 0.08$ in comparison with experimental profiles. There was insufficient change to the surfaces at the value of νa equal to 0.07, and on the other hand, there were large changes to the surfaces at the value of νa equal to 0.2. The same asperities as shown in Figure 3.9 were considered and the results have been improved by the changes introduced in equation (3.3). A good agreement was achieved between the synthesis results and the experimental profiles as shown in Figure 3.12.

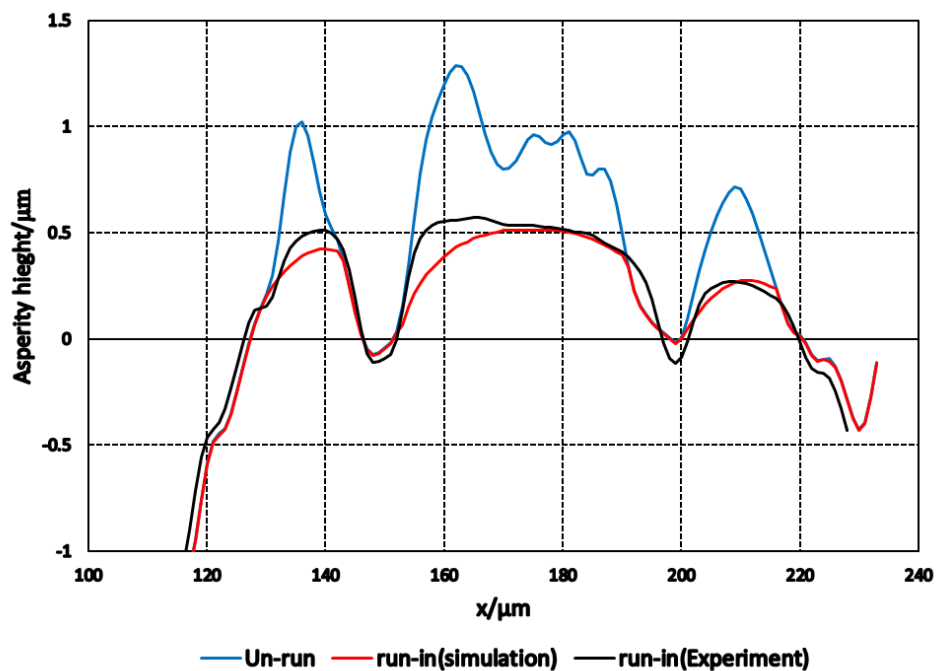


Figure 3.12 Shape of a group of three asperities as-manufactured, after running-in and using the EHL synthesis based on equation (3.3).

Further modification made to the program was to introduce a control aimed at ensuring that the program converges at a certain set hardness level of surfaces.

As each repeat passes out of the contact zone, the average of the eight largest contact pressures experienced by the surface mesh points is calculated. The value of P_{max} is monitored for diagnostic purposes and is used to terminate the synthesised running-in. This occurs when the average of P_{max} values for 20 consecutive repeats falls below a set threshold which corresponds to the effective hardness level.

However, program tests were run again with an operating condition as represented in Table 3.1. The code was converged at surface hardness level, which to 127540 cycles. The results are shown in Figure 3.13 and Figure 3.14 which show the profiles and also the number of points modified in each asperity.

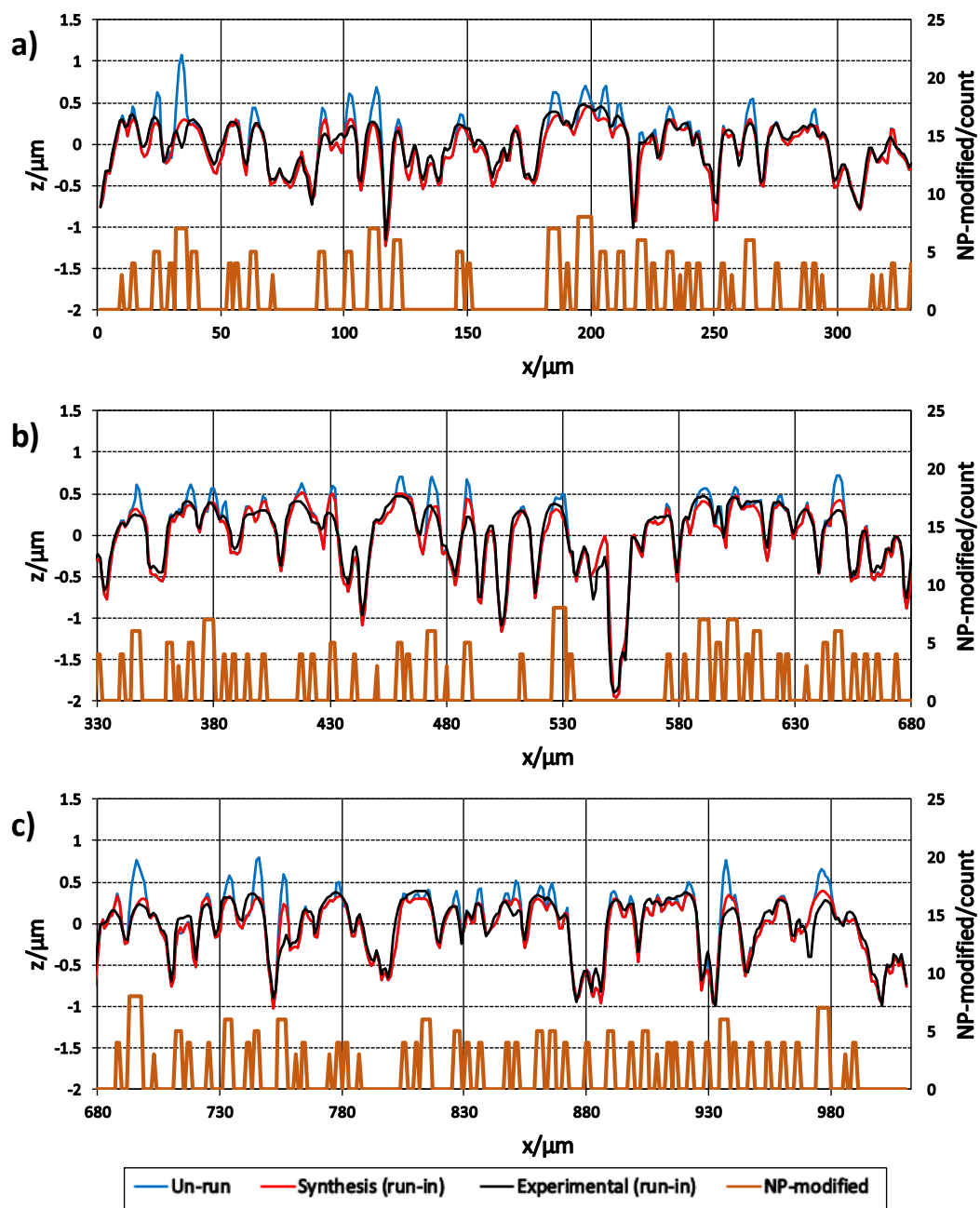


Figure 3.13 Fast surface profile from (Weeks 2015) for the EHL analysis showing the as-manufactured, synthesised run-in and experimental run-in profiles, a) , b) and c) show sub-lengths of the profile in sufficient detail to inspect individual asperity shape changes.

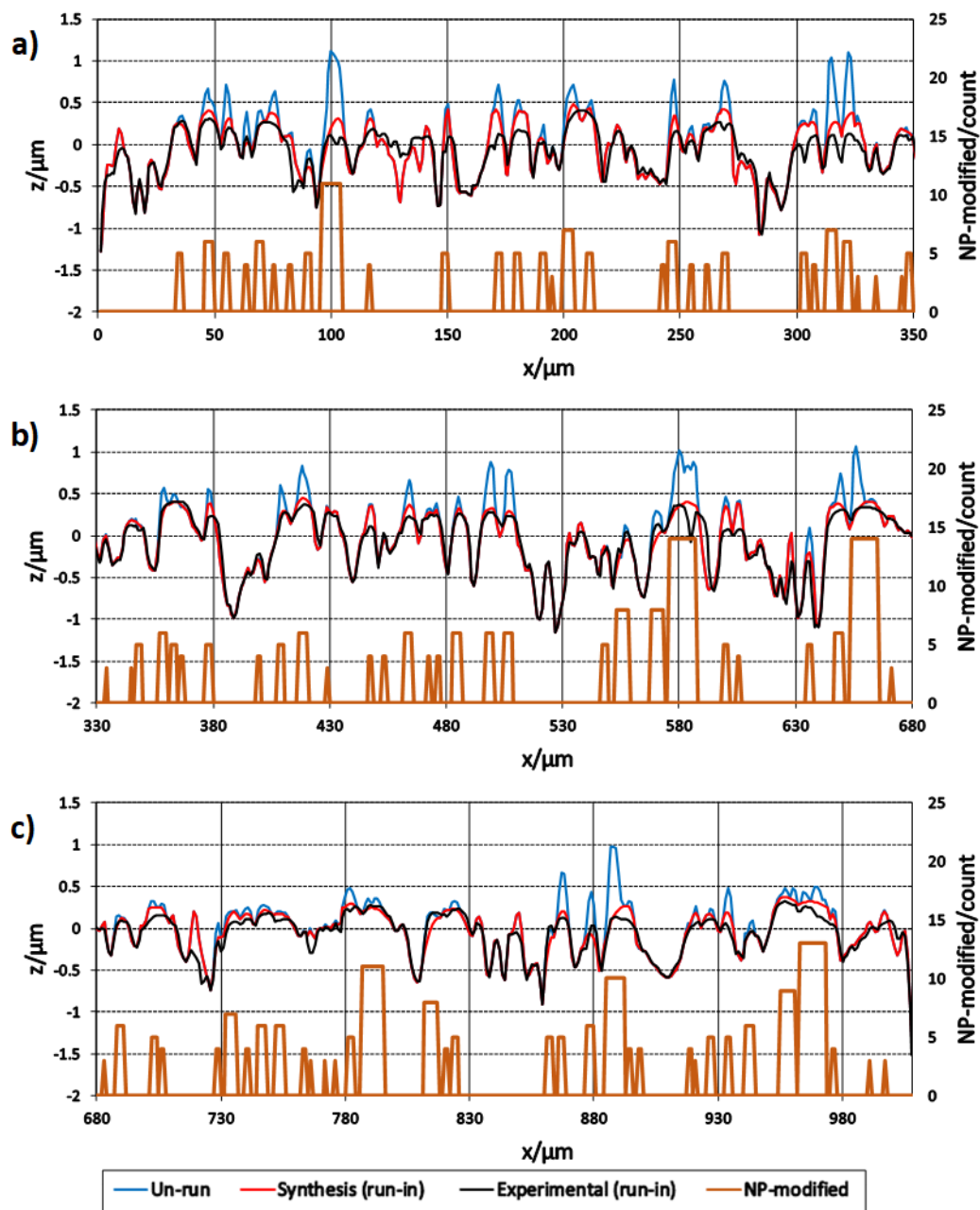


Figure 3.14 Slow surface profile from (Weeks 2015) for the EHL analysis showing the as-manufactured, synthesised run-in and experimental run-in profiles, a) , b) and c) show sub-lengths of the profile in sufficient detail to inspect individual asperity shape changes.

Figure 3.13 and Figure 3.14 show the synthesis results achieved from the numerical simulation test for both the fast and slow surfaces and compare them with the experimental profiles. It was noticed that there are promising results and reasonable agreement is shown with experiment results. There are differences between the results and it should be noted that the interaction between asperities in the numerical analyses

do not reproduce the interaction between the surfaces in the actual experiment. It is encouraging to see the level of agreement in the synthesised asperity shapes which show the same general trend.

3.8 Profile Sets Two and Three

Another two surface roughness profiles were obtained from work carried out by (Hutt et al. 2018) as a part of his study of micropitting and Acoustic Emission and they will be referred to as profile set 2 and 3. These profiles were taken from the fast disk (FD) and the slow disk (SD) in a micropitting experiment test. 12mm long profiles were taken at particular marked locations on the disk circumference in the as-manufactured condition. The test was then run for a 6 minutes' period with an oil meeting the OEP-80 specification at a Temperature of 93°C. The profiles were then retaken at the same specific circumferential locations of the disk. This method was used by Hutt to detect the changes occurring at roughness asperity features.

From the 11.2 mm long filtered profiles (about 22000 points), a representative portion 1mm long (2.5a, 2000 points) was selected from the centre line of the slow surface. Then this was moved along the complete fast surface profile in steps of 10 points using a small code written in FORTRAN. The purpose of this exercise was to know how much these profiles intersect each other. A 1 μm gap was set between the mean lines of the profiles, as shown in Figure 3.15. Variable x is the slow surface position as the profile is moved relative to the fast surface.

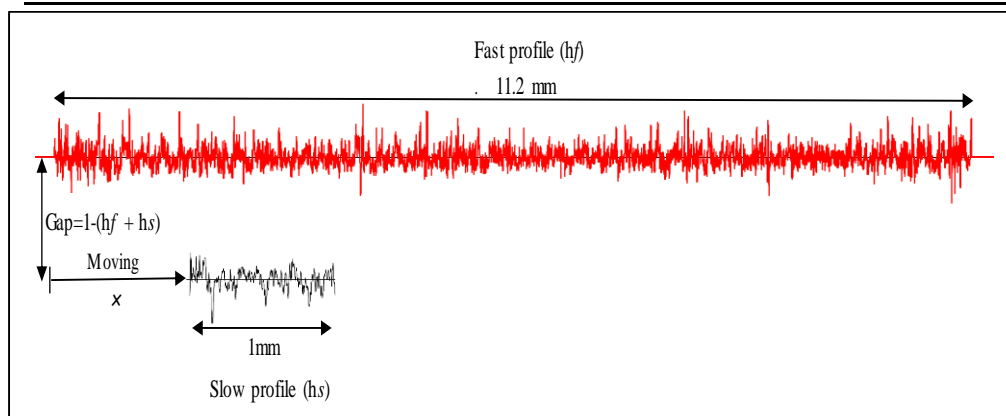


Figure 3.15 Traverse of un-run slow profile as it traverses the complete fast profile in order to detect the position of maximum and minimum penetration between profiles.

Figure 3.16 shows the average gap between the surfaces as their relative position changes. The smaller gap between steps 1315 to 1350 of the x -axis that means there is more penetration between the fast and slow surfaces in that relative orientation, whereas the biggest gap in the region between steps of 630 and 660 of the x -axis corresponds to less surface interaction in that relative orientation. The x -axis represents the number of steps through which the slow surface profile is moved over the complete fast surface.

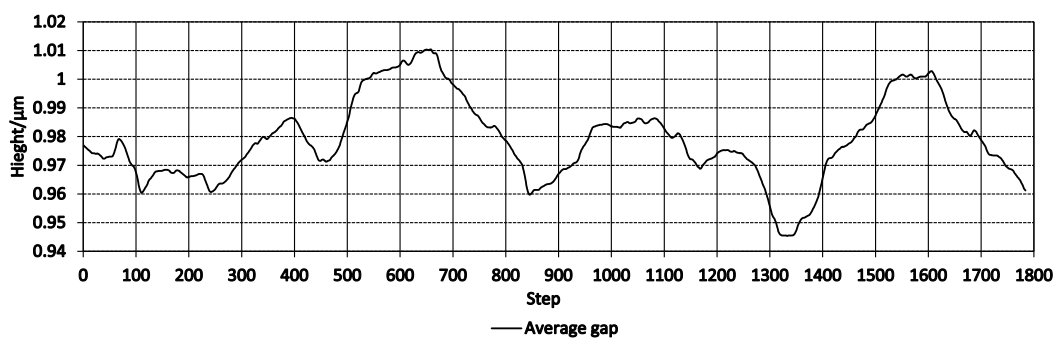


Figure 3.16 Average gap between the two surfaces as the offset position, x , is varied.

Two different representative samples each 1 mm long were taken from the fast surface to be used in EHL simulations as counter faces for the slow surface representative sample. These were taken at the positions of maximum and minimum penetration identified using Figure 3.16 so as to consider the sensitivity of the analysis to

variations in the counter face alignment. These representative profiles were taken for both the as-manufactured profile and those at the same positions after running in.

The representative profiles taken were $2a$ long for both the high and low penetration of fast and slow profiles. This was equal to 0.804 mm and the number of points in each representative profile was 1609. *Multiprofiles* were created for EHL analysis using 200 repeats for the fast disk and 160 repeats for the slow disk. The numerical analyses were then carried out with 10,000 timesteps and a $0.5\mu\text{m}$ mesh spacing with the operating Conditions given in Table 3.3.

Table 3.3 Operating Conditions

Fast surface velocity	U_1	3.99 m/s
Slow surface velocity	U_2	2.394 m/s
Oil viscosity	η	0.0098 Pa
Oil pressure viscosity coefficient	α	$1.348 \cdot 10^{-8} \text{ GPa}^{-1}$
lambda ratio	λ	0.24
slide roll ratio	ξ	0.5
nominal maximum contact pressure	P	1.2 GPa
Hertz contact dimension	a	0.402 mm

3.9 Lowest Penetration Surfaces

The comparison was made between EHL analyses using (i) surfaces obtained using the running-in synthesis model, and (ii) the corresponding profiles taken from the experimental profiles taken after running-in. Two comparisons were made, one using the representative slow surface running against the representative fast surface with minimum penetration, and the second running against the fast surface with maximum penetration. In this section, the low penetration analyses are considered, and this is referred to as Profile Set Two.

Figure 3.17 and Figure 3.18 demonstrate the synthesis results achieved from the numerical simulation test for the low penetration surfaces and compare them with the experimental profiles. It was noticed that there are promising results and reasonable agreement is shown with experiment results. There are differences between the results and it should be noted that the interaction between asperities in the numerical analyses do not reproduce the interaction between the surfaces in the actual experiment. It is encouraging to see the level of agreement in the synthesised asperity shapes which show the same general trend.

At the x positions of 273, 403, 478, 554, 993, 1144 and 1477 μm on low Penetration EHL analysis of the fast surface (Fast min) as seen in Figure 3.17, and x positions 154, 456, 1413 and 1594 μm on slow disk as shown in Figure 3.18, micropitting events happen, and this is not a feature of the simulation program.

The parameter *NP-modified* represents the number of points that have been modified for individual asperity features for the synthesised run-in surfaces. High values of *NP-modified* were found at the asperities that have clear micropits in the experimental run-in profile. Furthermore, the *NP-modified* value for valley features equal zero, which means that the MTP value is less than 2.5 GPa in these valleys. Thus, the simulation process does not detect events in these areas, so no changes happen to these valleys and this is in agreement with the experimental profiles.

In addition, it can be seen that some neighbouring asperities were merged together and became a single more rounded asperity. This effect can be seen at x positions of 275, 380, 400, 675, 880, 1145, and 1435 μm of the fast disk as seen in Figure 3.17, and x positions 160, 365, 755, 1150 and 1585 μm on slow disk as shown in Figure 3.18.

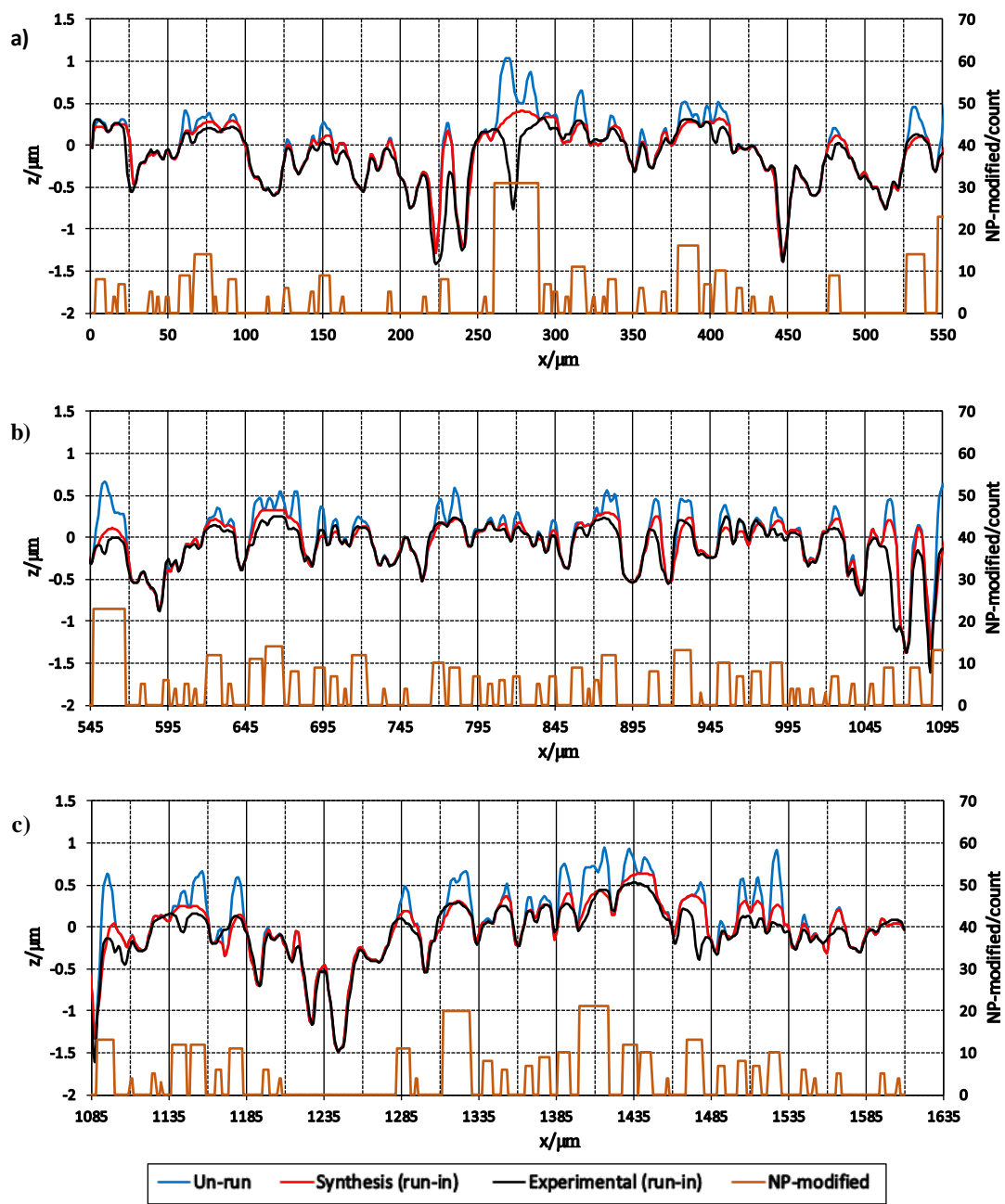


Figure 3.17 Fast surface representative section for the low Penetration EHL analysis showing the as-manufactured, synthesised run-in and experimental run-in profiles, a), b) and c) show sub-lengths of the profile in sufficient detail to inspect individual asperity shape changes.

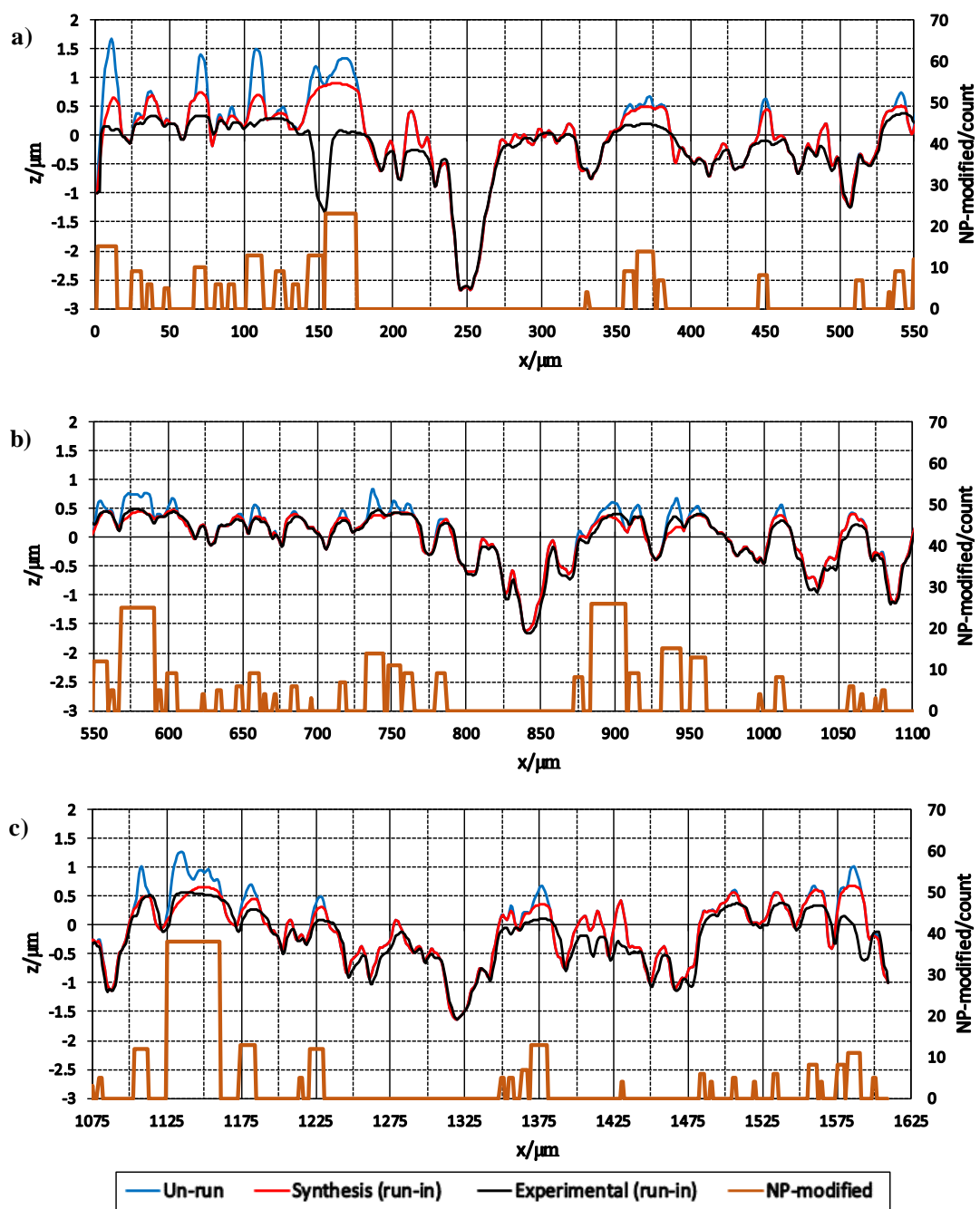
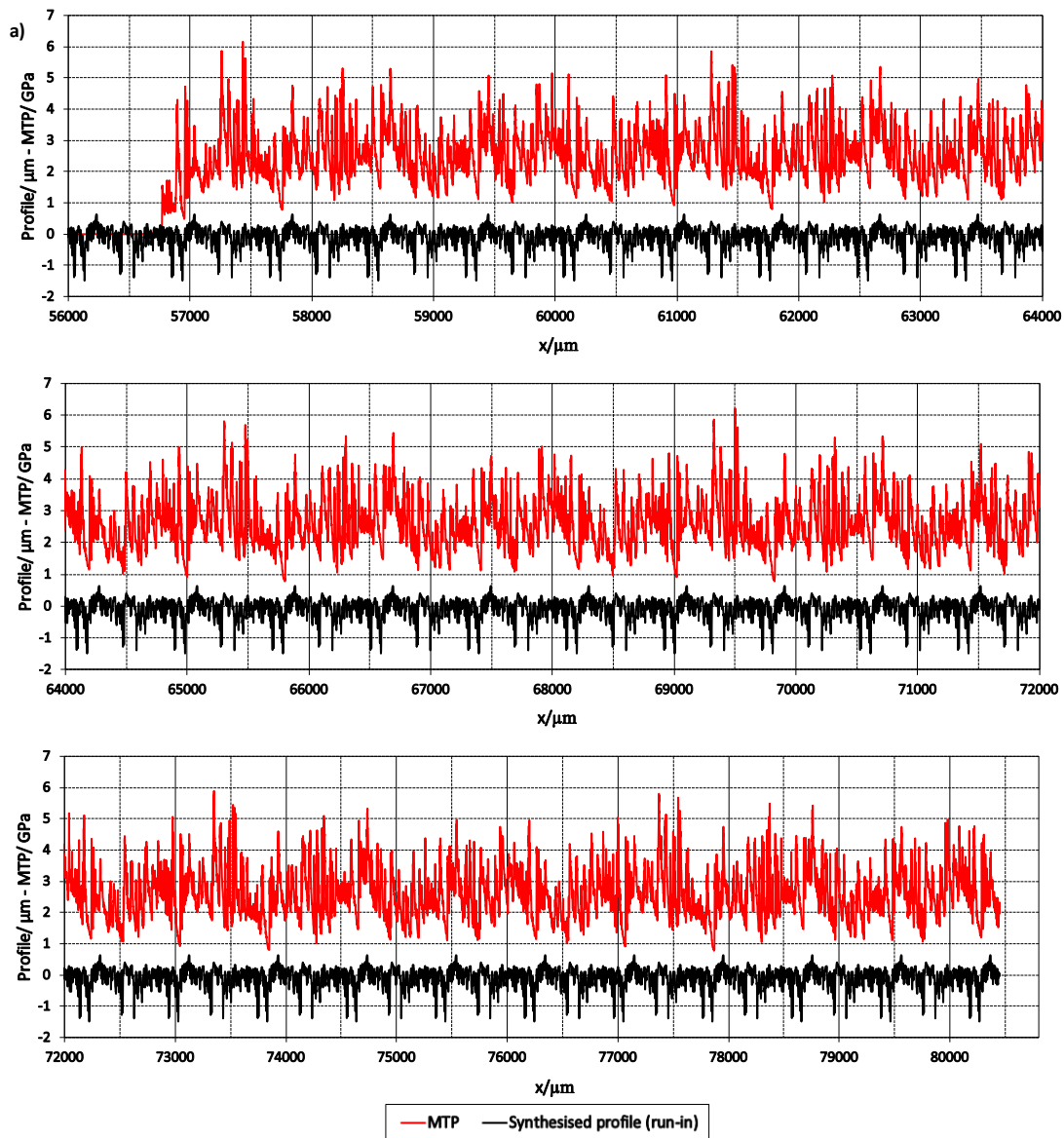


Figure 3.18 Slow surface representative section for the low Penetration EHL analysis showing the as-manufactured, synthesised run-in and experimental run-in profiles, a), b) and c) show sub-lengths of the profile in sufficient detail to inspect individual asperity shape changes.

The micro EHL analysis was carried out for 30,000 timesteps using the elastic analysis for each of the surface pairs. For the purpose of direct comparison, the experimental profiles were re-located as described previously so that common deep valley featured aligned with the synthesised roughness profiles.

The maximum transient pressure (MTP) experienced by the rough surface is shown in Figure 3.19a and Figure 3.19b for the complete multiprofiles used in the analysis. This shows that the synthesised run-in surfaces experienced occasional larger MTP values than the experimental profiles. However, generally the MTP values observed are similar over the whole analysis with peak levels below 5GPa.



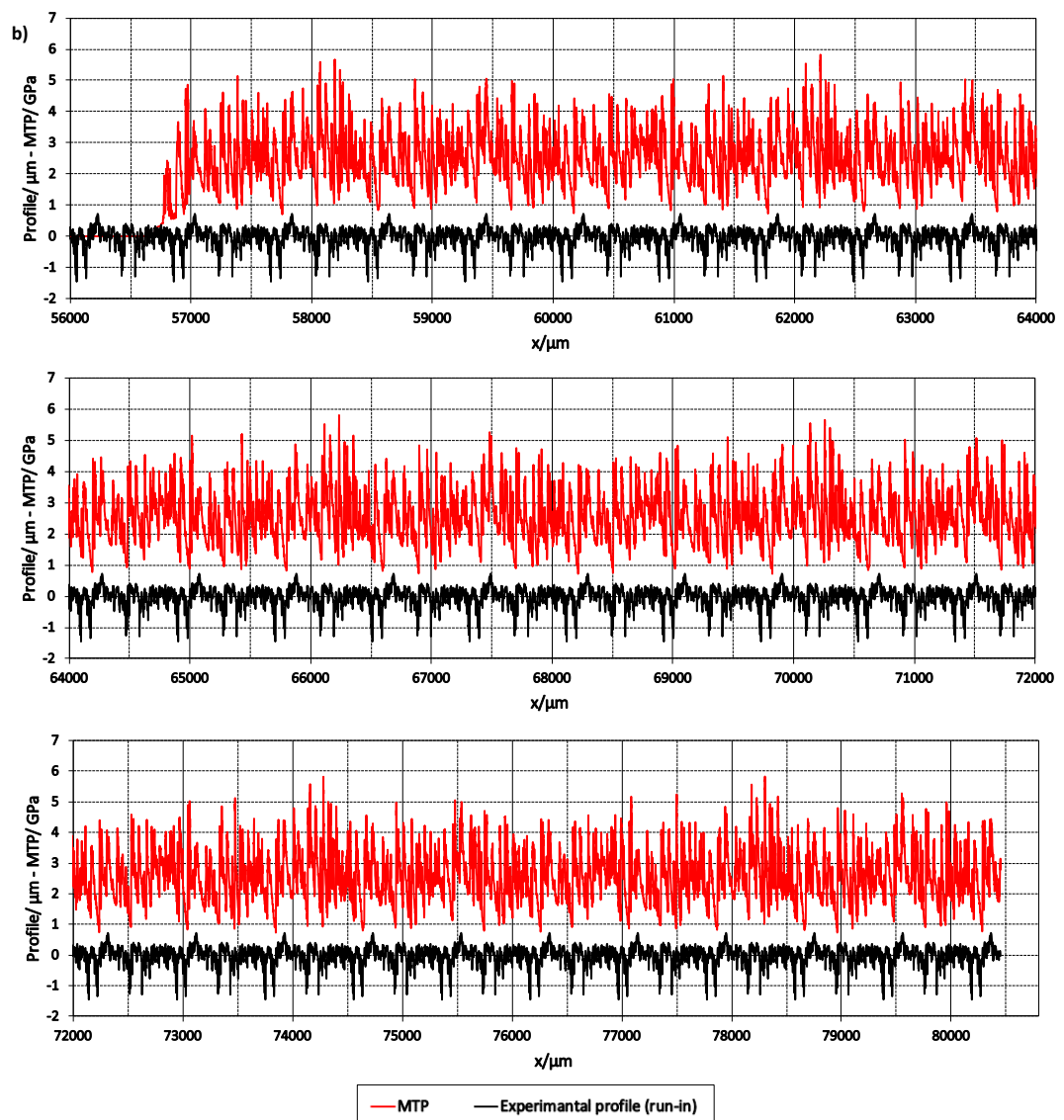


Figure 3.19 The MTP pressure distribution and fast surface heights for the multiprofile for 30,000 timesteps at the low Penetration case for a) experimental (run-in) profile and b) synthesised (run-in) profile.

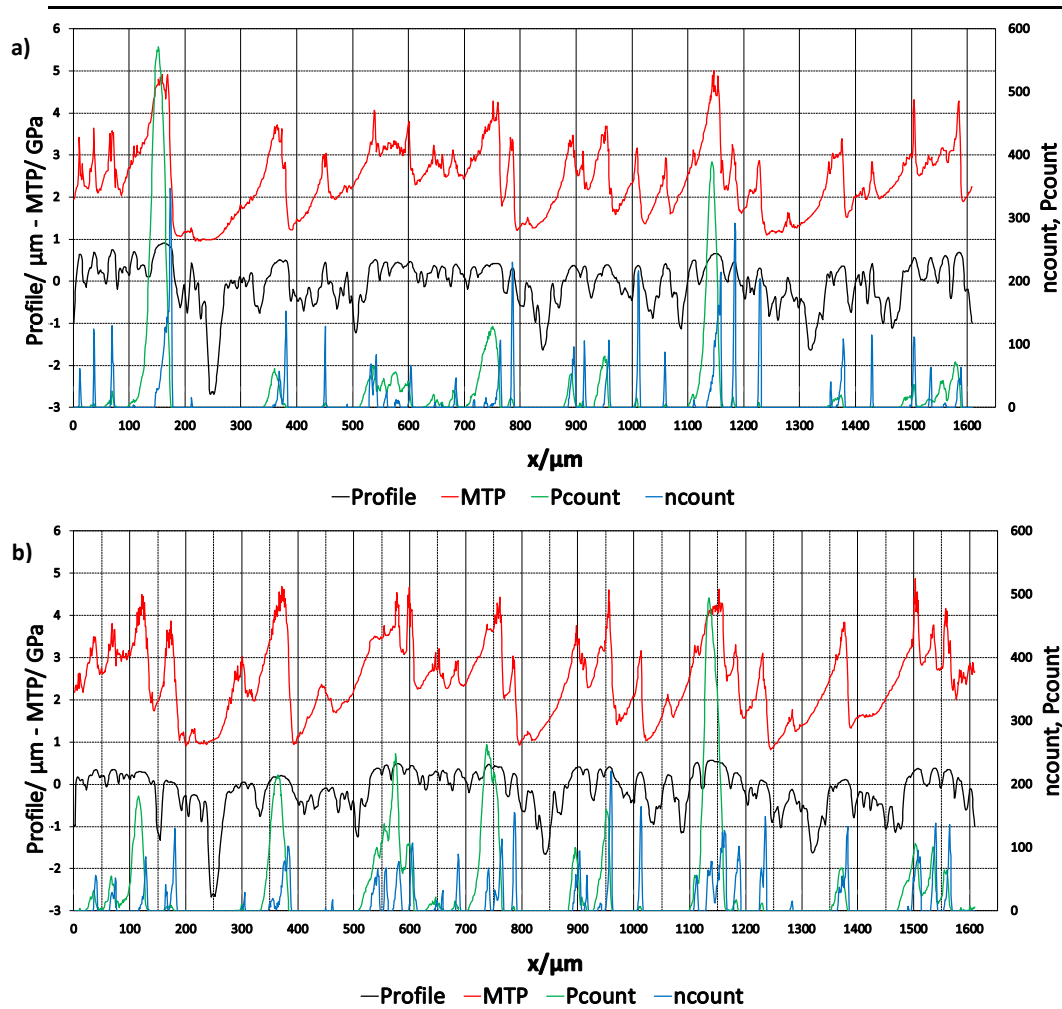


Figure 3.20 The MTP distribution, Pcount and contact count for the low Penetration profile EHL analysis of the slow surface representative section a) synthesised run-in profiles, and b) corresponding experimental run-in profiles.

Figure 3.20 and Figure 3.21 show the low Penetration parameters calculated for the slow and fast minimum Penetration surfaces. These are the maximum pressure experienced, and the number of timesteps where the pressure exceeds 2.5 GPa. The parameters are defined and calculated for the EHL analysis mesh. They are transferred to the rough surface mesh by interpolation.

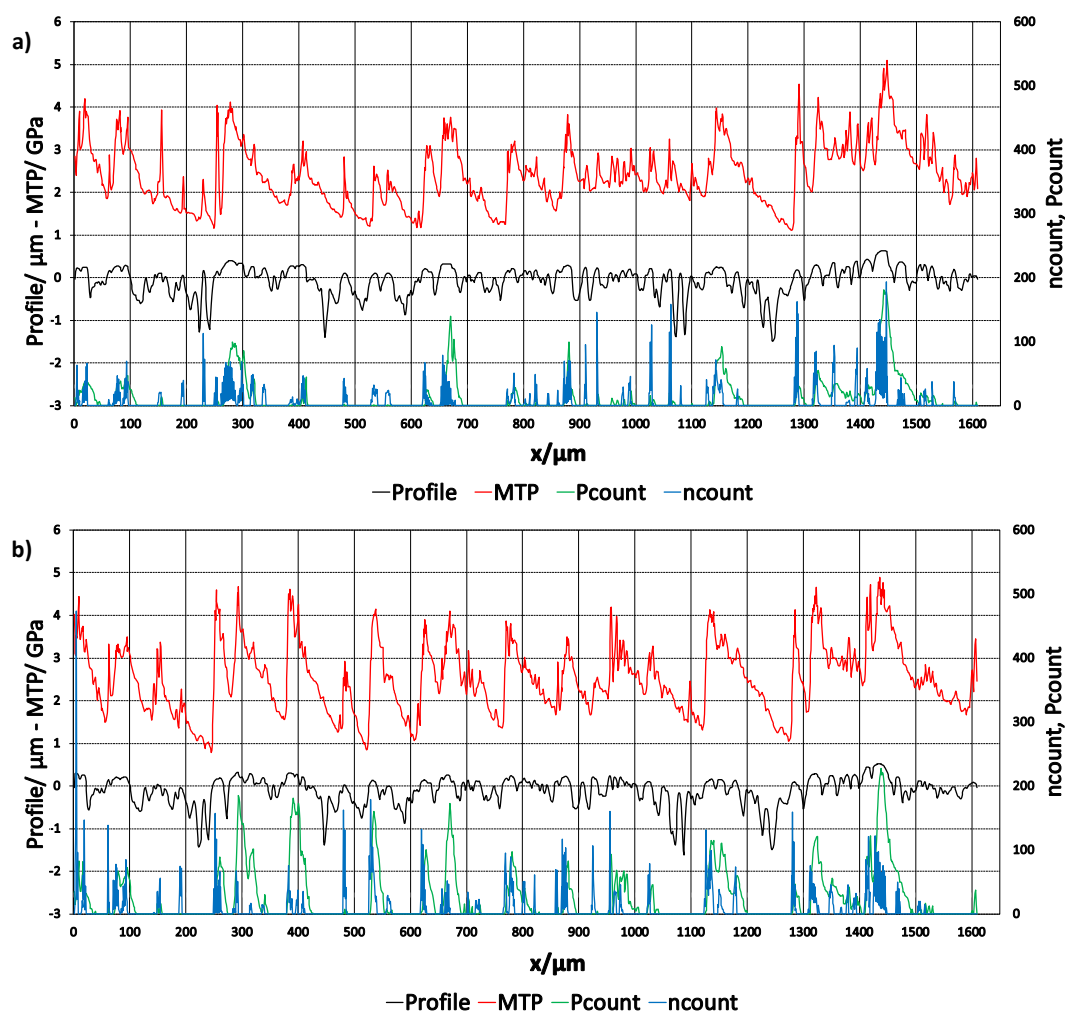


Figure 3.21 The MTP distribution, Pcount and contact count for the low Penetration profile EHL analysis of the fast surface representative section a) synthesised run-in profiles, and b) corresponding experimental run-in profiles.

The results were taken for the case where the centre of both fast and slow surfaces meet at the centre of EHL contact together. This is controlled as the code is modified to delay the fast surface to make the surfaces meet in this way at cycle 12001.

The figures show the parameters obtained for both the synthesis and experimental profiles. The parameters are different, as can be expected because the synthesised run-in surfaces are not the same as the experimental ones. However, there is a good level of correspondence between the parameters evaluated for the two analyses. The MTP curves show a difference in shape for the fast and slow surfaces. For the slow surface the MTP curve tends to build slowly with increasing x and then falls rapidly when it

has passed the maximum. For the fast surface MTP tends to build rapidly to a maximum and then fall slowly with increasing x . This hydrodynamic effect is a result of the asperity interaction kinematics. During an asperity interaction the pressure builds from the leading edge of the fast surface asperity and from the trailing edge of the slow surface asperity and as a result the MTP curves have the features reversed as described.

Generally speaking, the synthesised and experimental roughnesses analyses have the same tendency for the extreme pressure parameters in most positions along the profiles except for some positions. This is seen in Figures 3.22, 3.23 and 3.24 where the individual parameters are compared by superimposition.

Figure 3.22 compares the MTP curves for both analyses and each of the surfaces. The MTP curves are similar allowing for the inevitable difference due to differences in the counterface asperity details and alignment. However there are some examples of a micropit being formed in the experimental profile which is not present in the synthesised profile as indicated in discussing figures 3.17 and 3.18. The clearest examples of this are at $x = 270 \mu\text{m}$ for the fast surface and $x = 150 \mu\text{m}$ for the slow surface. This leads to different pressure experiences that cannot be replicated in the synthesis as the model simulation does not allow the pitting to develop.

Figure 3.23 shows that synthesised roughness has high *pcount*, and high maximum pressure at these positions, whereas the actual roughness has a low maximum pressure and very low *pcount* at the micropit position. In both cases there is a redistribution of load to the new asperities formed by removal of the micropit material.

The *pcount* parameter shows greater differences than the MTP parameter and is sensitive to the detail of the asperity features. Generally speaking the *pcount* for the synthesised profile asperities are lower than the corresponding experimental profile analyses. This is to be expected as the synthesised profile results are obtained from profiles that have been modified by running against each other in the synthesised model. The experimental profiles are not aligned against their counterfaces and so their asperities have not necessarily run-in against each other and it is not surprising that they have higher *pcount* values.

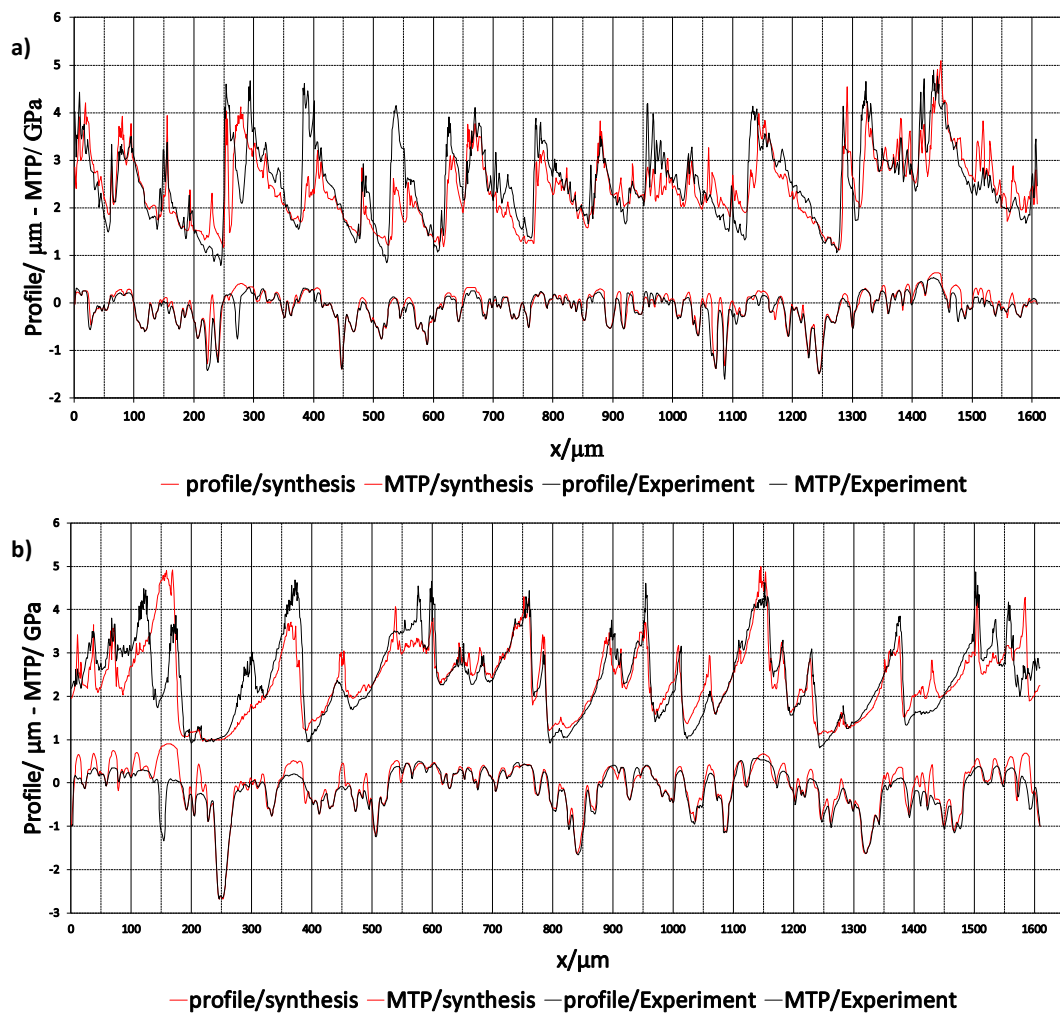


Figure 3.22 Comparison of the MTP distributions obtained for the synthesised and experimental surfaces for the lowest penetration, a) the fast surface and b) the slow surface.

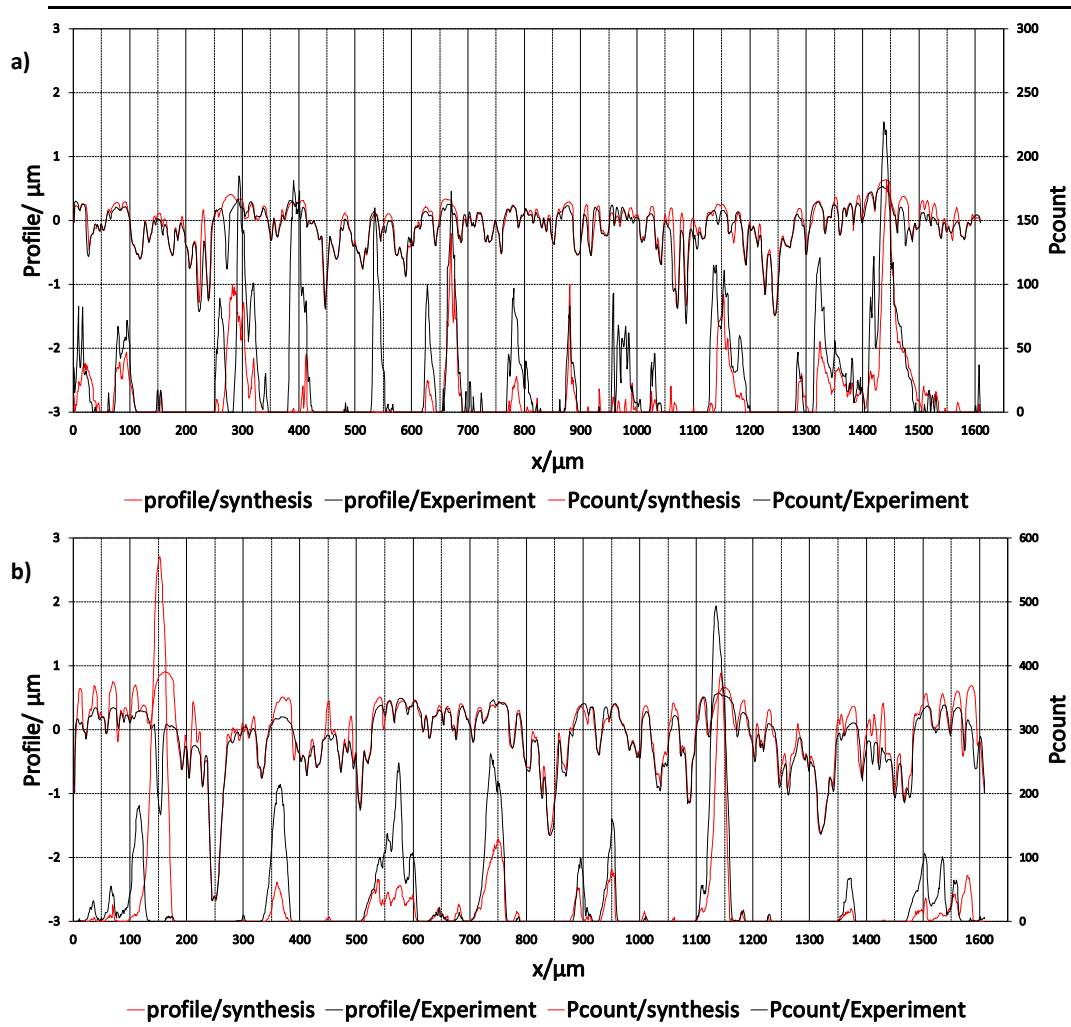


Figure 3.23 Comparison of the Pcount values obtained for the synthesised and experimental surfaces for the lowest penetration, a) the fast surface and b) the slow surface.

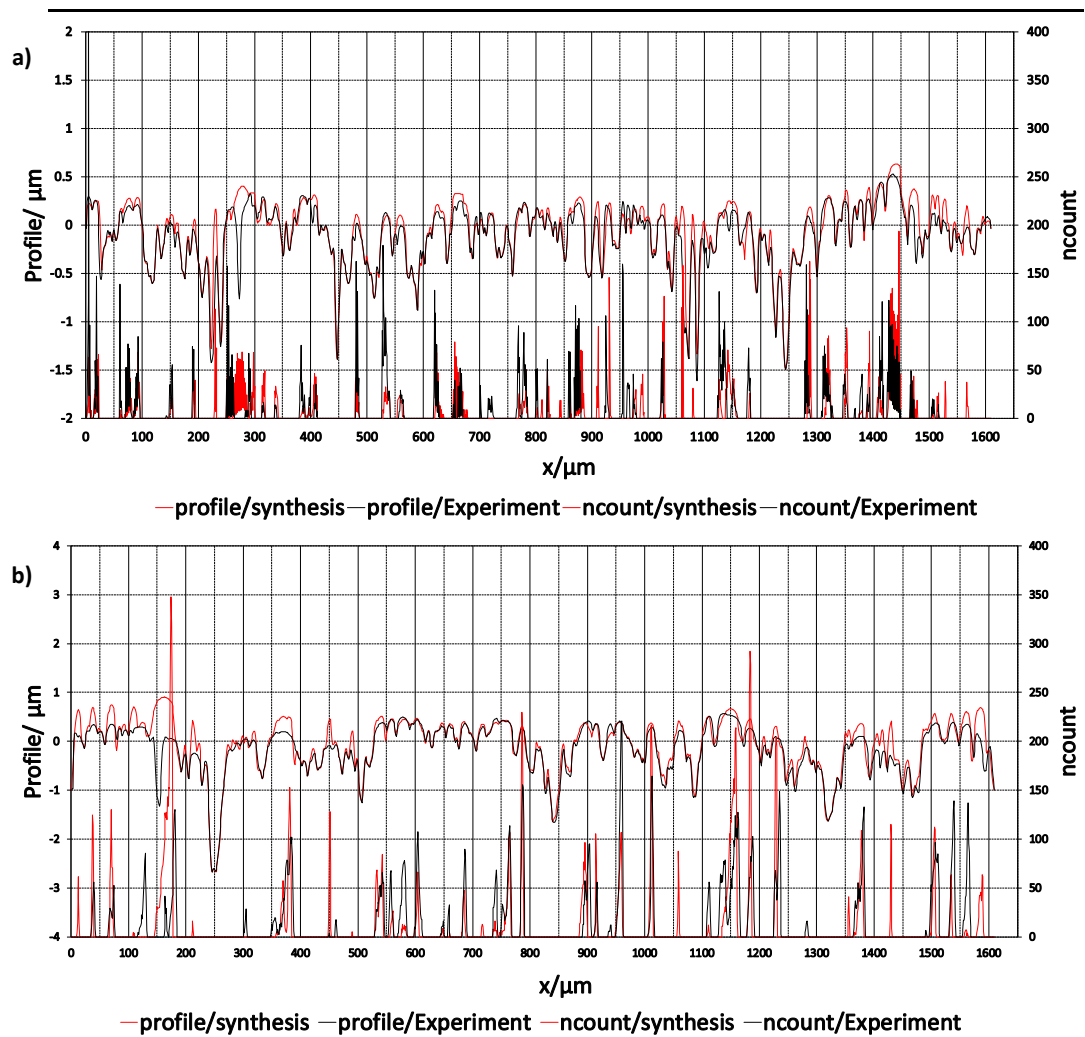


Figure 3.24 Comparison of the *ncount* results for the synthesised and experimental surfaces for the lowest penetration, a) the fast surface and b) the slow surface.

Figure 3.24 compares the number of direct contacts that occurred on the surface, *ncount*, for both the synthesised and experimental profiles. It can be seen that the behaviour of *ncount* is similar to the *pcount* parameter as explained above.

3.10 Highest Penetration Surfaces

The second pair of synthesised profiles selected for analysis was the high penetration pair identified using Figure 3.16, and this is referred to as Profile Set Three. The same procedure as was used as for the low penetration surfaces was followed in analysing these surfaces. The results show that there are no significant differences due to the penetration level. The slow surface is common to both analyses, and the same asperities are modified differently in the synthesised profile compared with the experiment. More modification happens in the high penetration case, and this is because they interact with a different counterface and different penetration. The results of the synthesised running-in are given in in Figure 3.25 and Figure 3.26 for the two surfaces.

Some micropits are observed occurring at prominent asperities at positions $x = 464, 995$ and $1231 \mu\text{m}$ of the fast surface and positions $x = 154, 456, 1413$ and $1594 \mu\text{m}$ of the slow disk. These positions have high values of *NP-modified* on the synthesised profiles which mean that more asperity points were modified and initial asperities were merged. The most significant difference between the experimental and synthesised profiles is at positions $x = 1231$ and $154 \mu\text{m}$ for the fast and slow profiles respectively.

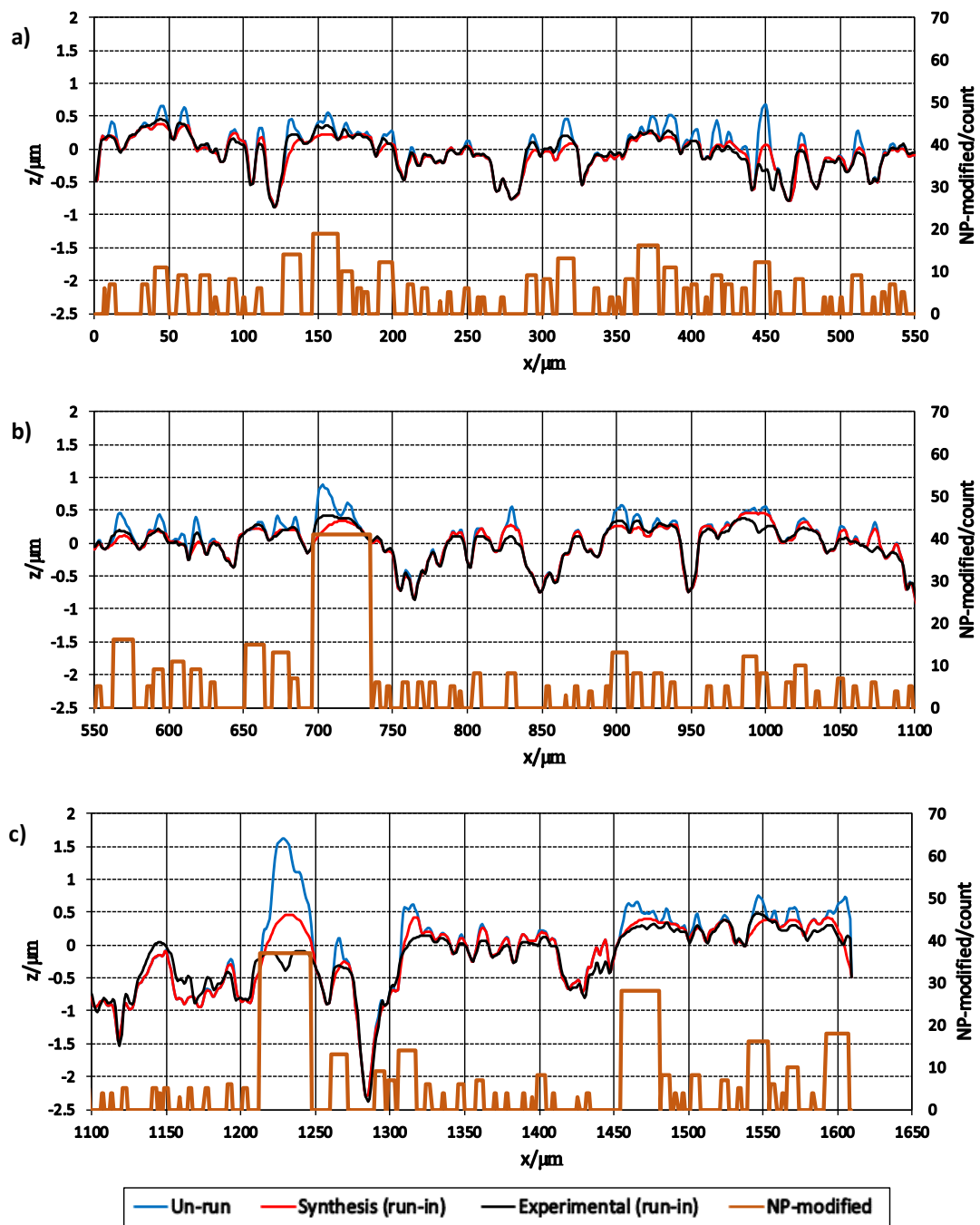


Figure 3.25 Fast surface representative section for the highest Penetration EHL analysis showing the as-manufactured, synthesised run-in and experimental run-in profiles, a), b) and c) show sub-lengths of the profile in sufficient detail to inspect individual asperity shape changes.

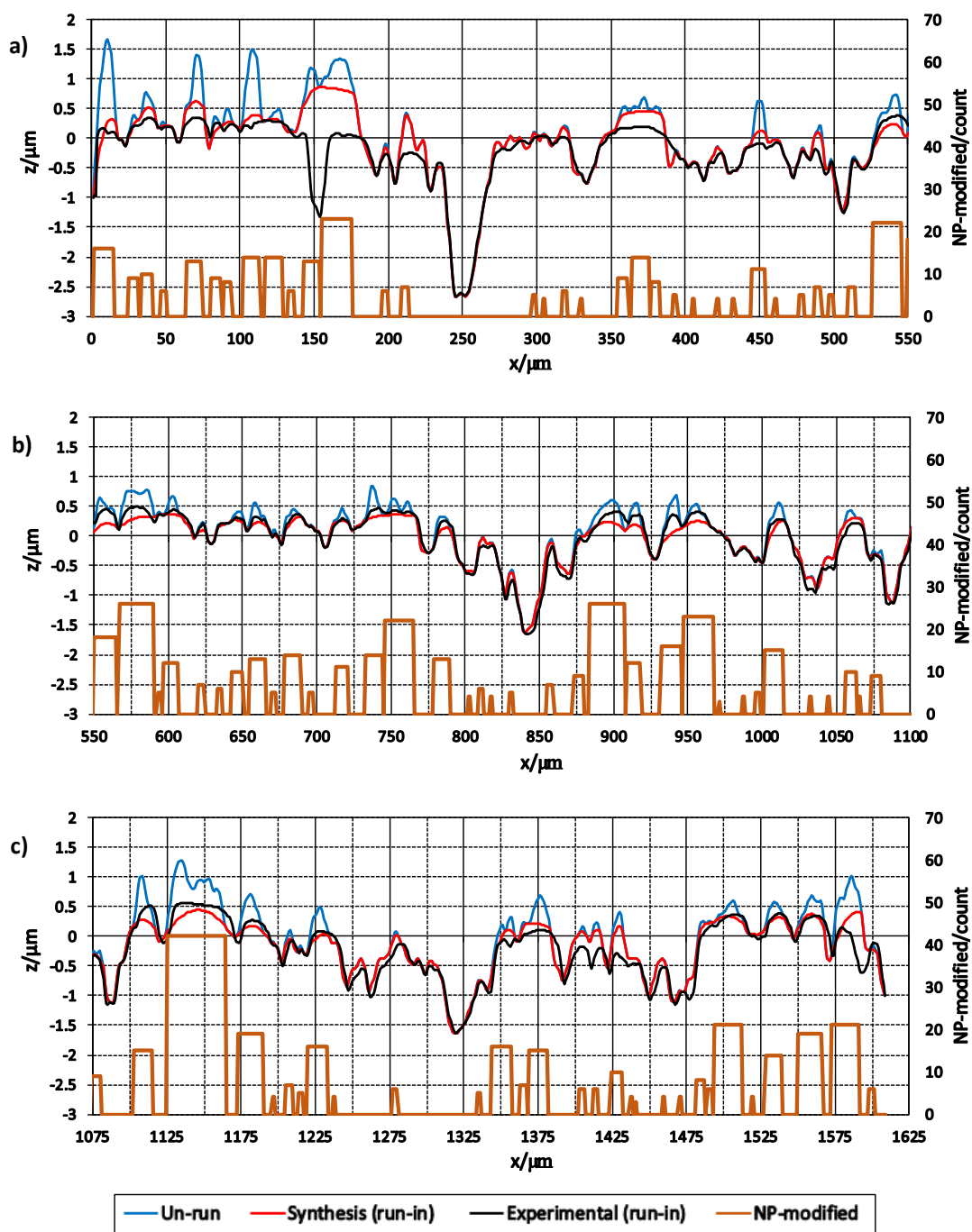


Figure 3.26 Slow surface representative section for the highest Penetration EHL analysis showing the as-manufactured, synthesised run-in and experimental run-in profiles, a), b) and c) show sub-lengths of the profile in sufficient detail to inspect individual asperity shape changes.

Figure 3.27 and Figure 3.28 show all the parameters of fast and slow surfaces for EHL analysis of the synthesised and experimental surfaces. The figures give a comparison overview for the slow surfaces when they run with the fast surfaces at the highest penetration position and are again obtained for the profiles in the pass where their

centres meet at the contact point. It can be seen that the asperities that have the highest MTP values tend also to have the highest *Pcount* values. In the corresponding experimental profile micropits are seen to develop. This is more clearly seen in figures 3.20, 3.21, 3.27 and 3.28.

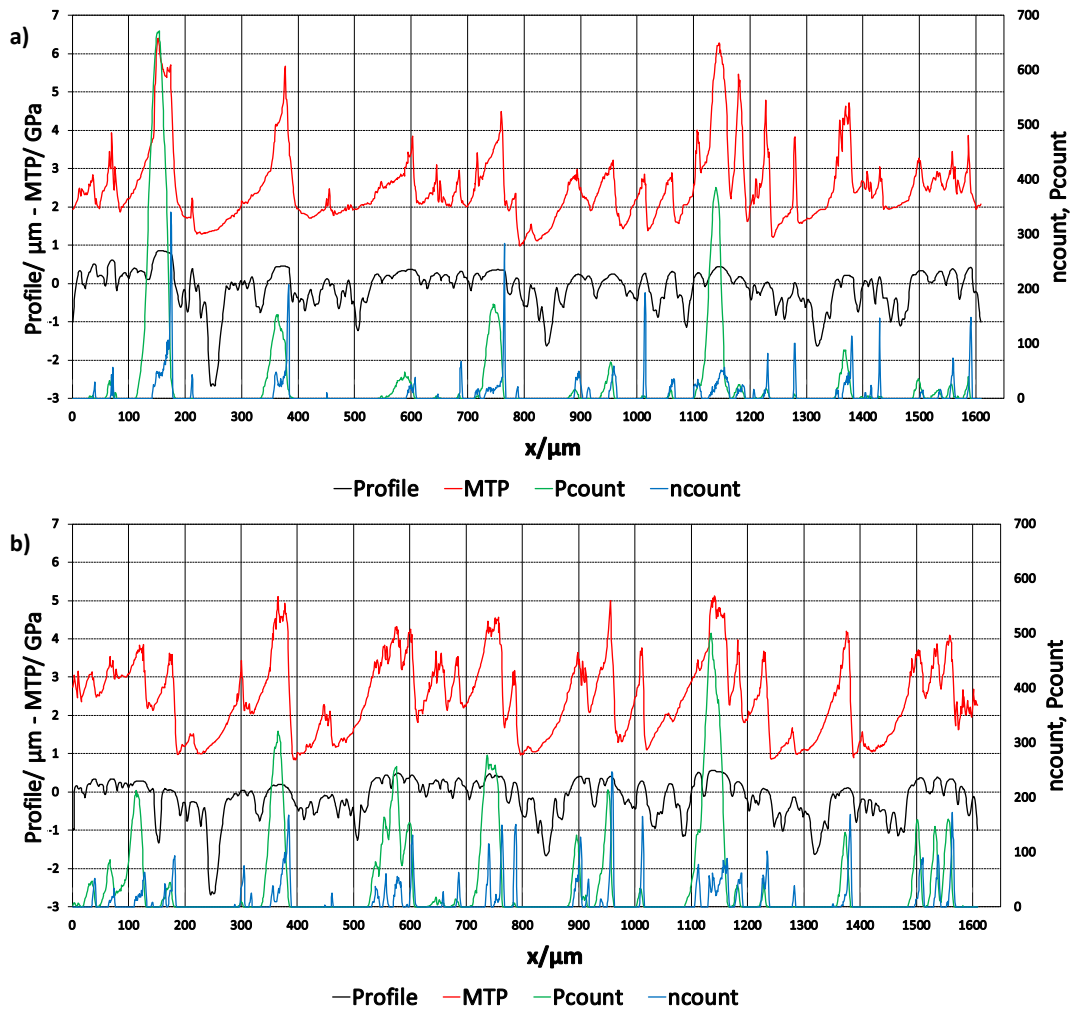


Figure 3.27 The MTP distribution, Pcount and contact count for high Penetration EHL analysis of the slow surface representative section a) synthesised run-in, and b) experimental run-in.

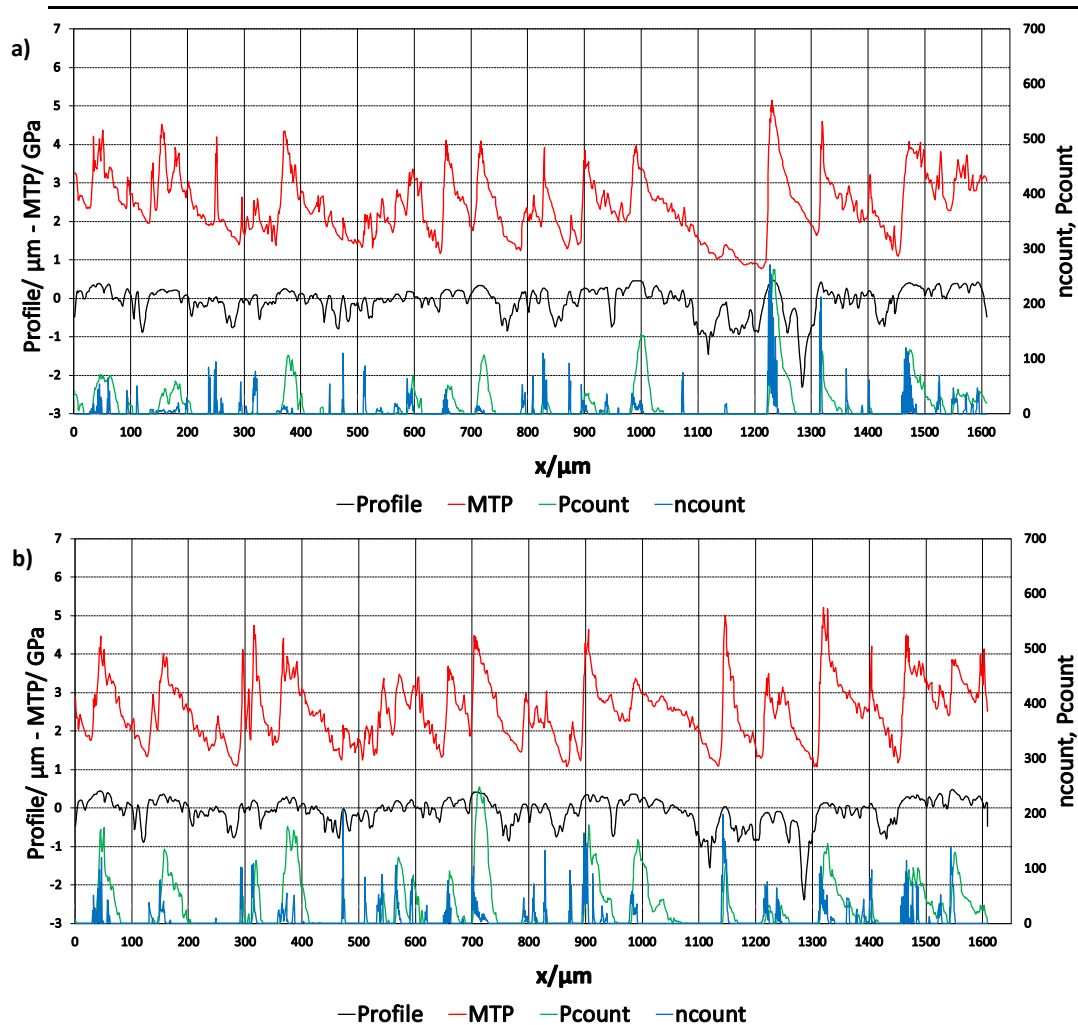


Figure 3.28 The MTP distribution, Pcount and contact count for high Penetration EHL analysis of the fast surface representative section a) synthesised run-in, and b) experimental run-in.

The parameters are plotted in direct comparison between the synthesised and experimental profiles in figures 3.28, 3.29 and 3.30. The common aspect between the low and high penetration profiles is that the slow profiles are the same.

The results represented in Figure 3.29 correspond to those shown in Figure 3.22 for the low penetration surfaces. In considering the parameters the same patterns of variation are seen, however the MTP curves for the slow synthesised surface are higher in the high penetration case where peak values of 6.3, 5.6, 6.0 and 4.8 GPa correspond to values of 5.0, 3.8, 5 and 3 GPa respectively for the low Penetration case.

At the position $x = 1225 \mu\text{m}$ on synthesised fast disk the MTP value is around 5 GPa but there is a pit at the corresponding experimental fast profile which leads to shifting

this value of MTP to the next asperity at position $x = 1150 \mu\text{m}$. The same tendency is seen in the slow disks at position $x = 150 \mu\text{m}$ in the synthesised profile where there is a high value of MTP while, in the corresponding experimental profile due to the pitting that has occurred, two close neighbouring asperities have nearly the same MTP values.

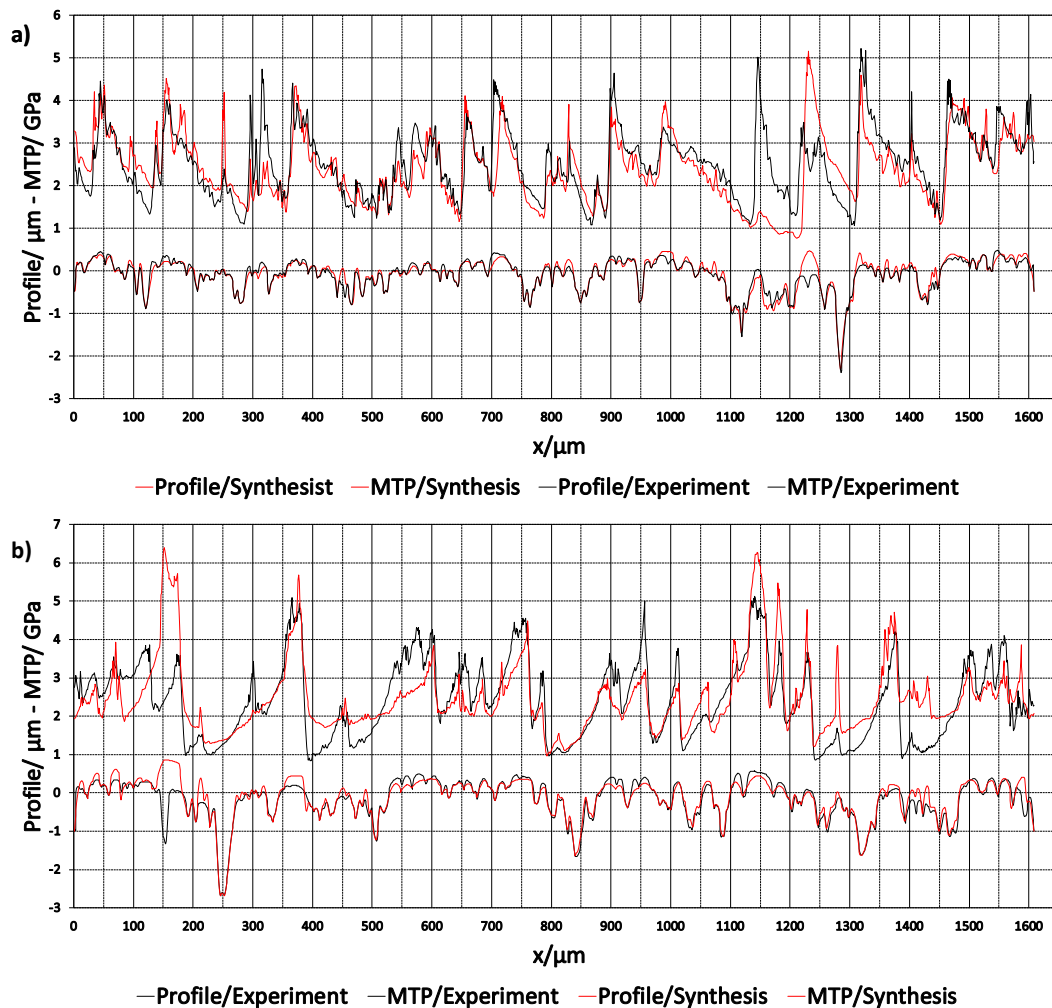


Figure 3.29 The MTP distribution between the synthesised and experimental surfaces for the high penetration of a) the fast surface and b) the slow surface.

It can be seen from Figure 3.22b and Figure 3.29b that at position $x = 1430 \mu\text{m}$, there is a difference between the synthesised and experimental slow profiles for the two EHL analyses. In both cases, the synthesised surfaces show that MTP has a peak value around 3 GPa while there is no peak for the corresponding experimental surfaces. This is thought to be due to the counter faces which interact with this portion of the slow

surface being different. In addition, another factor is that no filtering has been applied to the synthesised profiles but the experimental profiles have been filtered as part of the measuring process. This can make a difference between the profile mean lines and influence local loading. The opposite effect is seen at positions $x = 301$ and $1150 \mu\text{m}$ on high Penetration EHL analysis of the Fast disk as seen in Figure 3.29 and Figure 3.30a.

The format of Figure 3.30 and Figure 3.31 correspond to Figure 3.23 and Figure 3.24, respectively. In comparison between the slow profiles in these two figures in term of *Pcount*; there are small differences with the highest penetration case giving slightly higher values of *Pcount* than the lowest penetration case. These differences result from different interaction with fast surfaces. For example, at positions $x = 120, 175, 360, 900, 1230$ and $1365 \mu\text{m}$ on the experimental slow profile of the low penetration case the *Pcount* values are equal to 180, 5, 210, 100, 5 and 75 respectively and at the same position of experimental slow profile for the high penetration case, *Pcount* is equal to 205, 45, 310, 130, 50 and 140, respectively.

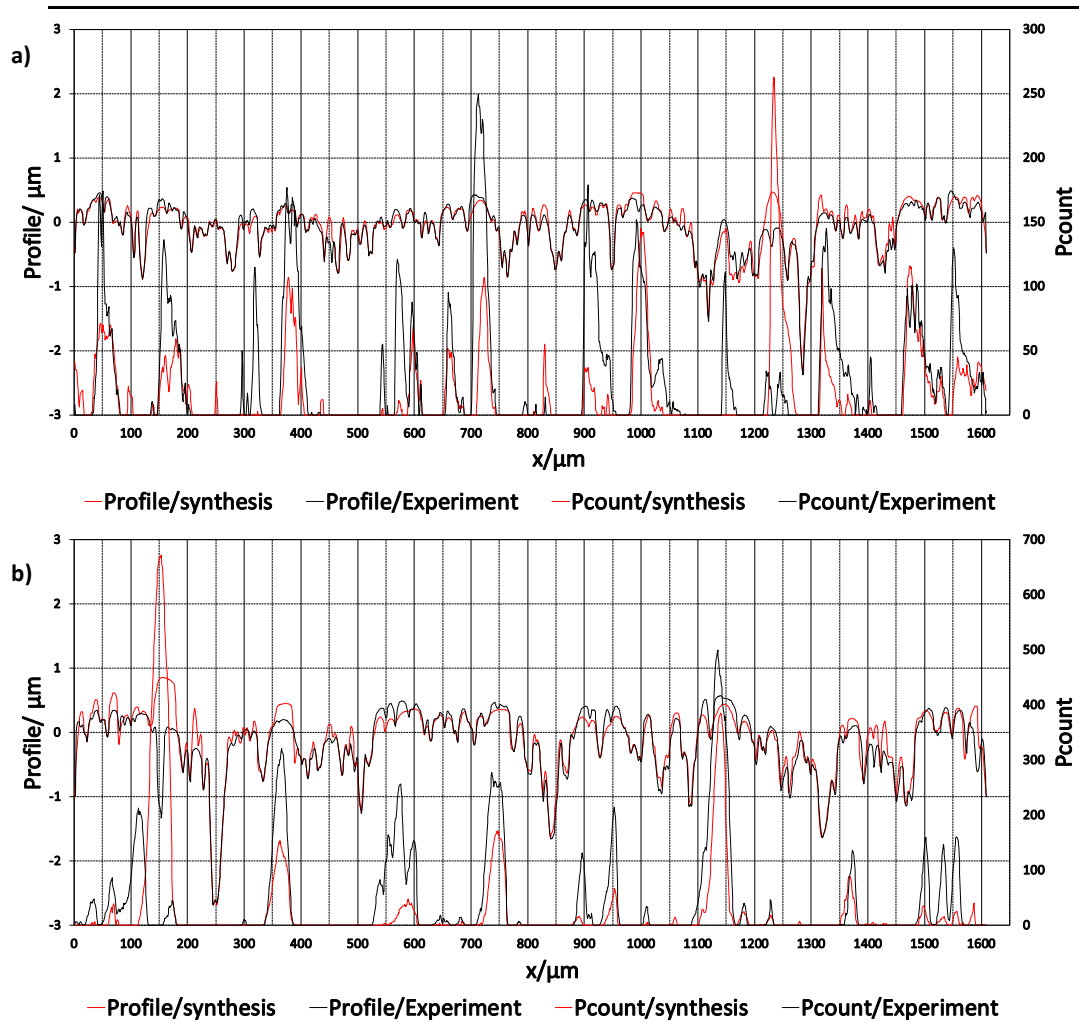


Figure 3.30 The comparison between the Pcount synthesised and experimental surfaces for the high penetration of a) the fast surface and b) the slow surface.

There is a general similarity between the synthesised and experimental profiles in the areas where micropits have not developed. There are clear differences in the pitted areas as can be expected as the synthesis attempts to model only the plastic deformation occurring in the contact.

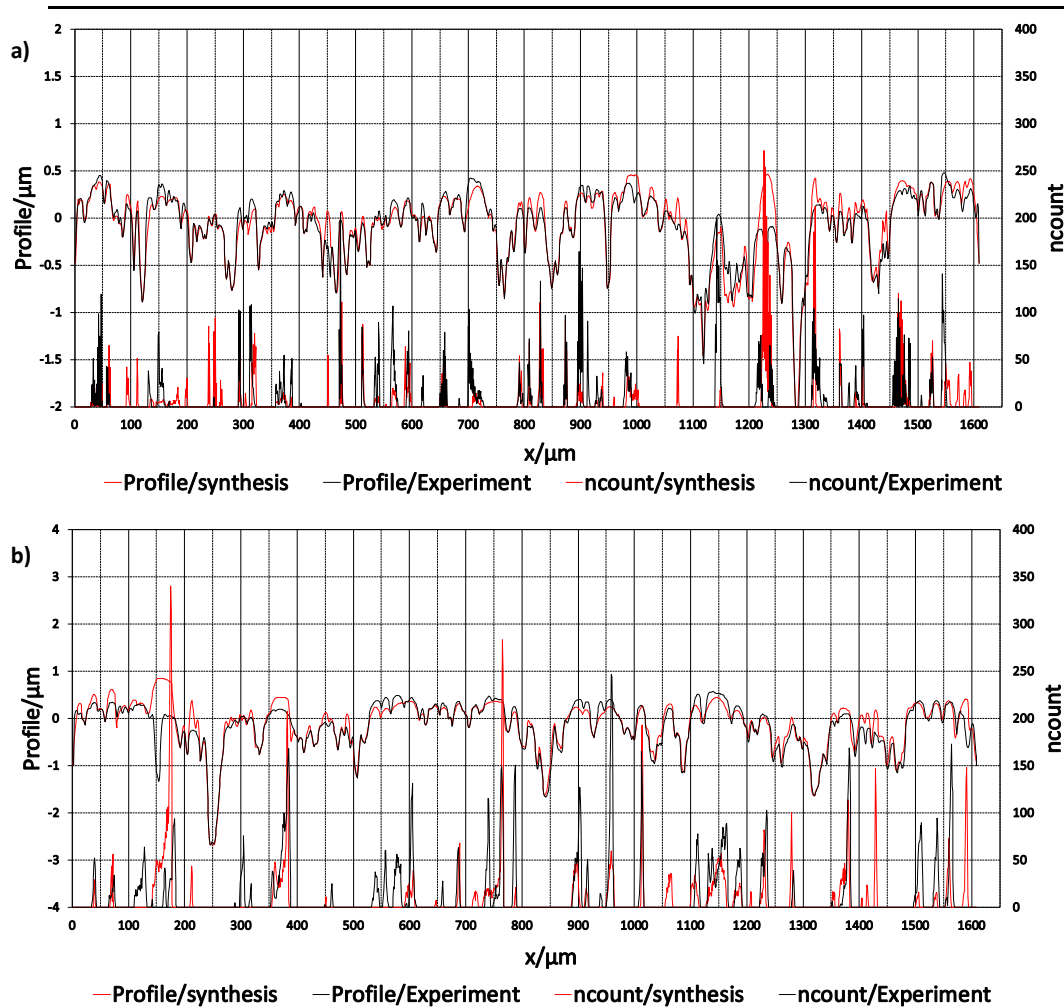


Figure 3.31 The comparison between the *ncount* synthesised and experimental surfaces for the high penetration of a) the fast surface and b) the slow surface.

As far as the *ncount* parameter is concerned, there are differences as mentioned in considering *Pcount* and these are due to interaction with a different counterface. Even though there are some differences, a good agreement of parameter *ncount* was achieved between synthesised and experimental highest Penetration profiles, as shown in Figure 3.31.

In these EHL comparisons, the rough surface heights are defined relative to the mean height obtained during the filtering process. For the synthesised run-in surface, the mean height is that of the original rough surface so that its profile may be lower at asperity peaks than is the case when the experimental profiles are used. To assess the sensitivity of the results to such offsets the experimental run-in profile was adjusted

in height so that its valleys were aligned with the as manufactured profile, as discussed in chapter 5.

Figure 3.32 and Figure 3.33 show the MTP and *Pcount* values obtained with and without this height adjustment respectively. The magnitude of the adjustment can be seen by comparing the roughness profiles shown in each of the figures. In terms of the pattern shown by these parameters, this makes a difference in magnitude in some positions but there is no significant change.

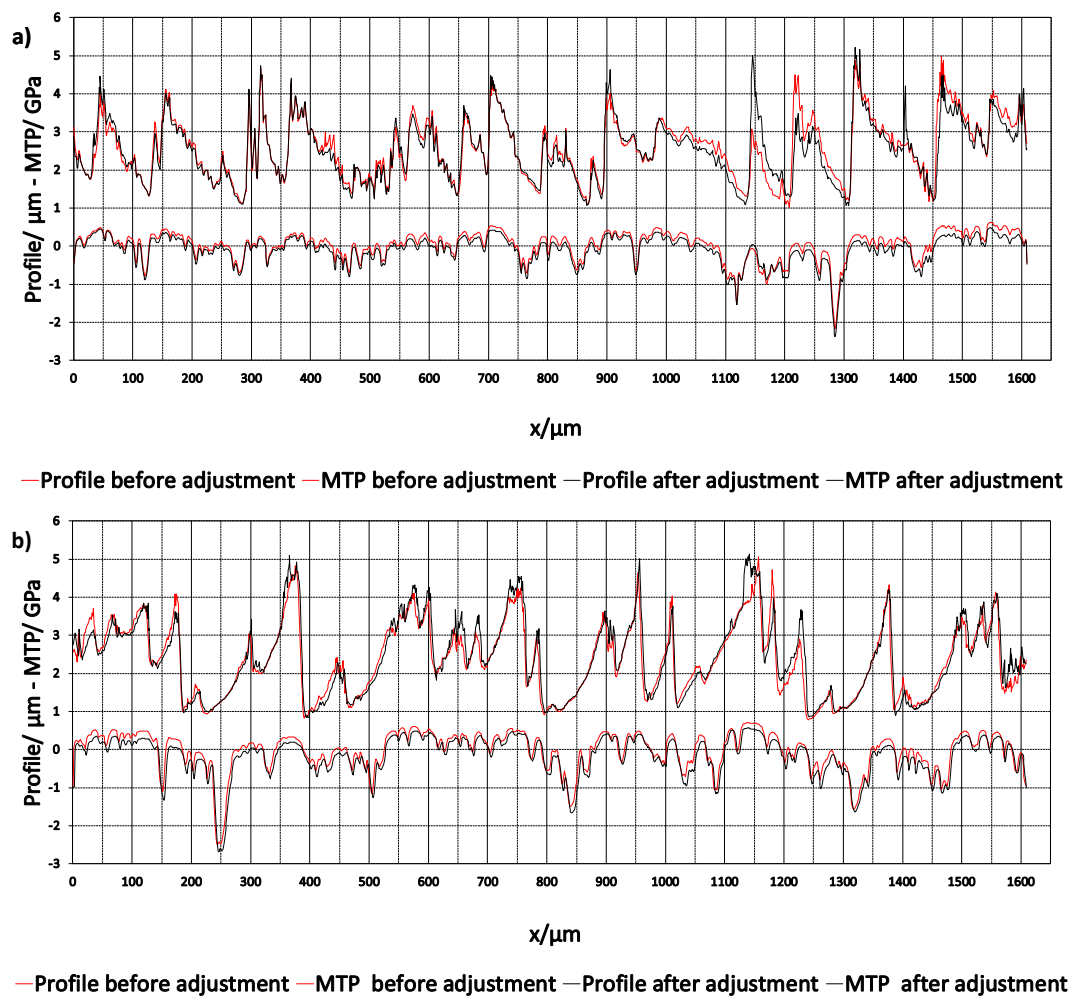


Figure 3.32 The MTP distribution for experimental profiles with and without height adjustment for the high penetration contact analysis of a) the fast surface and b) the slow surface.

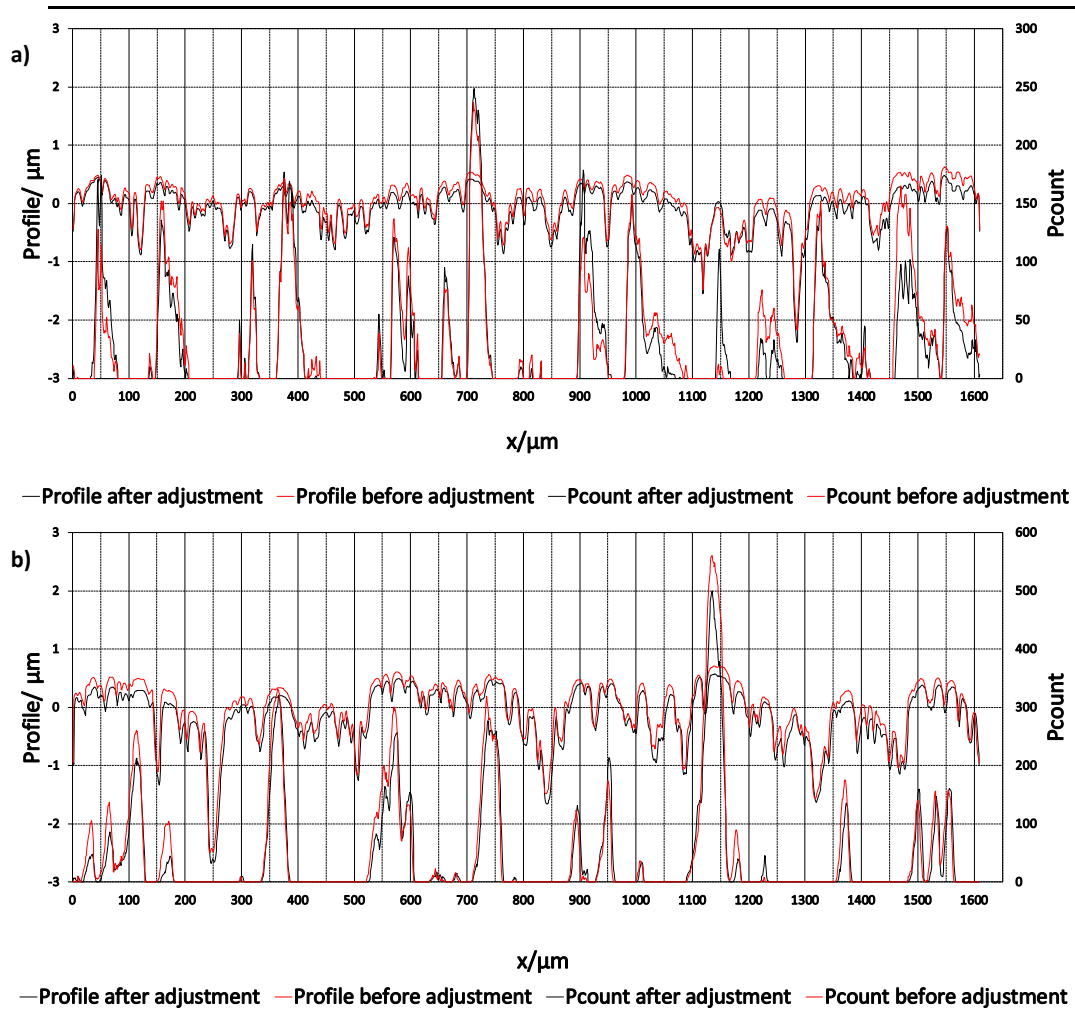


Figure 3.33 Comparison between the *Pcount* values for experimental profile with and without height adjustment for high penetration contact analyses of a) the fast surface and b) the slow surface.

As part of the study, the changes in roughness parameters were considered for comparison. Twenty repeats were made up for each representative profile for the manufactured, run-in and synthesised surfaces. The *multiprofiles* roughness parameters were measured after re-filtering using a Gaussian filter with a cut-off of 0.25mm and the results obtained using the profilometer software according to ISO 4287. The height distributions (histograms) for all roughness profiles are shown in figures 3.34, 3.35 and 3.36. The other parameters are compared in tables 3.4, 3.5 and 3.6.

R_p is the maximum profile peak height, R_v is the maximum profile valley depth, R_z the average maximum height of the peak. R_a is a roughness average, R_{sk} is skewness and R_{ku} is kurtosis. R_q is root mean square (RMS) roughness.

It can be seen from tables 3.4, 3.5 and 3.6 that the value of the R_p parameter in as-manufacture profiles decreased to the half in the corresponding running-in and synthesised profiles, while values of R_v , R_a , R_z and R_q reduced slightly. The value of the R_{ku} parameter increased slightly during running-in process.

Generally speaking, there are significant differences between the as-manufactured surface and each of the run-in and synthesised surfaces. However, the run-in and synthesised surfaces are statistically quite similar to each other.

Note that the histograms produced by the software are presented as bearing ratio curves and rotated through 90° compared to usual statistical practice. The ordinate variable is the depth from the highest point of the surface, D.

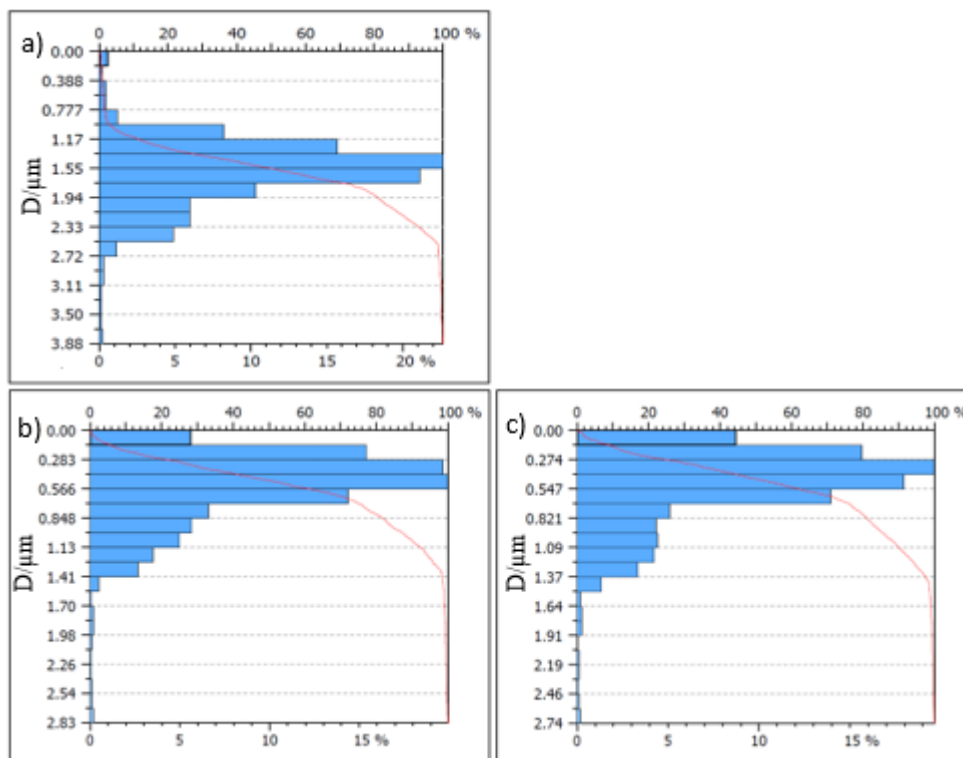


Figure 3.34 The height distributions (histograms) for the lowest penetration fast surface roughness profiles (a) as-manufactured, (b) run-in, (c) synthesised.

Table 3.4 The parameters of the lowest Penetration of the fast roughness in (μm).

Parameters	As-manufactured	Run-in	Synthesised
Rp	1.06	0.412	0.542
Rv	1.27	1.20	1.18
Rz	2.34	1.61	1.72
Ra	0.288	0.223	0.237
Rq	0.385	0.295	0.310
Rsk	-0.304	-1.28	-1.09
Rku	4.17	5.40	4.55

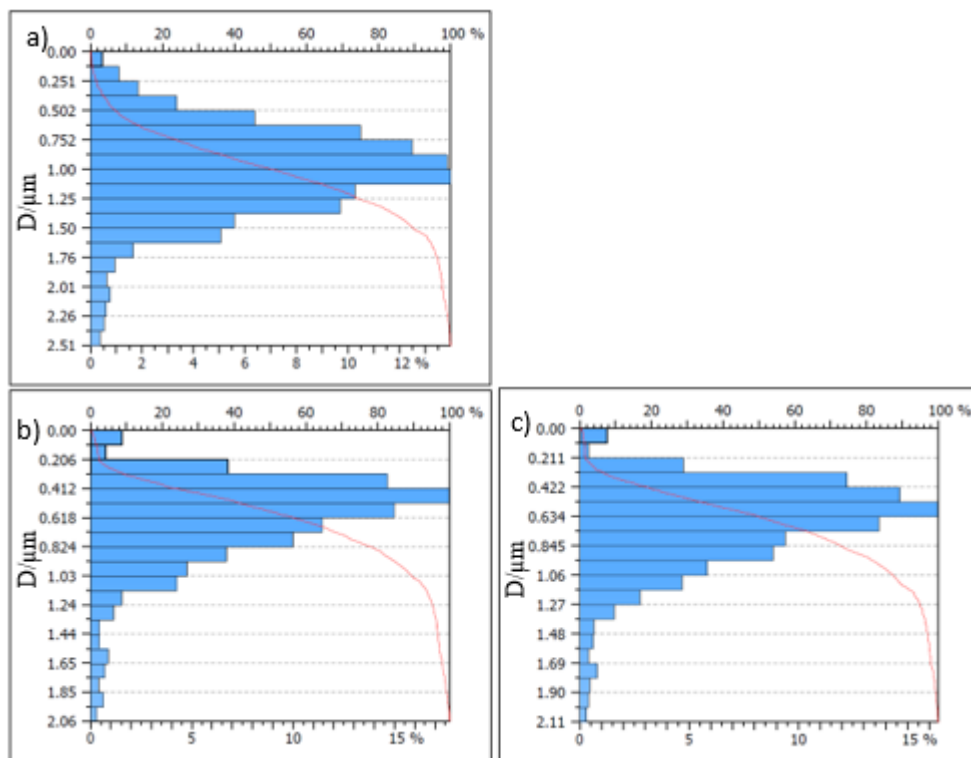


Figure 3.35 The height distributions (histograms) for the highest penetration fast surface roughness profiles (a) as-manufactured, (b) run-in, (c) synthesised.

Table 3.5 The parameters of the highest Penetration of the fast roughness in (μm).

Parameters	As-manufactured	Run-in	Synthesised
Rp	0.820	0.424	0.454
Rv	1.18	1.13	1.12
Rz	2.00	1.56	1.57
Ra	0.275	0.222	0.228
Rq	0.353	0.291	0.293
Rsk	-0.447	-1.21	-1.05
Rku	3.72	5.08	4.67

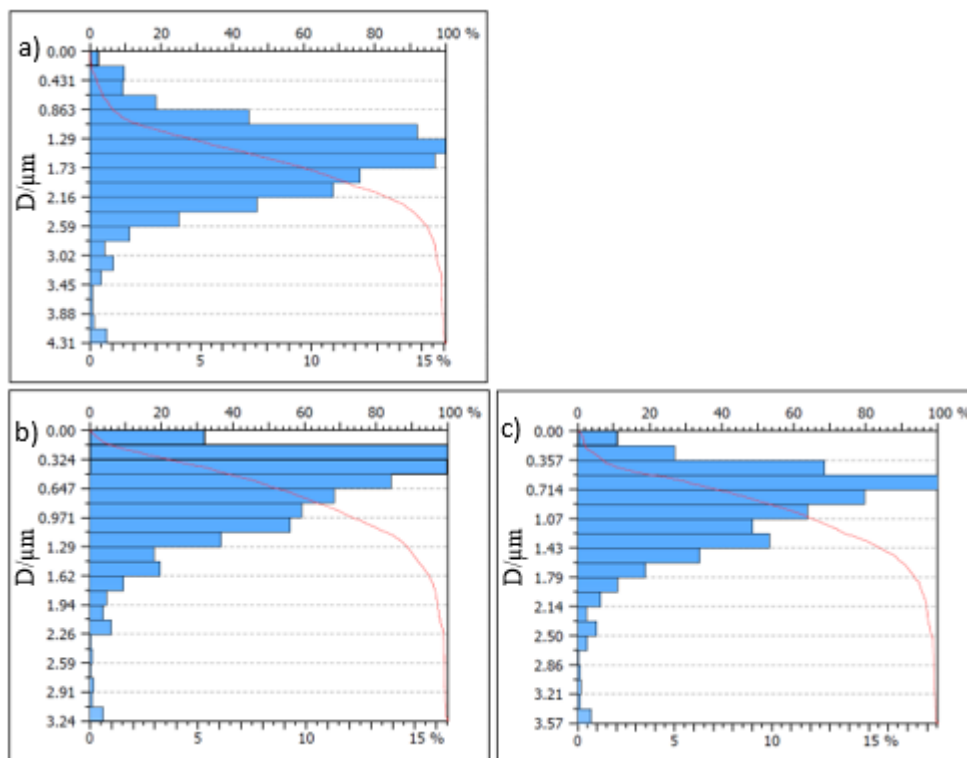


Figure 3.36 The height distributions (histograms) for the slow surface roughness profiles (a) as-manufactured, (b) run-in, (c) synthesised.

Table 3.6 The parameters of the slow roughness profile in (μm).

Parameters	As-manufactured	Run-in	Synthesised
Rp	1.11	0.561	0.727
Rv	1.74	1.61	1.69
Rz	2.85	2.17	2.42
Ra	0.405	0.340	0.361
Rq	0.536	0.449	0.478
Rsk	-0.703	-1.35	-1.17
Rku	4.36	5.43	5.08

3.11 Conclusion

A synthesised running-in model that replicates the real running-in process was developed in this chapter based on a limiting hardness level coupled with parameters that control the development of the load bearing lands in line with the observed stochastic distribution of asperity radii of curvature. Comparisons were made between these synthesised surfaces and the corresponding measured surfaces in terms of their geometry and their mixed EHL behaviour using peak asperity pressure and direct contact occurrence as parameters.

There are promising results and reasonable agreement between the synthesised and experimental profiles. There are differences between the results and that is to be expected as the interaction between asperities in the numerical analyses do not reproduce the interaction between the surfaces in the actual experiment. It is encouraging to see the level of agreement in the synthesised asperity shapes which show the same general trend.

The process of fatigue analysis to calculate the fatigue life and accumulated damage for the synthesised and experimental surfaces will be explained in the next chapter.

Chapter 4: Fatigue

4.1 Introduction

Fatigue failures on most structural mechanical components occur in those subjected to repeated, cyclic loading. This can be described as a local phenomenon, where cyclic evaluation of the stresses and deformations occur within a certain critical volume of material. Modelling the mechanical behaviour of a material under multiaxial elastic strain and cyclic deformation is fundamental in predicting damage and the safe operational life of many structural components.

Results of the transient micro-EHL solutions for the two rough surfaces in rolling/sliding contact provide the transient variation of the surface loading that is applied to the disks. This enables the stresses at and below the rough contact surface to be calculated, and this stress history for the disk material enables fatigue models to be applied and considered. Results of the micro-EHL modelling, which gives the full time-varying behaviour of lubricant pressure, surface shear stress and film thickness, have been used to predict the fatigue life and accumulated damage at the scale of surface asperity features.

This chapter gives an introduction to review the fundamental fatigue theory for application in the mixed EHL line contacts studied in this research. A shear strain model based on the critical plane approach is used to model fatigue for the micro-EHL transient problem in rough gear contact problems. The model used in this work is that of Fatemi and Socie (1988). In such a model, the stresses and strains are calculated during cyclic loading for all of the planes in the material, and the maximum cyclic shear strain range together with the maximum normal strain drives the fatigue crack initiation of the surface materials. It has generally been recognized that critical plane models often achieve better predictions for fatigue damage assessment. Critical plane models are established on a physical interpretation of the fatigue process where cracks can form and grow on critical planes (Bannantine & Socie 1992).

The research presented in this work has used a suite of software programmes written in the FORTRAN language, which have been developed by the Cardiff tribology group to analyse experimental and synthesised rough surface EHL cases.

4.2 Variable Amplitude Multiaxial Fatigue

The principles of strain-based characterisation of total fatigue life are only relevant for constant amplitude fatigue loading. In reality, however, engineering components are invariably subjected to varying cyclic stress amplitudes, mean stresses and loading frequencies. Variable amplitude fatigue analysis depends on the same approach as constant amplitude fatigue analysis with the addition of cycle counting and damage summation. For the micro or mixed lubrication problem, the stress history shows that severe stress cycling with variable amplitude occurs in the material during the traverse of the contact area, especially in the near surface area. The load experienced by different parts of the surface varies according to the compliance and the interaction of the surface roughness features of the contacting surfaces. Hence a variable amplitude fatigue analysis is necessary to achieve accurate lifetime predictions. To deal with variation in the loading amplitude, two problems have to be solved. One is how to identify complete stress cycles caused by the varying loading. An effective cycle counting method is required to determine the stress cycles and corresponding stress levels. The second problem is how to sum up the partial damage resulting from each of these different stress levels. To achieve this, a cumulative damage theory must be applied.

4.3 Rain-Flow Counting Method

Cycle counting methods are often used to reduce a complex irregular load history into a series of discrete events, which can be analysed using the test data obtained for constant amplitude fatigue loads. Various counting methods have been introduced over the years, which include level crossing counting, peak counting, simple range counting, and the rain-flow counting method (Suresh, 1998). Some of these methods are employed in the analysis of fatigue data to reduce a spectrum of varying load into a set of simple, uniform data histograms with constant amplitude cycle. Amongst these cycle counting algorithms, the rain-flow counting algorithm has been widely used, and is the most significant popular and probably the best method of cycle counting (Dowling, 2013).

The rain-flow counting method was introduced by Matsuishi and Endo (1968) and is considered to be the basis of the development of an overall cycle counting algorithm for estimating fatigue damage of components that are caused by randomly fluctuating

loading histories. A variety of variations of the rain-flow counting method for highly random fluctuations of the load with time have been developed by Dowling (2013), Suresh (1998), Musallam and Johnson (2012), Downing and Socie (1982), and Amzallag et al. (1994).

The classical rain-flow counting method is based on the cyclic material behaviour and counts a cycle with a load range from the highest peak to the lowest valley in the load history. It then seeks to count the further cycles experienced in a way that maximizes the ranges that are counted. This assumes that intermediate fluctuations are less important than the overall differences between high points and low points. The method counts cycles by identifying closed hysteresis loops in the stress-strain response. This is illustrated by the example given in Figure 4.1 (Anthes, 1997). The stress plot shows an irregular stress history that consists of a series of peaks and valleys, which are points where the direction of loading changes. The strain variation is in the form of hysteresis loops with end points corresponding to the reversals. The irregular stress history leads to the stress-strain path, as shown in the middle plot that forms the closed hysteresis loops shown which are registered in the order (4–3), (6–5), and (2–1). The shear strain amplitude and the maximum normal stress can then be determined for each of the cycles identified.

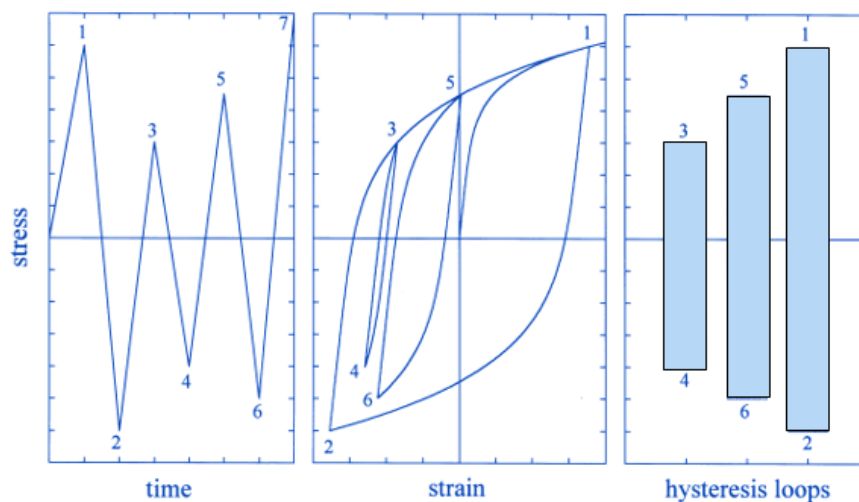


Figure 4.1 The stress-strain hysteresis loops extracted from the rain-flow cycle counting method.

4.4 Cumulative damage

Fatigue damage increases with applied cycles in a cumulative manner which may lead to fracture. The problem of summing partial damages resulting from different load cycles is dealt with by cumulative damage theories.

Several efforts have been made to estimate the life of a specimen in a cumulative damage test, and many data have been accumulated for the purpose of either deriving appropriate empirical relationships or to prove or disprove theoretical predictions. A simple criterion for predicting the extent of fatigue damage induced by a particular block of constant amplitude cyclic stresses, in a loading sequence consisting of various blocks of different stress amplitudes, is provided by the so-called Palmgren Miner cumulative damage rule (Palmgren, 1924; Miner, 1945).

Since the introduction of the damage accumulation concept by Palmgren, a variety of cumulative damage theories have been developed (Fatemi & Yang, 1998, Rao et al., 2001). Though many damage theories have been developed, unfortunately, there is no indication at present that any cumulative damage theory will give predictions significantly better than any other proposed theories. A comprehensive literature review of cumulative damage theories was given by Fatemi and Yang (1998).

Cumulative damage during the fatigue life of a structure subjected to variable amplitude loading is frequently calculated using the Palmgren-Miner rule, which assumes that the total life of a portion can be estimated by adding up the percentage of life consumed by each stress level:

$$\frac{n_1}{N_1} + \frac{n_2}{N_2} + \dots + \frac{n_k}{N_k} = 1$$

Where n_1, n_2, \dots, n_k are the number of cycles at a specific stress level, and N_1, N_2, N_k represent the fatigue life in cycles at the same stress level.

The reciprocal of the fatigue life is the damage caused by one cycle and the model predicts that failure would occur when the total damage, D , is unity:

$$D = \sum D_k = \sum \frac{n_k}{N_k} \geq 1 \quad (4.1)$$

(Clearly when all load cycles are the same and N_k loading cycles are applied the damage calculated by equation (4.1) is unity).

This rule should be used with caution. It is a linear relationship that does not take into consideration the effects of under stressing or overstressing. Under stress, in which relatively low-stress levels are firstly applied, can result in longer fatigue lives at a higher stress level, due to localised strain hardening. On the other hand, overstressing, in which high stresses are firstly applied, can result in shorter fatigue lives at a low-stress level, due to damage induced by the higher stress levels.

4.5 Critical Plane Approach

Fatigue life determination for all mechanical components and structures is an essential subject in the operating and design stages. Real service loading often generates random and multiaxial stress/strain states. They must then be reduced to a uniaxial state which is called the ‘equivalent’ state, and can then be used in fatigue life calculations. The critical plane can be defined as the plane subjected to the maximum damage. For the plane strain case this is identified by

$$D_{\max} = \max_{0^\circ \leq \theta \leq 180^\circ} [D(\theta)] \quad (4.2)$$

A value of D_{\max} equal to unity then corresponds to fatigue failure. In the following, the calculated damage D refers to the damage on the critical plane.

A critical plane approach is used when the loading is non-proportional to a significant degree. In this approach, stresses during cyclic loading are determined for various orientations (planes) in the material. The plane on which the tensile normal stress or the shear stress is a maximum is used to predict fatigue failure in the materials. This is based upon the experimental observation that fatigue cracks initiate on planes of high shear stress (mode II) and grow on certain material planes of high tensile stress (mode I) (Dowling, 2013).

4.6 Multiaxial Models based on the critical plane

Several models based on the critical plane approach have been proposed for the prediction of fatigue life of components subjected to complex loading. Although no universally completely accepted multiaxial fatigue criterion has been proposed in order to carry out fatigue analysis, it has been commonly recognized that critical plane models often achieve better predictions. Critical plane models are established on the physical interpretation of the fatigue progression where cracks can form and grow on the same critical planes (Fatemi A. et al., 2000, Bannantine and Socie, 1992).

Numerous models for the critical plane strain criterion that include the effect of the normal mean stress have been proposed, but they have been found to differ little in their predictions (Qiao, 2005). One interesting criterion was applied by Fatemi and Socie (1988) expressed here in the form of the Bannantine and Socie (1992) revision to incorporate mean stress using the maximum value of normal stress during a cycle to modify the damage parameter. In this criterion, fatigue damage is due to the shear strain amplitude influenced by the maximum normal stress, which is expressed in terms of the cycle to fatigue, N_f , as

$$\frac{\Delta\gamma_{\max}}{2} \left(1 + k \frac{\sigma_n^{\max}}{\sigma_y} \right) = \frac{\tau'_f}{G} (2N_f)^{b_0} + \gamma'_f (2N_f)^{c_0} \quad (4.3)$$

Where $\frac{\Delta\gamma_{\max}}{2}$ is the amplitude of shear strain variation on the critical plane, and σ_n^{\max} is the maximum tensile stress normal to the critical plane. Parameter k is a material constant with the range, $0.6 < k < 1.0$, G is the shear modulus, and σ_y is the yield strength for the cyclic stress-strain curve. The shear fatigue strength, τ'_f , and shear fatigue ductility coefficient, γ'_f , are obtained from fully reversed torsion fatigue tests in pure shear. In addition, b_0 and c_0 are shear fatigue strength and shear fatigue ductility exponents, respectively.

For damage modelling the material SAE4340 steel (BS970:En24) has been used where material properties can be found in Zahavi and Torbilo (1996) which are shown in Table 4.1. Dowling (1998) specifies the shear fatigue ductility coefficient and shear fatigue strength according to the following expression:

$$\tau'_f \approx \frac{\sigma'_f}{\sqrt{3}}, \gamma'_f \approx \sqrt{3}\varepsilon'_f$$

Table 4.1 Material parameters of SAE4340 steel.

b_o	-0.091	ε'_f	0.48
c_o	-0.60	σ'_f	2.0 GPa
E_1, E_2	200 GPa	σ'_o	827 MPa
K	1.0	ν_1, ν_2	0.3

For rolling contact fatigue initiation, there is evidence that cracks take place in shear under hydrostatic compression (Johnson, 1989) therefore the Fatemi and Socie (1988) shear strain model will be used to predict the variable amplitude multiaxial fatigue damage in this thesis.

4.7 Numerical Procedure

Having used the mixed EHL line contact solver to determine the transient surface loading (pressure and shear stress) acting on the contacting components the stress history for a block of the near surface material as it passes through the load bearing zone is calculated. At each timestep in the EHL analysis stored values of pressure, film thickness and surface traction are used to determine subsurface stress and strain history at each point in the representative block of material. The Cardiff tribology group created the procedure to estimate the fatigue damage analysis for EHL line contact and it is appropriate for multiaxial fatigue life estimations of an engineering component subjected to variable amplitude loading and is implemented in the analysis software (Qiao, 2005). This procedure is able to apply a range of fatigue models and in the current work the results obtained are based on the Fatemi and Socie (FS) shear strain based critical plane model. Rectangular trial blocks of material in the two surfaces were used for this model whose dimensions are taken to be $2a$ parallel to the surface and a perpendicular to the surface. The evaluation of this particular fatigue model involves using the stress history for the block as it passes through the EHL contact zone so that the fatigue evaluated corresponds to one rolling contact cycle of the surface material as shown in Figure 4.2, and one meshing cycle for the material in gear contacts.

The mesh for the block of material is set up for stress evaluation in such a way that the finest mesh is used near the surface to capture the possible high stress gradients due to asperity contact and that significantly improves the resolution of the numerical simulation results.

The block of material is subdivided with a rectangular mesh of 201 x 24 points. The spacing is uniform parallel to the surface in the x direction and non-uniform perpendicular to the surface. Perpendicular to the surface the depth of the fatigue analysis block is divided into 24 levels at $z/a = 0, 0.001, 0.002, 0.003, 0.004, 0.005, 0.006, 0.007, 0.008, 0.009, 0.01, 0.02, 0.03, 0.04, 0.05, 0.06, 0.07, 0.08, 0.09, 0.1, 0.2, 0.3, 0.4$ and 1.0.

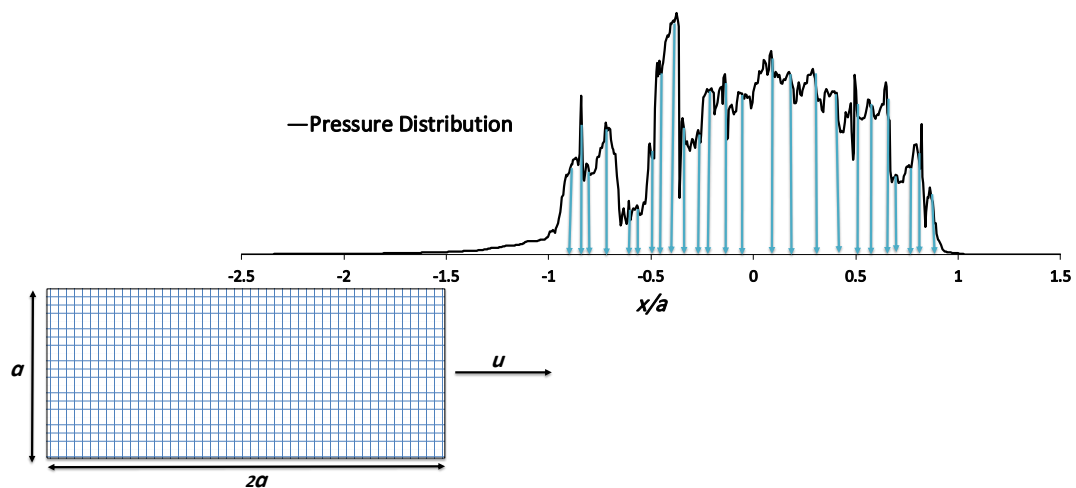


Figure 4.2 Block of surface material considered for fatigue analysis in the inlet region of the contact. The mesh shown is schematic as its spacing is non-uniform perpendicular to the surface.

To evaluate the total-life, the following procedure steps are taken for each point in the fatigue evaluation area:

1. Carry out a stress analysis for all the evaluation points in the material block considered for all time steps in the mixed Elastohydrodynamic lubrication (EHL) analysis of the surface as the block progresses through the contact zone. This involves interpolation between the axes for the EHL analysis whose origin is fixed at the contact point, and axes that are fixed in the moving material block.
2. Hooke's law is used for each evaluation point in turn using the stress component history to calculate the strain history as follows:

$$\begin{aligned}
\varepsilon_x &= \frac{1}{E} \left\{ (1-\nu^2)\sigma_x + (1-\nu)\sigma_z \right\} \\
\varepsilon_z &= \frac{1}{E} \left\{ (1-\nu^2)\sigma_z + (1-\nu)\sigma_x \right\} \\
\gamma_{xz} &= \frac{\tau_{xz}}{G} = \frac{2(1+\nu)}{E} \tau_{xz}
\end{aligned} \tag{4.4}$$

3. Since the transient micro-EHL solution is a plane problem, only the x - z plane is examined in the current research, where x is the tangential direction and z is normal to the surface. The normal and shear stress history on the critical plane at a material point can be calculated at time (t) from the directional components by using standard formulae given in Timoshenko and Goodier (1973) and the notation shown in Figure 4.3. Since the critical plane is not known before the analysis, all candidate planes have to be examined in order to identify the critical plane:

$$\sigma(t) = \sigma_x \cos^2 \theta + \sigma_z \sin^2 \theta + 2\tau_{xz} \sin \theta \cos \theta \tag{4.5}$$

$$\tau(t) = \tau_{xz} (\cos^2 \theta - \sin^2 \theta) + (\sigma_z - \sigma_x) \sin \theta \cos \theta \tag{4.6}$$

Where θ is the angle between the normal to the plane and the x -axis as shown in Figure 4.3. In the same way, the normal and shear strain on the same plane is determined by

$$\begin{aligned}
\varepsilon &= \varepsilon_x \cos^2 \theta + \varepsilon_z \sin^2 \theta + \gamma_{xz} \sin \theta \cos \theta \\
\frac{\gamma}{2} &= \frac{\gamma_{xz}}{2} = (\cos^2 \theta - \sin^2 \theta) + (\varepsilon_z - \varepsilon_x)
\end{aligned} \tag{4.7}$$

The value of θ is varied from 0° to 180° in 1° steps. So, the critical plane is given by the value of θ for which the calculated accumulated damage is greatest.

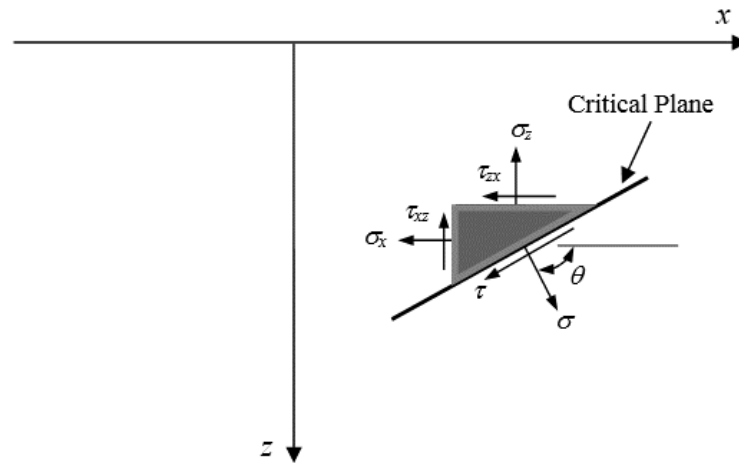


Figure 4.3 The orientation of the critical plane.

4. Count cycles based on the shear strain history by using rain-flow counting method.
5. Calculate the fatigue life, N_f for each cycle identified at step 4 using equation (4.3) where N_f is the cycles to failure.
6. Calculate the total cumulative damage using the Palmgren-Miner (1924) rule:

$$D = \frac{1}{N_f} = \sum_{k=1}^{all\ cycles} \frac{1}{N_{f,k}} \quad (4.8)$$

for the current candidate critical plane orientation.

7. Repeat steps 2 to 6 for all points in the fatigue evaluation area.
8. Plot the value of D_{max} for each point in the fatigue evaluation area.

4.8 Weibull Cumulative Density Function (CDF)

The Weibull distribution is one of the most widely used lifetime distributions in reliability engineering. The primary advantage of Weibull analysis is the ability to provide accurate failure analysis and failure calculations with extremely small samples. Also, it provides a simple and useful graphical plot.

To account for the effect of damage variation due to the varying interaction of the rough surface asperities, a statistical approach can be used to give a damage distribution for a particular depth beneath the surface in the materials based on the calculated damage values for all the material points at that depth. These distributions are useful in comparing results for different conditions when presented in the cumulative form $F(D)$. The damage probability density function is naturally skewed towards low damage and the Weibull distribution is an appropriate stochastic model to use for this purpose. The damage distribution expressed in the 3-parameter Weibull cumulative density function (CDF) has the form (Meeker & Escobar, 1998):

$$F(D) = 1 - \exp\left[-\left(\frac{D - \mu}{\eta}\right)^\beta\right], \quad 0 \leq \mu \leq D, \quad \eta, \beta > 0 \quad (4.9)$$

where η is the scale parameter, β is the shape parameter and μ is the location parameter. If $\mu = 0$, the 3-parameter distribution becomes the simpler 2-parameter Weibull distribution. Moreover, the skewness and coefficient of variation depend only on the shape parameter.

The calculated damage data at any specified depth was fitted to a Weibull distribution by using a suite of code written in the Fortran language, which has been built by Qiao (2005). This code was developed further to find also the cumulative damage for all the material within a specified depth from the surface.

4.9 Conclusion

This chapter presents an introduction to the fundamentals of theories that are used in fatigue analysis, and their application to rolling contact fatigue in mixed EHL line contact is studied. The loading condition for the surface material requires a varying amplitude multi-axial fatigue approach. The theory for this is discussed, and details are given for applying a suitable model to the mixed EHL contact results. This involves calculating the stress history throughout the material volume considered during its passage through the contact zone and using it to determine the accumulated damage due to the shear strain cycles experienced in the single pass through the contact area. The accumulated damage can then be treated stochastically using a Weibull distribution to model its cumulative density function.

Chapter 5: Experiment

5.1 Introduction

This chapter describes the principles, operating and measurement procedures of a two disk test rig. The purpose of this experimental work was to investigate the development of micropitting through an endurance test after extended running-in, using periodical observation and measurement of the surfaces of disks used. Two disk rigs are well established in the field of experimental tribology for their ability to provide researchers investigating EHL contacts with a steady state problem in terms of load and kinematics that can be compared to gear tooth surface contacts at a specific slide-roll ratio. The disk contact replicates the conditions found at a single point on the meshing cycle of gear teeth, i.e. it provides a 'snapshot' of contact conditions at a specific point in the gear contact cycle. The pair of rough disks used were axially ground, so that the finish is transverse to the entrainment direction, with a typical roughness Ra value of 0.40 μm . The test results used were surface roughness measurements that allowed the growth of micropitting to be quantified in terms of rotational cycles and used for comparison with the fatigue life analyses carried out in the current research.

5.2 Twin-Disk Test Rig

The twin disk rig used in this chapter was designed by Alanou (2006) based upon principles outlined by Merritt (1935) in order to study micro-pitting fatigue in aerospace transmission gearing. This disk rig was used for over a decade by many researchers (e.g. Davies, 2005; Weeks, 2015; Hutt, 2018) for different investigation purposes. Davies (2005) provided empirical data with which to validate mixed-EHL numerical simulations. Weeks (2015) studied the effects of mixed lubrication on both running-in and micro-pitting. Hutt (2018) studied the acoustic emission (AE) at the contact under mixed lubrication conditions due to running-in process. The twin disk rig has been used to examine how material hardness and the specific film thickness affect the surface wear, the contact friction and the electrical resistance of the lubricant film (Clarke et al., 2016). It has also been used to measure the acoustic emission generated during running-in and subsequent micropitting under mixed lubrication conditions (Hutt et al., 2018).

5.3 Load Application

Previous disk machine experiments used a weighted lever assembly to apply the load (Merritt, 1935, Williams et al., 1988). The loading mechanism used in the current rig is a hydraulic ram which allows the applied load to be varied whilst minimising shock loading that can occur if manually applied suspended weights are used. It also allows shock loading to be avoided when starting and stopping a test. In order to distribute the load equally across the contact, the parallel test shafts were mounted on self-aligning spherical roller bearings. The fast shaft bearing supports are fixed to the base of the test head, and the slow shaft bearings are mounted in a pivoted yoke with the pivot bearings mounted on the base of the test head. The disks are positioned on the shafts so that they are located centrally with respect to the yoke as shown in Figure 5.1. The load is applied hydraulically to the test disks through a push-rod acting on the yoke so that the yoke rotates about its pivot and the slow disk is pushed towards the fast disk. This configuration can provide a contact force of up to a maximum of 8 kN to the crowned disks which corresponds to a maximum Hertz pressure of 2.1 GPa. A photograph of the whole test head assembly is shown in Figure 5.1. The shafts are connected to the drive shafts (shown on the left) using flexible couplings to ensure that

the fast and slow shaft remain parallel. There is a small gap between disks, so when no load is applied, there is no contact between disks, such that there is no contact between them until load is applied. This allows the test rig to be run up to speed before the test is started.

The shafts are provided with central and radial feed holes for thermocouple and contact voltage wires which allow measurement of the bulk disk temperatures and the level of metallic contact occurring through the contact voltage.

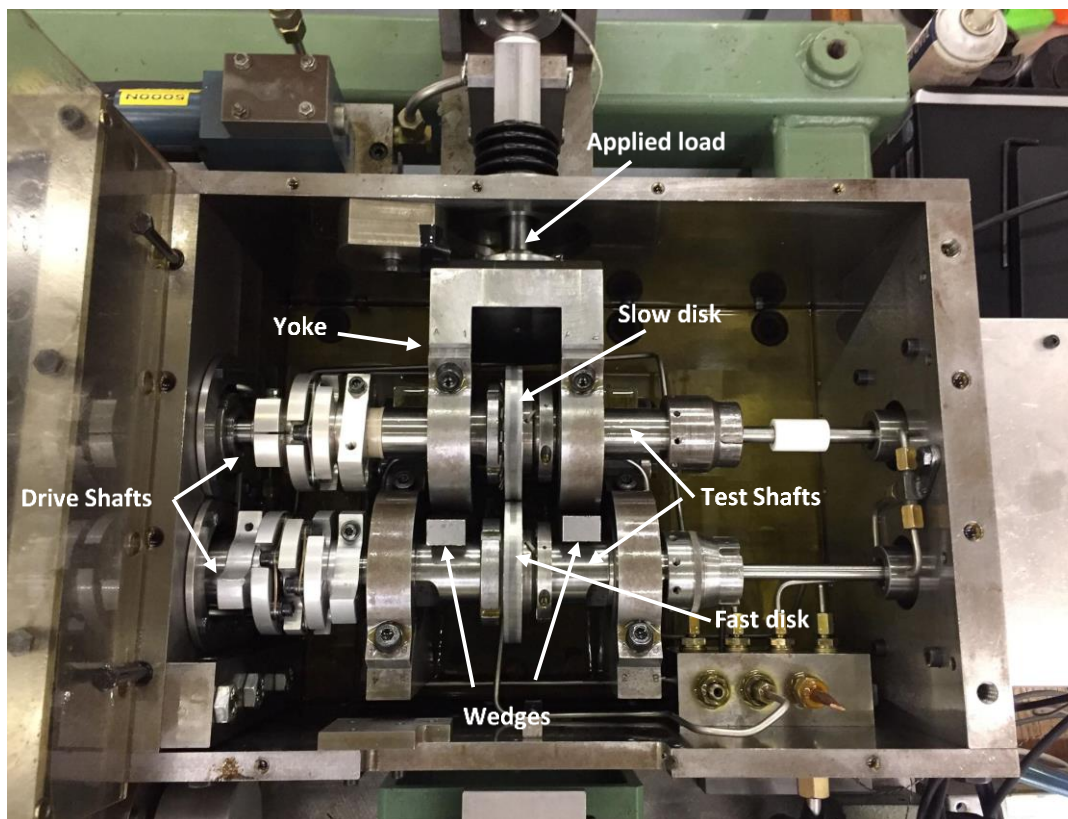


Figure 5.1 General view of the test rig showing the swinging yoke and the wedges used to separate the disks during the setting of the load.

5.4 Load Calibration

The applied load value to the disks is controlled manually by using a variable pressure relief valve which is set initially to the required pressure (load). A ball valve located after the control valve is initially open to allow the hydraulic fluid to return to tank. The ball valve is closed to apply the set pressure to the hydraulic ram so as to load the

disks. It is opened subsequently to remove the load. This arrangement allows the load to be applied in a controlled and repeatable way.

The contact load is measured directly by a load cell in the load path and this was calibrated initially over the full load range by adjustment of the hydraulic pressure supplied to the ram. During calibration, two wedges were placed in-between the fast test shaft and the slow test shaft bearing supports to keep the disks separated when the load was applied. This was to prevent the disks carrying the load during calibration as this would deform the asperities and affect the results obtained during testing. The wedges were removed after calibration so that the test could be carried out. The wedges are shown in position in Figure 5.1.

5.5 Description of Drive to Test Rig

The drive from the motor is transferred to the fast drive shaft through a pair of speed increasing helical gears as shown in Figure 5.2. The test shafts are geared together so that they turn at different speeds. A series of fixed SRR values can be obtained by using different helical gear pair combinations to drive the slow shaft from the fast shaft. The gear pair can be replaced allowing the relative speeds of the two shafts to be changed. Both surfaces rotate in the same direction relative to their contact, but with different speeds, depending on the gear ratio selected.

Previously, the test rig had been used with pairs of spur gears by Davies (2005) and Alanou (2006). However, these gears were replaced by Weeks (2015) with helical gears in order to reduce the misalignment between the disks and minimise backlash. This assembly is shown in Figure 5.2.

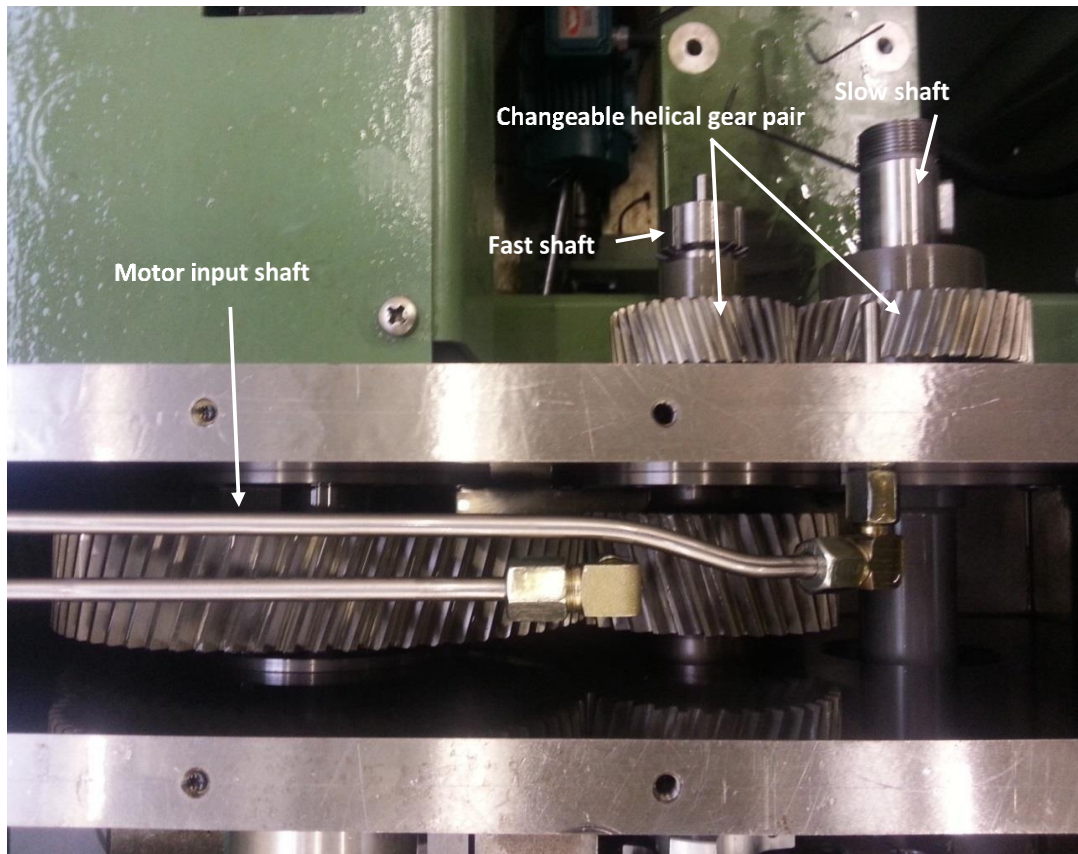


Figure 5.2 Helical gear pair and input shaft arrangement.

High speeds of the test rig had been required for the work undertaken by Davies (2005) to consider the electrical resistance signals and also for the extreme conditions which can be encountered in aerospace gears in the work carried out by Alanou (2006). Both authors used an inverter powered two-pole motor allowing a maximum test shaft speed of 12,000 rpm.

In contrast, the experiments carried out by Weeks (2015) were run at lower speeds to investigate mixed lubrication and encourage asperity interaction. The original high speed motor was found to be unsuitable in trying to maintain stability at the low entrainment speeds. Weeks then replaced the original motor by the current Marathon Electric 5.5kW three-phase asynchronous six-pole motor which provides the steady lower speeds required when examining mixed lubrication conditions. The new motor provides fast shaft speeds in the range of between 200 and 2000 rpm. The speed is computer controlled, and the disks can be run up to speed without being in contact. In

the experiment used as part of the current research the fast shaft speed was 1000 rpm with SRR equal to 0.5.

5.6 The slide/roll ratio (SRR)

The test disks used have equal diameters of 76.2mm, and both surfaces move in the same direction relative to the contact. An electric motor drives the fast drive shaft and the slow shaft is gear connected to the fast shaft so that a fixed SRR is imposed at the contact. This is in order to simulate the actual contacts as found in gear tooth contact which only have equal speeds when contact is at the pitch point. The SRR in gear tooth contacts varies linearly with distance from the pitch point during the meshing cycle. Four pairs of gears can be used to drive the shafts at different fixed slide/roll ratios. For the experiment used in this thesis, the SRR was 0.5. Micropitting tends to occur in the parts of the meshing cycle where sliding is high and so this SRR is representative of those circumstances.

When two disks are rolling and sliding together with two different velocities relative to the contact point the fast speed disk is denoted U_1 , and the slow speed disk U_2 .

The sliding speed is equal to:

$$U_s = U_1 - U_2$$

And the slide/roll ratio is:

$$\xi = \frac{2|u_1 - u_2|}{u_1 + u_2}$$

5.7 The Disks Geometry and Properties

The test disks were manufactured using a case hardened gear steel meeting Rolls-Royce material specification 6010. Previous extensive scuffing experiments carried out by the research group at Cardiff University (Patching et al., 1995) utilised this nickel-chromium steel supplied by Rolls Royce. The disk diameters are 76.2 mm (3 inches) and a thickness of 9.5 mm (3/8 inches) and a crown of radius 304.8 mm (12 inches). This geometry results in a spheroidal contact face that generates an elliptical test contact. The aspect ratio of the contact is 4:1. An internal conical abrasive wheel was used to produce the crown which has an approximately axial finish. The test specimen specification used is shown in Figure 5.3.

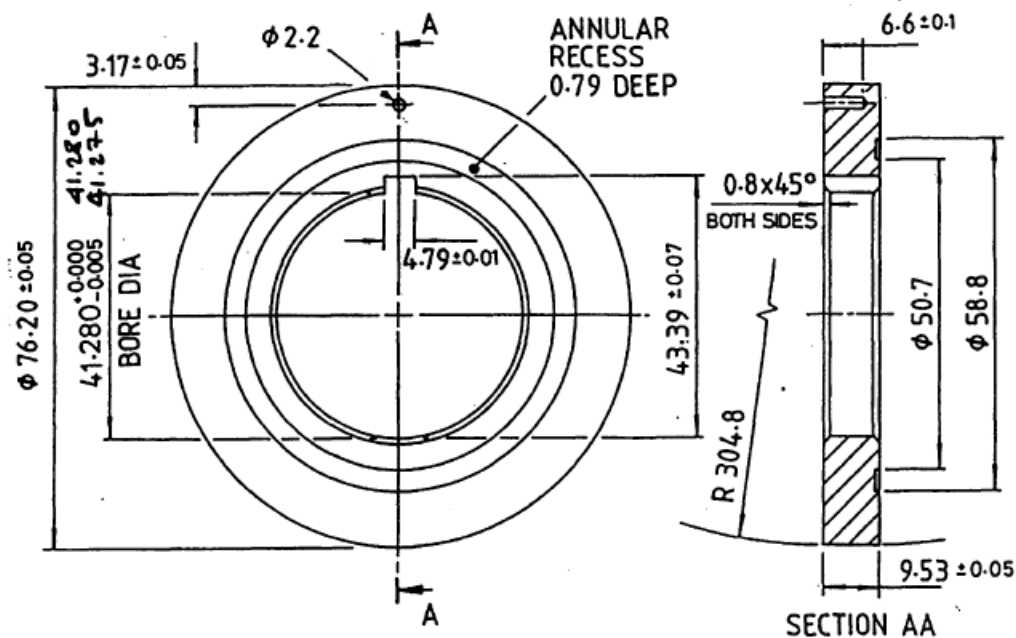


Figure 5.3 Drawing of test disks used (mm).

A 2.2mm diameter blind hole was made to allow the thermocouple to be positioned 3 mm below the disk contact surface on its mid plane as shown in section AA of Figure 5.3. The depth of the hole is half the thickness of the disk, and a type J thermocouple was placed into the hole and secured with two-part epoxy resin to mount the thermocouple in thermal contact with the hole blind end. This enabled the bulk temperature of each disk to be measured and recorded during the tests providing the continuous measurement of the almost steady state temperatures 3mm beneath the

surfaces of the disks. These are taken to be representative estimates of the mean bulk temperatures of the disks (and hence lubricant viscosity) as they enter the EHL contact zone.

5.8 Surface Orientation and Grinding Process

The effect of roughness orientation on contact and lubricant film thickness has been an important issue of surface manufacturing, attracting much attention since the 1970s. Surface finish by a machining process may result in features of a certain preference of surface asperity distribution. There are basically three types of machined surfaces which include transverse, longitudinal, and isotropic roughness. The direction of common asperity ridges for the first two processes is parallel or normal to that of the surface relative motion, while the isotropic roughness typically refers to randomly distributed asperities that do not show any apparent direction. Therefore, the hydrodynamic lubricant flow could be affected significantly by the roughness pattern, which could affect the lubrication performance. Examples of the importance of the orientation of the roughness in contact performance can be seen in the work of Zhu and Wang (2013) who carried out an investigation using a mixed lubrication model using the three types of machined surfaces mentioned above with contacts having various ellipticity ratios. It was found that a circumferential roughness orientation in elliptical contacts provides effective lubrication where the aspect ratio is around one or less. In this work, the elliptical contacts had an approximately 4 to 1 aspect ratio with the major dimension in the disk axis direction. This is a case where a perpendicular roughness orientation has been shown to be a benefit as side leakage no longer dominates the flow of lubricant in the contact (Zhu and Wang, 2013).

The direction of surface finish is the key feature of the disks. Since the disk experiment test was designed to replicate the roughness orientation that is found in ground gear teeth, it was considered necessary to reproduce the same direction of gear tooth finish. The gear tooth flanks finished by classical grinding have a finish direction roughly normal to the rolling/sliding direction. So the required roughness finishing direction is the axial direction of the disk test samples, i.e. the grinding marks need to be normal to the circumferential direction. The grinding process for the axial surface finish was developed by Patching et al. (1995) and Alanou (2006) who used a special set-up,

which combines a surface-grinding machine fitted with a grinding wheel dressed to the form of a shallow internal cone and the tailstock of a cylindrical grinder, as shown in Figure 5.4.

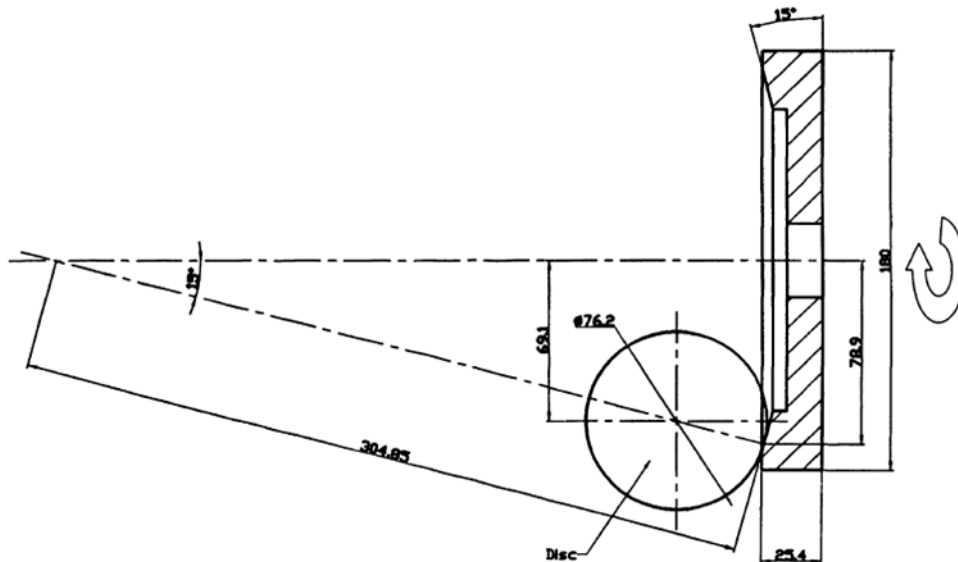


Figure 5.4 Scale drawing of the generation of surface geometry and axial finish by grinding (Patching et al., 1995).

The disks were generated using this special grinding technique and produced a surface with the ridges and valleys aligned almost perpendicular to the direction of slide/roll ratio. These ridges and valleys are ‘extruded’ across the disk width along a swept curve. The two disks are then mounted on the shafts with the direction of roughness sweep for one disk opposed to that of the other, thus creating a shallow angle cross-hatched compound roughness pattern.

5.9 In Situ Talysurf Measurements

The rig has a platform on which a Taylor Hobson Form Talysurf 2D profilometer is positioned to measure both disk profiles. This is done at different stages starting from the as ground manufactured disk, and progressing to the running-in experiment (Davis, 2005 and Alanou, 2006) and finally to the endurance stage where the development of micropitting is measured for each successive load stage. The platform has holes for a three-point kinematic location arrangement. This consists of a vee groove, a conical seating and a flat that engages with the spherical ends of the feet of the Talysurf unit. This arrangement allows the flexibility of movement required for the portable Talysurf to measure both disks by providing two separate locations, the backward and forward positions, located so as to measure roughness profiles on the fast and slow disks respectively. This arrangement is shown in Figure 5.5.

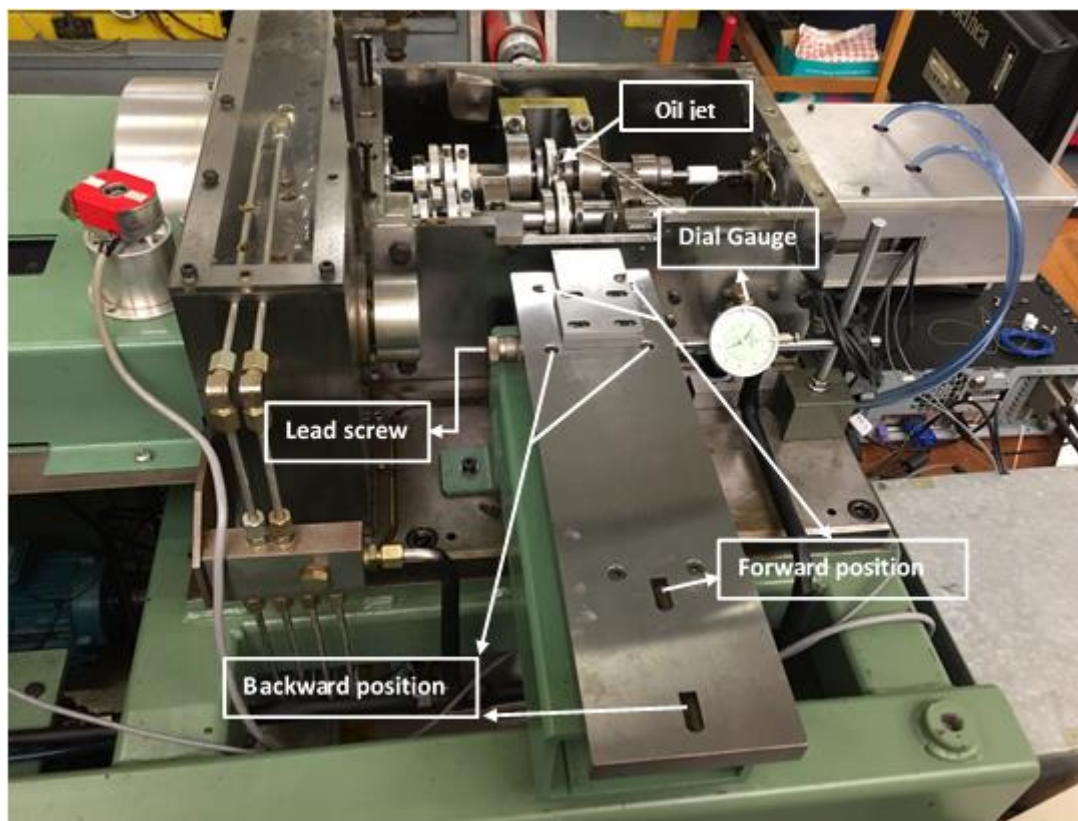


Figure 5.5 The platform used to locate the portable Talysurf showing the forward and Backward positions.

The platform can be moved in the direction parallel to the axis of the test disks (y-direction). This motion is controlled manually by a lead screw. This allows

circumferential profiles of the two test disks to be taken at different axial positions. The position of the platform within its range of motion is monitored using a dial gauge mounted on the test rig base with its measuring plunger in contact with the plane side of the platform.

This design enables profiles to be taken in the circumferential direction, which is perpendicular to the (axial) lay of the surface roughness at various axial positions across the width of the disks. Also, it provides the ability to relocate the unit accurately and easily so that the portable Talysurf can measure a series of profiles of both disks at the same axial positions for each stage of the test. Figure 5.6 shows the Talysurf mounted in its forward position taking a profile from the fast disk and illustrates the Cartesian axes used for this process. The profilometer is removed from its measuring position prior to conducting the next load stage of the experiment and stored in a purpose made storage case that maintains its cleanliness and isolates it from any vibration.

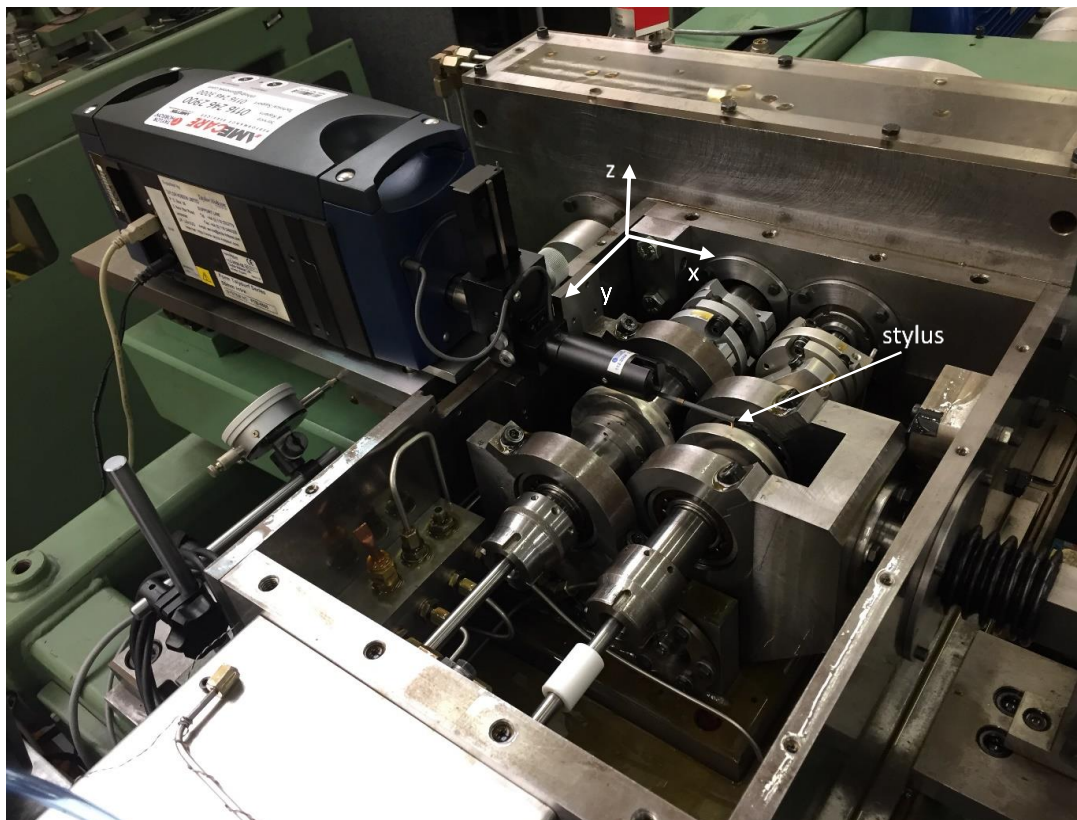


Figure 5.6 Photograph of in-situ longitudinal profile measurements for the slow disk surface with the Talysurf unit positioned in the forward position.

The main purpose of using the portable Talysurf in-situ is to be sure that the disks remain in the same position relative to one another during the repeated measurement of surface profiles at various stages during the running-in and endurance testing process, without the need to remove the test disks from the rig. This was very important in preventing any misleading results during the investigation, as any misalignment between interacting surfaces could generate high pressures and lead to additional running-in, i.e. more plastic deformation (Tudor, 1948).

The Talysurf device uses a stylus having a conical diamond tip (90° apex angle) with a $2\ \mu\text{m}$ tip radius. A sharp stylus tip may lead to damage a surfaces, especially on a soft surface, and more details about various other roughness measurement techniques can be seen in (Williams, 1994, Bhushan, 2002).

The stylus is drawn past the disk surface in the axial direction at a constant speed and produces an analogue voltage signal proportional to its vertical displacement. The instrument samples this at uniform time increments to produce a series of height measurements (z direction) that are equally spaced in the traverse (x) direction. The vertical dynamic measurement range of the Talysurf is 1 mm which allows profiles of up to 12 mm long to be obtained from the disks.

The in-situ disk profiles were obtained prior to and following each load stage during the testing process to monitor the development of the surface features. A score mark was made as a reference point on the side of each disk for the circumferential position used. This reference point was used for all axial measurements. This procedure provided an approximate relocation in the longitudinal direction. Therefore, precise relocation of profiles taken at different stages of the experiments was achieved by re-alignment of the profile after measurement based on recognisable valley features. For each measurement 12 mm long profiles were taken across the lay of the ridges and valleys at a single circumferential position and at nine axial positions for each disk. The axial measurement positions were on the disk centre line and offset from the centre in steps of ± 0.25 mm. All profiles were therefore taken within the Hertz contact area.

The visual similarity between axially offset profile traces is demonstrated in Figure 5.7 where profile measurements at stage 5 taken at the same circumferential location

are shown. The profiles were relocated precisely by using the alignment of the unique deep valley features of the profiles in the trace direction. This was performed by shifting the profile along with an adjustable offset to achieve the best valley alignment.

It is clear that suitable agreement between the prominent asperity features exists which is due to the highly directional lay of the surface finish. Note that the grinding process leading to the crowned disk profiles involves a conical grinding wheel. Consequently, it is inevitable that there will be differences in the profiles obtained at different axial positions.

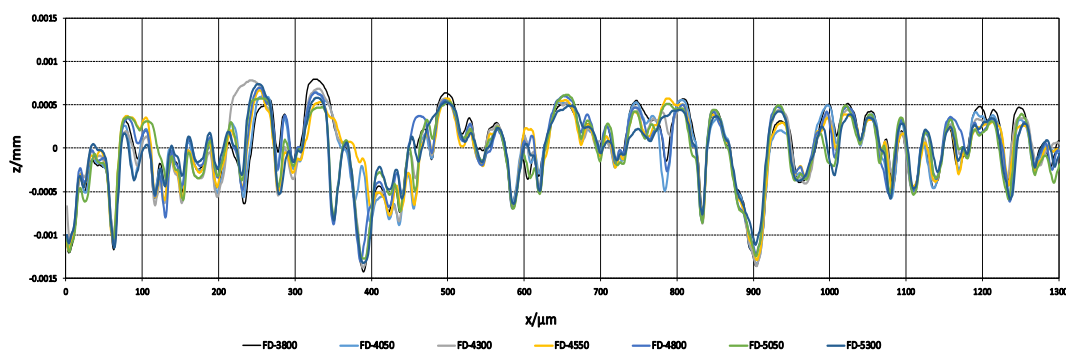


Figure 5.7 Filtered traverse of 1.3 mm of fast roughness profile traces at 20000 cycles taken at different positions of the disk with an axial offset of 0.25 parallel to the y-axis.

The portable Talysurf was re-calibrated for each measuring stage in order to be sure that the measurements taken were correct. This was achieved by measuring a calibration ball of known radius of curvature as shown in Figure 5.8. The calibration was carried out with the Talysurf positioned on the floor of the laboratory because this reduced the interference from vibrations.



Figure 5.8 Talysurf calibration using calibration ball on the floor.

5.10 Filtering the raw profile

For each measurement performed, the raw profiles were obtained from a profilometer gauge that determined all the roughness parameters of the disk surface, in terms of roughness, waviness and form. These terms are shown in Figure 5.9a. Once the form has been removed, it is required to separate the waviness and the roughness. This is a critical aspect of surface measurement. High pass filtering was required to analyse the raw profile data and remove the unwanted longer wavelength features that include waviness and form. A Gaussian filter was used having a cut-off length value of 0.25mm, being the same order as the Hertzian contact dimension for the disk contacts. This will normally remove any features which have a wavelength greater than 0.25mm. The various steps in this process are illustrated in Figure 5.9. Each roughness surface is produced by the Gaussian filter and it represents a trace of the material height relative to the mean line. This is not a line but the profile of the moving average which is the weighted mean produced by the Gaussian filter.

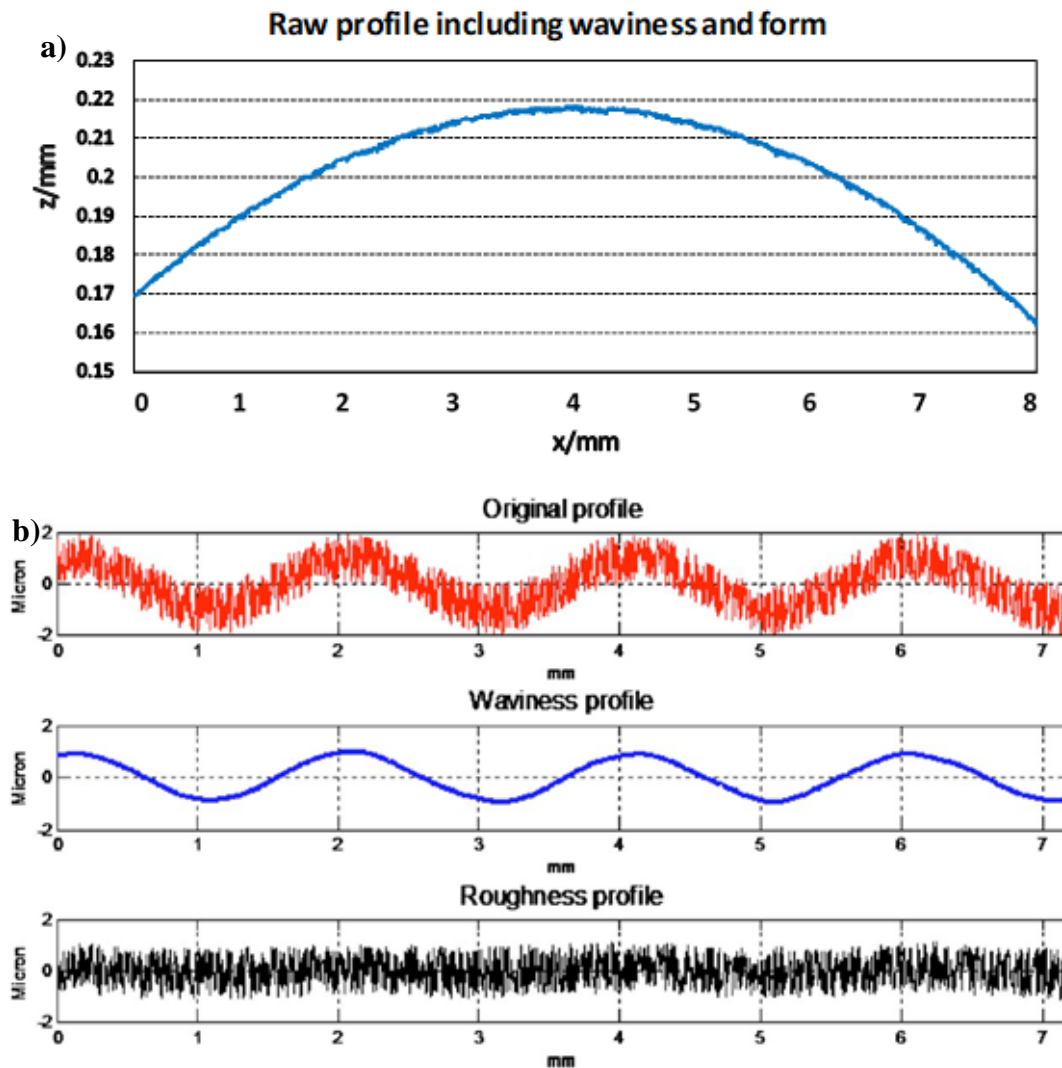


Figure 5.9 The disk surface features including form, waviness and roughness (ISO-Standardized Filtering, 2019) .

In this study a Gaussian filter with a cut-off of 0.25mm was used to remove waviness elements and the form of the disks, leaving the roughness profile for evaluation. This process produces filtered heights for points which are further than the cut off length from the profile ends. The original profile was 8 mm long and as 0.25mm was lost at each end, so the filtered profile became around 7.5 mm long. Both filtered and unfiltered profile data were saved for the fast and slow disks in order to provide data for further examination.

5.11 Realignment of run-in surfaces

Figure 5.10 shows an un-run profile and a post running-in profile superimposed and it is clear that they have significant differences. The changes are due to plastic deformation at the asperity level which has happened during running-in. The profiles are taken at the same nominal position and have been filtered to produce the roughness profiles. Adjustment of position in the trace direction was achieved by using recognizable deep valley features located between peak features to align the profiles. It is clear from this figure that the valley features are unaffected by the loading applied during running-in. The profiles do not match each other in most locations. However, there are many valley features in the run-in profile that have been shifted in the vertical direction (z) relative to the un-run profile. For example, this occurs at $x = 27 \mu\text{m}$ and $x = 233 \mu\text{m}$, and between $x = 447$ and $x = 1087 \mu\text{m}$, etc. The presence of a small scatter in the profile difference could be due to the noise or systematic measurement error. However, the local vertical deviation could also be introduced by the filtering process, which evaluates the mean line using a Gaussian filter. The heights shown are relative to the mean line which is different to that of the un-run surface.

Adjustment in the height direction was required to make a clear comparison between profiles to give the actual asperity level shape and this was achieved using a technique for aligning the pre and post-running surfaces, taking into account the distortion introduced by the profile filtering process and other factors.

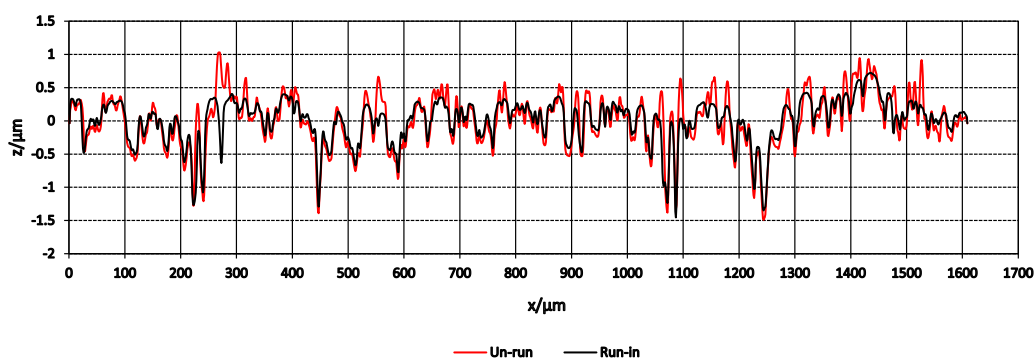


Figure 5.10 The un-run and measured run profiles before vertical adjustments.

5.12 Vertical alignment of the deepest common features

This approach is based on choosing the deepest common valley features for the run and un-run profiles. After identifying the deep valley locations for both surfaces the selected valley bottoms are connected with a smooth curve, as shown in Figure 5.11 a, b and c. Figure 5.11c shows that there is considerable similarity between the connection curves but they are different in shape in places. Several factors contribute to the difference. These are the variation in the sub surface valley plastic deflection, differences in the mean lines of the surfaces obtained by the filtering process, and minor valley feature differences due to minor differences in the axial sampling positions. In addition, distortions can occur due to debris particles retained on the disk surface during the measurement process in spite of the cleaning process used. Together these introduce a vertical deviation in the measured height.

The connection line curves for the deepest valley points of both surfaces were calculated for the pre and post running profiles with the same discrete data points at a $0.5\ \mu\text{m}$ spacing by using a MATLAB interpolation routine programme. The option 'shape preserving interpolation' was selected for fitting to the data. This process of fitting was conducted for each profile independently. Having identified the two connection curves, the difference between them was determined. This difference represents the local relative distortion normal to the surface. This is shown in Figure 5.11d which compares the connection line curve and plots the difference between them. The un-run surface deep valley points were taken as the reference positions and the post running profile was realigned relative to those valleys. The difference between the connection curves was then added to the run-in surface as shown in Figure 5.12.

Figure 5.13 shows the realigned comparison of the two surfaces. Comparing Figure 5.13 and Figure 5.10 shown that a successful vertical adjustment has been made by using this approach. This method was used for all the surface profile comparisons with selection of the reference deep valley features involving a degree of judgement and choice. The comparisons after realignment were used to fine tune the process for each surface. The objective was to ensure that the re-aligned run-in surface was always below the un-run surface as this has always been seen in the results of FEA contact analysis of the rough surfaces carried out within the research group.

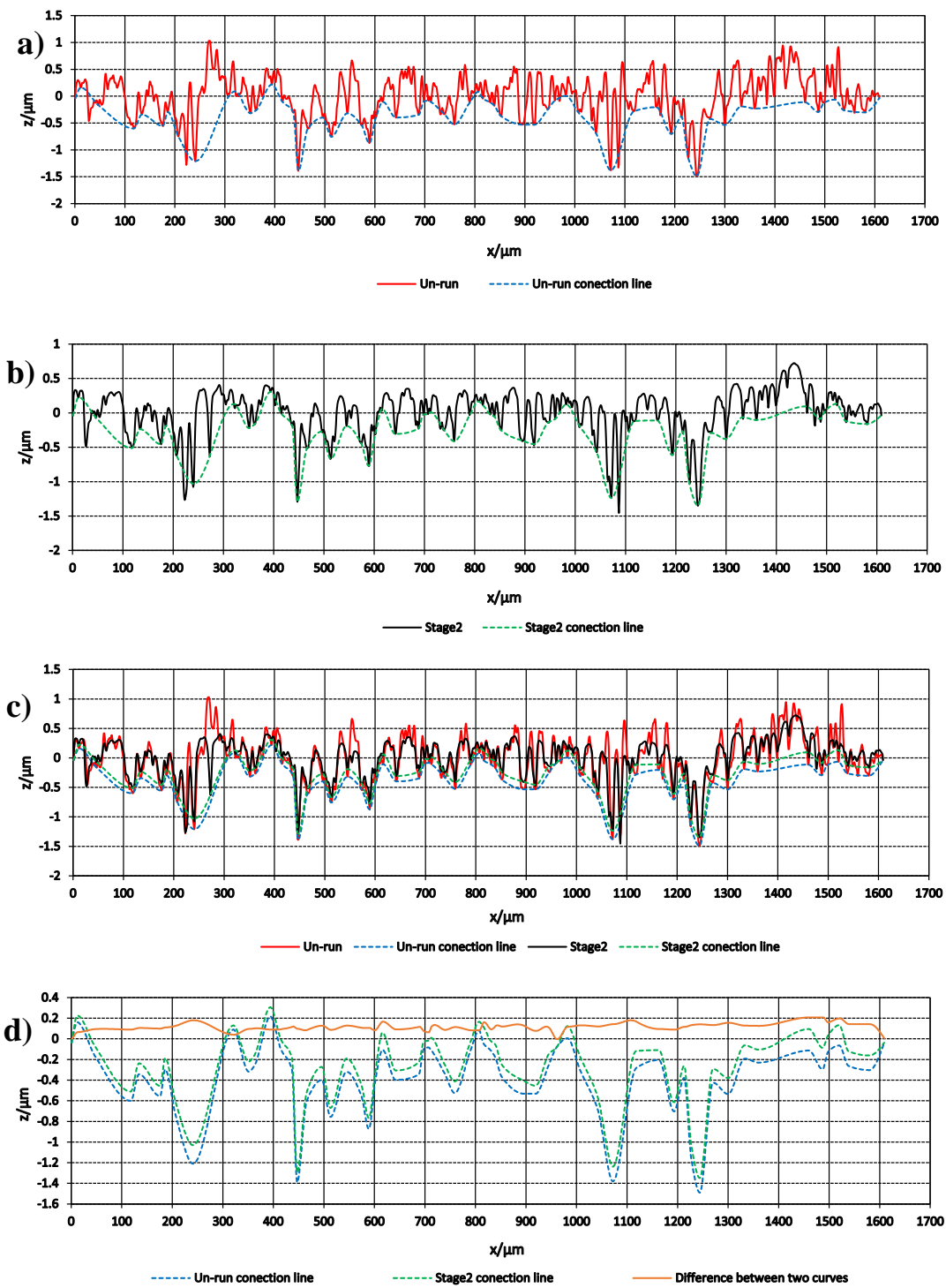


Figure 5.11 Profiles and the connection line curves between the deepest valleys; a) un-run surface, b) measured running surface, c) pre and post run surfaces, and d) connection curves and the difference between them.

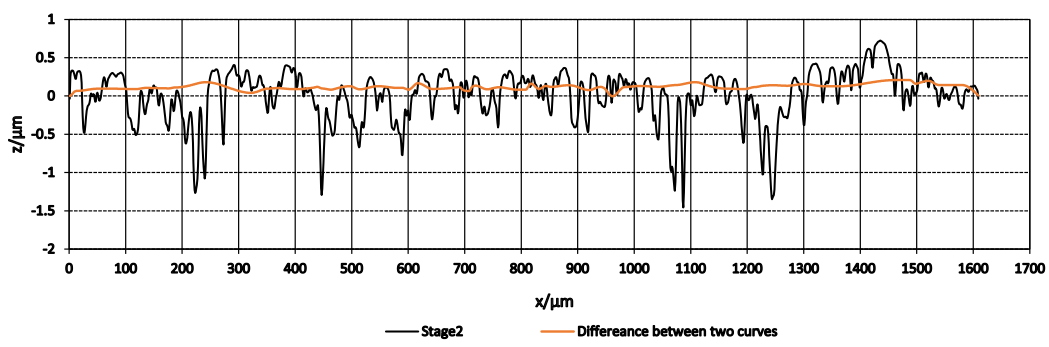


Figure 5.12 Measured running profile and the difference between connection line curves

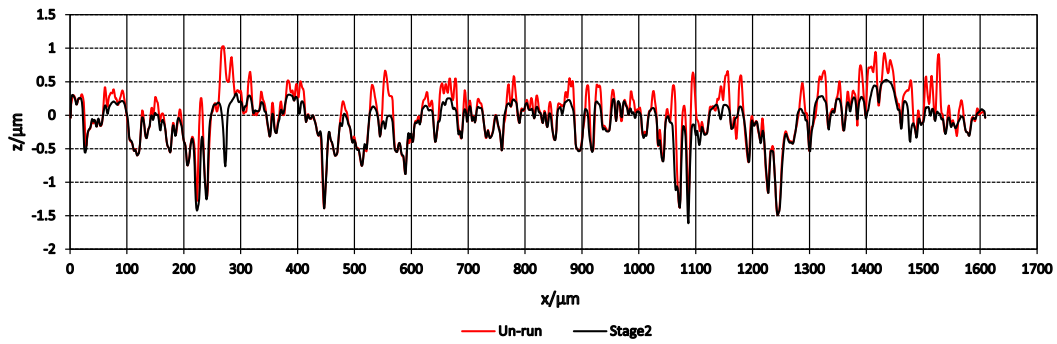


Figure 5.13 The un-run and measured run profiles after vertical realignment.

5.13 Experimental Procedure

The experiment was conducted on a twin disk rig in a number of test stages. The test simulates the contact between heavily loaded gears. The Vickers hardness of the alloy steel fast and slow disks was similar with a value of approximately 760 Hv. The operating conditions were constant in all test stages, as given in Table 5.1 .

Table 5.1 Test conditions

Slide/roll ratio	0.5,(5/3)
Fast disk Speed	1000 rpm
Mean Entrainment velocity	3.2 m/s
Maximum Hertzian contact pressure	1.2 GPa
Load	1460 N
Hertzian contact dimensions	0.8×3.0 mm
Oil bath temperature	80° C

The purpose of the test is to study the running-in and the micro-pitting fatigue history within the test time under mixed lubrication conditions. There was just one varying parameter between the test stages which was the stage duration. The length of stage period was chosen, starting at 3 min based on previous running-in experiments of (Hutt et al. 2018) using the same operating conditions and similar disks. The test adopted a greater number of test stages so that the initial occurrence of micro pits could be determined and the early stages of micropitting development could be monitored. A total of 33 test stages was carried out according to the schedule specified in Table 5.2.

The lubricating oil used for the test conformed to Defence Standard OEP-80. The test oil was circulated to the test disks at a feed temperature of 80°C lubricating the support bearings, drive gears and the disk contact with sprays directed on the inlet and outlet zones of the test contact. The inlet zone spray jet pipe can be seen in Figure 5.5 and is fitted with a thermocouple to measure the oil jet temperature.

Table 5.2 Running schedule

Number of stages	Description	Duration per stage (min)	Fast disk cycles per stage	Cumulative fast disk cycles at the end of stage/s
1	Run-in	3	3000	3000
2	Run-in validation	3	3000	6000
3 to 4	Fatigue testing	3	3000	~ 12000
5	Fatigue testing	8	8000	2×10^4
6 to 7	Fatigue testing	10	10000	$\sim 4 \times 10^4$
8 to 15	Fatigue testing	20	20000	$\sim 2 \times 10^5$
16 to 23	Fatigue testing	50	50000	$\sim 6 \times 10^5$
24 to 33	Fatigue testing	200	200000	$\sim 2.6 \times 10^6$

Prior to each test stage, the oil was allowed to circulate through the test rig for about 2 hours with the rig running with the disks unloaded in order to minimise the effect of temperature transients at the start of each running-stage. When the test specimens had approached thermal equilibrium, the load was set and the disks were brought into contact.

In terms of the surface measurements of the disks, the profile data were taken after each load stage at the same specific circumferential locations of the disk when the disk temperatures had cooled to room temperature. Wiping and solvent cleaning was used to reduce measurement contamination by residual oil and debris on the test specimen. After the disks had been cleaned, the portable Taylor Hobson 2D profilometer was set up and located on the axial linear stage whose position is measured by a dial gauge. Several steps were followed to find the position of the plane side of the disk. The profilometer stylus was approximately located by eye at the crown of the disk specimen. It was brought into contact and then the Autocrest function provided in the measurement software was used to locate the disk crest. The measurement stage was then moved carefully in the negative y-direction until the Talysurf height reading (z) showed a drop of 60 μm . This indicated that the stylus tip had reached the edge of the

disk. The error occurring in axial positioning using this method is of the order $7\ \mu\text{m}$ due to the resolution of the dial gauge and error in locating the disk edge. The dial gauge scale was set to 9.6 mm (which is the width of the disk) at this position. The stylus was then moved out of contact with the surface. Next, the disk was rotated manually to align the stylus with circumferential score marking. Then, the stylus was lowered back into contact and the measurement stage moved 5.8 mm in the y-direction to measure the first profile position.

The remaining profiles were measured at positions offset at steps of 0.25 mm across the width of the disk. This resulted in 9 profiles taken over a 2 mm range centred on the disk centre line within the contact area.

Chapter 6: Results

6.1 Introduction

The results shown in this chapter cover a full transient EHL line contact analysis for the eight pairs of surfaces considered.

Software code has been written in a general form to make changes to the geometry of the surfaces that simulates the running-in surfaces. Simulations were conducted for a number of different surface roughness pairs that have different Ra values, applied load, and operating conditions.

Three pairs of disk surfaces were obtained from the experimental work of (Weeks, 2015) and (Hutt, 2018). Four pairs of gear surfaces were measured at the Design Unit laboratory of Newcastle University for test gears before and after the running-in stage. Finally, one pair of disk surfaces was obtained from a current micropitting test where pitting growth was evaluated against more finely resolved contact cycles.

The first section of this chapter presents the results for synthesised run in gear surfaces which are compared with corresponding results for the measured run in surfaces. Two cases are considered with different roughness values. The results for synthesised running in of disk surfaces were presented in Chapter 3.

The second section presents the results of the calculated fatigue damage for both the synthesised and experimental surfaces for all eight sets of profiles. Weibull damage distributions are used to quantify the damage for all the material points at a particular specific depth, and also for specific volumes beneath the surface.

The third section compares the fatigue results obtained for the gear profiles with different roughness values, and also for results obtained for two disk profiles where the alignment of the surface asperities in the contact is adjusted to maximise and minimise the asperity interaction to test sensitivity of the analyses to counterface alignment.

Finally, the fourth section presents the experimental results that show the developing micropits during the disk machine endurance test and compares that with the calculated damage model of measured surfaces.

6.2 Comparison of Model and Experimental Micropitting Results

The test gear profiles used were obtained from gear testing at the Design Unit of Newcastle University as reported by Clarke et al. 2017 and resulted from a collaborative research project. Tests were carried out by the Design Unit team on pairs of helical gears in a power recirculating gear testing facility. The test gears whose dimensions are specified in Table 6.1. The gears were lubricated with an ISO VG 100 oil in order to promote micropitting and were loaded so that the corresponding maximum Hertzian pressure was 1.6 GPa.

Table 6.1 Test gear pair dimensions

Normal module / mm	6
Pinion tooth number	23
Wheel tooth number	24
Reference pressure angle / °	20
Base Helix Angle / °	26.27
Pinion tip diameter / mm	168.8
Pinion base diameter / mm	144.6
Pinion tip relief diameter / mm	162.1
Wheel tip diameter / mm	175.2
Wheel base diameter / mm	150.9
Wheel tip relief diameter / mm	168.6
Centre distance / mm	160
Face width / mm	44

To take stylus profilometer profiles of the gear teeth the gears were mounted in a purpose made jig that inclines the gear axis to the vertical by the tooth base helix angle, β_b . The tooth surface to be measured was then nominally horizontal and rotating the gear to an optimal position enabled root to tip profile measurements to be taken within the 2 mm range of the profilometer gauge. This optimum position was fixed by a fixed stop on the jig bearing against another tooth of the gear. Profiles were taken before and after running in and at other times in the testing program when the gears were

dismounted for measurement. The profiles taken included the gear tip as a clearly identified reference point.

A typical root to tip profile is illustrated in Figure 6.1 which consists of approximately 40,000 measured heights giving the form of the tooth and its roughness measurement. Two points of interest are the tip of the tooth, T, and the highest point of the form, C. The profile heights were measured in direction y_c , perpendicular to the profile tangent at C. Due to the gear axis inclination the measurements are taken in the normal direction to the tooth flank and a $\cos\beta_b$ scaling gives the heights in the transverse plane where the form is a nominal involute.

The coordinates of C were obtained by fitting a least squares parabola to the raw data over a 2 mm length centred on the observed position of C and locating the maximum height position of this parabola. The coordinates of T were obtained by fitting two straight lines to the data on either side of T and locating their intersection. The involute curve for the gear was obtained from the co-ordinates of C and T as described by Clarke et al. 2017.

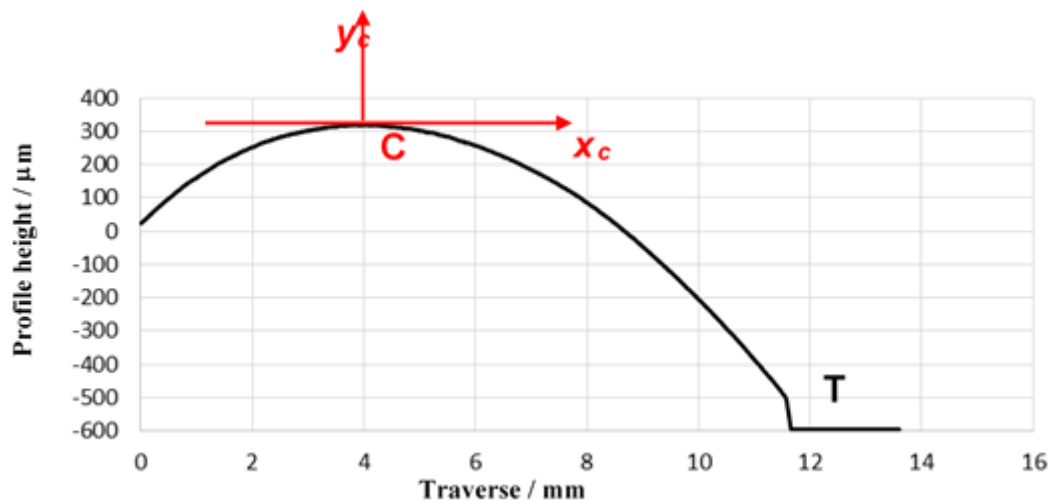


Figure 6.1 Root to tip gear profile measurement taken from test gear (Clarke et al., 2017).

The analytic fit to the involute was used to remove the form to obtain the deviation from the involute. Figure 6.2 shows the measured profile in terms of roll angle which can be obtained in terms of the profile traverse coordinate from the involute geometry and the position of point C on that involute. The positions of the start of active profile (SAP) and tip relief (STR) are defined in terms of roll angle in the gear geometry specification and it is clear that the specified STR position corresponds to the location where the tip relief becomes apparent in the involute form-removed profile, h_{diff} .

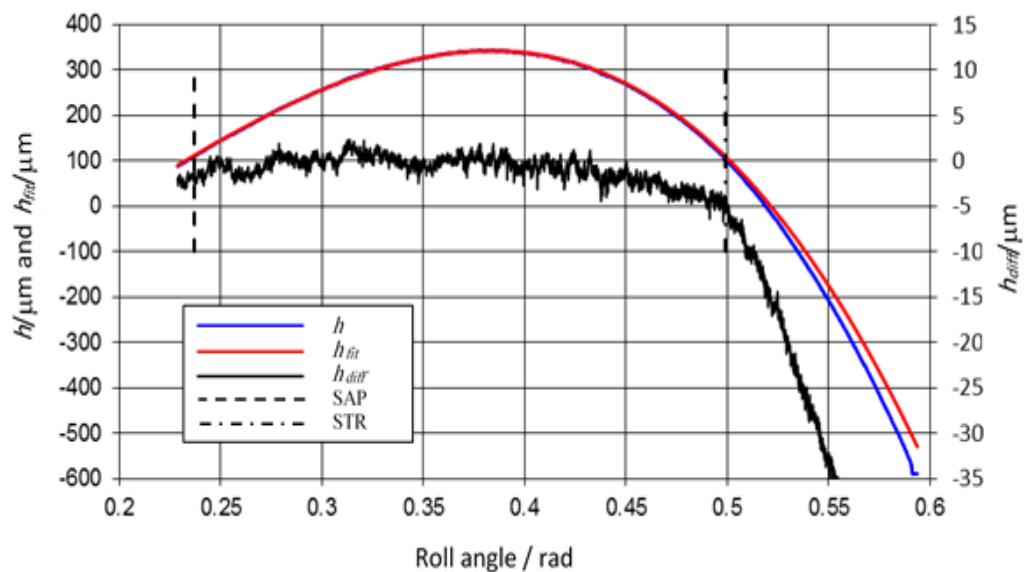


Figure 6.2 Profile measurement, h , involute fit, h_{fit} , and profile with fit removed, h_{diff} . Also shown are start positions of active profile, SAP, and tip relief, STR (Clarke et al., 2017).

Profile h_{diff} was then processed using the profilometer software. Firstly, any remaining form in the involute section was removed with a 4th order polynomial fitted between the SAP and STR positions. This was applied to the whole profile so that the true involute section, from SAP to STR had a mean profile value of zero. The profile was then filtered using an ISO standard Gaussian profile to provide the roughness profiles.

The profiles produced from the test gears were provided for inclusion in the research reported in this thesis. Two gear pairs were analysed in detail where the final grinding of the hardened gears was achieved by different manufacturers to the same gear specification. The form grinding manufacturing processes used are referred to as process A and process B. The manufacturing specification was for an Ra value less than $1\ \mu\text{m}$ and both gear pairs were in specification. However, the process A gears had high roughness with Ra values of $0.43\ \mu\text{m}$ and $0.42\ \mu\text{m}$ for the pinion and wheel, respectively, and the process B gears had low roughness with Ra value of $0.2\ \mu\text{m}$ and $0.22\ \mu\text{m}$ for the pinion and wheel, respectively. For each case considered the analyses were carried out for contact between tooth 1 and tooth 13 of each gear. (The pinions had 22 teeth and the wheels had 23 teeth.) The time period of running-in in the gears was longer than the disk tests with a lower temperature.

For each gear pair, two contact positions are considered for detailed analysis. These are called Analysis Point 1 (close to the tip of the wheel tooth) and Analysis Point 2 (close to the tip of the pinion tooth). They are positioned on the involute surfaces a distance $1.5a$ away from the start of tip relief positions, where a is the Hertz contact dimension, as shown in Figure 6.3. The slow roughness profiles (l_s) had length $l_s = 1.08$ mm long and the fast roughness profiles (l_f) had length $l_f = l_s * u_f / u_s$. These profiles were centred at the Analysis positions and were used in running the two meshing teeth against each other in the transient EHL analysis so as to replicate the counterface alignment in the contact between the gears

Table 6.2 Parameters used for 2D transient rough surface analysis.

		Analysis Point 1	Analysis Point 2
Radius of curvature pinion	R_p	28.096 mm	39.198 mm
Radius of curvature wheel	R_w	40.355 mm	29.253 mm
Radius of Relative Curvature	R	16.564 mm	16.751 mm
Pinion speed	u_p	7.915 m/s	11.04 m/s
Wheel speed	u_w	10.89 m/s	7.898 m/s
Entrainment velocity	u	9.405 m/s	9.470 m/s
Slide Roll Ratio	ξ	0.316	0.332
Load per unit length (Maximum contact pressure 1.6 GPa)	w'	1.172 MN/m	1.172 MN/m
Hertz contact semi dimension	a	0.466 mm	0.469 mm
Lubricant viscosity	η	0.017 Pas	0.017 Pas
Pressure viscosity coefficient	α	16.2 GPa ⁻¹	16.2 GPa ⁻¹

The wheel represents the fast surface and the pinion is the slow surface for Analysis Point 1. While, the pinion is the fast surface and the wheel is the slow surface for Analysis Point 2.

The gear profiles were taken at Newcastle from the root to the tip of the gear, so the pinion profiles for both cases were reversed in order to ensure that motion of the roughness features in the analysis replicated the motion in the actual contact. The speed direction of both the wheel and the pinion surfaces at AP1 and AP2 are shown in Figure 6.3.

Two kinds of EHL analysis were carried out.

- (i) The first kind is to find synthesised run –in profiles and compare with the measured ones by using transient Elastohydrodynamic (EHL) analysis of the contact between two meshing teeth from their two contact positions, as described in Chapter 3.

-
- (ii) The second kind is to use the transient micro-EHL solutions for the experimental and synthesised run-in surfaces to predict high cycle fatigue damage in the vulnerable thin surface layers, as described in chapter 4.

6.3 High Roughness Gears (Process A)

6.3.1 Profile Set Four

These profiles correspond to Analysis Point 1 for the high roughness surfaces (Process A). In this case, the wheel is the fast surface and a section of the profile 1.486 mm long was selected, centred at the analysis point. The pinion is the slow surface and a profile 1.08 mm long was selected. The different lengths of the profiles are in the ratio of their speeds. The numerical simulation code was developed so as to ensure that the profiles met at their centre points at the centre of the EHL contact in order to make the analysis simulate the real contact conditions. The only difference is that in this model the wheel tooth surface contacts with just one corresponding pinion surface tooth, while in reality each tooth contacts with all of the tooth surfaces of the meshing gear in turn. The numerical analysis was carried out with the operating conditions given in Table 6.2. The transient EHL solution for the synthesised running-in was converged at surface hardness level (corresponding to a maximum pressure of 5 GPa).

The results obtained using the running-in synthesis model were compared with the corresponding profiles taken from the experiment after running-in. These results are shown in Figure 6.4 and Figure 6.5.

It can be seen that there is a good agreement between the synthesised run in profile and the experimental profile for both the wheel and pinion profiles. Although there is a generally good fit between the synthesised and experimental surfaces, there are some zones where higher peaks are retained in the synthesised surface and this is seen in Figure 6.4c at the range of x positions of (1030-1250) μm , and x positions (625- 660) μm on the slow gear surface as shown in Figure 6.5b. This may be because the tooth surface interacts with all the teeth of the meshing gear in the experiment.

In addition, it can be seen that some neighbouring peaks were merged together and became one more rounded peak in the synthesis due to the high contact pressure that they experience. This effect can be seen at x positions of 30, 115, 280, 405, 630, 660, 735, 880, 1070 and 1150 μm of the fast profile of wheel as seen in Figure 6.4 and x

positions 100, 450, 900, 955 and 1035 μm on slow gear surface as shown in Figure 6.5.

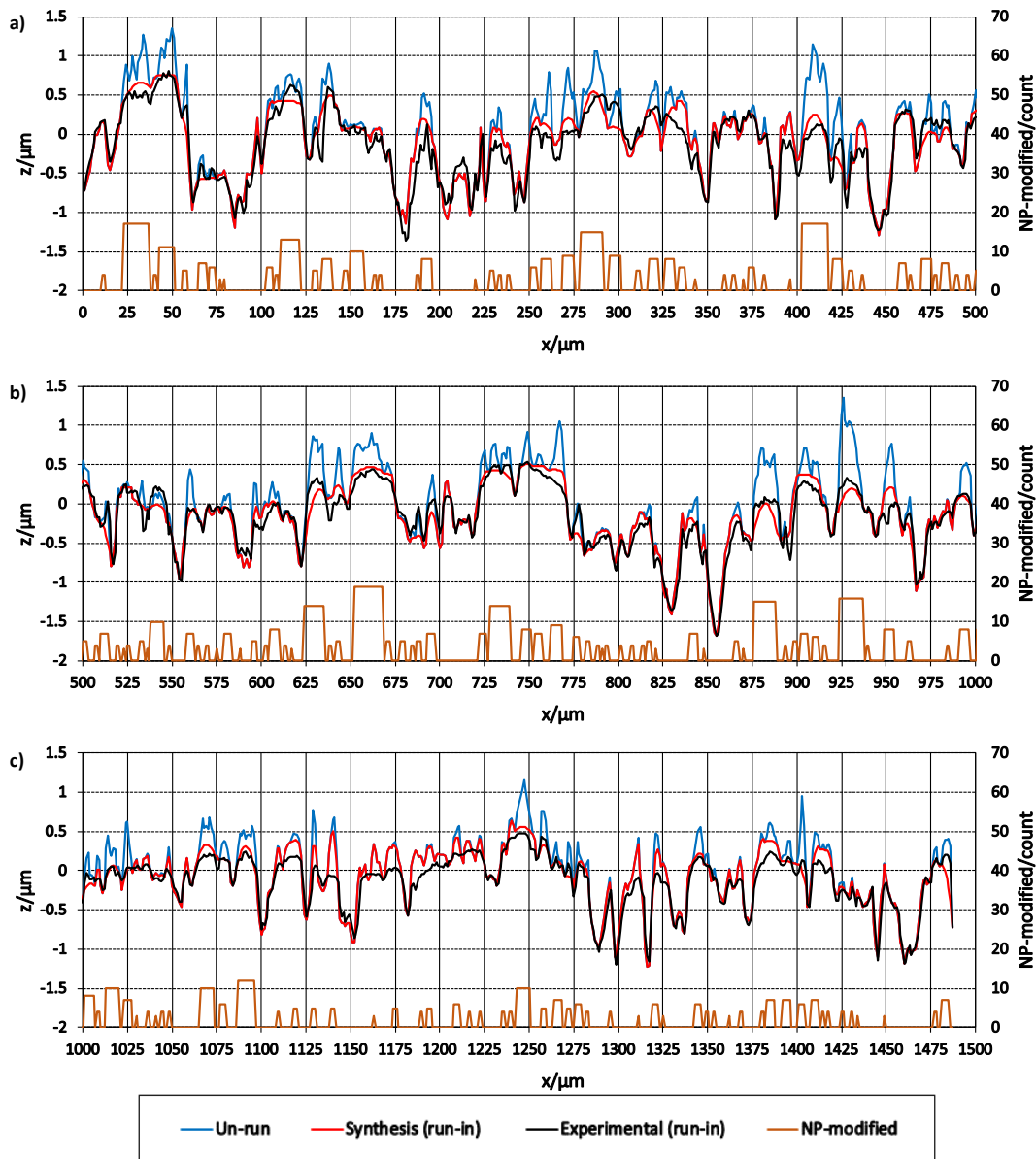


Figure 6.4 Un-run, synthesised and experimental run-in relocated profiles for the fast (wheel) surface for Profile Set Four.

Higher values of parameter *NP-modified* were found at the asperities that experienced high MTP values and became more rounded. The highest value of *NP-modified* for the fast surface was 20 points and 14 points for slow surface. This means that the wheel profile was modified more than the pinion as it is more aggressive in shape than the pinion profile. Furthermore, the *NP-modified* value for valley features equals zero as

expected, which means that no changes happens to these valleys and this is in agreement with the experimental profiles.

There were unexpected differences between the as manufactured and relocated experimental run-in profiles where the run-in profile is higher than the as manufactured one. These differences cannot be found in the synthesised surfaces, and this is seen in Figure 6.5a at the range of x position of (0-110) μm of pinion surface. These features are probably caused by error in the valley height alignment.

In spite of the numerical analysis not reproducing the exact interaction between the surfaces in the actual experiment, the results are encouraging and the level of agreement between the experimental and synthesised asperity shapes shows the same general trend.

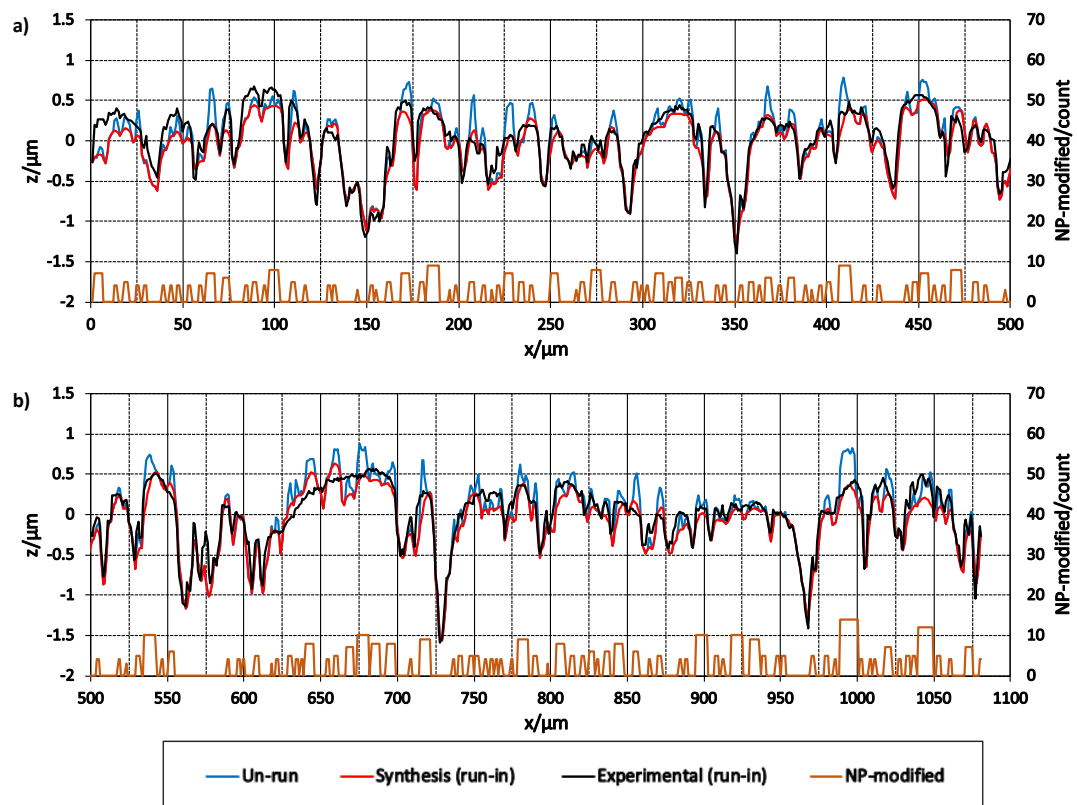


Figure 6.5 Un-run, synthesised and experimental run-in relocated profiles for the slow (pinion) surface for Profile Set Four.

6.3.2 Profile Set Five

This set of profiles is for Analysis Point 2 of the high roughness surfaces manufactured using Process A. In this case, the pinion is the fast surface and a section of the profile 1.51 mm long was selected centred at the analysis point. The wheel is the slow surface and its profile was 1.08 mm long. This approach of selecting profile lengths in the speed ratio was explained in section 6.2.1. The numerical analysis was carried out with the operating conditions given in Table 6.2. The transient EHL solution was converged at a surface hardness level of 5 GPa for the synthesis of running-in.

In addition to the running-in, there is some early micropitting (a portion of the surface material removed) which can be seen in Figure 6.6a for the measured wheel profile at x position 355 μm , and in Figure 6.7b for the measured pinion profile at x position 580 μm . Pits of this form are not a feature of the simulation program as that process is designed to replicate the plastic deformation of the asperities.

It is clear that the wheel gear surface for both AP1 and AP2 were modified more than the pinion gear surface, in spite of the wheel representing the fast surface for AP1 and the slow surface for AP2. The average value of *NP-modified* for fast surface (pinion) was 5 points and 10 points for slow surface (wheel) for AP2 process. The experiment profiles show that the plastic deformation in the wheel surface is more than the pinion one. Thus, both the synthesised and the experimental results have the same behaviour.

There were unexpected differences between the as manufactured and experimental run-in profiles where the run-in profile is higher than the as manufactured one. These differences cannot be found in the synthesised surfaces. This is seen in Figure 6.7 at the range of x position of (175-200), (552-625), (660-680), (775-825) and (1050-1075) μm of pinion.

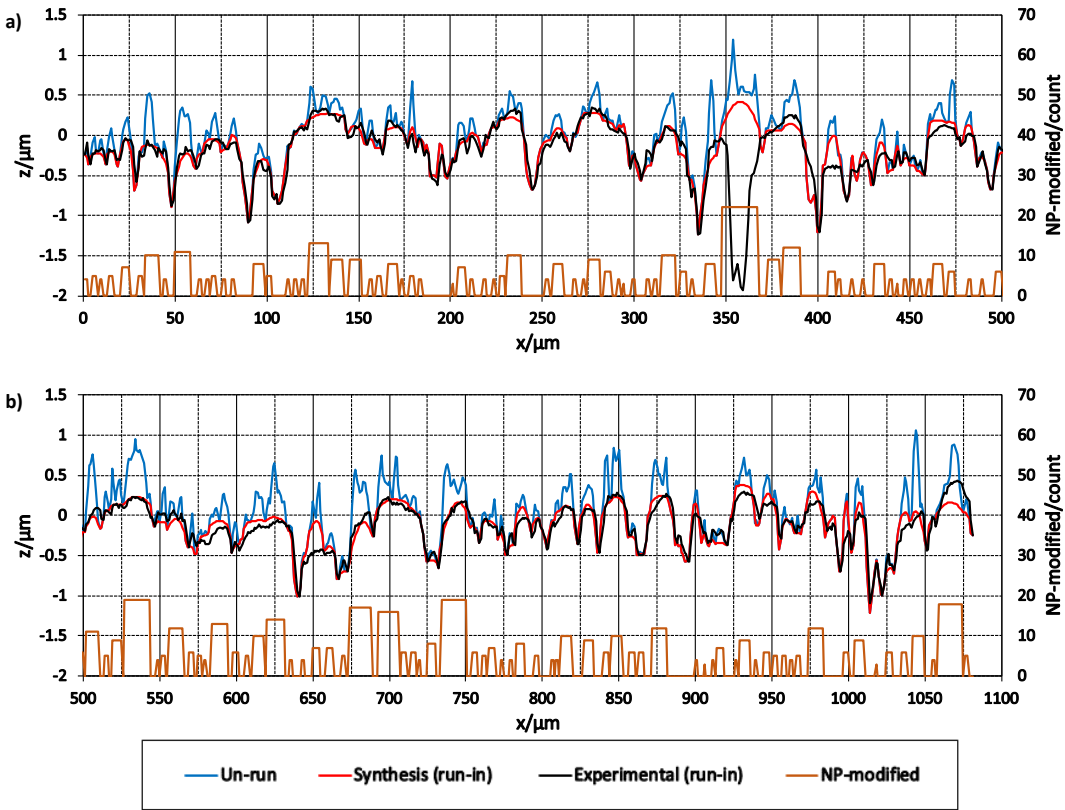


Figure 6.6 Un-run, synthesised and experimental run-in relocated profiles for the slow (wheel) surface for Profile Set Five.

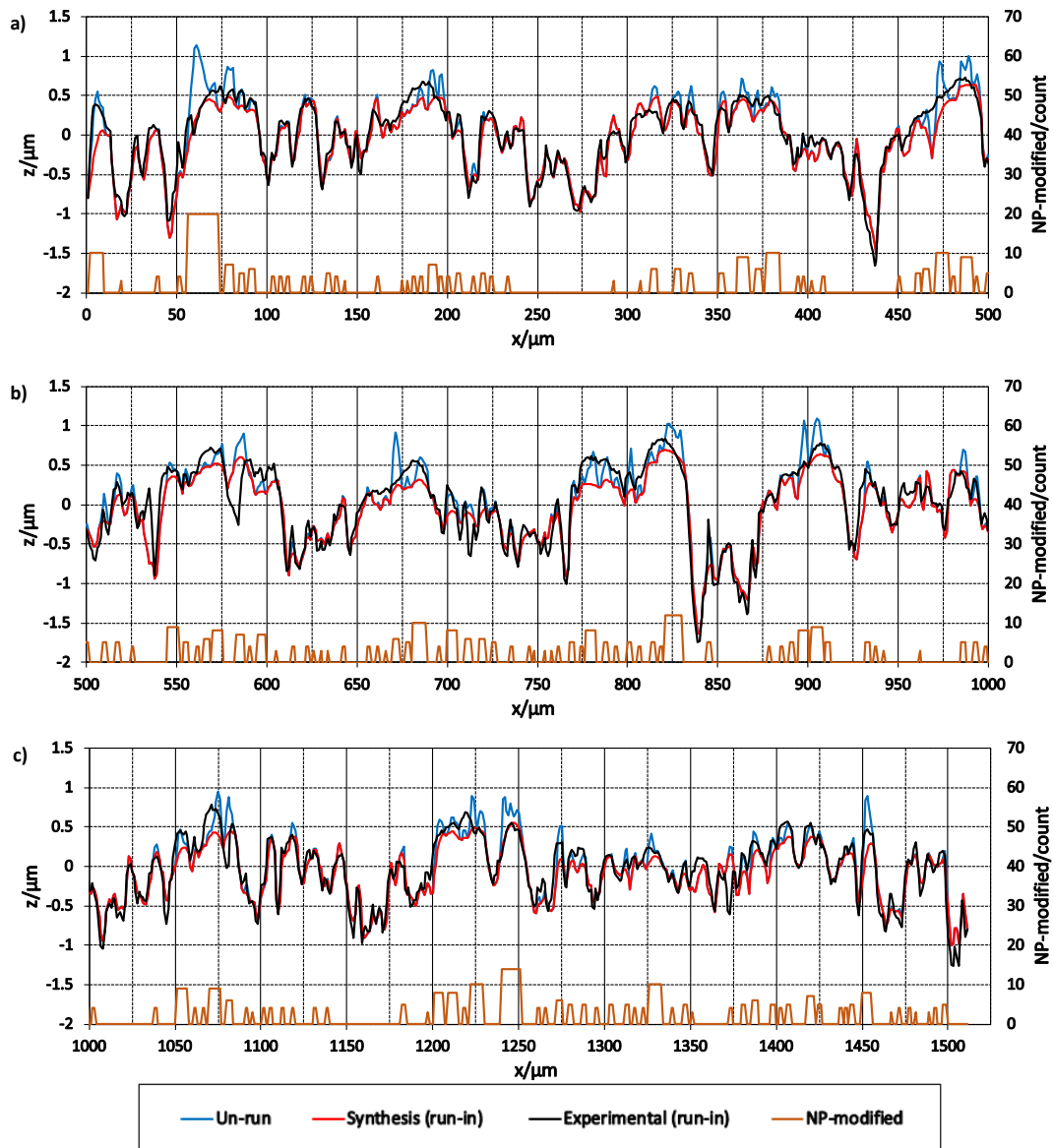


Figure 6.7 Un-run, synthesised and experimental run-in relocated profiles for the fast (pinion) surface for Profile Set Five.

6.4 Low Roughness Gears

6.4.1 Profile Set Six

This set of profiles corresponds to Analysis Point 1 of the low roughness surfaces produced by Process B. The same analysis was carried out for the Process B gears at the AP1 and AP2 gear points. The numerical analysis was carried out with the operating conditions given in Table 6.2. The transient EHL solution was converged at different surface hardness parameters of 3.5 GPa and 4 GPa for the fast and slow surfaces, respectively. The hardness for these surfaces is not known, and the different hardness levels specifies give the best match between the synthesised and experimental results. The AP1 results are presented in Figure 6.8 and Figure 6.9. It is seen that there is a good match between experimental and synthesised profiles. There is no micropitting seen in these surfaces.

There are some locations where the synthesised peaks are higher than the experimental peaks. This is seen at x positions 390, 510, 670, 685 and 1230 μm of the pinion surface, as shown in Figure 6.8, and also for the wheel surface at x positions 65, 270, 565, (650-805) μm , as shown in Figure 6.9. On the other hand, some locations have the opposite; the experimental peaks are higher than the synthesised peaks. This is seen at x positions 40, 275, 755, 800, 820, 1260, 1360 and 1380 μm of the pinion surface, as shown in Figure 6.8, and also for the wheel surface at x positions (80-135), (460-540) μm , as shown in Figure 6.9.

It can be seen that the shape of the pinion surface asperities has been modified more than those of the wheel surface for both the experimental and synthesised run-in surfaces, and some of them have merged to become one rounded asperity.

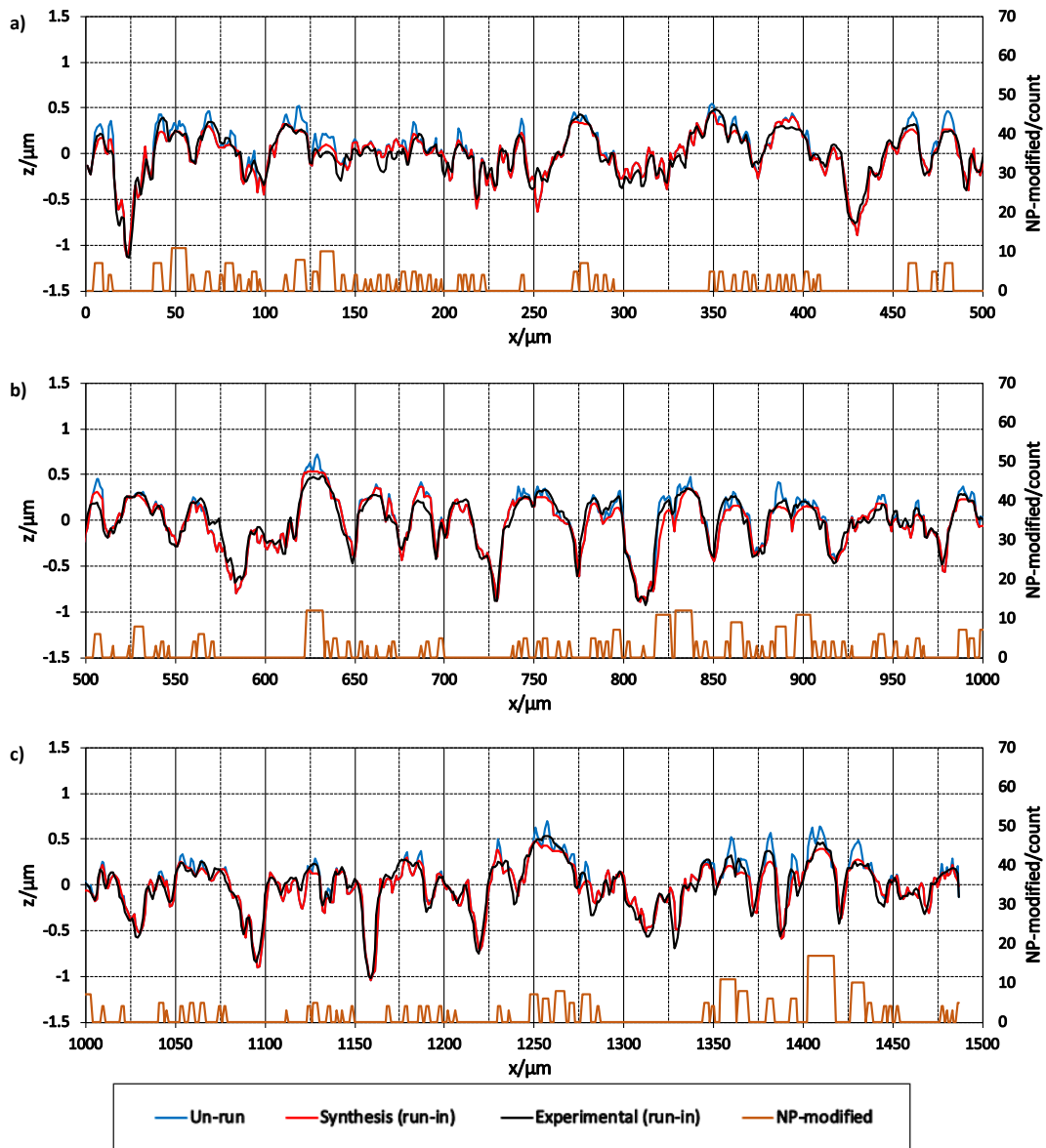


Figure 6.8 Un-run, synthesised and experimental run-in relocated profiles for the fast (wheel) surface for Profile Set Six.

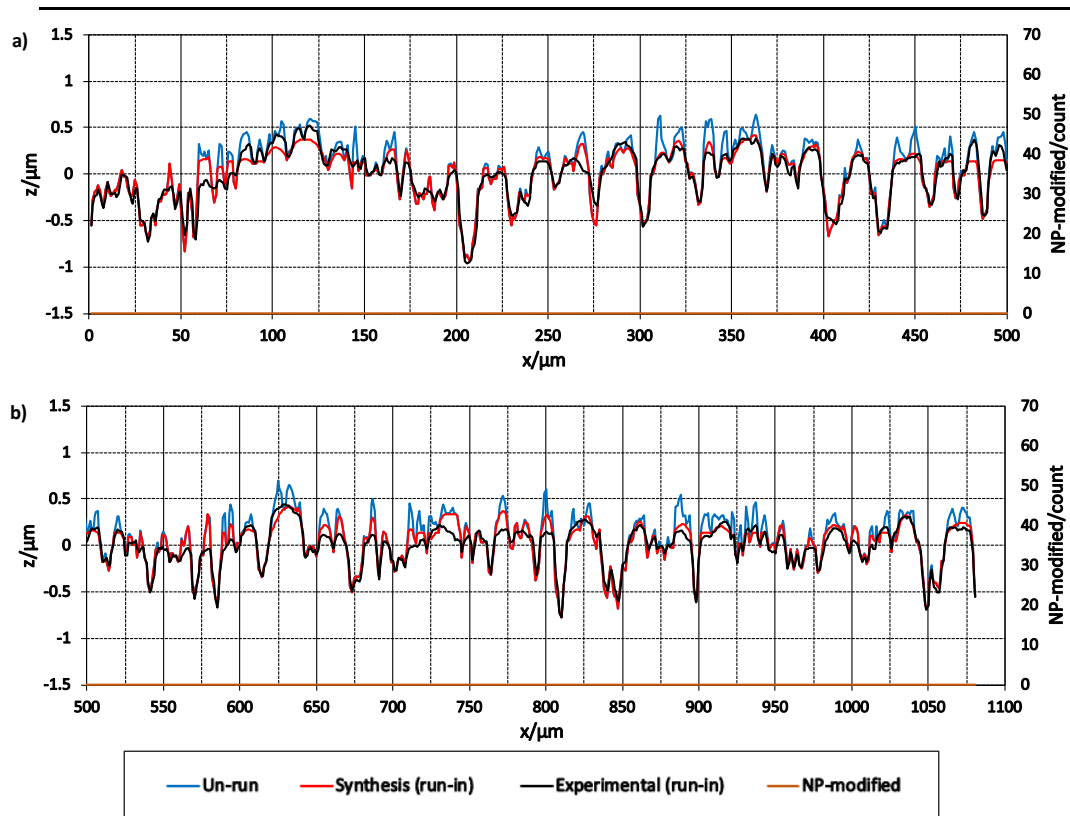


Figure 6.9 Un-run, synthesised and experimental run-in relocated profiles for the slow (pinion) surface for Profile Set Six.

6.4.2 Profile Set Seven

This set of profiles corresponds to Analysis Point 2 of the low roughness surfaces produced by Process B. The same analysis processes used for the AP2 high roughness gears were repeated for these profiles. The transient EHL synthesis solution was converged at a surface hardness level of 3.5 GPa. The results for the Process B gears at Point AP2 are shown in Figure 6.10 and Figure 6.11.

It can be seen that the wheel surface gear for AP1 was modified more than the pinion surface gear for both the experimental and synthesised run-in surfaces. In contrast, the opposite was seen in the Profile Set Seven results. The shape of asperities of the wheel surface have modified more than the pinion one and some of them have merged to become one rounded asperity. However, a good geometrical agreement was shown between the experimental profiles and those results obtained by numerical simulation.

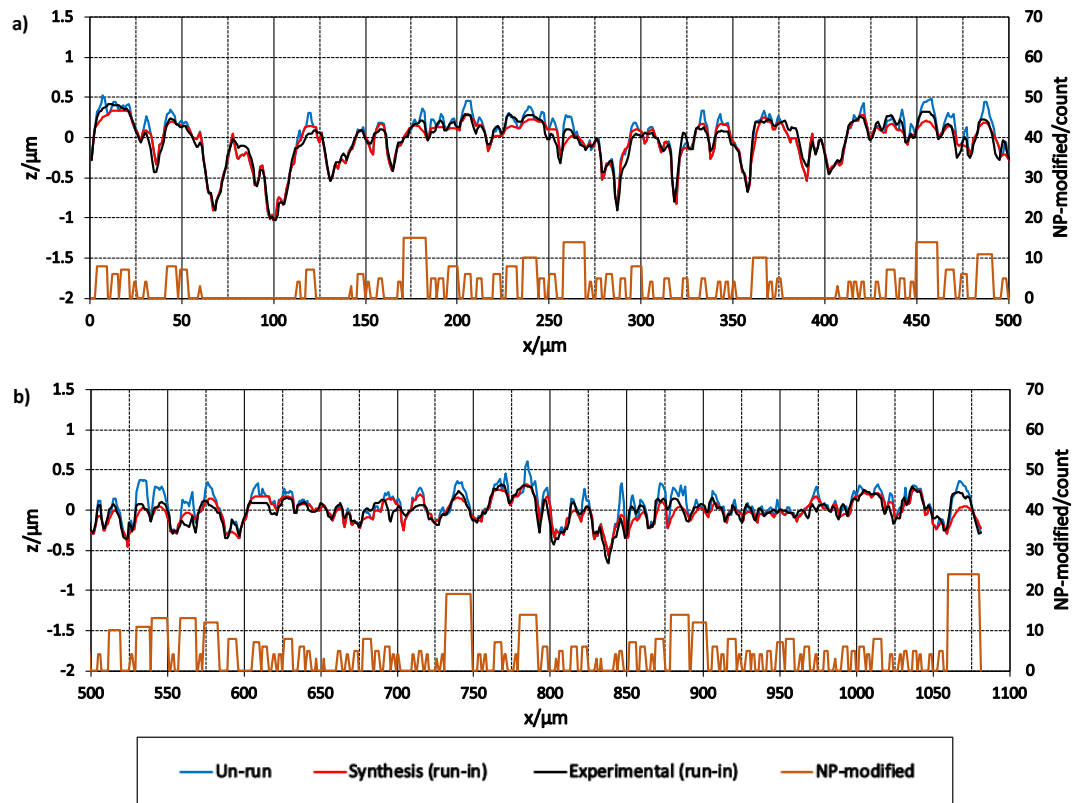


Figure 6.10 Un-run, synthesised and experimental run-in relocated profiles for the slow (wheel) surface for Profile Set Seven.

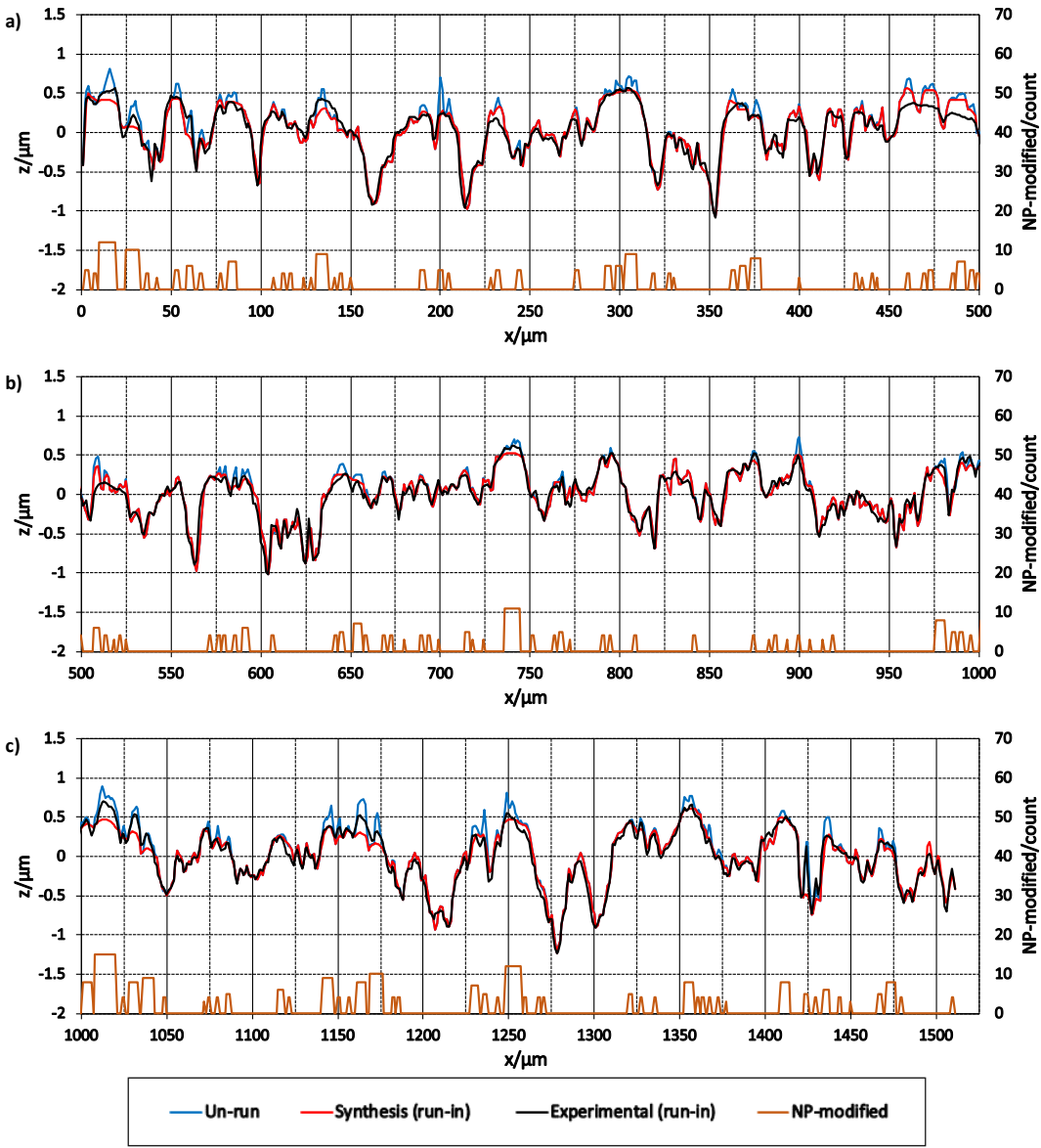


Figure 6.11 Un-run, synthesised and experimental run-in relocated profiles for the fast (pinion) surface of Profile Set Seven.

6.5 Profile Set Eight

Another two surface roughness profiles were obtained from the experimental work mentioned in Chapter 5. These profiles were taken from the fast disk (FD) and the slow disk (SD) in a twin disk rig test. 12mm profiles were taken at particular marked locations on the disk circumference in the as-manufactured condition. The test was then started for 6000 cycles with running in taking place during that time. The representative profiles used for EHL analysis were $2a$ long for both the fast and slow surfaces, and had a $0.5\mu\text{m}$ mesh spacing. The Hertz contact dimension was $a=0.402\text{mm}$ and the number of points in each representative profile was 1609. *Multiprofiles* were created for EHL analysis using 200 repeats for the fast disk and 160 repeats for the slow disk. The numerical analysis was carried out to the hardness level of 5 GPa at 162,071 timesteps and with the operating conditions given in Table 5.1.

The results were obtained using the running-in synthesis model, and compared with the corresponding profiles taken from the experiment after running-in. These results are shown in Figure 6.12 and Figure 6.13.

In general, there is a good agreement between the synthesised and corresponding experimental profiles. There are some aggressive asperities in the representative fast profile that became micropits after running-in for a relatively short time, and this is seen at x positions 250, 810 and 990 μm in Figure 6.12. The slow representative profile is less aggressive, and no micropits were seen at the end of running-in.

The shape of some asperities in both surfaces merged and became one wide and rounded asperity. In this synthesis some of these asperities have a value of the *NP-modified* parameter of about 50 points. However, a good geometrical agreement is shown between experimental and synthesised profiles.

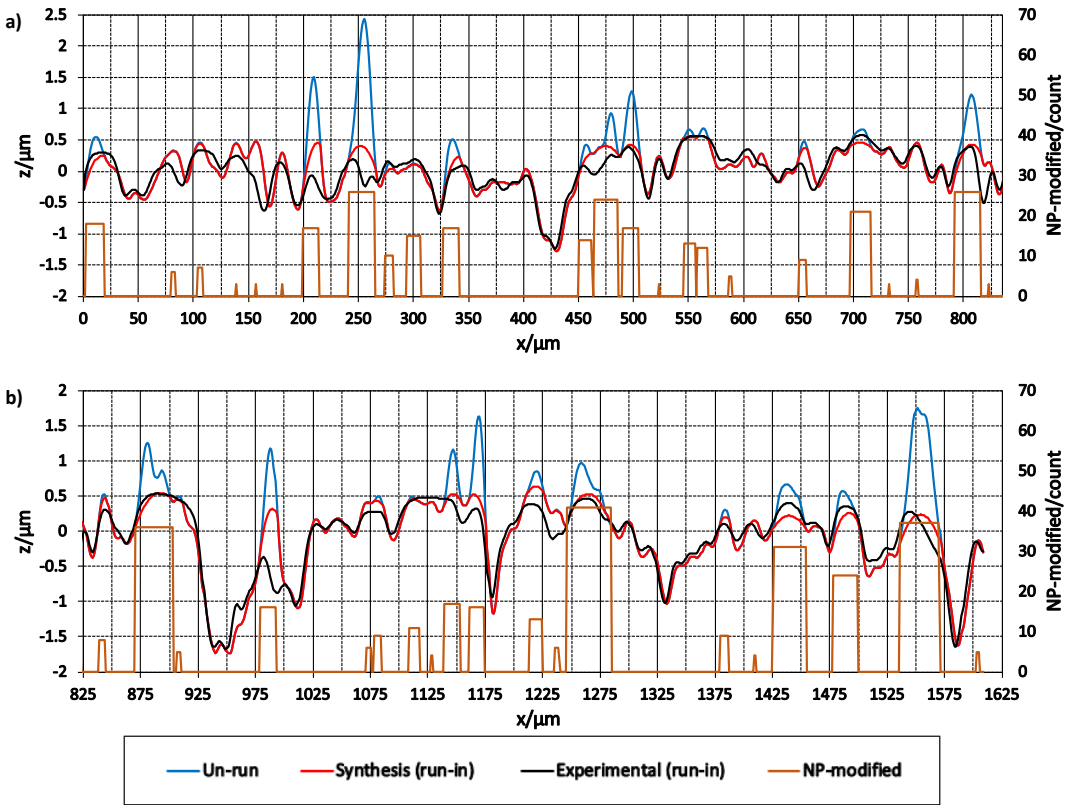


Figure 6.12 Un-run, synthesised and experimental run-in relocated profiles for the fast surface of Profile Set Eight.

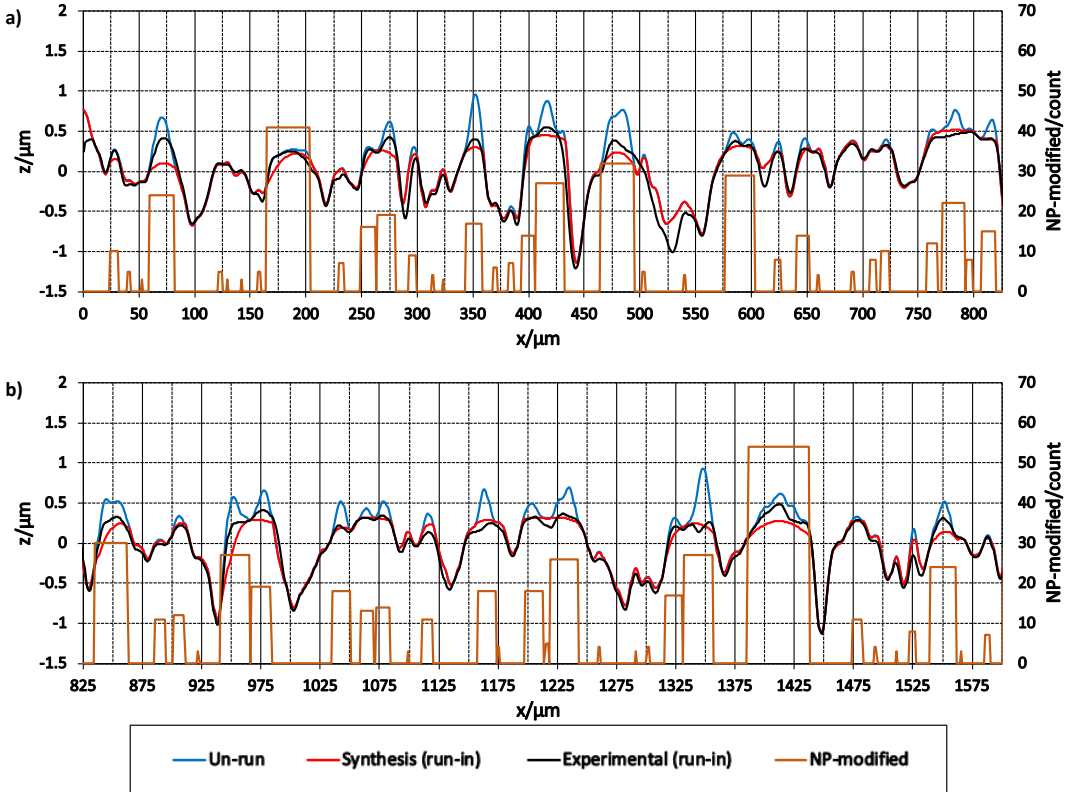


Figure 6.13 Un-run, synthesised and experimental run-in relocated profiles for the slow surface of Profile Set Eight.

6.6 Surface and near surface fatigue analysis.

Detailed results from the transient micro-EHL solutions can be used to predict high cycle fatigue damage in the vulnerable near-surface layer. The processes of predicting the fatigue life and accumulated damage were explained in detail in section 4.7. To present the calculated predicted fatigue based on the run-in surface roughness, Weibull damage distributions are used to quantify the damage for all the material points at a particular depth (d) beneath the surface as explained in section 4.7. The analysis is for a single meshing cycle (a single pass through the EHL contact). Logarithmic scales are used to allow a convenient graphical representation of the predicted damage in terms of contact cycles. The emphasis in this chapter is on the slower surfaces because they suffer more fatigue than the fast ones.

This study is interested in the way that micropits develop. The micropits detected at the surface have a depth of 2 μm or less. For the cases considered here $d/a = 0.005$ which is equal to about 2.4 μm and the material to that depth is the band of material that will be examined in detail. Micropitting seems to be associated with surface contact fatigue and plastic deformation on the scale of roughness asperities (Evans et al., 2012). The experimental work of Hutt et al. (2018) investigated micro pit formation and growth by considering how the mean height of the pitted and un-pitted points of the profiles changed during an endurance micropitting test consisting of 17 load stages. Profiles were measured at the same nominal position at the end of each load stage and relocated so that the deep valley features coincided.

Figure 6.14 shows the variation of the mean height of the surface measured with 5 profilometer traces taken in the circumferential direction. Each profile is about 11 mm long. The profiles were split into two groups of points, one where no micropitting occurred and the other where micropits were detected at same point during the test. The figure shows the evolution of the mean height of the two groups and the entire profiles over the test.

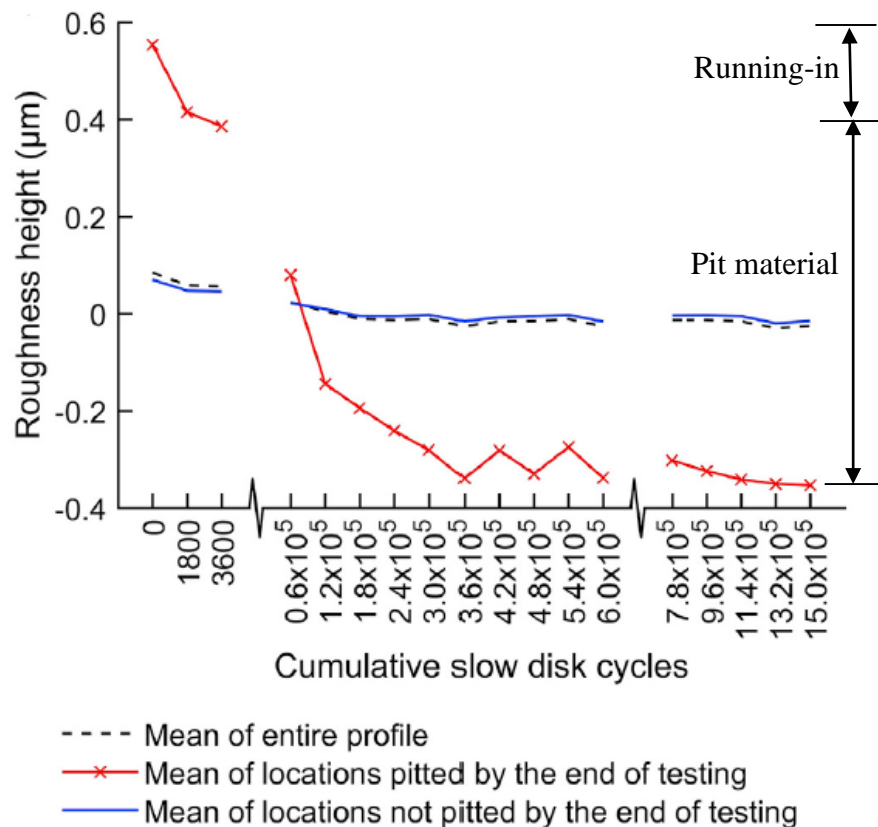


Figure 6.14 Comparison of the change in mean roughness height for locations that had pitted by the end of the test and those that had not. Calculations using five axial profile positions within the contact path for the slow surface (Hutt et al., 2018).

The mean height of the unpitted points is very close to that of the entire profile, falling gently from 0.08 to 0 μm . The red line of the mean height of pitted points is initially high during the running-in process, since pits tend to form at the locations of aggressive asperities. By cycle 300,000 their mean height has stabilised about 0.3 μm below the mean height of the un-pitted points. It can be concluded that on average the pits have a depth of 0.3 μm below the mean height of the surface.

For these reasons, and because of the focus on near surface damage, the primary curves of interest are these between the surface and depth $d/a = 0.005$ which is about 2.4 μm .

The cumulative Weibull distributions are manipulated to give life curves of the form shown in Figure 6.15. Each curve corresponds to the accumulated damage at the specified depth for example, for $d/a = 0.005$, 10 % is predicted to experience fatigue damage by 10^6 cycles, and 50 % by 10^7 cycles. There is a clear sensitivity to depth with the $d/a = 0.002$ curve showing a 10-fold increase in life in comparison, and the $d/a = 0.001$ curve a hundred-fold increase.

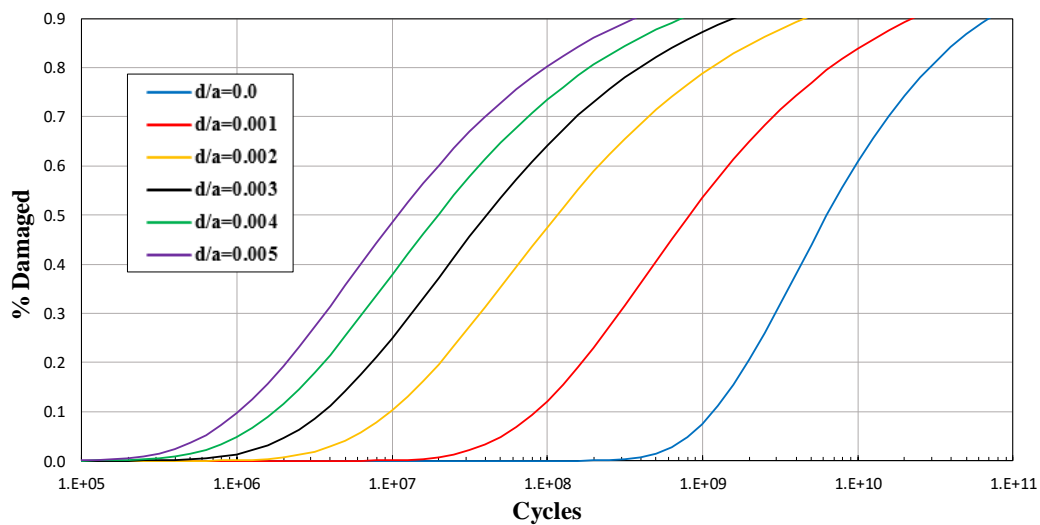


Figure 6.15 Cumulative damage distributions at a series of particular depths d/a beneath the surface.

Note that the % Damaged value is the percentage of points at that level that are predicted to have fatigue damage. This description should not be confused with the calculated damage D defined in equation (4.1).

6.7 Comparison between the predicted damage for the synthesised and measured surfaces

Life curves in the form shown in Figure 6.15 were obtained for each analysis at a series of five depth levels, and are given in Figure 6.17, 6.16, 6.17, 6.18 and 6.19 to show the predicted damage comparison between synthesised and experimental run-in surfaces at the surface and the near surface layers at depths of $d/a = 0, 0.001, 0.002, 0.003, 0.004$ and 0.005 . In all these results, those for the experimental surfaces reach the 20% damage level before the synthesised ones. The difference between experimental and synthesised profiles is not constant. In some cases, it is maintained and the other cases the curves cross. In order to make comparison between the experimental and synthesised curves, a life offset (ΔL), and a damage offset (ΔD) are defined.

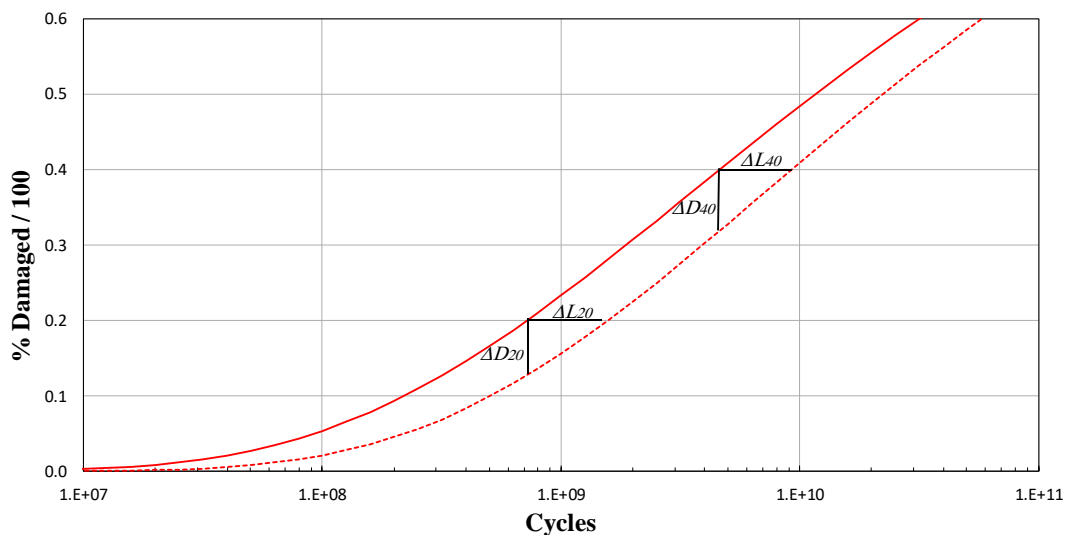


Figure 6.16 Shows the life offset (ΔL), and a damage offset (ΔD) at two damage levels, 20% and 40%.

These are illustrated in Figure 6.16 and are measured from a specified point on the experimental profile fatigue curve, 20% for example. ΔL_{20} is the additional life calculated for the synthesised profile at the same damage level. In this example:

$$\Delta L_{20} = \log(1.8 \cdot 10^9) - \log(7.3 \cdot 10^8) = \log(1.8 \cdot 10^9 / 7.3 \cdot 10^8) = 0.39.$$

The additional life is $10^{0.39}$, i.e. a factor of 2.45. So that the units of ΔL are orders of magnitude (OOM). ΔD_{20} is the reduction in damage for the same number of cycles. In general, it is found that ΔL and ΔD are positive during the initial damage phase.

20% damage is a good level to make the comparison because both curves tend to be parallel at that damage level.

The fatigue analysis procedure was conducted for Profile Set One as described in section 2.3 for both the measured and synthesised run-in profiles in order to allow like with like comparisons to be made. The comparison is made with the same nominal clearance, and the load difference was less than 0.2 % of the nominal load applied. The predicted damage results of the measured and synthesised profiles are compared and presented in Figure 6.17.

It is clear that all curves have the characteristic (s) shape of these cumulative distributions. The curves show that calculated damage is greatest at the level of $d/a = 0.005$ for both synthesised and experimental surfaces. At greater depth of $d/a = 0.01$, the predicted damage is lower. The synthesised profiles have less calculated damage than the experimental ones in each case at any given number of cycles with an offset of up to 10 % in the calculated damage.

The predicted damage starts to occur after about 10^5 cycles at the $d/a = 0.005$ level for both types of surface. At the $d/a = 0.005$ for the measured surface, 20% of material points experience calculated damage by 3×10^6 cycles, while about 5% of material at a depth of $d/a = 0.002$ is calculated to be damaged at the same number of cycles.

At the 20% damage level of the measured surfaces as shown in Figure 6.17a, the life differences between the $d/a = 0$ and $d/a = 0.001$ curves are more than 3 orders of magnitude. The life difference between the $d/a = 0.001$ and $d/a = 0.002$ is 1.49 orders of magnitude, and between the $d/a = 0.002$ and $d/a = 0.003$ is 0.59 orders of magnitude. Subsequently, the curves become close to each other between $d/a = 0.003$, 0.004 and 0.005.

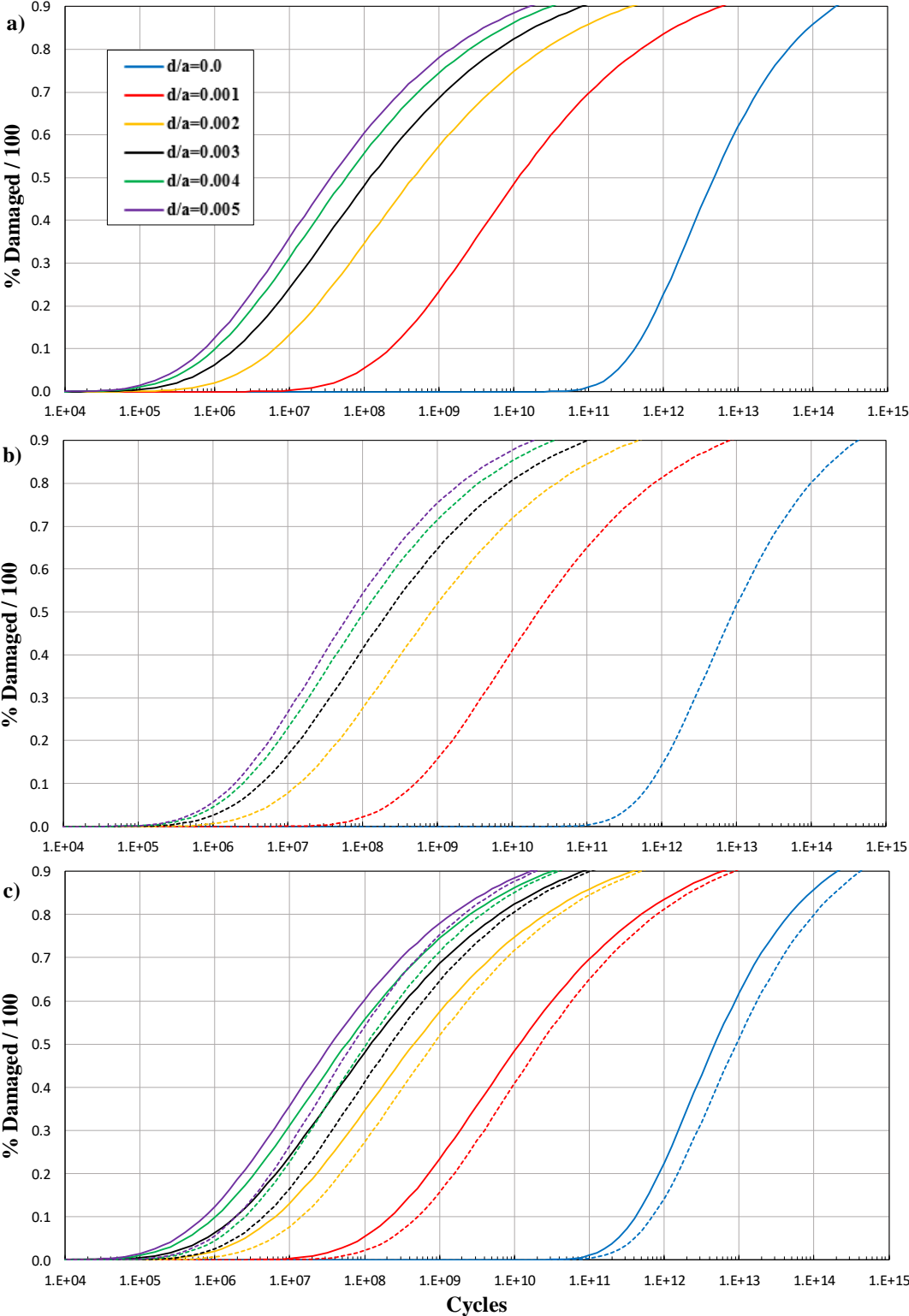


Figure 6.17 Cumulative damage distributions for the slower surface of Profile Set One at a series of depths below the surface. The solid lines are for the experimental profiles, and the dashed lines are for the synthesised profiles. Hertz dimension, $a = 468 \mu\text{m}$.

The life differences of the synthesised surfaces as shown in Figure 6.17b are similar to those for the experimental surfaces. There are 3 orders of magnitude in life difference between $d/a = 0$ and 0.001, 1.5 orders of magnitude difference between $d/a = 0.001$ and 0.002, and 0.49 orders of magnitude difference between $d/a = 0.002$ and 0.003. The differences became small between $d/a = 0.003$, 0.004 and 0.005. The synthesised curves are clearly offset to the right of the experimental ones, and the comparison is made in Figure 6.17c. The offsets between curves at the same depth are quite similar, and this is borne out by the ΔD_{20} and ΔL_{20} figures given in Table 6.3.

Table 6.4 Percentage damage offset and life offset at 20% damage for slow surface of Profile Set One.

Depth level (d/a)	ΔD_{20} %	ΔL_{20} (OOM)
0	8.6	0.29
0.001	6.4	0.31
0.002	5.7	0.29
0.003	7.3	0.4
0.004	7.5	0.4
0.005	8.5	0.4

The predicted damage results for Profile Set Four as described in section 6.2.1 for both the measured and synthesised run-in profiles are compared and presented in Figure 6.18.

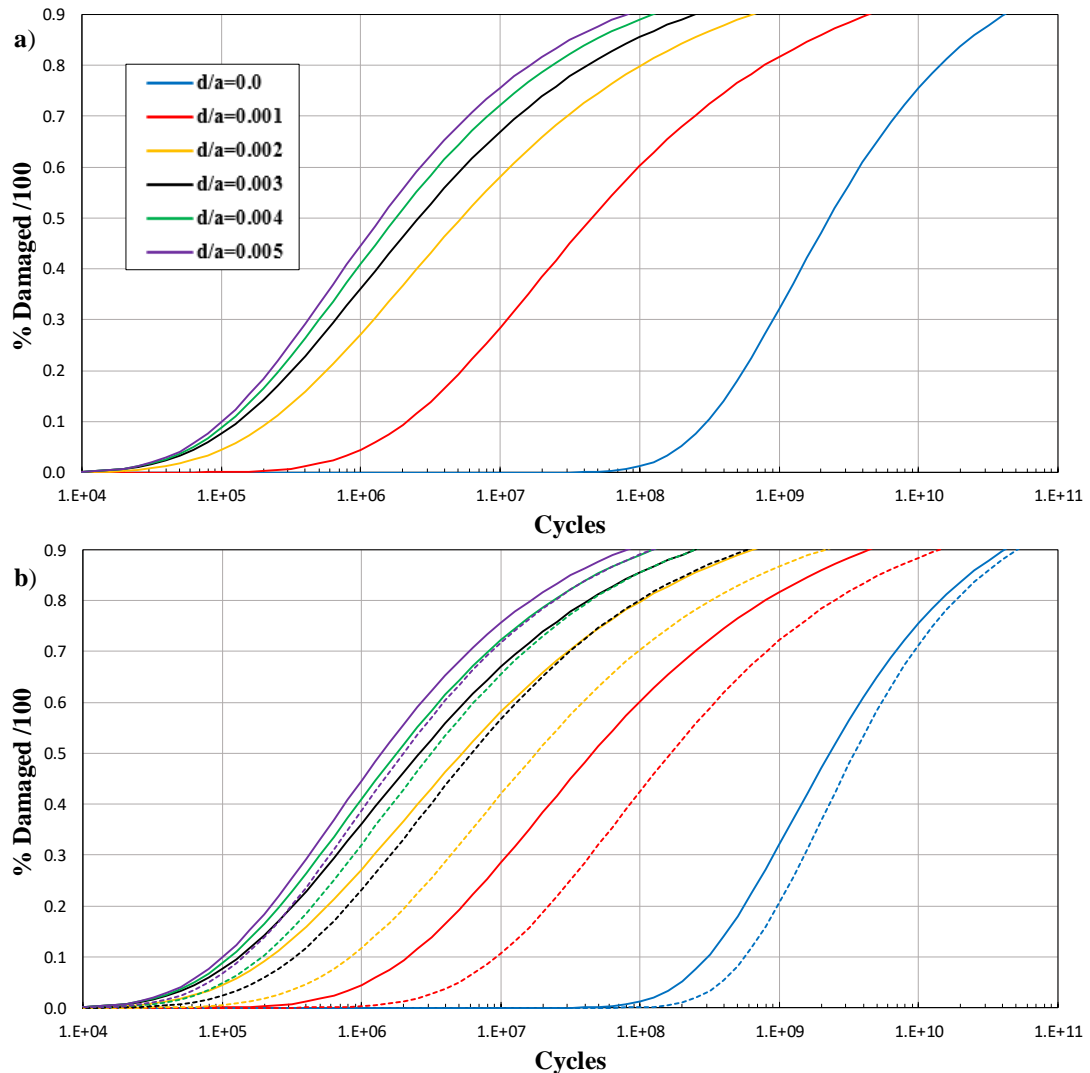


Figure 6.18 Cumulative damage distributions for the slower surface of Profile Set Four at a series of depths below the surface. The solid lines are for the experimental profiles, and the dashed lines are for the synthesised profiles. Hertz dimension, $a = 466 \mu\text{m}$.

The micropitting damage predicted started to occur after about $3 \cdot 10^4$ cycles at the $d/a = 0.005$ level for both synthesised and experimental surfaces. At this depth for the measured surface 20% of material points experience calculated damage by $2 \cdot 10^5$ cycles, while 10% of material at a depth of $d/a = 0.002$ is calculated to be damaged at the same number of cycles.

At the 20% damage level of the measured surfaces as shown in Figure 6.18a, the life differences between successive solid curves from $d/a = 0$ to $d/a = 0.005$ are order of magnitude factors of 2, 1, 0.2, 0.1 and 0.1, respectively. The synthesised profile curves are clearly offset to the right of the experimental ones in the comparison made in Figure 6.18b. The life differences of the synthesised surfaces are similar to those for the experimental ones for some curves and different for others. The differences between successive dashed curves from $d/a = 0$ to $d/a = 0.005$ are OOM factors of 1.7, 1, 0.4, 0.3 and 0.1, respectively.

The offsets between the experimental and synthesised curves at the same depth are quite similar at depth $d/a = 0, 0.003, 0.004$ and 0.005 , and this is confirmed by the ΔD_{20} and ΔL_{20} figures given in Table 6.5

Table 6.5 Percentage damage offset and life offset at 20% damage for slow surface of Profile Set Four.

Depth level (d/a)	ΔD_{20} %	ΔL_{20} (OOM)
0	9.8	0.3
0.001	14.2	0.6
0.002	12.4	0.6
0.003	10.5	0.4
0.004	6.7	0.2
0.005	4.5	0.2

The procedure of calculating predicted damage was repeated for the high roughness surfaces of Profile Set Five as explained in section 6.2.2, and the results for both the experimental and corresponding synthesised surfaces are shown in Figure 6.19. The micropitting damage predicted started to occur by 1.1×10^4 cycles at the $d/a = 0.005$ level for both surface cases.

For the $d/a = 0.005$ measured surface depth 20% of material points experience calculated damage by 6.3×10^4 cycles, while 2.5% of material at a depth of $d/a = 0.002$ was calculated to be damaged at the same number of cycles.

At the 20% damage level of the measured surfaces as shown in Figure 6.19a, the life differences between successive solid curves from $d/a = 0$ to $d/a = 0.005$ are OOM factors of 1.8, 1, 0.4, 0.2 and 0.1, respectively. The life differences of the synthesised surfaces as shown in Figure 6.19b are quite similar to the experimental ones, the differences between successive dashed curves from $d/a = 0$ to $d/a = 0.005$ are OOM factors of 1.78, 1, 0.4, 0.2 and 0.1, respectively.

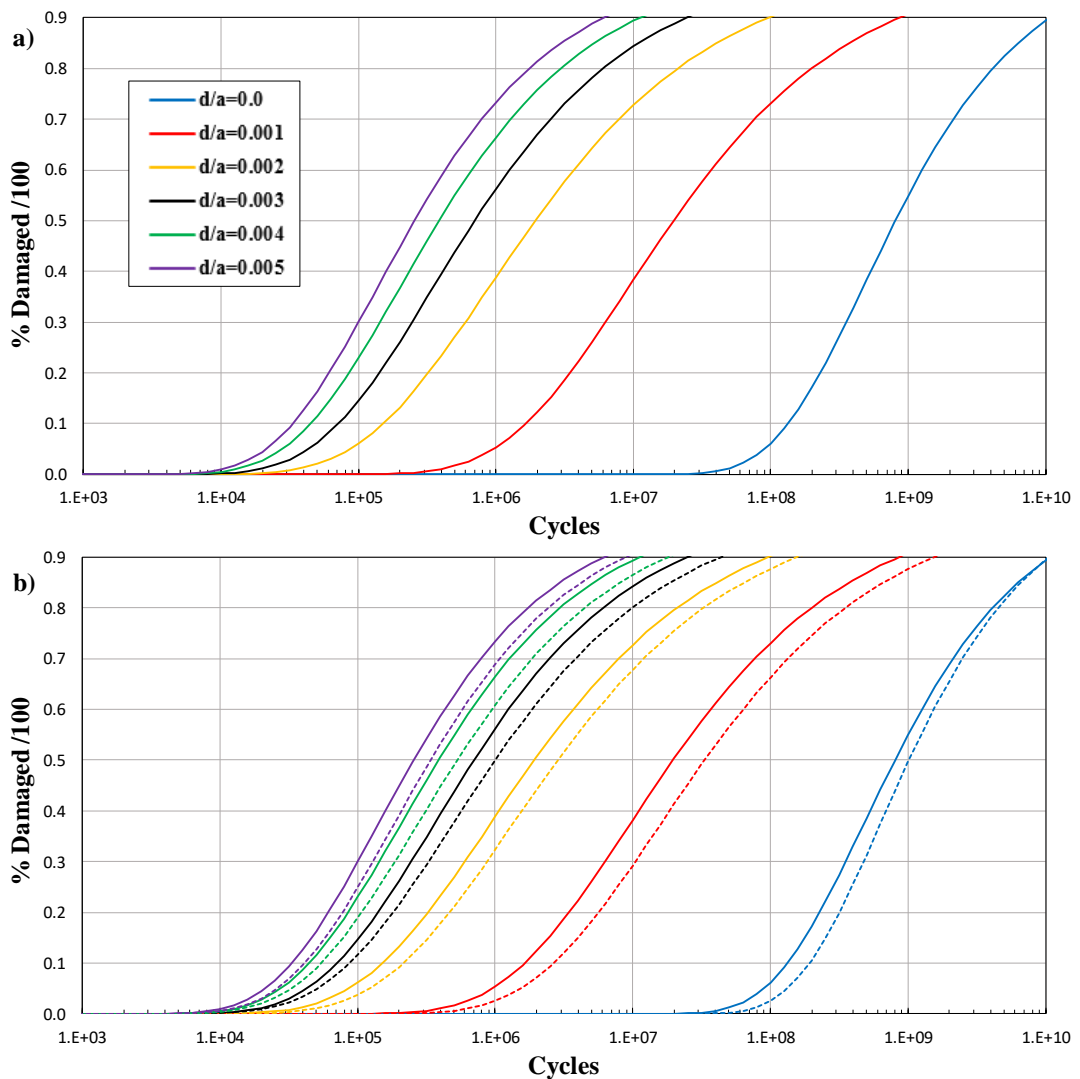


Figure 6.19 Cumulative damage distributions for the slower surface of Profile Set Five at a series of depths below the surface. The solid lines are for the experimental profiles, and the dashed lines are for the synthesised profiles. Hertz dimension, $a = 469 \mu\text{m}$.

The offsets between the experimental and synthesised curves at the same depth are similar, and this is seen in the ΔD_{20} and ΔL_{20} figures given in Table 6.6.

Table 6.6 Percentage damage offset and life offset at 20% damage for slow surface of Profile Set Five.

Depth level (d/a)	ΔD_{20} %	ΔL_{20} (OOM)
0	6.5	0.19
0.001	6.7	0.2
0.002	5	0.1
0.003	3.5	0.1
0.004	3.6	0.1
0.005	3.9	0.1

The calculated damage for the small roughness surfaces of Profile Set Six as explained in section 6.3.1 was obtained for both the experimental and the corresponding synthesised surfaces and the results are shown in Figure 6.20. In general, the synthesised profile has less fatigue than the measured one in each case at any given number of cycles.

There is more damage calculated for the experimental surface than the synthesised one. The predicted damage starts to occur by $2 \cdot 10^5$ cycles at the $d/a = 0.005$ level for the measured profiles and by 10^6 cycles for the synthesised ones.

At the $d/a = 0.005$ of measured surface 20% of material points experience calculated damage by $2.1 \cdot 10^6$ cycles, while the material at a depth of $d/a = 0.002$ does not experience fatigue at the same number of cycles.

At the 20% damage level for the measured surfaces, the life differences between successive solid curves from $d/a = 0$ to $d/a = 0.005$ are order of magnitude factors of 1.1, 0.9, 0.5, 0.3 and 0.2, respectively. The synthesised curves are clearly offset to the right of the experimental ones in the comparison made in Figure 6.20b. The life differences of the synthesised profiles are slightly different to the experimental ones.

The differences between successive dashed curves from $d/a = 0$ to $d/a = 0.005$ are OOM factors of 1.2, 1, 0.4, 0.2 and 0.2, respectively.

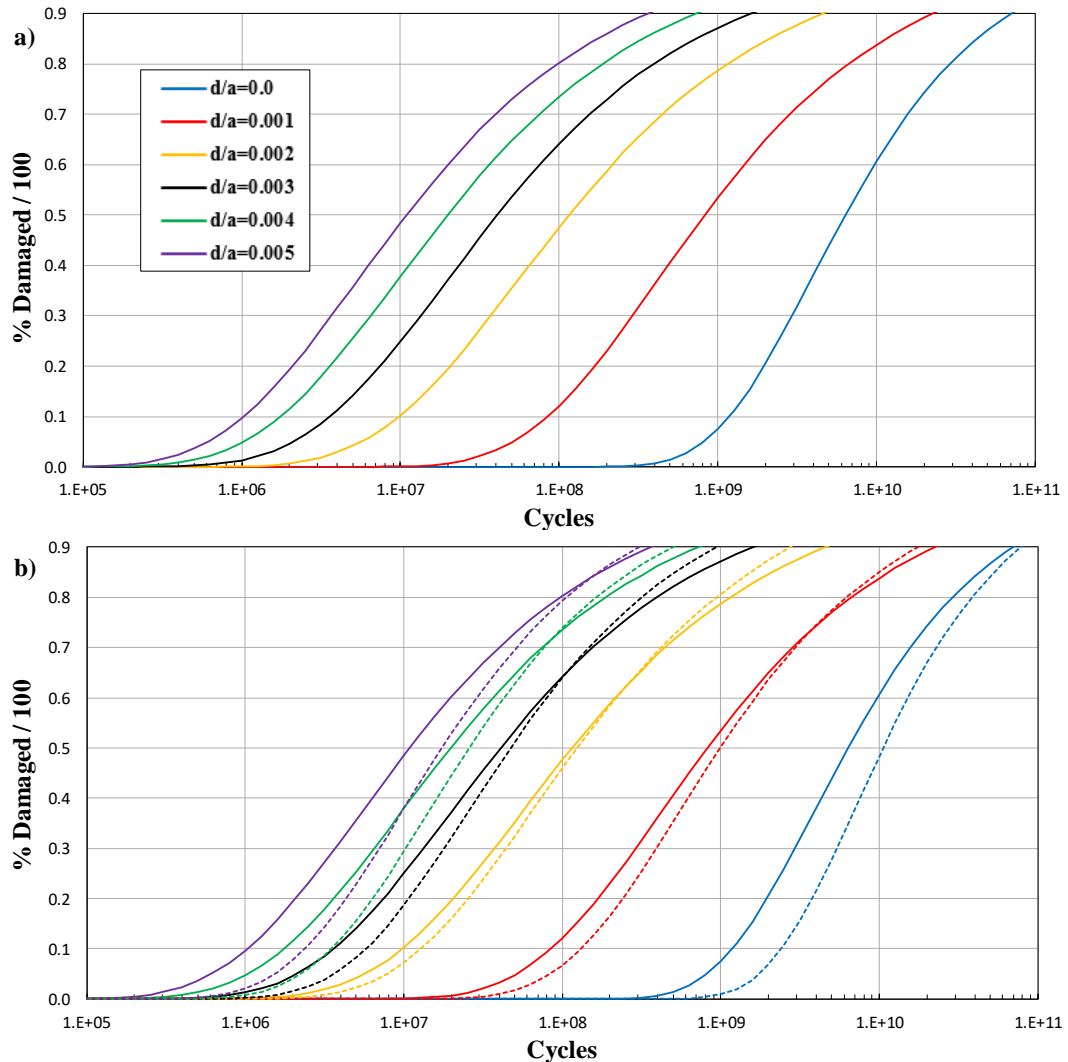


Figure 6.20 Cumulative damage distributions for the slower surface of Profile Set Six at a series of depths below the surface. The solid lines are for the experimental profiles, and the dashed lines are for the synthesised profiles. Hertz dimension, $a = 466 \mu\text{m}$.

The offsets between the solid and dashed curves at the same depth are small at depths $d/a = 0.001, 0.002$ and 0.003 , and this is again borne out by the ΔD_{20} and ΔL_{20} figures given in Table 6.7.

The differences of the life and the damage offset are reasonably small. It can be seen that the level of $d/a = 0.002$ gave the smaller value of ΔD_{20} and ΔL_{20} than other depth

levels. In contrast, the level of $d/a = 0$ and 0.005 has higher differences of the ΔD_{20} and ΔL_{20} .

Table 6.7 Percentage damage offset and life offset at 20% damage for slow surface of Profile Set Six.

Depth level (d/a)	ΔD_{20} %	ΔL_{20} (OOM)
0	13.6	0.3
0.001	6.3	0.2
0.002	3.5	0.1
0.003	6.2	0.2
0.004	10	0.29
0.005	11.6	0.3

The same procedure of fatigue analysis above was applied for the small roughness of Profile Set Seven as explained in section 6.3.2 for the case of measured and the synthesised surfaces and the results are presented in Figure 6.21. The predicted micropits started to occur by 10^5 cycles at the $d/a = 0.005$ level for both cases of surfaces.

It can be seen from Figure 6.21b that the curves for experimental and synthesised roughness profiles at $d/a = 0, 0.001,$ and 0.003 are clearly offset to the right at low damage levels and then they cross each other as the damage level increases.

At $d/a = 0.005$ for the measured surface analysis 20% of material points experience calculated damage by 5×10^5 cycles, while 0.19% of material at a depth of $d/a = 0.002$ is calculated to be damaged at the same number of cycles.

At the 20% damage level of the measured surfaces, the life differences between successive solid curves from $d/a = 0$ to $d/a = 0.005$ are OOM factors of 1.4, 1, 0.4, 0.29 and 0.2, respectively. The corresponding life differences for the synthesised profiles are very similar to those for the experimental ones.

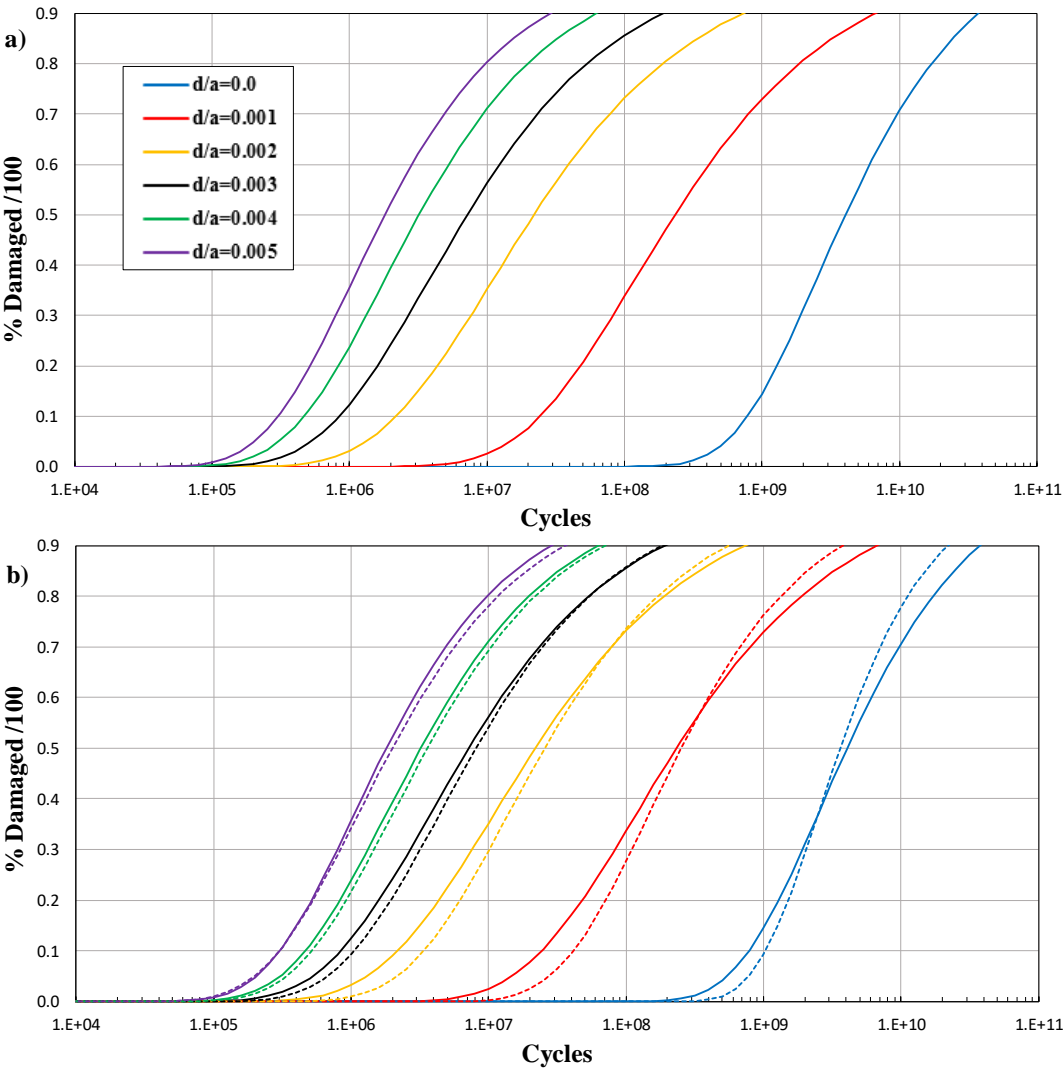


Figure 6.21 Cumulative damage distributions for the slower surface of Profile Set Seven at a series of depths below the surface. The solid lines are for the experimental profiles, and the dashed lines are for the synthesised profiles. Hertz dimension, $a = 469 \mu\text{m}$.

The offsets between the solid and dashed curves at the same depth are quite similar, and this is seen in the ΔD_{20} and ΔL_{20} figures given in Table 6.8. It can be noticed that the calculated damage for the experimental and synthesised surfaces at the depths of $d/a = 0.005$ and 0.004 are quite similar, while there is a minor life difference at the depths of $d/a = 0.003$.

Table 6.8 Percentage damage offset and life offset at 20% damage for slow surface of Profile Set Seven.

Depth level (d/a)	ΔD_{20} %	ΔL_{20} (OOM)
0	4.7	0.1
0.001	7.6	0.2
0.002	6.1	0.2
0.003	3.4	0.1
0.004	1.2	0.04
0.005	0	0

In general, for all four sets of the gear surface profiles analysed and reported above, the differences between the calculated damage of the synthesised analysis and the real surfaces analysis are an offset in the damage curves which correspond to small orders magnitude but with both cases showing the same behaviour. The synthesised surfaces are at least showing the right effect in terms of sensitivity of surface roughness.

In considering these differences, it can be argued that they can be expected. A better fit cannot be achieved as there is a different interaction between the real contact profiles and the simulation ones. Each tooth in the real contact interacts with 20 different tooth surfaces of the meshing gear and this forms the final surfaces. In contrast in the synthesised method, the profile only interacts with one repeated surface. To reduce this difference in counterforce interaction it would be possible to measure all 20 of these teeth and bring them into the interaction with the current tooth. The interaction between real contact disks is different to the real gear interactions and depends on the value of slide roll ratio. For example, for the slide roll ratio of 0.25,

each point on the fast surface interacts with three points on the slow one, and each point on the slow surface interacts with five points on the fast surface.

The difficulties in measuring the true interaction of the disk profiles in terms of counterface alignment are considerable and at the current stage of development it was not possible to incorporate this effect. The profiles of the gears were measured on a small number of teeth in the experiment which again limited the scope for a more representative interaction regime to be implemented.

A further difference is that the synthesised approach does not respond to micropits that develop during the test. The model does not create micropits while there are many micropits in the real surfaces. As this pitting develops the load is redistributed, and it can be expected that some points carry a higher load as a result, with others carrying a lower load.

Prediction of micropitting with the current approach is therefore focused on the onset of micropitting and its initial rate of growth.

6.8 Comparison between the high and small roughnesses for gear profiles

An investigation into the high and small roughness gear profiles for Analysis Points 1 and 2 was made in terms of the cumulative Weibull damage distributions in order to examine the sensitivity of the simulation method and compare the results for both cases. A comparison between the Analysis Point 1 profiles of set four and set six was carried out. A further comparison between the Analysis Point 2 profiles of set five and set seven was also made. In both cases the analyses were carried out for the measured run-in profiles and also for synthesised profiles, and compared in terms of the fatigue analysis results. The results for these cases of profiles are shown in Figure 6.22 to Figure 6.25.

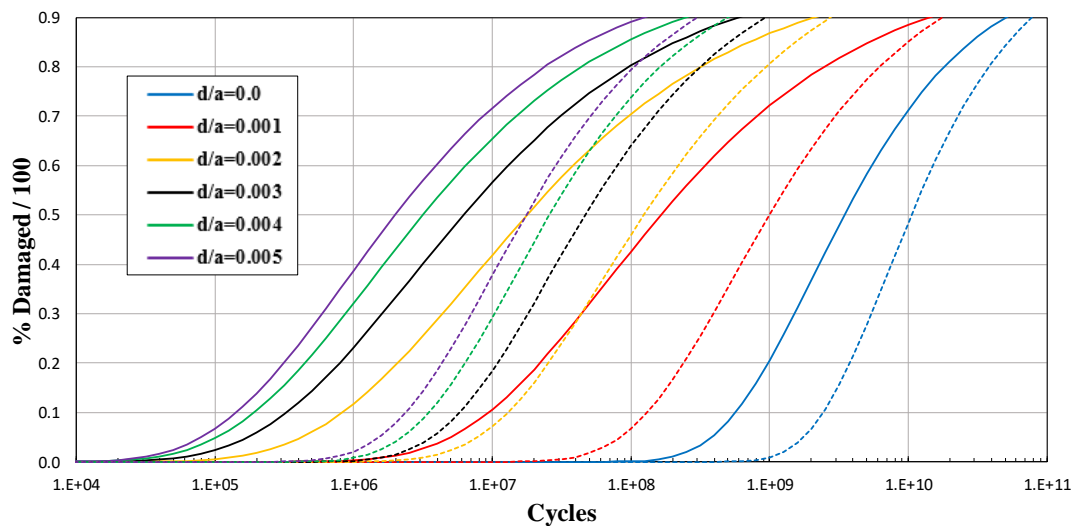


Figure 6.22 Comparison of the Weibull cumulative damage distribution curves for the synthesised slow surfaces of high (solid curves) and low (broken curves) roughness for Analysis Point 1.

Figure 6.22 shows the slow surface results for the synthesised surfaces with high and low roughnesses for Analysis Point 1 conditions. It can be seen that the high roughness surfaces have much higher calculated damage than the small roughness surfaces at all depth levels. The solid and dashed curves have the same characteristic (s) shapes.

At the 20% damage level, the solid curves for high roughness are offset from the corresponding low roughness curves by approximately the same amount of 1 OOM. Depth $d/a=0$ is the exception to this with an offset of 0.6 OOM.

The predicted micropitting damage starts to occur after $1.3 \cdot 10^4$ cycles at a depth of $d/a = 0.005$ level for the high roughness surfaces, while the calculated failure of the small roughness surfaces starts to occur after 10^6 cycles at the same depth. It is also noticed that the predicted damage for the high roughness surfaces at a depth of $d/a = 0.001$ is similar to that for the low roughnesses surfaces at a depth of $d/a = 0.002$.

The corresponding results for the experimental slow surface profiles with high and low roughnesses for Analysis Point 1 are shown in Figure 6.23. It can be seen that the experimental profile results gave similar behaviour to the synthesised surface results for Analysis Point 1. The high roughness surface has much higher calculated damage than the small roughnesses. At the 20% damage level of the high roughness and low roughness measured surfaces, the life differences between successive solid and dashed curves from $d/a = 0$ to $d/a = 0.005$ are orders of magnitude factors of 0.6, 1.5, 1.6, 1.4, 1.1 and 1, respectively.

The predicted micropitting damage starts to occur after $2 \cdot 10^4$ cycles at the $d/a = 0.005$ level for the high roughness surface, while the calculated damage of the small roughness surfaces starts to occur after $3 \cdot 10^5$ cycles at the same depth. It is clear that the predicted damage of the solid curve at a depth of $d/a = 0.001$ close to the broken curve $d/a = 0.003$.

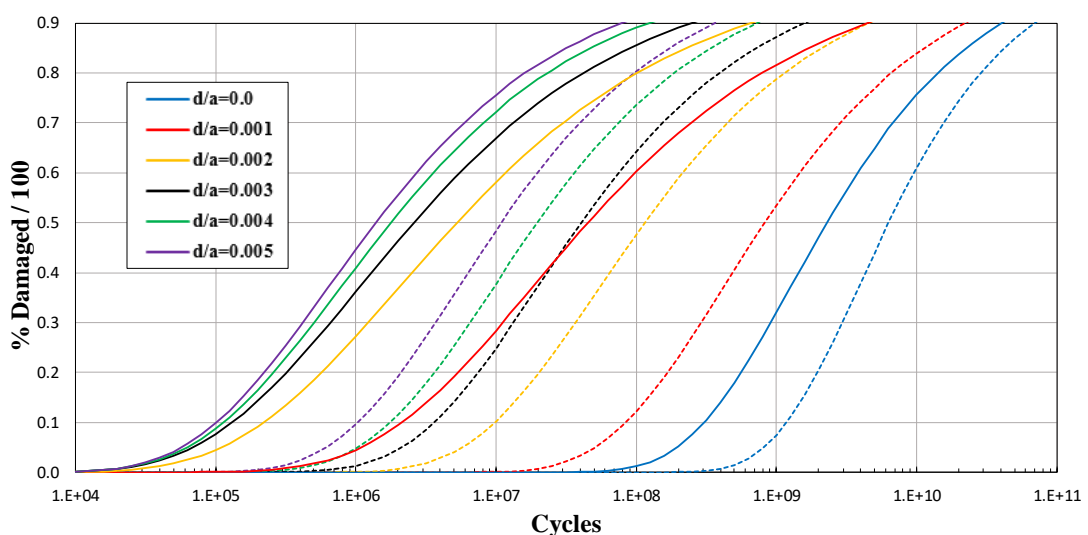


Figure 6.23 Comparison of the Weibull cumulative damage distribution curves for the experimental slow surfaces of high (solid curves) and low (broken curves) roughness for the Analysis Point 1.

The same comparisons were made for Analysis Point 2 conditions. The results are shown in Figure 6.24 and Figure 6.25 and again it is clear that the high roughness surfaces have a greater damage than the low roughness surfaces, for the case of both the synthesised and the experimental profiles. The results shown are quite similar between the two cases. For example, the micropitting damage predicted starts to occur about 1.5×10^4 cycles at the $d/a = 0.005$ level for the high roughness surfaces, and after about 10^5 cycles at the same depth for the small roughness surfaces for both the experimental and synthesised cases.

At the 20% damage level of the high and low roughness synthesised surfaces in Figure 6.24, the life differences between successive solid and dashed curves from $d/a = 0$ to $d/a = 0.005$ are orders of magnitude factors of 0.7, 1, 1.1, 1.1, 1 and 0.8, respectively.

At the 20% damage level of the high and low roughness measured surfaces in Figure 6.25, the life differences between successive solid and dashed curves from $d/a = 0$ to $d/a = 0.005$ are orders of magnitude factors of 0.8, 1.2, 1.1, 1.1, 1 and 0.9, respectively.

The predicted damage at the depth level of $d/a = 0.001$ for the high roughness surfaces gave quite similar damage to the small roughness surfaces at $d/a = 0.002$ in both figures. It can be noticed that there is just one clear difference between Figure 6.24 and Figure 6.25 which is that the solid yellow curve crosses the dotted purple curve in different places. They cross each other at higher damage level for the experimental profiles compared with the synthesised ones. Otherwise, the figures are very similar.

The comparison between the synthesised and experimental surface results of Analysis Point 2 are better than the results of Analysis Point 1. Overall, the synthesised method produced similar behaviour to the measured experimental profile results with a different offset magnitude.

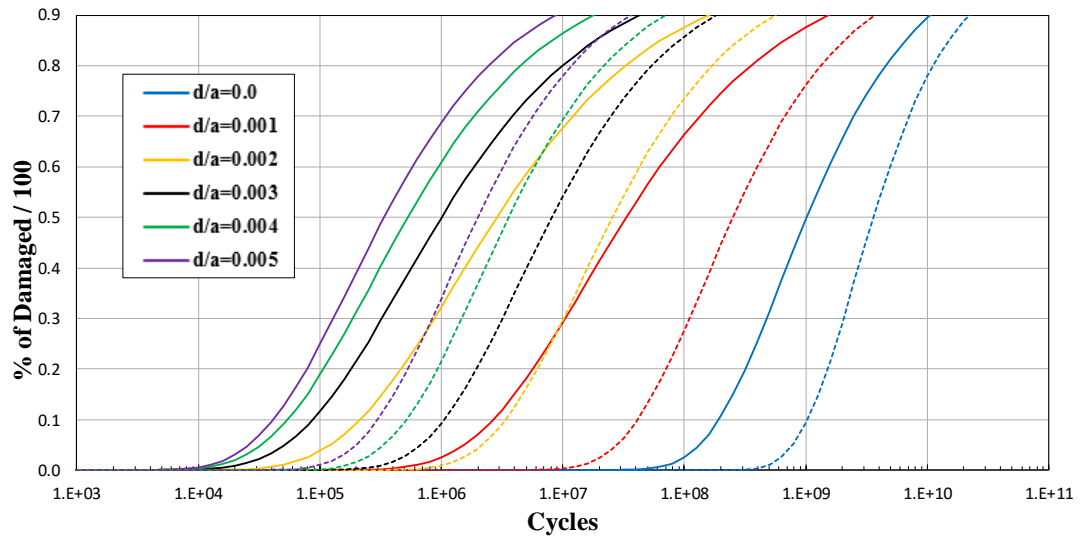


Figure 6.24 Comparison of the Weibull cumulative damage distribution curves for the synthesised slow surfaces of high (solid curves) and low (broken curves) roughness for Analysis Point 2.

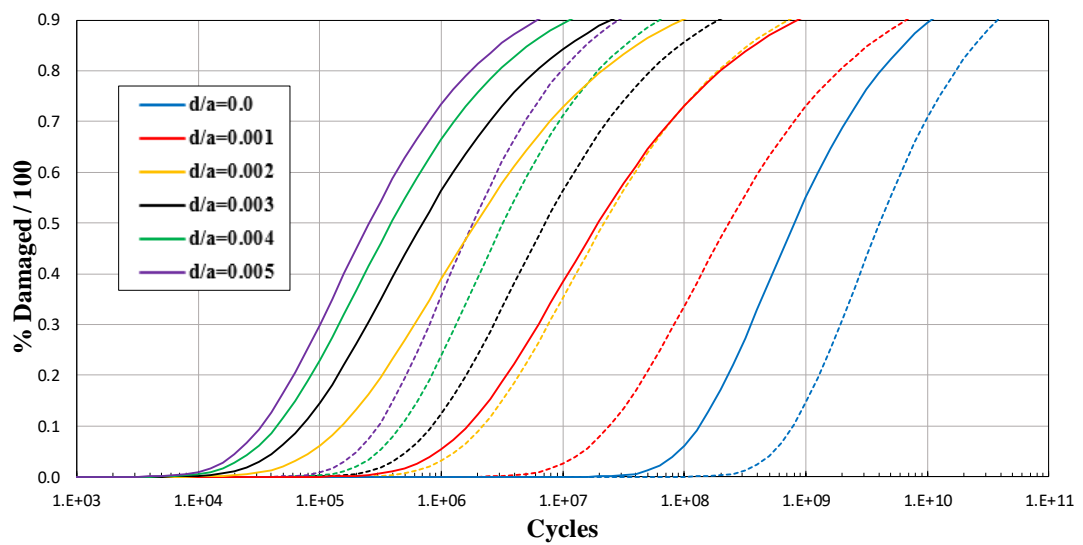


Figure 6.25 Comparison of the Weibull cumulative damage distribution curves for the experimental slow surfaces of high (solid curves) and low (broken curves) roughness for Analysis Point 2.

6.9 Comparison with disk tests where micropitting occurred

The actual micropitting damage for the experimental profiles obtained from the endurance test disks, as described in Chapter 5, was measured at each endurance stage. This was carried out using a software tool to detect pits in measured profile data which is being developed by colleagues in the research group using Matlab. This calculates the percentage of pitted points at each test stage for the nine profilometer traces taken in the circumferential direction for each measured surface. Each profile is around 11 mm long when processed.

The micropit detection software aligns the 2D profiles measured at the end of each loading stage. It then calculates the standard deviation of the measured heights at each point in the profile. Points with a high standard deviation are considered to be pitted. The amount of micropitting is expressed as a percentage of the total number of relocated points and is plotted against test cycles in Figure 6.26 and Figure 6.27.

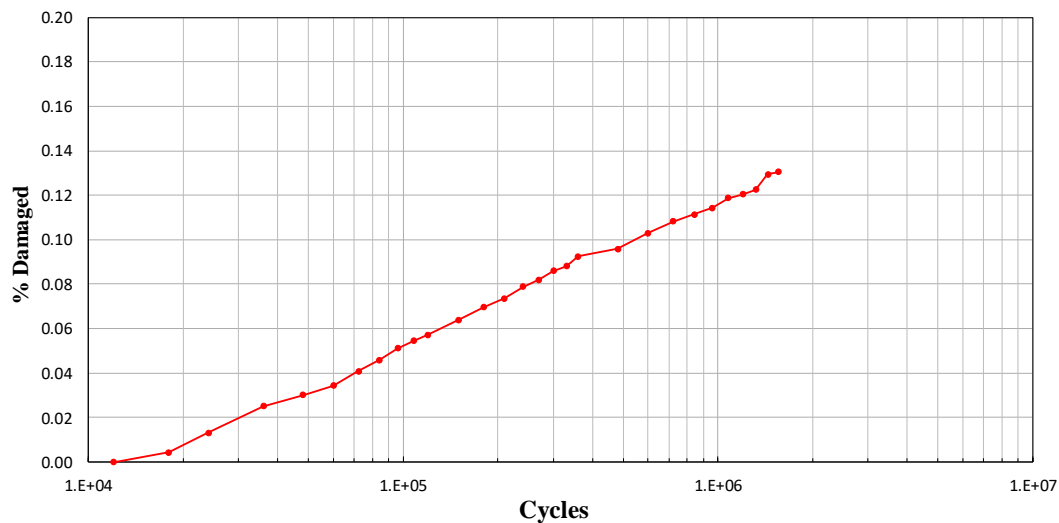


Figure 6.26 Growth of measured micropits for the slow disk of the disk test experiment

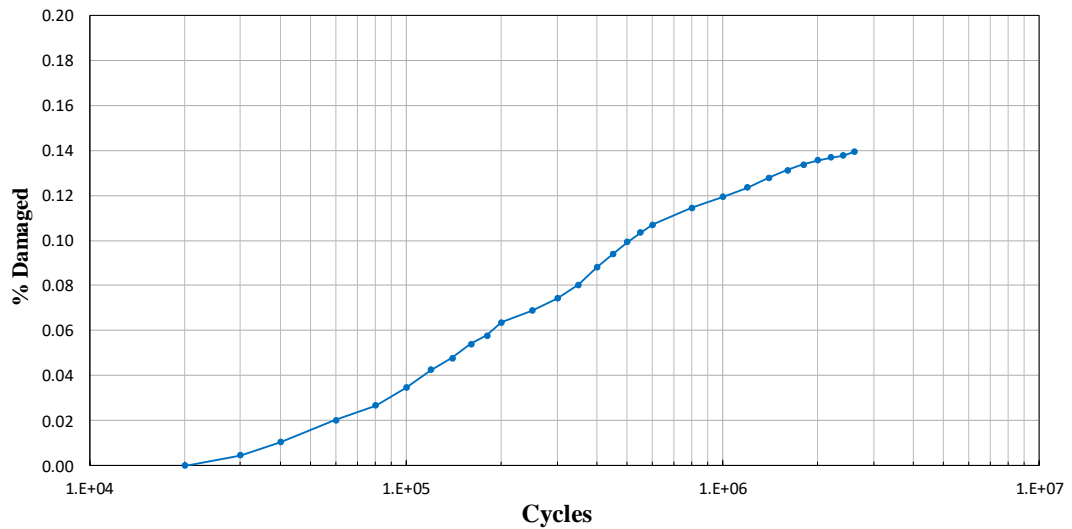


Figure 6.27 Growth of measured micropits for the fast disk of the disk test experiment

In making a comparison between the observed micropits and the fatigue predictions of the model of measured surfaces, it was noted that the calculated Weibull fatigue curves vary considerably with depth. The slope of the initial rise of experimental data is more consistent with accumulated damage by volume rather than with the curves at specific depths. The decision was made therefore to accumulate the predicted damage by volume from the surface to each specific depth, i.e. cumulative volume over the zone where micropits occur. This approach gives curves that are less sensitive to depth. Thus, the prediction of failure in the form of Weibull cumulative distributions is not for material at a particular depth but for material volume from the surface to a particular depth. This approach was implemented by developing the code for the Weibull distribution as described in Chapter 5. A comparison between these two cumulative distributions is made in Figure 6.28.

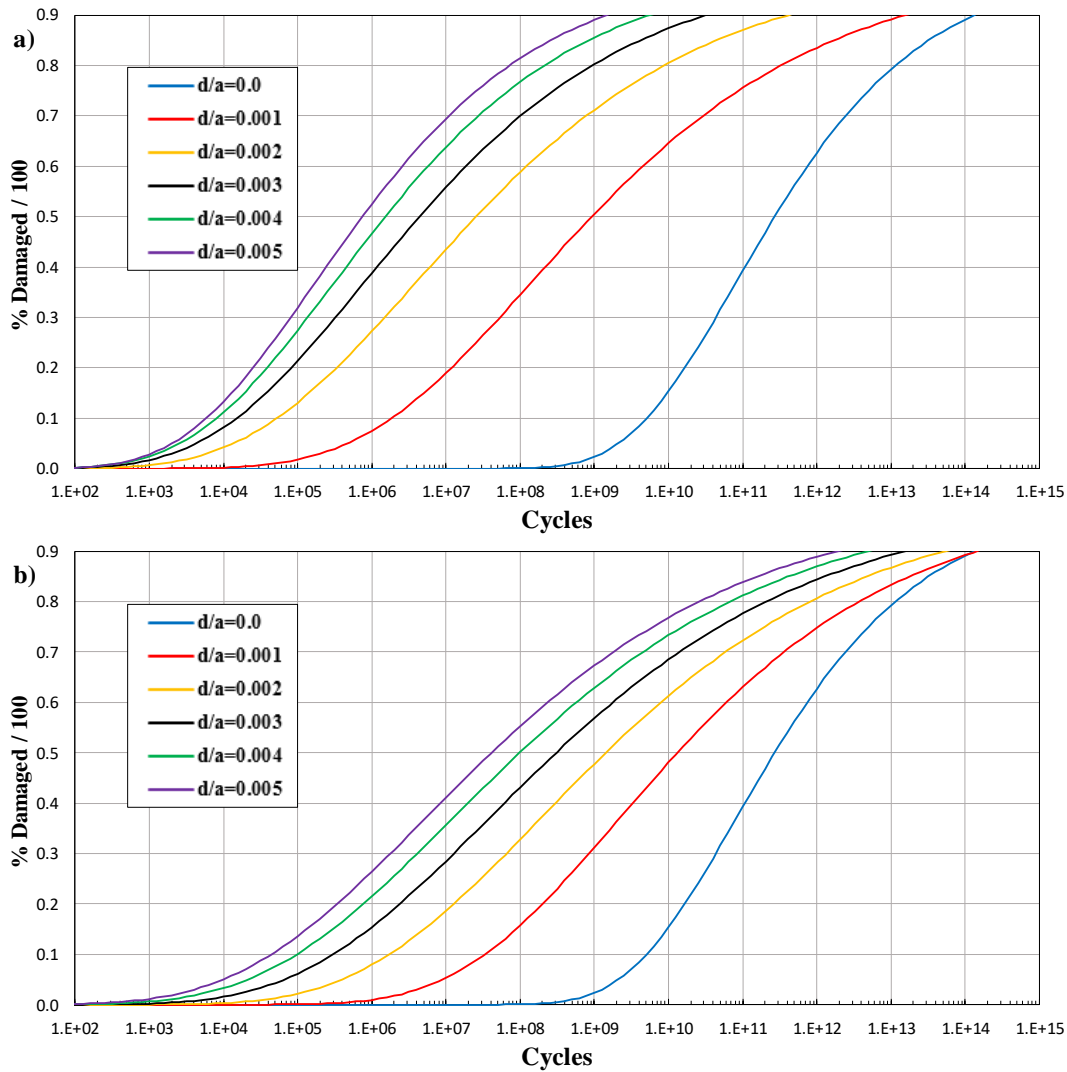


Figure 6.28 Cumulative damage distributions beneath the surface at a series of a) particular depths d/a , and b) volumes from the surface to particular depths (volume accumulation).

The fatigue analysis procedure was conducted for Profile Set Eight as described in section 6.4 for the measured and synthesised run-in surfaces of both the fast and slow disks. The accumulative damage by volume to specified depths of the measured and synthesised slow surfaces are shown in Figure 6.29.

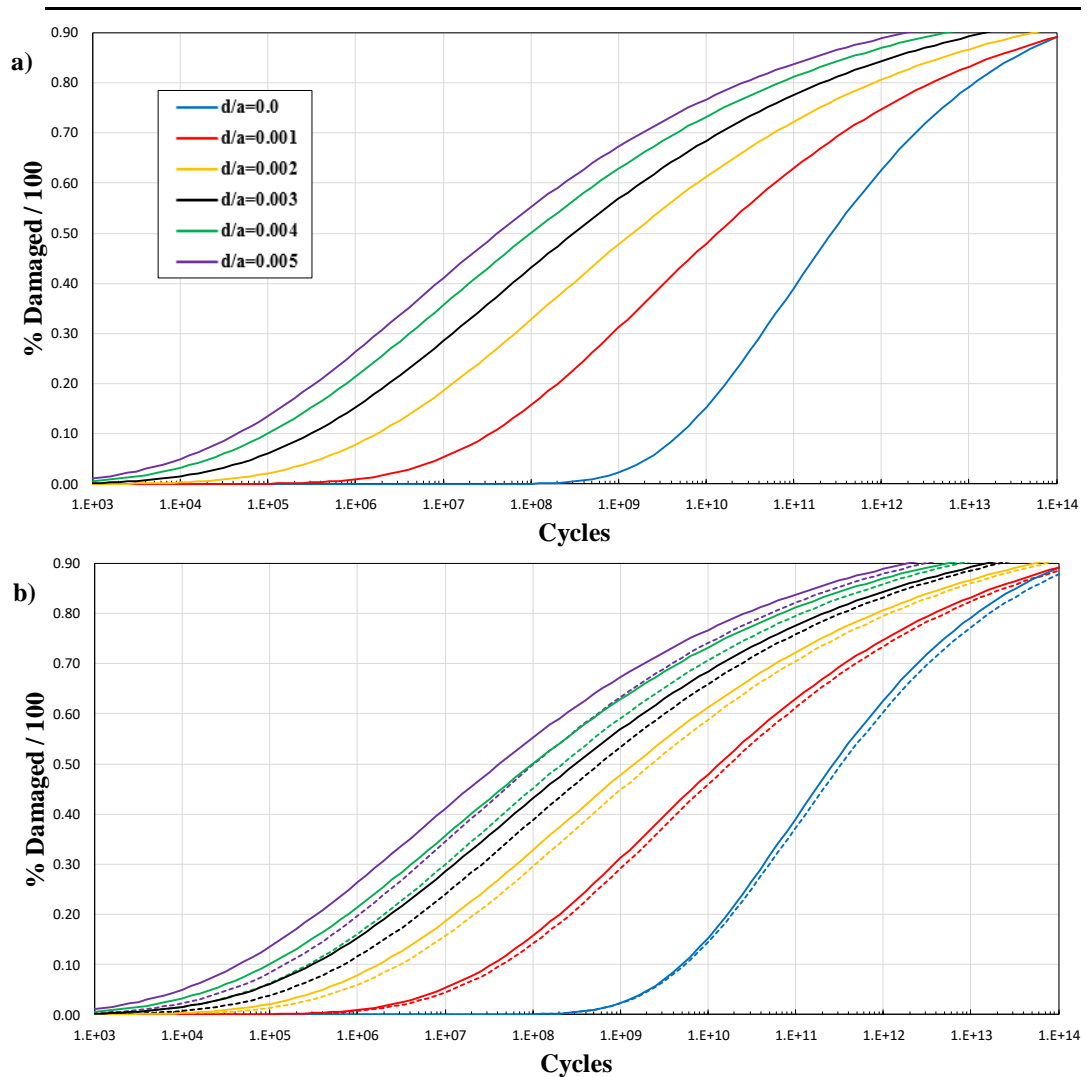


Figure 6.29 Cumulative damage distribution for the slower surface of Profile Set Eight for the volume to specified depths d/a below the surface. The solid lines are for measured experimental profiles, and the dashed lines are for the synthesised profiles. Hertz dimension, $a = 402 \mu\text{m}$.

The micropitting damage predicted started to occur at around 10^3 cycles for the cumulative volume to depth $d/a = 0.005$ for the experimental surfaces.

For the cumulative damage distribution by volume to depth $d/a = 0.005$ for the measured surface 20% of material points experience calculated damage by $3.16 \cdot 10^5$ cycles, while 4.4% of material at accumulated depth of $d/a = 0.002$ is calculated to be damaged at the same number of cycles.

At the 20% damage level of the measured surfaces as shown in Figure 6.29a, the life differences between successive solid curves from $d/a = 0$ to $d/a = 0.005$ are OOM factors of 1.9, 1.2, 0.7, 0.5 and 0.4, respectively. The experimental and synthesised curves are offset to the right, and the comparison is made in Figure 6.29b. The life differences of the synthesised surfaces are similar to the experimental ones. The differences between successive dashed curves for depths of $d/a = 0$ to $d/a = 0.005$ are order of magnitude factors of 1.8, 1, 0.7, 0.39 and 0.3, respectively.

The offsets between the experimental and synthesised curves over the specified depths are quite similar, and this is seen in the ΔD_{20} and ΔL_{20} figures given in Table 6.9.

Table 6.9 Percentage damage offset and life offset at 20% damage for slow surface of Profile Set Eight.

Accumulation Depth (d/a)	ΔD_{20} %	ΔL_{20} (OOM)
0	0.7	0
0.001	1.7	0.07
0.002	2.9	0.14
0.003	4.1	0.29
0.004	4.3	0.39
0.005	5.2	0.5

The predicted damage was also calculated for the fast surface of Profile Set Eight.

The results are shown in Figure 6.30.

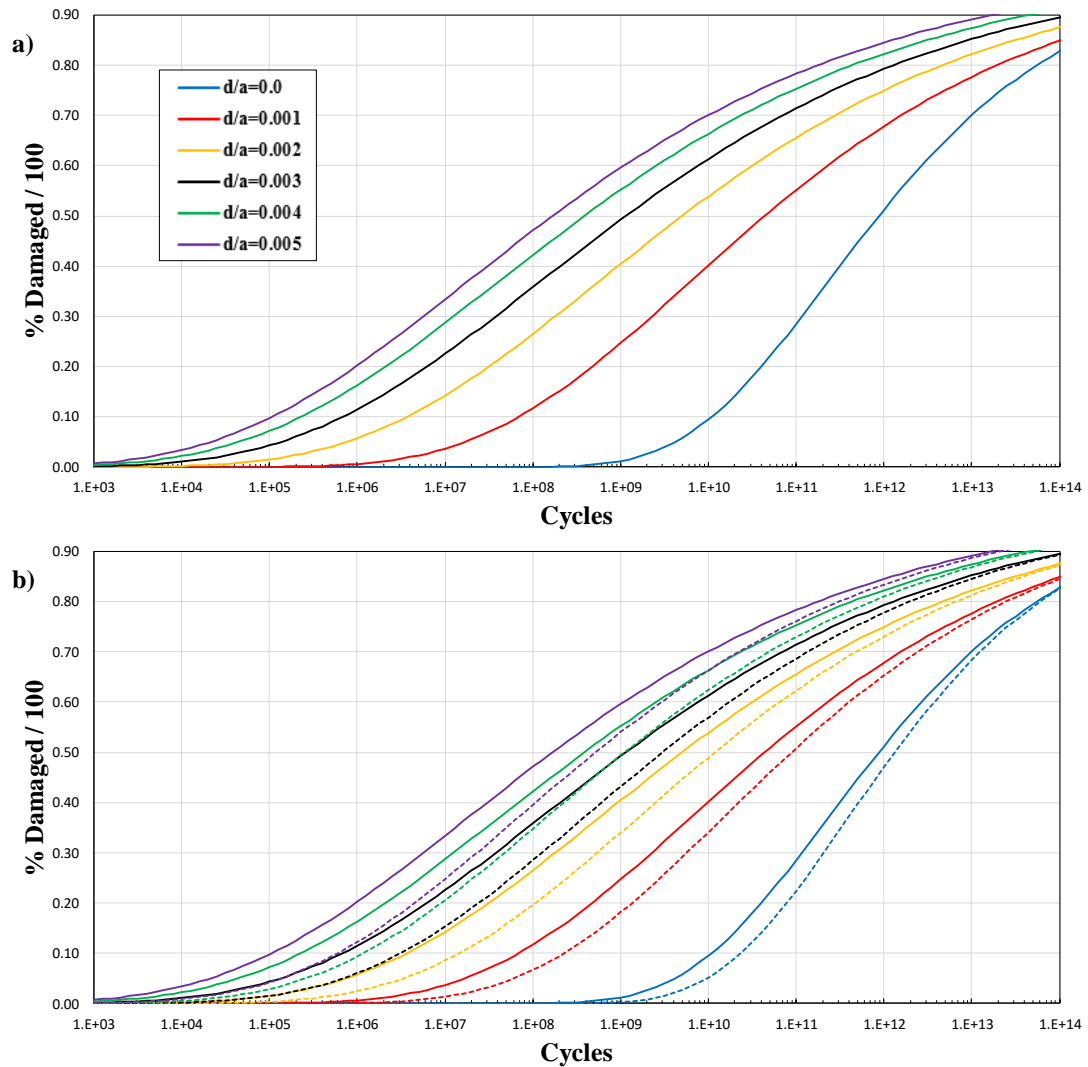


Figure 6.30 Cumulative damage distribution for the faster surface of Profile Set Eight for the volume to specified depths d/a below the surface. The solid lines are for experimental profiles, and the dashed lines are for synthesised profiles. Hertz dimension, $a = 402 \mu\text{m}$.

The micropitting damage predicted started to occur at around $2 \cdot 10^3$ cycles for the accumulative volume to depth $d/a = 0.005$ for the experimental surfaces.

At a cumulative damage distribution for volume to $d/a = 0.005$ for the measured surface, 20% of material points experience calculated damage at 10^6 cycles, while 6%

of material at a cumulative depth of $d/a = 0.002$ is calculated to be damaged at the same number of cycles.

At the 20% damage level of the measured surfaces as shown in Figure 6.30a, the life differences between successive solid curves from $d/a = 0$ to $d/a = 0.005$ are order of magnitude factors of 2, 1.2, 0.65, 0.5 and 0.3, respectively. The experimental and synthesised curves are offset to the right, and the comparison is made in Figure 6.30b. The life differences of the synthesised surfaces are similar to the experimental ones. The differences between successive dashed curves for depths of $d/a = 0$ to $d/a = 0.005$ are OOM factors of 1.8, 1.1, 0.6, 0.39 and 0.3, respectively.

The offsets between the experimental and synthesised curves over the certain depth are quite similar, and this is borne out by the ΔD_{20} and ΔL_{20} figures given in Table 6.10.

Table 6.10 Percentage damage offset and life offset at 20% damage for slow surface of Profile Set Eight.

Accumulation Depth (d/a)	ΔD_{20} %	ΔL_{20} (OOM)
0	5.8	0.3
0.001	6.2	0.4
0.002	6.5	0.47
0.003	7	0.59
0.004	7.5	0.65
0.005	8	0.76

The comparison between the predicted micropitting of the experimental slow surface and the actual micropitting observed for the slow disk surface is shown in Figure 6.31.

It can be seen that the measured micropits (red curve) correspond initially to the calculated accumulative damage from the surface to a depth of $d/a= 0.002$ (yellow curve), then it rises towards the black curve becoming parallel to it with a damage offset of about 1%. It then falls away after about $3 \cdot 10^5$ cycles. By this time about 10% of the surface was pitted and that can be expected to have caused a load re-distribution. So it is not expected that the micropitting will follow the predicted damage to high damage cycles because as soon as pitting starts, the load is redistributed and some points carry higher pressures and others carry lower values. This does not happen in this model of fatigue because its only takes the run-in profiles into account. From this point of view, it might be worthwhile to calculate the predicted damage for the experimental profiles after each stage of the endurance test. This approach could build a more realistic picture of the expected longer-term pitting growth, as far as applying this fatigue model is concerned.

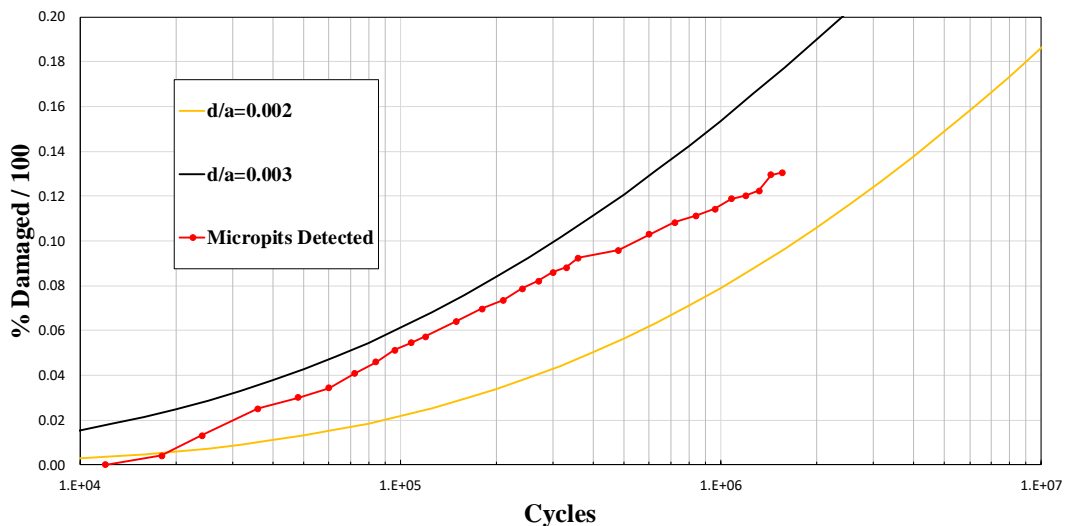


Figure 6.31 Comparison between growth of measured micropits over the slow disk surface and its calculated damage from the fatigue analysis.

The comparison between the predicted micropits of the experimental fast surface and the actual micropits developed over the fast disk surface are shown in Figure 6.32.

It can be seen that the actual micropits detected (blue curve) corresponds initially to the calculated cumulative damage from the surface to a depth of $d/a=0.002$ (yellow curve), then it rises to meet and cross the black curve before falling away after about 10^6 cycles. By this time about 12% of the surface was pitted.

It can be noticed that both the model of predicted micropits and the actual growth of measured micropits are similar. The slow surface has more damage than the fast one for both the actual and predicted micropits. For example, about 5.5% of the slow disk surface was pitted by 10^5 cycles, while 3.5% of the fast disk surface was pitted at the same number of cycles. At the $d/a= 0.003$, 6% of the measured slow surface is calculated to be pitted at 10^5 cycles, while 4.2% of the fast surface is calculated to be pitted at the same number of cycles.

There is a consistency between what is predicted by the fatigue model and the actual micropits measured for both the fast and slow surfaces. The model parameters simply correspond to the steel type and have not been adjusted to generate the correspondance. The accumulated volume for which this correspondance is observed is that to a depth of $d/a= 0.003$ or thereabouts. This corresponds to a depth of 1.2 μm . The typical pit depth is approximately 0.8 μm from analysis such as that represented in Figure 6.14.

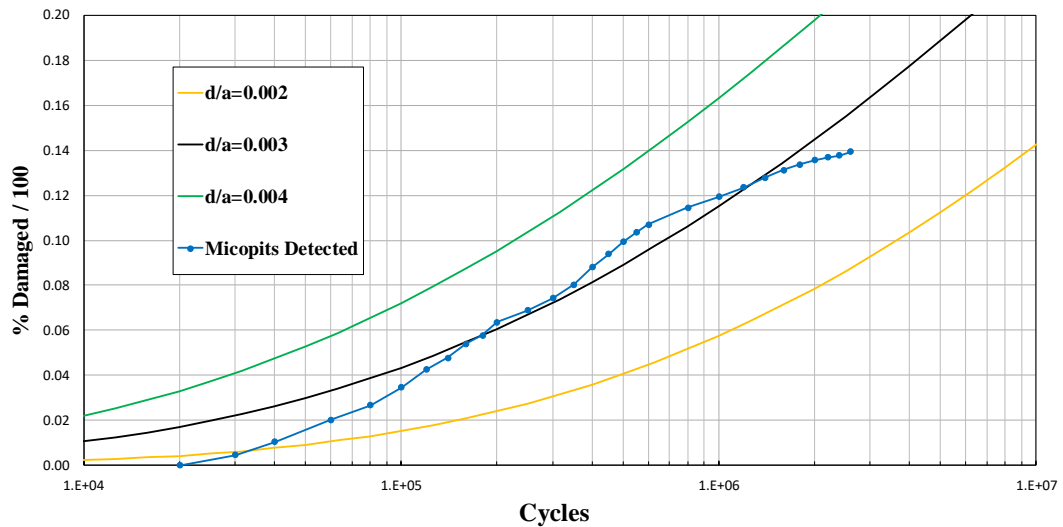


Figure 6.32 Comparison between growth of measured micropits over the fast disk surface and its calculated damage from the fatigue analysis.

A second comparison with a disk test where micropitting occurred was for the case of Profile Set 2. For this earlier test the first post running-in measurement stage was after 60,000 fast disk revolutions. The fatigue analysis procedure was implemented for the lowest penetration of Profile Set Two as explained in Chapter 3 for the measured and synthesised run-in surfaces of both the fast and slow surfaces. The cumulative damage by volume to specified depths of the measured and synthesised slow surfaces is shown in Figure 6.33.

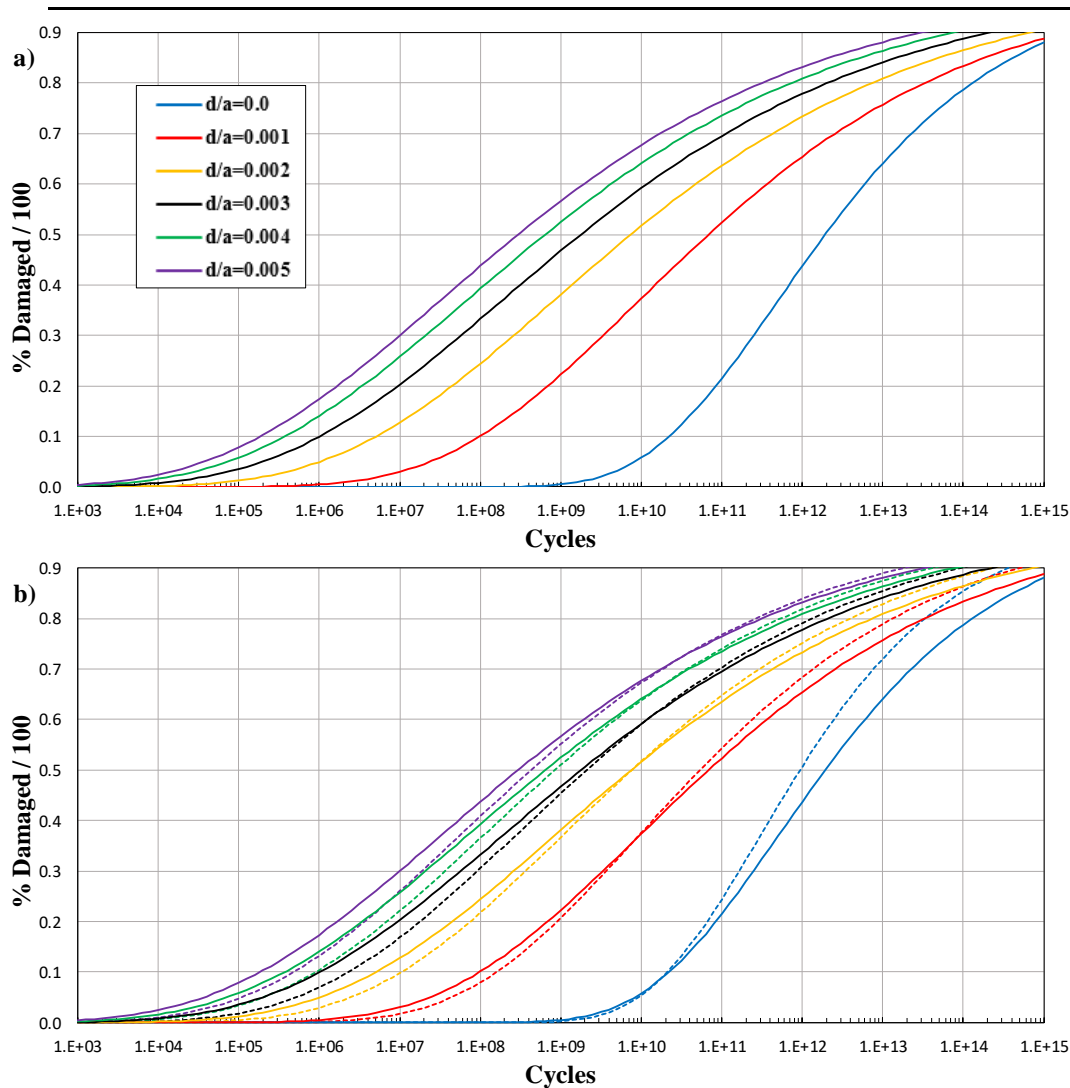


Figure 6.33 Cumulative damage distribution for the slower surface of Profile Set Two for the volume to specified depths d/a below the surface. The solid lines are for measured experimental profiles, and the dashed lines are for the synthesised profiles. Hertz dimension, $a = 402 \mu\text{m}$.

For the volume to depth $d/a = 0.005$ for the measured surface 20% of material points experience calculated damage by 1.5×10^6 cycles, while 5% of material at a cumulative depth of $d/a = 0.002$ is calculated to be damaged at the same number of cycles.

At the 20% damage level of the measured surfaces as shown in Figure 6.33a, the life differences between successive solid curves from $d/a = 0$ to $d/a = 0.005$ are order of magnitude factors of 2.1, 1.1, 0.7, 0.5 and 0.3, respectively. The experimental and synthesised curves are offset to the right, and the comparison is made in Figure 6.33b. The life differences of the synthesised surfaces are similar to the experimental ones.

The differences between successive dashed curves for depths of $d/a = 0$ to $d/a = 0.005$ are OOM factors of 1.79, 1, 0.6, 0.39 and 0.4, respectively.

It can be seen from Figure 6.33b that the synthesised curves are offset to the right of experimental surface curves at the beginning and they then cross each other after different numbers of cycles. The offsets between the experimental and synthesised curves over different cumulative depths are varied, as quantified by the ΔD_{20} and ΔL_{20} figures given in Table 6.11.

Table 6.11 Percentage damage offset and life offset at 20% damage for slow surface of Profile Set Two.

Accumulation Depth (d/a)	ΔD_{20} %	ΔL_{20} (OOM)
0	-3.3	-0.1
0.001	2	0.1
0.002	3.1	0.2
0.003	3.4	0.24
0.004	4	0.32
0.005	4.3	0.27

At the 20% damage level, it can be noticed that the synthesised profiles have less calculated damage than the experimental ones at each cumulative depth except for the surface layer $d/a = 0$ where it is higher.

The predicted damage for fast surface of Profile Set Two are shown in Figure 6.34.

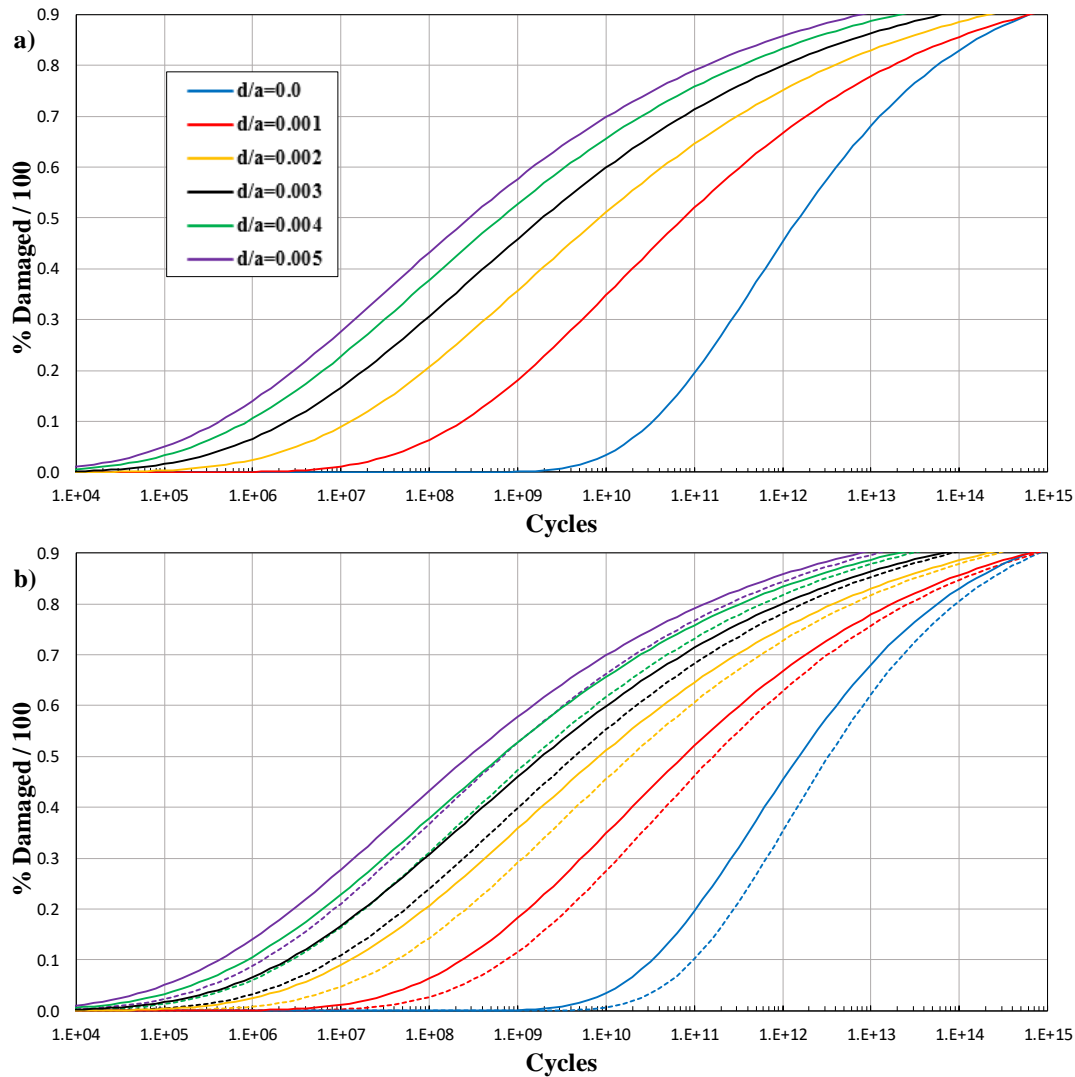


Figure 6.34 Cumulative damage distribution for the faster surface of Profile Set Two for the volume to specified depths d/a below the surface. The solid lines are for experimental profiles, and the dashed lines are for the synthesised profiles. Hertz dimension, $a = 402 \mu\text{m}$.

The micropitting damage predicted started to occur at around 10^4 cycles for the cumulative volume to depth $d/a = 0.005$ for the experimental surfaces.

At a cumulative damage distribution for volume to $d/a = 0.005$ for the measured surface, 20% of material points experience calculated damage at 3.2×10^6 cycles, while 4.3% of material at accumulated depth of $d/a = 0.002$ is calculated to be damaged at the same number of cycles.

At the 20% damage level of the measured surfaces as shown in Figure 6.34a, the life differences between successive solid curves from $d/a = 0$ to $d/a = 0.005$ are order of magnitude factors of 1.9, 1.15, 0.7, 0.5 and 0.4, respectively. The experimental and

synthesised curves are offset to the right, and the comparison is made in Figure 6.34b. The life differences of the synthesised surfaces are quite similar to the experimental ones. The differences between successive dashed curves for depths of $d/a = 0$ to $d/a = 0.005$ are OOM factors of 1.8, 1.2, 0.7, 0.4 and 0.4, respectively.

The offsets between the experimental and synthesised curves over different volume depths are relatively similar, and this is borne out by the ΔD_{20} and ΔL_{20} figures given in Table 6.12.

Table 6.12 Percentage damage offset and life offset at 20% damage for fast surface of Profile Set Two.

Accumulation Depth (d/a)	ΔD_{20} %	ΔL_{20} (OOM)
0	10	0.39
0.001	7	0.47
0.002	6	0.47
0.003	6	0.5
0.004	5.9	0.45
0.005	6	0.46

The fatigue analysis procedure was conducted for the highest penetration of Profile Set Three as described in Chapter 3 for the measured and synthesised run-in surfaces of both the fast and slow surfaces. The cumulative damage for volume to specified depths of the measured and synthesised slow surfaces is shown in Figure 6.35.

At a cumulative damage distribution for volume to $d/a = 0.005$ for the measured surface 20% of material points experience calculated damage by 1.2×10^6 cycles, while 8% of material at accumulated depth of $d/a = 0.002$ is calculated to be damaged at the same number of cycles.

At the 20% damage level of the measured surfaces as shown in Figure 6.35a, the life differences between successive solid curves from $d/a = 0$ to $d/a = 0.005$ are OOM factors of 2.2, 1.2, 0.6, 0.4 and 0.3, respectively. The synthesised surface curves are offset to the right for these for the measured run-in surfaces, and the comparison is

made in Figure 6.35*b*. The life differences of the synthesised surfaces are similar to the experimental ones. The differences between successive dashed curves for depths of $d/a = 0$ to $d/a = 0.005$ are order of magnitude factors of 2.3, 1.1, 0.7, 0.4 and 0.3, respectively.

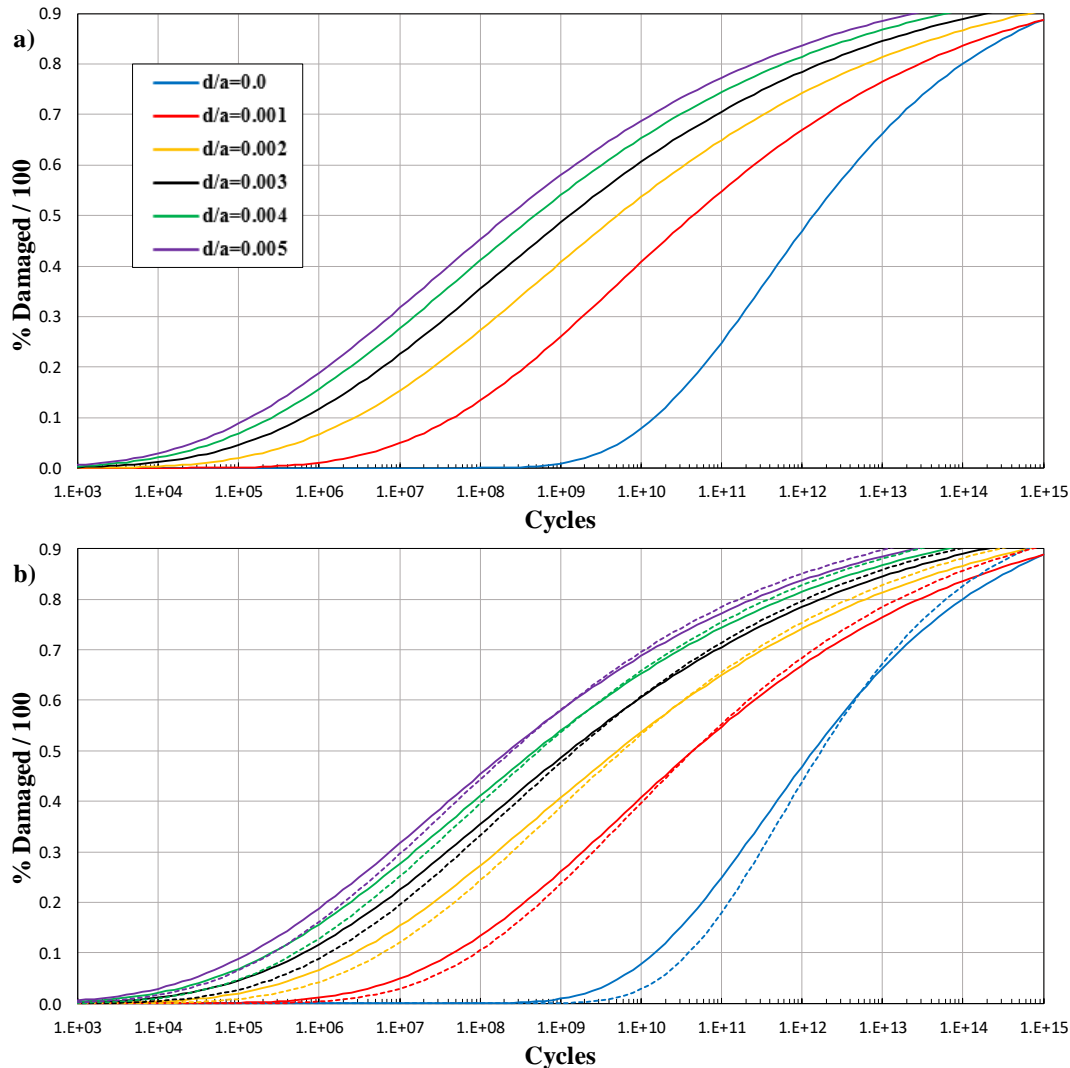


Figure 6.35 Cumulative damage distribution for the slower surface of Profile Set Three for the volume to specified depths d/a below the surface. The solid lines are for measured experimental profiles, and the dashed lines are for the synthesised profiles. Hertz dimension, $a = 402 \mu\text{m}$.

It can be seen from Figure 6.35*b* that the synthesised surface curves are offset to the right at the beginning and they then cross each other after different number of cycles. The offsets between the experimental and synthesised curves over volume to specified depths are very similar, and this is borne out by the ΔD_{20} and ΔL_{20} figures given in Table 6.13.

Table 6.13 Percentage damage offset and life offset at 20% damage for slow surface of Profile Set Three.

Accumulation Depth (d/a)	ΔD_{20} %	ΔL_{20} (OOM)
0	3.2	0.3
0.001	2.4	0.2
0.002	2.6	0.26
0.003	2.4	0.24
0.004	2.4	0.2
0.005	2.4	0.2

The predicted damage was also calculated for the fast surface of Profile Set Three. The results are shown in Figure 6.36.

The micropitting damage predicted started to occur at around 10^4 cycles for the cumulative volume to depth $d/a = 0.005$ for the experimental surfaces.

At a cumulative damage distribution for volume to $d/a = 0.005$ for the measured surface, 20% of material points experience calculated damage at $2.5 \cdot 10^6$ cycles, while 5% of material at accumulated depth of $d/a = 0.002$ is calculated to be damaged at the same number of cycles.

At the 20% damage level of the measured surfaces as shown in Figure 6.36a, the life differences between successive solid curves from $d/a = 0$ to $d/a = 0.005$ are order of magnitude factors of 1.9, 1.3, 0.7, 0.5 and 0.3, respectively. The experimental and synthesised curves are offset to the right, and the comparison is made in Figure 6.36b. The life differences of the synthesised surfaces are quite similar to the experimental ones. The differences between successive dashed curves for depths of $d/a = 0$ to $d/a = 0.005$ are OOM factors of 2.1, 1.2, 0.7, 0.5 and 0.4, respectively.

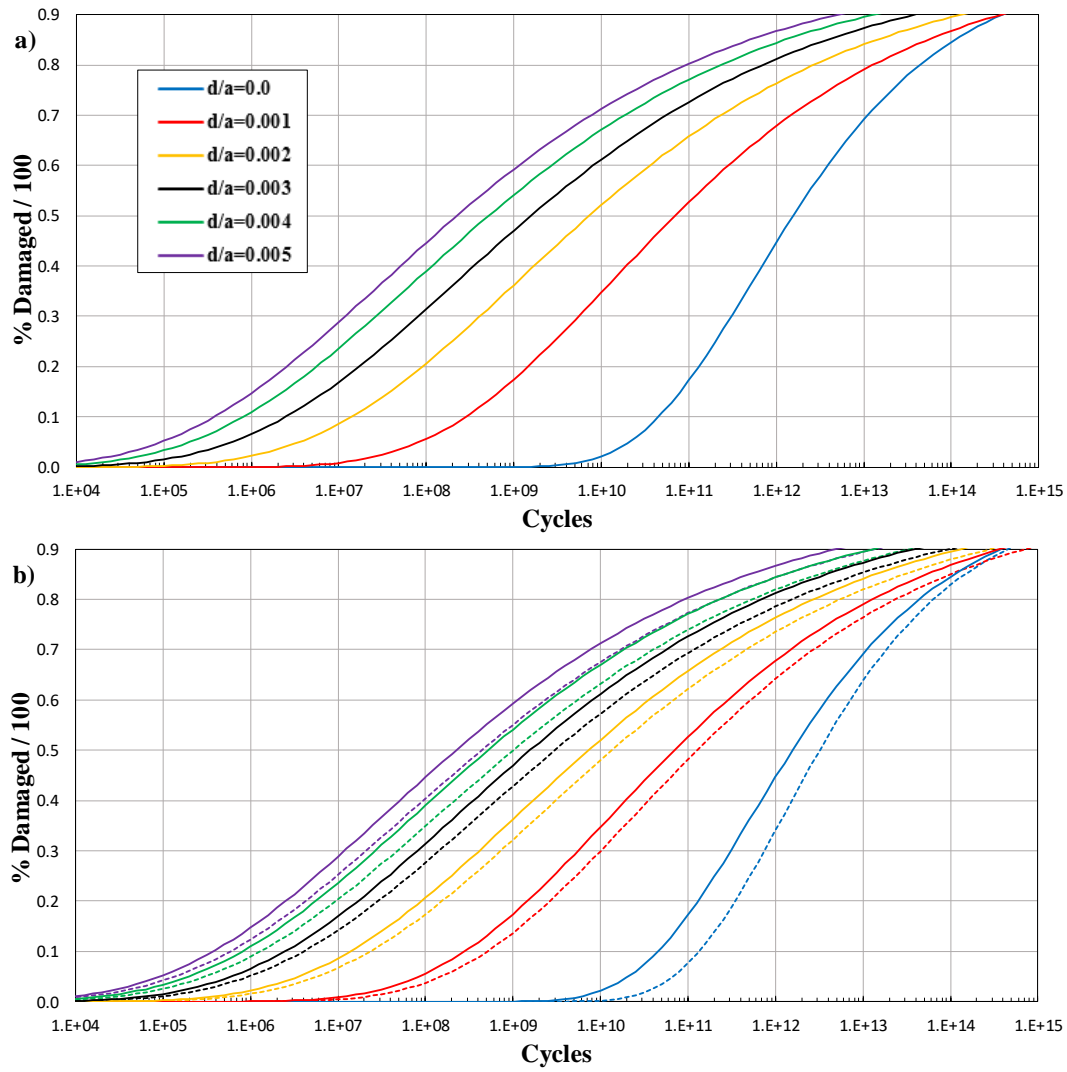


Figure 6.36 Cumulative damage distribution for the faster surface of Profile Set Three for the volume to specified depths d/a below the surface. The solid lines are for experimental profiles, and the dashed lines are for the synthesised profiles. Hertz dimension, $a = 402 \mu\text{m}$.

The offsets between the experimental and synthesised curves over the certain depth are similar, and this is borne out by the ΔD_{20} and ΔL_{20} figures given in Table 6.14.

Table 6.14 Percentage damage offset and life offset at 20% damage for fast surface of Profile Set Three.

Accumulation Depth (d/a)	ΔD_{20} %	ΔL_{20} (OOM)
0	10	0.4
0.001	4	0.28
0.002	3	0.2
0.003	3	0.2
0.004	3	0.2
0.005	3	0.2

6.10 Comparison between the highest and the lowest penetration disk surfaces.

The comparison between the highest and the lowest penetration surfaces are shown in Figure 6.37. It can be seen that there is an offset between the calculated damage for the high and the low penetration as expected that low penetration has less fatigue and an expectedly this difference is larger for the slow surface than it is for the fast surface and this may be due to the time spent in the contact zone.

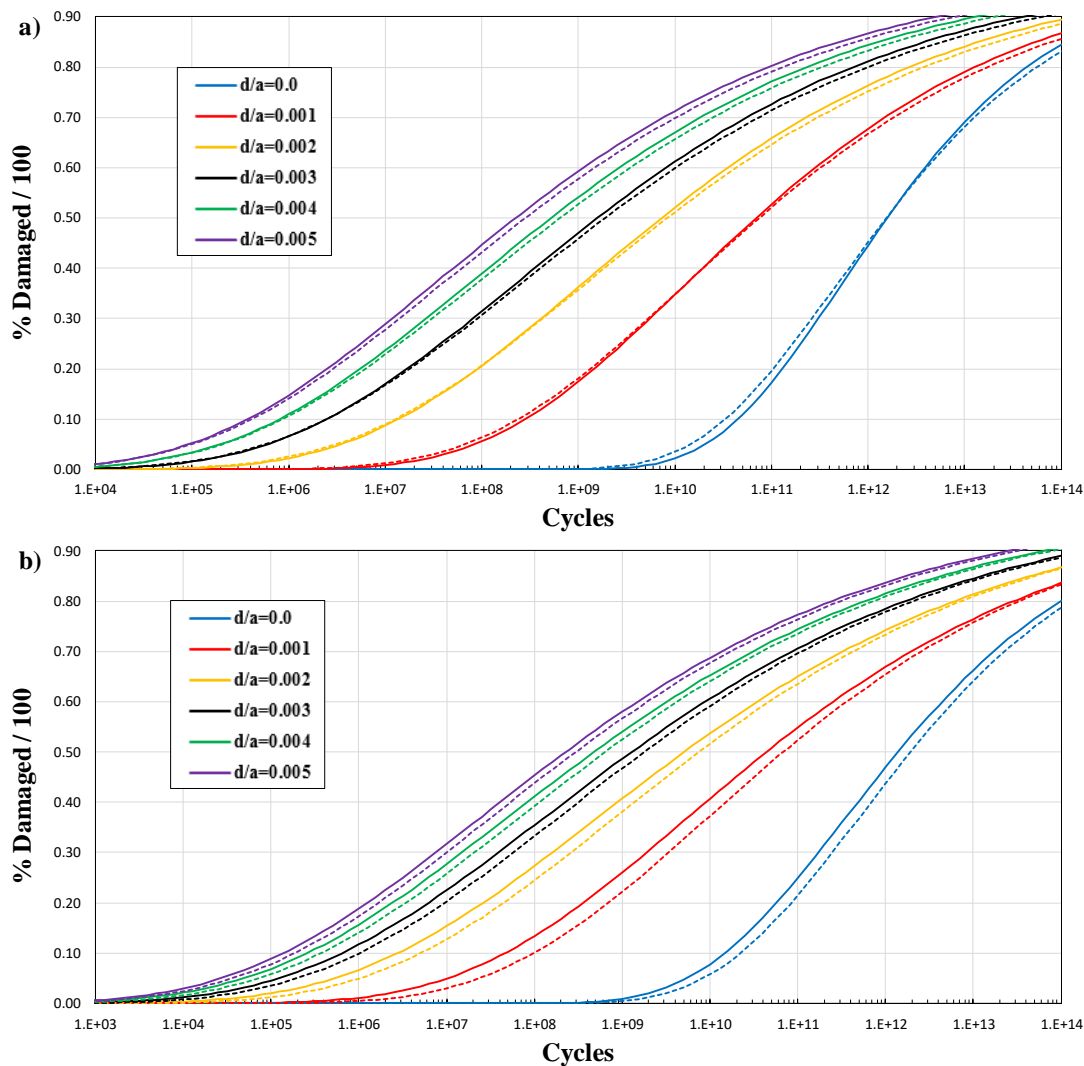


Figure 6.37 The comparison between calculated damage of the experimental surfaces for the lowest penetration of Profile Set 2 (dashed) and the highest penetration of Profile Set 3 (solid) for the a) fast surfaces, and b) slow surfaces.

The slow surface has more damage than the fast one for both the high and low penetration. For example, at the $d/a=0$, 24% of the measured slow surface is calculated to be damaged at 10^{11} cycles, while 19% of the fast surface is calculated to be damaged

at the same number of cycles. At the $d/a=0.005$, 19% of the measured slow surface is calculated to be damaged at 10^6 cycles, while 14% of the fast surface is calculated to be damaged at the same number of cycles.

The comparison between the predicted micropitting of the experimental slow surface of Profile Sets 2 and 3 and the actual micropitting observed for the slow disk surface for the test carried out by colleagues in the research group are shown in Figure 6.38. This is the test illustrated in Figure 6.14. It had two running-in stages each of 1800 slow disk cycles. It then had a measurement stage at 6×10^4 cycles and subsequently at 6×10^4 cycle increments with an increase to 18×10^4 cycle increments towards the end of the test. The number of cycles where micropitting first occurred is not therefore known.

It can be seen that the measured micropits (red curve) corresponds initially to the calculated cumulative damage from the surface to a depth of $d/a=0.003$ (black curve) at 6×10^4 cycles for the low penetration surfaces. It has a lower slope than the $d/a=0.003$ curve and crosses the $d/a=0.002$ curves for both the high and low penetration surfaces at about 5×10^5 and 10^6 respectively, then reaching an apparent asymptote of 5% damage.

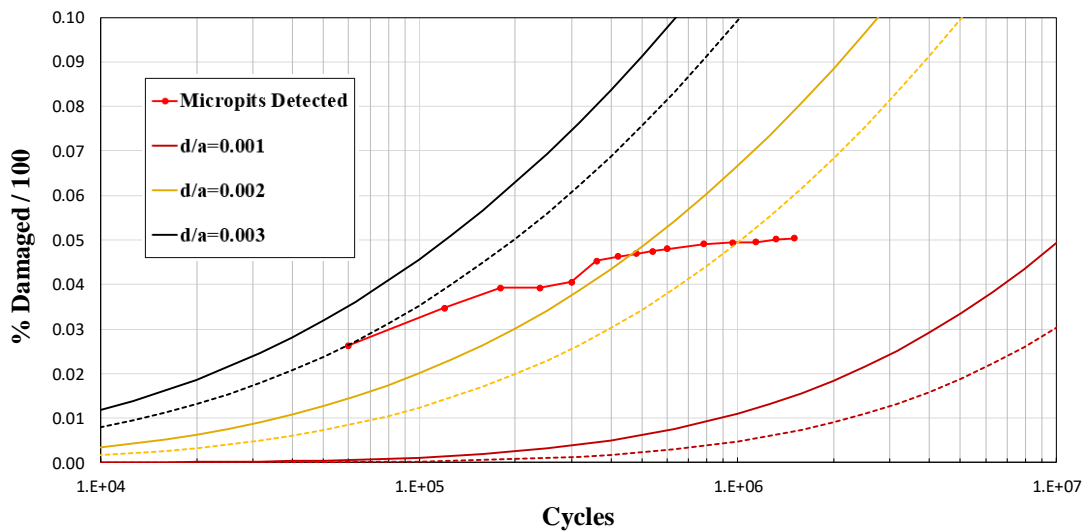


Figure 6.38 Comparison between growth of measured micropits over the slow disk surface and its calculated damage from the fatigue analysis for Profiles Set 2 and 3.

Generally speaking, the experimental points cross from the 0.003 curve to the 0.002 curve for the low penetration calculated results and straddle the 0.002 curve for the high penetration calculation.

The comparison between the predicted micropits of the experimental fast surface of Profile Sets 2, 3 and the actual micropits that develop over the fast disk surface are shown in Figure 6.39. It can be seen that there is no significant damage difference between the low and high penetration for the fast surface.

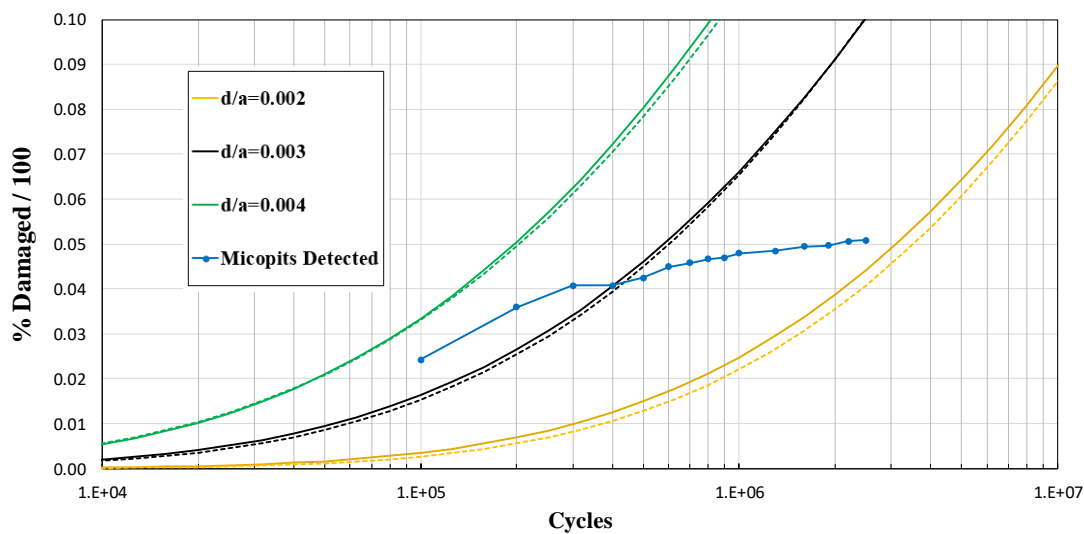


Figure 6.39 Comparison between growth of measured micropits over the fast disk surface and its calculated damage from the fatigue analysis for Profiles Set 2 and 3.

The first two points on the micropitting growth curve are midway between the calculated accumulated damage curves for volumes to depths of $d/a=0.003$ (black curves) and $d/a=0.004$ (green curves). Its slope then falls with increasing cycles as it crosses the $d/a=0.003$ curves at 4×10^5 cycles. At the last measurement point of 2.5×10^6 cycles, it is close to crossing the $d/a=0.002$ curves with 5% of the surface pitted which again appears to be an asymptote.

The slow surface has more damage than the fast one for both the actual and predicted micropits. For example, about 3.3% of the slow disk surface was pitted by 10^5 cycles, while 2.4% of the fast disk surface was pitted at the same number of cycles. At the $d/a=0.003$, 3.6% of the measured slow surface is calculated to be pitted at 10^5 cycles, while 1.7% of the fast surface is calculated to be pitted at the same number of cycles. The accumulated volume for which this correspondance is observed is that to a depth

of $d/a = 0.003$ or thereabouts. This corresponds to a depth of $1.2 \mu\text{m}$. The typical pit depth approximately $0.7 \mu\text{m}$ from the experiment data in Figure 6.14.

6.11 Comparison with gear micropitting experiments

In the two gear test experiments the high roughness gears gave early micropitting, and the low roughness gears had had longer lives. Unfortunately, the experiments had no intermediate measurements and for the high roughness test the micropitting life is much lower than endurance cycles experienced in the test. There was therefore no possibility to make a proper comparison with the real experiments because the tests were carried out over 8×10^6 cycles without intermediate surface measurements. The tests were part of a research project at Newcastle University. The high roughness pair of gears were found to be badly micropitted at the end of the test. The low roughness pair showed very little sign of damage. There were concerns that the tooth flanks may have had a reduced hardness due to softening of the material in the grinding process.

6.12 Sensitivity of calculated fatigue to counter face orientation

The fatigue analysis was conducted for the run-in profile of Profile Set Three for a range of specific counterface orientations. The counterface was advanced / retarded in increments of $160 \mu\text{m}$ to provide a set of five counterface interaction positions in order to examine the sensitivity of the analysis to counterface orientation. The maximum offset between the cases is therefore $640 \mu\text{m}$ which is $1.6 a$. The results of this examination are shown in Figure 6.40 for the fast and slow surfaces accumulated for the volume to specified depths. There is a small variation in the calculated damage for each different counterface alignment but the results follow a very similar pattern.

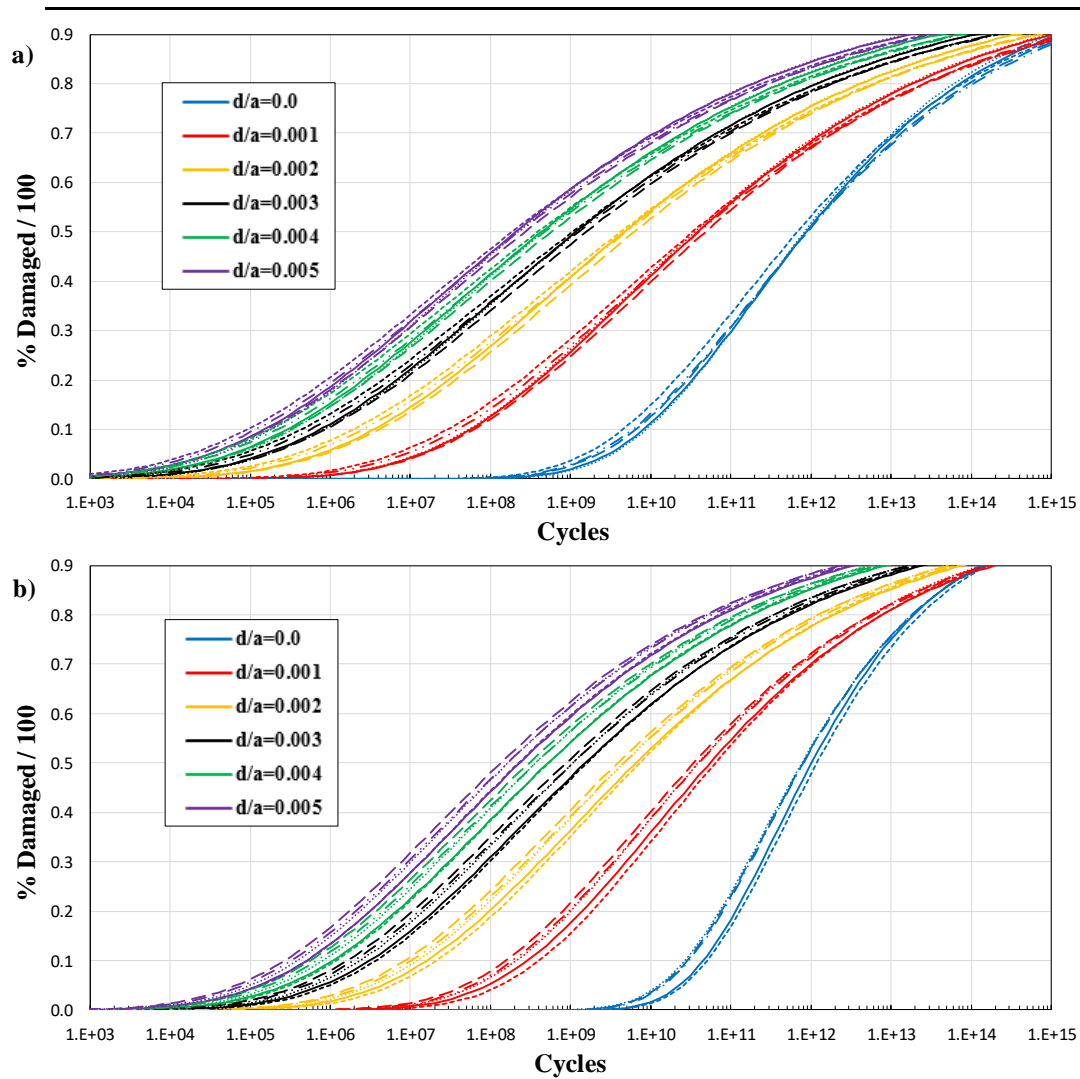


Figure 6.40 Cumulative damage distributions for the volume to specified depths d/a below the surface for five different counterface alignment interaction positions for a) the slower surface, and b) the faster surface. Hertz dimension, $a = 402 \mu\text{m}$.

In order to have a clear comparison between the five different curves for each depth level, the mean curve was calculated and is presented in Figure 6.41 together with the maximum and minimum damage from the set of five results for the fast and slow surfaces.

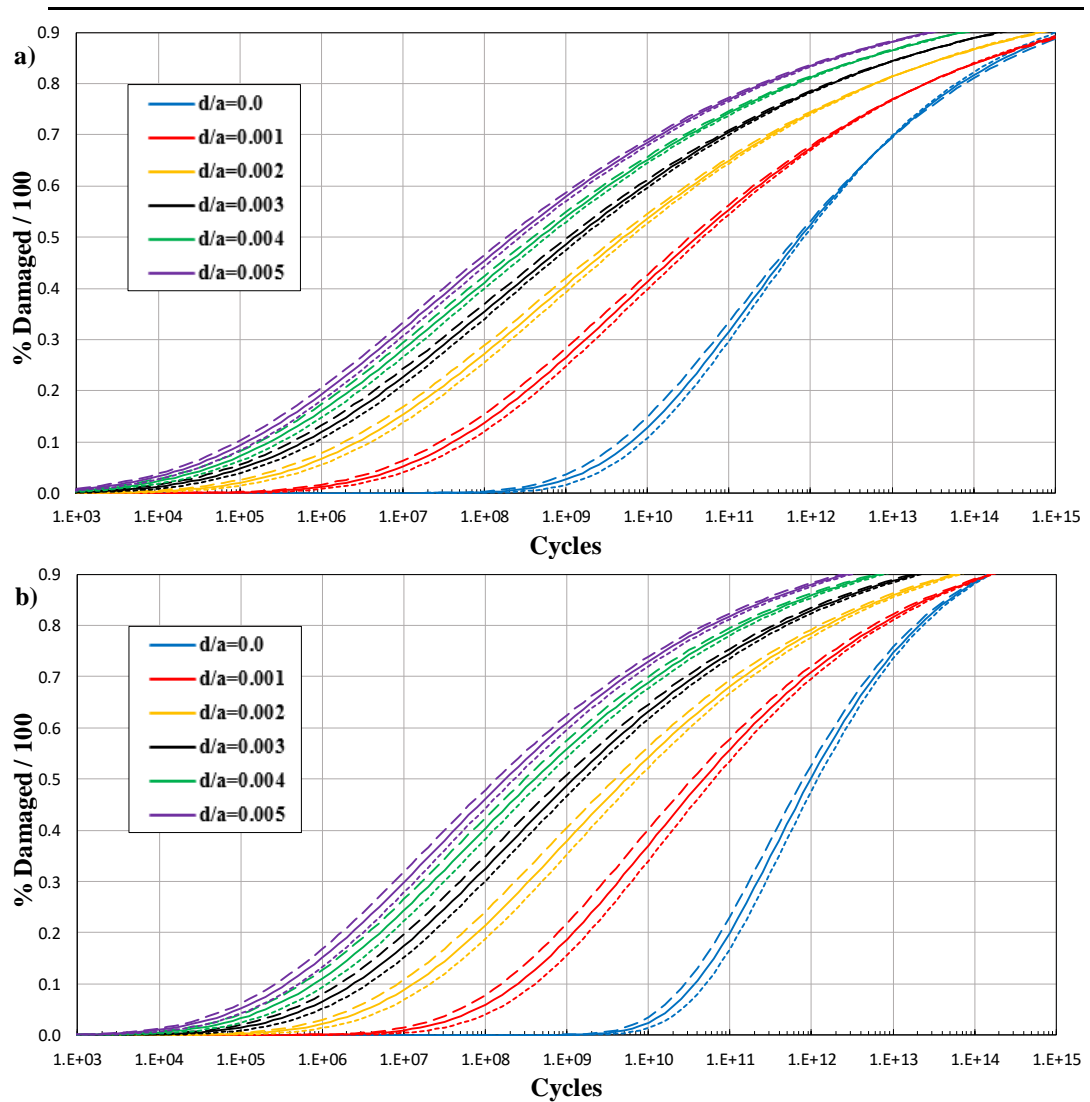


Figure 6.41 Cumulative damage distribution for five different counterface alignment interaction positions showing the maximum (dashed), mean (solid) and minimum (dotted) curves for each depth level for a) the slow surface, and b) the fast surface.

The biggest difference between the maximum and minimum curves correspond to no more than 5% damage, and the mean curve gives the damage to within 2.5% when compared to any other orientation.

This suggests that for the same portion of material coming into the contact, there is a small sensitivity to exactly how the counterface interacts with it. The calculated damage varies by up to 5% due to this factor.

Tables 6.14 and 6.15 show the OOM factors from proceeding d/a value for damage accumulated by depth and volume, respectively, for all eight sets of profiles. It can be seen that there is no obvious pattern. The patterns are varied from model to model according to the rough surfaces.

Table 6.15 Depth effect summary for OOM factors from proceeding d/a value when damage is accumulated at specific depths.

Profile	Surface	OOM factor from proceeding depth at depth d/a				
		0.001	0.002	0.003	0.004	0.005
PS1	S	3	1.49	0.59	0.27	0.18
PS4	S	2	1	0.2	0.1	0.1
PS5	S	1.8	1	0.4	0.2	0.1
PS6	S	1.1	0.9	0.5	0.3	0.2
PS7	S	1.4	1	0.4	0.29	0.2
PS4	F	1.5	1	0.4	0.3	0.2
PS5	F	1.3	1.1	0.6	0.3	0.2
PS6	F	0.7	1	0.4	0.3	0.2
PS7	F	0.9	0.9	0.5	0.4	0.2

Table 6.16 Depth effect summary for OOM factors from proceeding d value when damage is accumulated by volume to specified depths.

Profile	Surface	OOM factor from proceeding depth at depth d/a				
		0.001	0.002	0.003	0.004	0.005
PS1	S	2	1.2	0.59	0.5	0.29
PS4	S	1.3	0.7	0.4	0.3	0.1
PS5	S	1.1	0.8	0.5	0.3	0.2
PS6	S	0.7	0.6	0.4	0.4	0.2
PS7	S	0.9	0.8	0.4	0.4	0.2
PS2	S	2.1	1.1	0.7	0.5	0.3
PS3	S	2.2	1.2	0.6	0.4	0.3
PS8	S	1.9	1.2	0.7	0.5	0.4
PS3	F	1.9	1.3	0.7	0.5	0.3
PS2	F	1.9	1.15	0.7	0.5	0.4
PS8	F	2	1.2	0.65	0.5	0.3

To look for patterns between the test conditions and the fatigue calculation. The number of cycles to 10% ($N_{10\%}$) for damage accumulated by volume to depth $d/a = 0.003$ was used.

Table 6.17 shows the operating conditions and the parameters used for all eight sets of profiles with the $N_{10\%}$ values for the fast surface ($N_{10\%F}$), and the slow surface ($N_{10\%S}$).

Table 6.17 Surfaces parameters, operating conditions and $N_{10\%}$ values for eight profile sets. Square symbols are used for disk tests and tringles for gear tests.

PS	Rq-F (μm)	Rq-S (μm)	Rq-m (μm)	Λ	$N_{10\%F}$ (cycle)	$N_{10\%S}$ (cycle)	U	ξ	w' (kN/m)
PS1 ■	0.34	0.31	0.32	0.12	$8.2 \cdot 10^6$	$3.16 \cdot 10^6$	0.63	0.5	$1.03 \cdot 10^6$
PS2 ■	0.3	0.53	0.43	0.26	$2.51 \cdot 10^6$	$1.0 \cdot 10^6$	3.19	0.5	$7.58 \cdot 10^5$
PS3 ■	0.37	0.53	0.46	0.25	$2.2 \cdot 10^6$	$6.3 \cdot 10^5$	3.19	0.5	$7.58 \cdot 10^5$
PS4 ▲	0.4	0.3	0.35	1.14	$7.94 \cdot 10^6$	$6.31 \cdot 10^5$	9.40	3.16	$1.17 \cdot 10^6$
PS5 ▲	0.43	0.29	0.36	1.15	$1.0 \cdot 10^7$	$3.16 \cdot 10^5$	9.47	0.33	$1.17 \cdot 10^6$
PS6 ▲	0.25	0.2	0.23	1.79	$3.98 \cdot 10^8$	$2.0 \cdot 10^7$	9.40	3.16	$1.17 \cdot 10^6$
PS7 ▲	0.32	0.18	0.25	1.57	$2.51 \cdot 10^8$	$3.98 \cdot 10^6$	9.47	0.33	$1.17 \cdot 10^6$
PS8 ■	0.42	0.34	0.38	0.34	$7.9 \cdot 10^5$	$3.12 \cdot 10^5$	3.19	0.5	$7.58 \cdot 10^6$

In order to find possible relationships between parameters, various plots were produce and those where parameters were plotted against $N_{10\%}$ on log-linear axes were most useful.

it was plotted the calculated fatigue of the fast surfaces ($N_{10\%F}$) against the root mean square of the fast surfaces (Rq-F) and the mean equivalent root mean square of both the fast and slow surfaces (Rq-m) on a log-linear axes, as shown in Figure 6.42.

Figure 6.42 shows plots of RMS roughness of the fast surface, $Rq-F$, and the composite RMS roughness for the two surfaces, The $Rq-m$ given by equation:

$$R_{q-m} = \sqrt{\frac{R_{q-F}^2 + R_{q-S}^2}{2}}$$

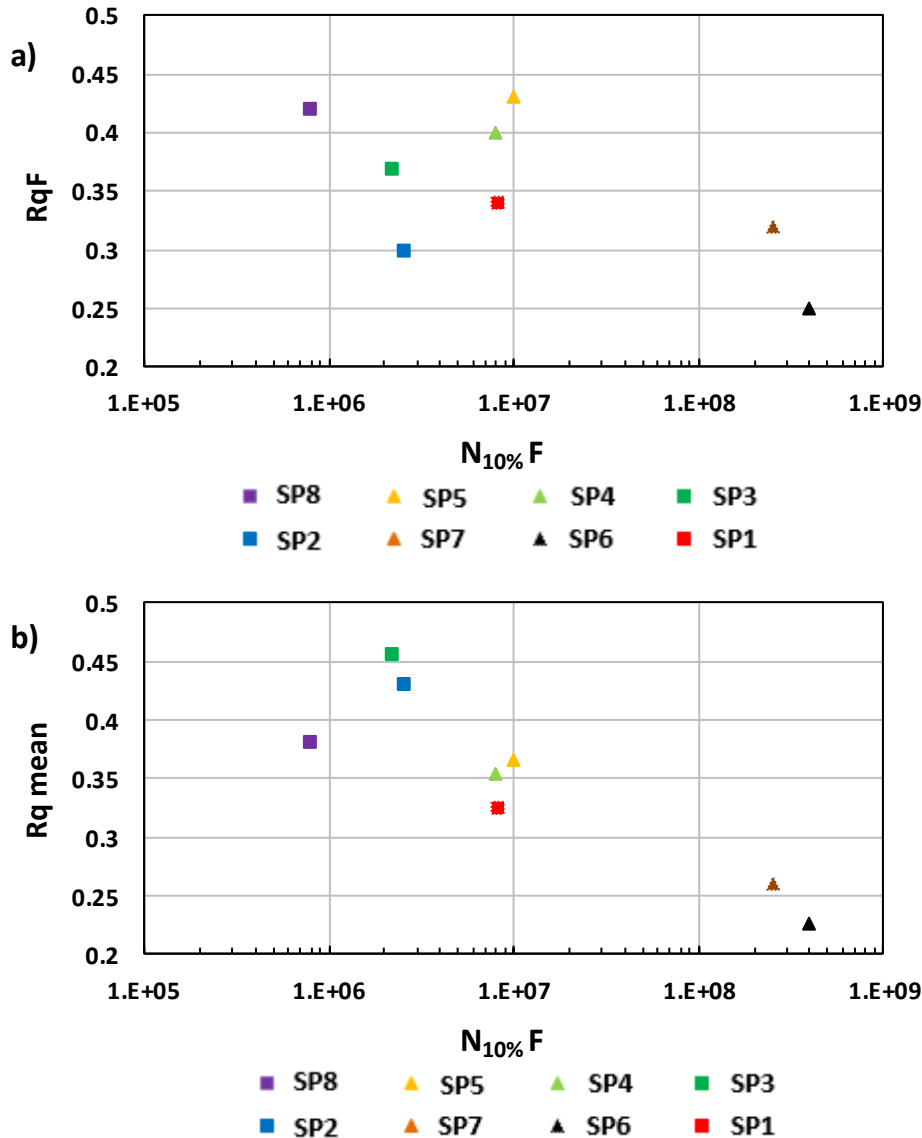


Figure 6.42 $N_{10\%}$ for the fast surfaces of eight profile sets vs a) the root mean square of the fast surfaces, and b) the mean equivalent root mean square for each profile set.

It can be seen from the figure above that there is a longer life for the surfaces that have lower Rq compared to higher Rq , and that behaviour is expected as the interaction between surfaces that have low Rq will be less intense at the asperities than those with the higher Rq values. The corresponding results for the slow surface ($N_{10\%S}$) are given in Figure 6.43.

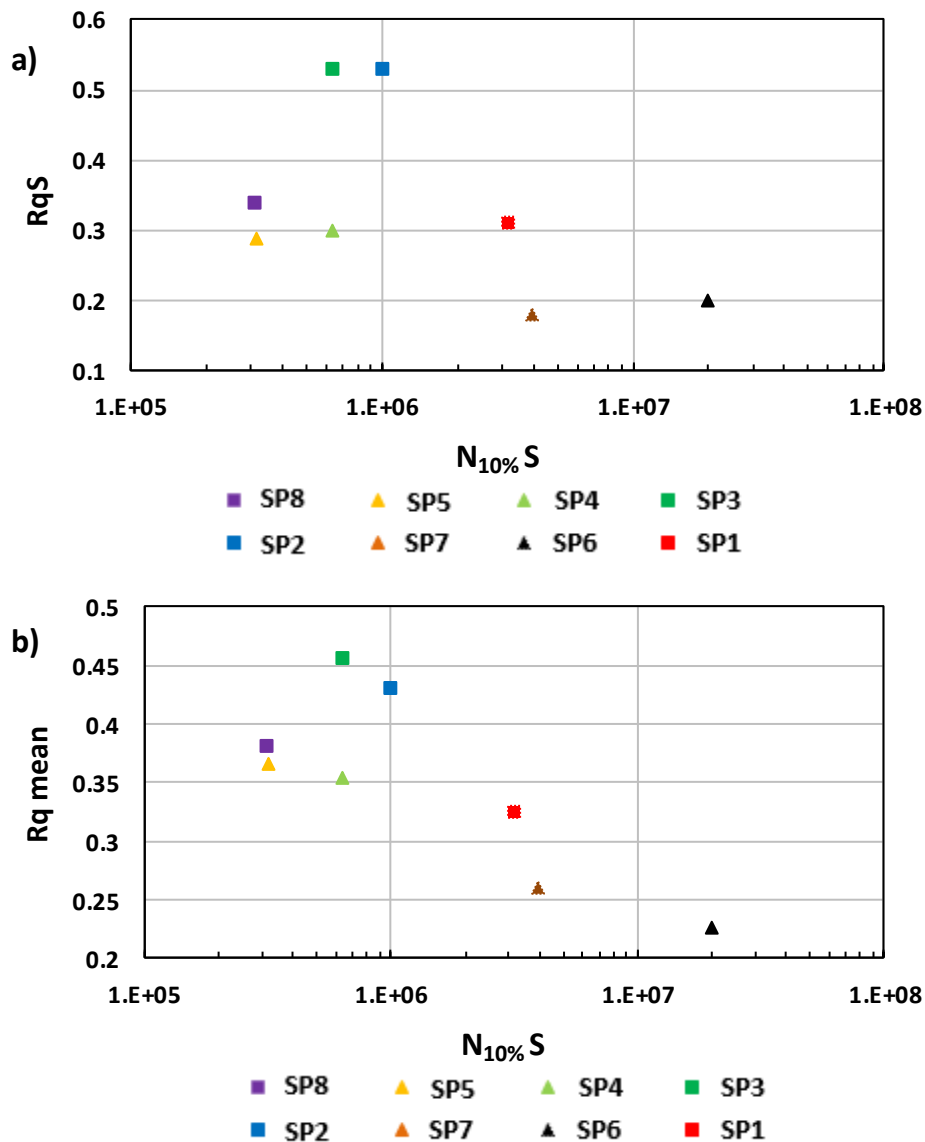


Figure 6.43 $N_{10\%}$ for the slow surfaces of eight set of profiles vs a) the root mean square of the fast surfaces, and b) the mean equivalent root mean square for each profile set

Again, it can be seen that there is a longer life for the surfaces that have lower Rq compared to higher Rq .

Generally speaking, it can be seen that the $Rq-m$ parameter plotted in Figures 6.42b and 6.43b has a clearer relation to $N_{10\%}$ for both cases. This is not surprising because the interaction between the asperities depends on both surfaces and not only the surface being analysed. General trend lines can be drawn for these figures but there is considerable deviation from them.

The lambda ratio (Λ) was plotted against the $N_{10\%F}$ and $N_{10\%S}$, and this is shown in Figure 6.44.

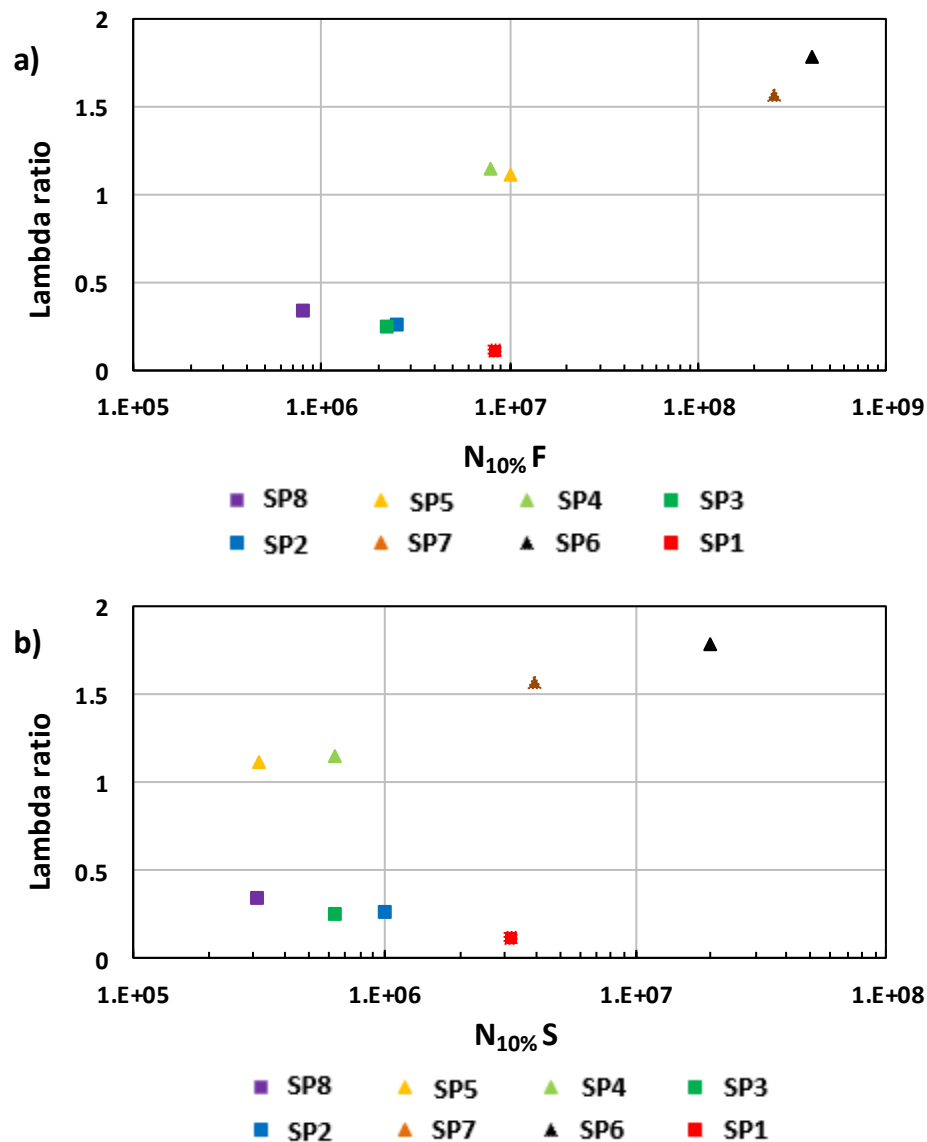


Figure 6.44 lambda ratio for all profile sets vs a) $N_{10\%}$ for the fast surfaces, and b) $N_{10\%}$ for the slow surfaces.

It can be seen that there are two different behaviours. These are for the gear profile sets (rectangular shapes), and the disk profile sets (square shapes). The gear behaviour is as expected with the lambda ratio corresponding to longer surface life. However, the disk machine test behaviour is not as expected. This may be because these gear tests are all well into mixed lubrication regime so that other parameters may be dominant. In particular, PS8 has a higher Λ ratio value than PS1 but also carries a considerably higher load which would lead to higher asperity pressures.

Chapter 7: Conclusions and Future Work

7.1 Conclusion

This study has been concerned with using EHL analysis to simulate the plastic deformation that happens to as-manufactured rough surfaces as they undergo a process of running-in in the early stages of operating life. This is typically seen on hardened and ground gear tooth surfaces which is the focus of the investigation.

The current study makes several contributions by introducing a numerical simulation model to simulate the running-in process that works with a range of realistic surface roughness values and operating conditions. Various aspects of this procedure are described in detail and it is tested and assessed by comparison with experimentally observed surface modification.

Predicted fatigue damage results were also calculated using both the experimentally measured and synthesised roughness profiles for eight sets of real surfaces. The main findings to emerge from this study are as follows.

1. Comparison between the synthesised and measured surfaces in terms of the shape of asperity geometry changes and mixed EHL behaviour.

For the tests conducted there are significant differences between the as-manufactured surface and each of the run-in and synthesised surfaces. However, the run-in and synthesised surfaces are quite similar to each other in terms of roughness profile comparisons. There are differences between the shapes of some run-in asperity features but it should be noted that the interaction between asperities in the numerical analyses do not reproduce the detailed interaction between the surfaces in the actual experiment.

The synthesised and experimentally measured roughness profiles were run in mixed - EHL analyses and have the same tendency for the extreme pressure parameters and asperity contact parameters in most positions along the profiles, but there are exceptions to this general observation at some positions. There are clear differences in

the pitted areas as can be expected as the rough surface profiles are also different at those positions.

2. Comparison between the predicted damage for the synthesised and measured surfaces.

The synthesised running-in procedure was also tested in terms of the endurance behaviour of the mixed lubrication contacts considered. This was achieved by using a cumulative damage fatigue model with the damage established in each load cycle calculated from the Fatemi and Sochie shear strain life model. This was applied to the material stress histories obtained from the calculated mixed - EHL surface loading. The calculated damage was fitted with Weibull distributions to provide cumulative fatigue distributions that were used for comparison.

The calculated damage for all eight sets of the surface profiles analysed and reported in Chapter 6 show that some of synthesised profiles gave a good Weibull distribution match with experimentally measured profiles, and others have some differences. The differences between the predicted fatigue of the synthesised analysis and the real surfaces analysis are an offset in the damage curves which correspond to small OOM amounts of fatigue life but with both cases showing the same behaviour.

3. Comparison between the high and small roughnesses for gear profiles.

As expected, the higher roughness gear surfaces generate much greater calculated damage than the lower roughness gear surfaces at all depth levels, for the case of both the synthesised and the experimental profiles. Overall, the synthesised method produced similar behaviour to the measured experimental profile results with a different offset magnitude.

4. Comparison with disk tests where micropitting occurred

The comparison between the predicted micropitting of the experimental disk surfaces and the actual micropitting observed for the disk surfaces show that both the model of predicted micropits and the growth of measured micropits give similar behaviour. The slow surface has more damage than the fast one for both the actual and predicted micropits, and the initial growth of micropitting corresponds to the calculated damage accumulated by volume to a depth of 1.2 μm .

It is not to be expected that the micropitting will follow the predicted damage to high damage cycles because as micropitting starts, the load starts to be redistributed and some points carry higher pressures and others carry lower values.

There is a consistency between what is predicted by the fatigue model and the actual micropits measured for both the fast and slow surfaces. The fatigue model parameters simply correspond to the steel type and have not been adjusted to generate the correspondence.

5. Sensitivity of calculated fatigue to counter face orientation

There is a small variation in the calculated damage for each different counterface alignment but the results follow a very similar pattern. This suggests that for the same portion of material coming into the contact, there is a small sensitivity to exactly how the counterface interacts with it.

The main achievement from this study is that by using a numerical EHL analysis contact to find the plastic deformation (surface geometry changes) to the real un-run surfaces under heavy loaded using real operating conditions. This study provides a good approximation of predicted fatigue (fatigue life) to the as-manufactured surfaces at all the operating conditions studied. This is encouraging and attempts could be made to extend the synthesis by constructing a model of the pit formation process.

7.2 Future work

The current study only takes the run-in profiles into account for analysing the model of fatigue. From this point of view, it is recommended that it would be worthwhile to calculate the predicted damage for the experimental profiles after each stage of the endurance test. This approach could build a more realistic picture of the expected longer-term pitting growth, as far as applying this fatigue model is concerned.

The way in which the experimental micropitting develops suggests that an asymptotic stable state is being approached. This difference may be partly due to the assumed Weibull distribution as the fitting process involves logarithmic transformations of the data. A means to develop life curves by scaling the single contact cycle damage to generate the 'true' cumulative distributions would be a useful tool preventing any distortion introduced by the Weibull fitting process. It would also allow the effects of earlier micropitting to be introduced into the cumulative distributions to test the reasons for the asymptotic behaviour.

Applying the methods developed to further endurance tests with different contact operating parameters will develop confidence in using it as a predictive tool. There is also scope for developing a material removal synthesis to simulate the pitting process which could be developed and calibrated against the observations in further endurance tests.

References

Akbarzadeh, S. and Khonsari, M.M. 2010. On the Prediction of Running-In Behavior in Mixed-Lubrication. 132(July), pp. 1–11. doi: 10.1115/1.4001622.

Akbarzadeh, S. and Khonsari, M.M. 2011. Experimental and theoretical investigation of running-in. Tribology International 44(2), pp. 92–100. Available at: <http://dx.doi.org/10.1016/j.triboint.2010.09.006>.

Akbarzadeh, S. and Khonsari, M.M. 2013. On the optimization of running-in operating conditions in applications involving EHL line contact. Wear 303(1–2), pp. 130–137. Available at: <http://dx.doi.org/10.1016/j.wear.2013.01.098>.

AL-Mayali, M.F. et al. 2017. Assessment of the effects of residual stresses on fatigue life of real rough Surfaces in lubricated contact.

Alanou, M.P. 2006. Study of parameters influencing surface distress of gears. PhD thesis, Cardiff University.

Andersson, M. et al. 2016. Tribology International The effect of running-in on the efficiency of super finished gears. Tribology International journal 93, pp. 71–77. doi: 10.1016/j.triboint.2015.08.010.

Aslantaş, K. and Taşgetiren, S. 2004. A study of spur gear pitting formation and life prediction. Wear 257(11), pp. 1167–1175. doi: 10.1016/j.wear.2004.08.005.

Arnell, R.D. 1976. Friction Theories. In: Halling, J. ed. Principles of Tribology. London and Basingstoke: The Macmillan Press Ltd., pp. 72–93.

Amzallag, C., Gerey, J.P., Robert, J.L. and Bahuaud, J., 1994. Standardization of the rainflow counting method for fatigue analysis. International journal of fatigue, 16(4), pp.287-293.

Anthes, R.J., 1997. Modified rainflow counting keeping the load sequence. International journal of fatigue, 19(7), pp.529-535.

Bannantine, J.A. and Socie, D.F., 1992. A multiaxial fatigue life estimation technique. In Advances in fatigue lifetime predictive techniques. American Society for Testing and Materials, Philadelphia, 1992, pp.249- 275.

Barus, C., 1893. Isothermals, isopiestic and isometrics relative to viscosity. *American journal of science*, 266, pp.87-96.

Barber, G.C. et al. 1987. Materials and Surface Finish Effects in the Breaking-in Process of Engines. *ASME J. Eng. Gas Turbines Power* 109(October), pp. 380–387.

Bergseth, E. et al. 2012. Effect of Gear Surface and Lubricant Penetration on Mild Wear. *Tribol Lett* 48(2), pp. 183–200. doi: 10.1007/s11249-012-0004-y.

Berthe, D. et al. 1980. Micropitting in Hertzian Contacts. *Journal of Lubrication Technology* 102(4), p. 478. doi: 10.1115/1.3251583.

Berthe, L. et al. 2014. Plastic deformation of rough rolling contact: An experimental and numerical investigation. *Wear* 312(1–2), pp. 51–57. Available at: <http://dx.doi.org/10.1016/j.wear.2014.01.017>.

Bhushan, B. 1998. Contact mechanics of rough surfaces in tribology: multiple asperity contact. 4, pp. 1–35.

Bhushan, B. 2013. *Introduction to Tribology*. Second edi. Columbus, Ohio USA: John Wiley & Sons, Ltd. doi: 10.1002/9781118403259 M4 - Citavi.

Bhushan, B. 2002. *Introduction to Tribology*, John Wiley & Sons.

Bishop, I.F. and Snidle, R.W. 1982. Some experimental aspects of running-in and scuffing failure of steel discs operating under elastohydrodynamic conditions. In: Dowson, D. et al. eds. *The Running-in Process in Tribology*. Butterworth-Heinemann, pp. 62–70. Available at: <http://www.sciencedirect.com/science/article/pii/B9780408012263500159>.

Blau, P.J. 2008. On the nature of running-in. *Tribology International* 38(11), pp. 1007–1012.

Blok H. 1937. General Discussion on Lubrication & Lubricants. *Proc.* 2, pp. 14–20.

Bosman, R. et al. 2011. Running-in of metallic surfaces in the boundary lubrication regime. *Wear* 271(7–8), pp. 1134–1146. Available at: <http://dx.doi.org/10.1016/j.wear.2011.05.008>.

Bower, A.F. 1988. The Influence of Crack Face Friction and Trapped Fluid on Surface Initiated Rolling Contact Fatigue Cracks. *Journal of Tribology* 110(4), p. 704.

Available at:
<http://tribology.asmedigitalcollection.asme.org/article.aspx?articleid=1459381>
[Accessed: 12 June 2018].

Brechot, P. et al. 2000. Micropitting resistant industrial gear oils with balanced performance. *Industrial Lubrication and Tribology* 52(3), pp. 125–136. Available at: <https://www.emeraldinsight.com/doi/10.1108/00368790010371762> [Accessed: 12 June 2018].

Brimble, K, Atkins I, Blencoe K, et al 2001. A Comparison of Micropitting Performance of Identical Oils Using Standard FZG Test Gears and Helical Test Gears. In: BGA Annual Congress. Burton on Trent, London, UK: British Gear Association, p. pp 40-50.

Bryant, M.J. et al. 2012a. Plastic deformation in rough surface line contacts, a finite element study. *Tribology International journal* 46, p. 269–278 Contents. Available at: https://ac.els-cdn.com/S0301679X11001940/1-s2.0-S0301679X11001940-main.pdf?_tid=d63b5d28-a51a-4074-8cc2-97401701a557&acdnat=1528831141_783a93caae89ea93588e1fd96c2f9c70
[Accessed: 12 June 2018].

Bryant, M.J. et al. 2012b. Plastic deformation in rough surface line contacts — a finite element study. *Tribology International* 46(1), pp. 269–278. Available at: <http://dx.doi.org/10.1016/j.triboint.2011.06.024>.

Bull, S.J. et al. 1999. The effect of the white layer on micro-pitting and surface contact fatigue failure of nitrided gears. *Proceedings of the Institution of Mechanical Engineers, Part J: Journal of Engineering Tribology* 213(4), pp. 305–313. doi: 10.1243/1350650991542695.

Burbank, J. and Woydt, M. 2016. Optimization of pre-conditioned cold work hardening of steel alloys for friction and wear reductions under slip-rolling contact. *Wear* 350–351, pp. 141–154. Available at: <http://dx.doi.org/10.1016/j.wear.2016.01.011>.

Britton, R. D., Elcoate, C. D., Alanou, M. P.; Evans, H. P.; Snidle, R. W., 2000, Effect of surface finish on gear tooth friction, *Journal of Tribology, Transactions of the ASME*, v 122, n 1, pp. 354-360.

Cavatorta, M.P. and Cusano, C. 2000. Running-in of aluminum r steel contacts under starved lubrication Part II. Effects on scuffing., pp. 133–139.

Cen, H. et al. 2018. Effect of slide to roll ratio on the micropitting behaviour in rolling-sliding contacts lubricated with ZDDP-containing lubricants. *Tribology International* 122, pp. 210–217. Available at: <http://linkinghub.elsevier.com/retrieve/pii/S0301679X18301257> [Accessed: 12 June 2018].

Cheng, W. and Cheng, H.S. 1995. Effect of Surface Roughness Orientation on Pitting Resistance of Lubricated Rollers. *Tribology Transactions* 38(2), pp. 396–402. Available at: <http://www.tandfonline.com/doi/abs/10.1080/10402009508983420> [Accessed: 12 June 2018].

Chue, C.H. and Chung, H.H. 2000. Pitting formation under rolling contact. *Theoretical and Applied Fracture Mechanics* 34(1), pp. 1–9. doi: 10.1016/S0167-8442(00)00019-7.

Clarke, A. et al. 2015. Understanding micropitting in gears. *Proceedings of the Institution of Mechanical Engineers, Part C: Journal of Mechanical Engineering Science* 230(7–8), pp. 1276–1289. doi: 10.1177/0954406215606934.

Clarke, A., Sharif, K.J., Evans, H.P., & Snidle, R.W., 2006, “Heat partition in rolling/sliding elastohydrodynamic contacts”, *Trans. ASME Journal of Tribology*, v.128, pp. 67-78.

Clarke, A. et al. 2016. Running-in and micropitting behaviour of steel surfaces under mixed lubrication conditions. *Tribology International* 101, pp. 59–68. Available at: <http://dx.doi.org/10.1016/j.triboint.2016.03.007>.

Clarke, Jamali, H.U., Sharif, K J, Evans, H P, Frazer, R, Shaw, B. A. Effects of profile errors on lubrication performance of helical gears, *Tribology International* , (2017) 10.1016/j.triboint.2017.02.0034, 111, pp184-191

Conry, T. F., Wang, S., and Cusano, C., 1987. A Reynolds-Eyring Equation for Elastohydrodynamic Lubrication in Line Contacts. *Journal of Tribology*. 109, 648.

Davies, C.N. 2005. Effects of non-newtonian rheology on the line contact elastohydrodynamic lubrication problem. PhD thesis. Cardiff University.

-
- Dowson, D. and Higginson, G.R., 1979. History of tribology, Longman London.
- Dowson, D., and Higginson, G. R., 1977. Elasto-hydrodynamic lubrication. Oxford [England], Pergamon Press.
- Dowson, D. and Higginson, G.R., 1959, “A numerical solution to the elastohydrodynamic problem”, Proceedings of the IMechE: Journal of Mechanical Engineering Science, v.1, pp. 6-15.
- Dowson, D., Higginson, G.R., & Whitaker, A.V., 1962, “Elastohydrodynamic lubrication: a survey of isothermal solutions”, Journal of Mechanical Engineering Science, v.4, pp121 onwards.
- Dowson, D., Toyoda, 1978. A central film thickness formula for elastohydrodynamic line contacts, in Proceedings of 5th Leeds-Lyon Symposium on Tribology, Leeds, pp. 60–65.
- Dowson, D., and Higginson, G. R., 1966. Elasto-hydrodynamic lubrication. London, Pergamon Press.
- Dowling, N.E., 1998. Mechanical Behaviour of Materials-Engineering Methods for Deformation, Fracture and Fatigue, second edition. Prentice Hall, Englewood Cliffs, NJ.
- Dowling, N. E. 2013. Mechanical behavior of materials: engineering methods for deformation, fracture, and fatigue. Fourth edition, Pearson education, Inc.
- Downing, S.D. and Socie, D.F., 1982. Simple rainflow counting algorithms. International Journal of Fatigue, 4(1), pp.31-40.
- Ebner, M. et al. 2018. On the effect of starved lubrication on elastohydrodynamic (EHL) line contacts. Tribology International 118, pp. 515–523. doi: 10.1016/j.triboint.2017.06.004.
- Elcoate, C.D., 1996. Coupled solution methods for the elastohydrodynamic lubrication problem. PhD thesis, Cardiff University.
- Elcoate, C.D., Evans, H.P., Hughes, T.G. 1997. Fully coupled elastohydrodynamic solution techniques for the analysis of real rough line contacts using finite element and finite difference models. Tribology Series, 32, pp. 27-36.

Elcoate, C.D., Evans, H.P., Hughes, T.G. and Snidle, R.W., 2001. Transient elastohydrodynamic analysis of rough surfaces using a novel coupled differential deflection method. *Proceedings of the Institution of Mechanical Engineers, Part J: Journal of Engineering Tribology*, 215(4), pp.319-337.

Erte A. M., 1945. *Hydrodynamic Calculation of Lubrication of Curved Surfaces. Gears, Rolling Bearings, Highly Loaded Journal Bearings etc.* Akad. Nauk, Moscow, p. 64.

Ertel, A.M., 1939. Hydrodynamic lubrication based on new principles. *Akad. Nauk. SSSR, Prikladnaya Matematika i Mekhanika* 3(2), 41–52.

Ertel, A. M., 1945. *Hydrodynamic Calculation of Lubrication of Curved Surfaces (Gears, Rolling Bearings, Highly Loaded Journal Bearings etc.)* (Akad. Nauk, Moscow), p. 64.

Evans, H.P. and Snidle, R.W., 2009. The future of engineering tribology in concentrated contacts. *Proceedings of the Institution of Mechanical Engineers, Part C: Journal of Mechanical Engineering Science*, 223(12), pp.2939-2948.

Evans, H.P. et al. 2012. Predictive modelling of fatigue failure in concentrated lubricated contacts. 44(0), pp. 105–121. doi: 10.1039/c2fd00116k.

Evans, H.P. et al. 2012. Analysis of Micro-Elastohydrodynamic Lubrication and Prediction of Surface Fatigue Damage in Micropitting Tests on Helical Gears. *Journal of Tribology* 135(1), p. 011501. doi: 10.1115/1.4007693.

Evans, H.P. et al. 2013. Analysis of Micro-Elastohydrodynamic Lubrication and Prediction of Surface Fatigue Damage in Micropitting Tests on Helical Gears. *Journal of Tribology* 135(1), pp.1–9. Available at: <http://tribology.asmedigitalcollection.asme.org/article.aspx?doi=10.1115/1.4007693>.

Evans, H.P. and Hughes, T.G. 2000. Evaluation of deflection in semi-in finite bodies by a differential method. *Proc Instn Mech Engrs* 214, pp. 563–584.

Freeth, T. et al. 2006. Decoding the ancient Greek astronomical calculator known as the Antikythera Mechanism. 444(November), pp. 587–591. doi: 10.1038/nature05357.

Fatemi, A. and Yang, L. Cumulative fatigue damage and life prediction theories: a survey of the state of the art for homogeneous materials. *International Journal of Fatigue*, 1998; 20(1): 9-34.

Fatemi, A. and Socie, D.F., 1988. A Critical Plane Approach to Multiaxial Fatigue Damage Including out-of-Phase Loading. *Fatigue and Fracture of Engineering Materials and Structures*, 11(3), pp.149-165.

Fatemi A., Stephens R.I, Stephens R.R. and Fuchs H.O. 2000. *Metal Fatigue in Engineering*, Wiley Interscience.

Ghosh, A. and Sadeghi, F. 2015. A novel approach to model effects of surface roughness parameters on wear. *Wear* 338–339, pp. 73–94. Available at: <http://dx.doi.org/10.1016/j.wear.2015.04.022>.

Gould, B. and Greco, A. 2016. Investigating the Process of White Etching Crack Initiation in Bearing Steel. *Tribology Letters* 62(2), pp. 1–14. doi: 10.1007/s11249-016-0673-z.

Greenwood, J.A. 1992. Fundamentals of Friction: Macroscopic and Microscopic Processes. In: *Contact of rough surfaces*. Dordrecht: Springer Netherlands, pp. 37–56.

Greenwood, J.A. and Williamson, J.B.P. 1966. Contact of Nominally Flat Surfaces. *Proceedings of the Royal Society of London. Series A, Mathematical and Physical Sciences (1934-1990)* 295(1442), pp. 300–319.

Grubin, A.N. and Vinogradova, I.E. 1949. Investigation of the Contact of Machine Components. Central Scientific Research Institute for Technology and Mechanical Engineering Book No 30(DSIR Translation No 337).

Hamrock, B.J. and Anderson, W.J. 1983. NASA Reference Publication 1105. Rolling-element bearings.

Hertz, H. 1882. On the contact of elastic solids. *J. reine angew. Math* 92, pp. 156–171.

Hamrock, B.J., Schmid, S.R. and Jacobson, B.O., 2004. *Fundamentals of fluid film lubrication*. CRC press.

Holmberg, K. and Matthews, A. 2009. *Coatings tribology: properties, mechanisms, techniques and applications in surface engineering*. Amsterdam, The Netherlands.

Holmes, M.J.A. et al. 2005. Analysis of Mixed Lubrication Effects in Simulated Gear Tooth Contacts. In: Tribology-Transactions of the Asme. ASME, pp. 61–69. Available at:

<http://proceedings.asmedigitalcollection.asme.org/proceeding.aspx?articleid=1647178> [Accessed: 15 June 2018].

Hornig, J. et al. 2002. The contact characteristics of rough surfaces in line contact during running-in process. *Wear* 253, pp. 899–913.

Hutchings, L.M. 1992. Tribology: Friction and wear of engineering materials.

Hutchings, I.M. 2003. Tribology: Friction and Wear of Engineering Materials. Oxford: Butterworth- Heinemann.

Hutt, S. et al. 2018. Generation of Acoustic Emission from the running-in and subsequent micropitting of a mixed-elastohydrodynamic contact. *Tribology International* 119(July), pp. 270–280. Available at: <https://doi.org/10.1016/j.triboint.2017.11.011>.

Hughes, T.G., Elcoate, C.D. and Evans, H.P., 2000. Coupled solution of the elastohydrodynamic line contact problem using a differential deflection method. *Proceedings of the Institution of Mechanical Engineers, Part C: Journal of Mechanical Engineering Science*, 214(4), pp.585- 598.

Holmes, M.J. Transient analysis of the point contact elastohydrodynamic lubrication problem using coupled solution methods. PhD thesis, University of Wales, 2002.

Holmes, M.J.A., Evans, H.P., Hughes, T.G. and Snidle, R.W., 2003a. Transient elastohydrodynamic point contact analysis using a new coupled differential deflection method Part 1: Theory and validation. *Proceedings of the Institution of Mechanical Engineers, Part J: Journal of Engineering Tribology*, 217(4), pp.289-304.

Holmes, M.J.A., Evans, H.P., Hughes, T.G. and Snidle, R.W., 2003b. Transient elastohydrodynamic point contact analysis using a new coupled differential deflection method Part 2: Results. *Proceedings of the Institution of Mechanical Engineers, Part J: Journal of Engineering Tribology*, 217(4), pp.305-322.

Holmes, M.J.A., Qiao, H., Evans, H.P. and Snidle, R.W., 2005. Surface contact and damage in micro-EHL. *Tribology and interface engineering series*, 48, pp.605-616.

Houpert L.G., Hamrock B.J., 1986. Fast approach for calculating film thicknesses and pressures in elastohydrodynamically lubricated contacts at heavy loads. *J. Tribol.* 108, 411–420.

Horng, J.H., Len, M.L. and Lee, J.S., 2002. The contact characteristics of rough surfaces in line contact during running-in process. *Wear*, 253(9), pp.899-913.

Ichimaru, et al. 1992. Effect of Lubricant Additives on Scoring-Proof Capability of Gear Oils. *JSME Int* 35(4), pp. 652–659. Available at: https://www.jstage.jst.go.jp/article/cpb1958/33/4/33_4_1660/article.

ISO-Standardized Filtering for DektakXT Stylus Profilers. 2019. Available at: <https://www.azom.com/article.aspx?ArticleID=12816> [Accessed: 9 May 2019].

Jackson A., Webster M.N., J.C.E. 1994. The Effect of Lubricant Traction on Scuffing. *Tribol. Trans.* 37(2), pp. 387–395.

James, S.R. et al. 1989. Hominid Use of Fire in the Lower and Middle Pleistocene: A Review of the Evidence. *Current Anthropology* 30(1), pp. 1–26.

Jeng, Y.-R. et al. 2004. Changes of Surface Topography During Running-In Process. *Journal of Tribology* 126(July), pp. 620–625. doi: 10.1115/1.1759344.

Jenson, A.D. et al. 2018. The evolution of hardness and tribo film growth during running-in of case carburized steel under boundary lubrication. *Tribology International* 118(May), pp. 1–10. doi: 10.1016/j.triboint.2017.09.019.

Johnson, K. 1989. The strength of surfaces in rolling contact. *Proceedings of the Institution of Mechanical Engineers, Part C: Journal of Mechanical Engineering Science*, 203, pp. 151-163.

Jost, P. (1966), *Lubrication (Tribology) – A Report on the Present Position and Industry's Needs*, Dept. of Education and Science, H.M. Stationary Office, London.

Johnson, K.L. 1985. *Contact mechanics*. Cambridge university press.

Johnson, K.L. and Tavaarwerk, J.L., 1977, “Shear Behaviour of Elastohydrodynamic Films”, *Proc. R. Soc. Lond. A.*, Vol. 356, pp. 215 – 236.

Kadicic, A. and Rycerz, P. 2016. Influence of Contact Conditions on the Onset of Micropitting in Rolling-Sliding Contacts Pertinent to Gear Applications. AGMA Technical Paper.

Kang, J. et al. 2014. A Rolling contact fatigue in martensitic: Subsurface hardening and crack formation. *Materials Science & Engineering A* 607, pp. 328–333. Available at: <http://dx.doi.org/10.1016/j.msea.2014.03.143>.

Kim, H.J., Ehret, P., Dowson, D. and Taylor, C.M., 2001. Thermal elastohydrodynamic analysis of circular contacts part 2: Non-Newtonian model. *Proceedings of the Institution of Mechanical Engineers, Part J: Journal of Engineering Tribology*, 215(4), pp.353-362.

Kragelsky, I. et al. 1982. Running-in and equilibrium roughness. *Frict Wear*, pp. 297–316.

Kumar, R. et al. 2002. A systematic methodology to characterise the running-in and steady-state wear processes. 252, pp. 445–453.

Korres, S. 2013. *On-Line Topographic Measurements of Lubricated Metallic Sliding Surfaces*, KIT Scientific Publishing.

Lainé, E. et al. 2008. Effect of lubricants on micropitting and wear. Available at: https://ac.els-cdn.com/S0301679X08000777/1-s2.0-S0301679X08000777-main.pdf?_tid=7fda1ea5-692d-4e05-afc6-44358830bd54&acdnat=1528722399_eebec8ec9d9d1a3f51610b917eb1ccfa [Accessed: 11 June 2018].

Larsson, R. et al. 2011. Elastohydrodynamic lubrication friction mapping – the influence of lubricant, roughness, speed, and slide-to-roll ratio. *Engineering Tribology* 225(7), pp. 671–681. doi: 10.1177/1350650111403363.

Leighton, M. et al. 2016. Boundary interactions of rough non-Gaussian surfaces. *Proceedings of the Institution of Mechanical Engineers* 230(11), pp. 1359–1370. doi: 10.1177/1350650116656967.

Li, S. 2013. Influence of Surface Roughness Lay Directionality on Scuffing Failure of Lubricated Point Contacts. *Journal of Tribology* 135(October), pp. 1–10. doi: 10.1115/1.4024783.

Li, S. 2015. Influence of Surface Roughness Lay Directionality on Scuffing Failure of Lubricated Point Contacts. *Journal of Tribology* 135(4), p. 41502. Available at: <http://dx.doi.org/10.1115/1.4024783>.

Li, S. and Kahraman, A. 2013. Micro-pitting fatigue lives of lubricated point contacts: Experiments and model validation. *International Journal of Fatigue* 48, pp.9–18. Available at: https://ac.els-cdn.com/S0142112312003507/1-s2.0-S0142112312003507_main.pdf?_tid=786df7a8-1eaf-42a2-8edd59e5829ffa33&acdnat=1528829543_21f66d629d8b34933f9e9d887ec2b280 [Accessed: 12 June 2018].

Mang, T., Bobzin, K., Bartels, T., 2011. *Industrial Tribology: Tribosystems, Friction, Wear and Surface Engineering, Lubrication*. WILEY-VCH Verlag GmbH & Co. KGaA, Weinheim.

Martin, H.M., 1916, “The lubrication of gear teeth”, *Engineering*, v.1 02, pp. 199-204.

Maeda, K. et al. 1980. The inclination of cracking in the peeling failure of a ball bearing steel and its relation to the inclination of the principal residual stress. *Wear* 65(2), pp. 175–190. Available at: <https://www.sciencedirect.com/science/article/abs/pii/0043164880900204> [Accessed: 12 June 2018].

Mallipeddi, D. et al. 2017. Tribology International Influence of running-in on surface characteristics of efficiency tested ground gears. *Tribology International journal* 115, pp. 45–58. doi: 10.1016/j.triboint.2017.05.018.

Mallipeddi, D. et al. 2018. Influence of running-in on surface characteristics of efficiency tested ground gears. *Tribology International* 115, pp. 45–58. doi: 10.1016/j.triboint.2017.05.018.

Mallipeddi, D. et al. 2019. The effect of manufacturing method and running-in load on the surface integrity of efficiency tested ground, honed and super finished gears. *Tribology International* 131(October 2018), pp. 277–287. doi: 10.1016/j.triboint.2018.10.051.

Mayali, M. F.A.L. et al. 2018. Experimental and Numerical Study of Micropitting Initiation in Real Rough Surfaces in a Micro-elastohydrodynamic Lubrication Regime. *Tribology Letters* 66(4), pp. 1–14. Available at: <http://dx.doi.org/10.1007/s11249-018-1110-2>.

Matsuishi, M. and Endo, T., 1968. Fatigue of metals subjected to varying stress. *Japan Society of Mechanical Engineers, Fukuoka, Japan*, 68(2), pp.37-40.

Meeker, W.Q. and Escobar, L.A. 1998. *Statistical Methods for Reliability Data*. John Wiley & Sons, New York.

Merritt, H. E. 1935. Worm Gear Performance. *Proceedings of the Institution of Mechanical Engineers*, 129, 127-194.

Miner, M. A. Cumulative damage in fatigue. *J. Appl. Mech.*, 1945, 12, 159–164.

Musallam, M. and Johnson, C.M., 2012. An efficient implementation of the rainflow counting algorithm for life consumption estimation. *IEEE Transactions on Reliability*, 61(4), pp.978-986.

Morag, Y. and Etsion, I. 2007. Resolving the contradiction of asperities plastic to elastic mode transition in current contact models of fractal rough surfaces. *262(February)*, pp. 624–629. doi: 10.1016/j.wear.2006.07.007.

Morales-Espejel, G.E. et al. 2018. Prediction of micropitting damage in gear teeth contacts considering the concurrent effects of surface fatigue and mild wear. *Wear* 398–399(June 2017), pp. 99–115. Available at: <https://doi.org/10.1016/j.wear.2017.11.016>.

Morales, E. and Gabelli, A. 2018. Rolling bearing seizure and sliding effects on fatigue life. *Engineering tribology*, pp. 1–16. Available at: <http://journals.sagepub.com/doi/pdf/10.1177/1350650118779174> [Accessed: 12 June 2018].

Nakatsuji, T. and Mori, A. 1998. Tribological Properties of Electrolytically Polished Surfaces of Carbon Steel. *41(2)*, pp. 179–188. doi: 10.1080/10402009808983737.

Nogueira, I. et al. 2002. An experimental model for mixed friction during running-in. *Wear* 253, pp. 541–549.

Novex.com 2018. online. Available at: <https://www.novexa.com/audit/>.

Oila, A. 2003. Micropitting in Phenomena Related and Case Carburised Gears. PhD thesis, Newcastle Upon Tyne University.

Oila, A. et al. 2005. Martensite decay in micropitted gears. Proceedings of the Institution of Mechanical Engineers, Part J: Journal of Engineering Tribology 219(2), pp. 77–83. doi: 10.1243/135065005X9790.

Oila, A. and Bull, S.J. 2005. Assessment of the factors influencing micropitting in rolling/sliding contacts. Wear 258, pp. 1510–1524. Available at: https://ac.els-cdn.com/S0043164804004065/1-s2.0-S0043164804004065_main.pdf?_tid=64bb59ca-4912-48d184363316e7688ea9&acdnat=1528829435_2eecd094a728e0afc2ca9b31983a811 [Accessed: 12 June 2018].

Ostvik, R. and Christensen, H. 1968. Changes in surface topography with running-in. In Proceedings of the Institution of Mechanical Engineers 183(16), pp. 57–65.

Pang, G.B. et al. 2009. Surface Topography Characteristic and Statistical Characteristic of 1Cr18Ni9Ti Polished by Electrochemical Polishing. Materials Science Forum. Trans Tech Publications, pp. 309–314. doi: 10.4028/www.scientific.net/MSF.626-627.309.

Patching, M.J. et al. 1995. Conditions for Scuffing Failure of Ground and Superfinished Steel Disks at High Sliding Speeds Using a Gas Turbine Engine Oil. Journal of Tribology 117(3), p. 482. Available at: <http://tribology.asmedigitalcollection.asme.org/article.aspx?articleid=1460671>.

Patching, M.J. et al. 1996. Micro-EHL Analysis of Ground and Superfinished Steel Discs Used to Simulate Gear Tooth Contacts. Tribology Transactions 39(3), pp. 595–602. Available at: <https://doi.org/10.1080/10402009608983571>.

Patching, M. J., Kweh, C. C., Evans, H. P. & Snidle, R. W. 1995. Conditions for Scuffing Failure of Ground and Superfinished Steel Disks at High Sliding Speeds Using a Gas Turbine Engine Oil. Journal of Tribology, 117, 482-489.

Palmgren, A. Die Lebensdauer von Kugellagern. Z. Ver. Deutsch. Ing., 1924, 68, 339–341.

Pflumm, M.F. and Botchan, M.R. 2001. Orc mutants arrest in metaphase with abnormally condensed chromosomes. doi: 10.1007/978-0-387-92897-5.

Pogacnik, A. and Kalin, M. 2013. How to determine the number of asperity peaks, their radii and their heights for engineering surfaces: A critical appraisal. *wear* 300, pp. 143–154.

Popova, E. and Popov, V.L. 2015. On the history of elastohydrodynamics: The dramatic destiny of Alexander Mohrenstein-Ertel and his contribution to the theory and practice of lubrication. *ZAMM Zeitschrift für Angewandte Mathematik und Mechanik* 95(7), pp. 652–663. doi: 10.1002/zamm.201400050.

Prajapati, D.K. and Tiwari, M. 2019. Assessment of Topography Parameters During Running-In and Subsequent Rolling Contact Fatigue Tests. *Journal of Tribology* 141(May), pp. 1–13. doi: 10.1115/1.4042676.

Predki, P.W. et al. 2011. Micropitting of Big Gearboxes: Influence of Flank Modification and Surface Roughness. *Vdi* (May)

Qiao, H. 2005. Prediction of Contact Fatigue for the Rough Surface Elastohydrodynamic Lubrication Line Contact Problem under Rolling and Sliding Conditions. PhD thesis, Cardiff University.

Otto, H.-P. 2009. “Flank Load Carrying Capacity and Power Loss Reduction by Minimized Lubrication.” Diss., TU München.

Okamura, H., 1982. A contribution to the numerical analysis of isothermal elastohydrodynamic lubrication. *Proceedings of 9th Leeds-Lyon Symposium on Tribology, Leeds*, pp. 313–320.

Rao, J. S., Pathak, A., and Chawla, A. Blade life: a comparison by cumulative damage theories. *Transactions of the ASME, Journal of Engineering for Gas Turbines and Power*, 2001; 123: 886-892.

Reynolds, O., 1875. On rolling friction. *Phil. Trans. R. Soc.*, 166, Pt1, 155.

Reynolds, O. 1886. On the Theory of Lubrication and Its Application to Mr. Beauchamp Tower’s Experiments, Including an Experimental Determination of the Viscosity of Olive Oil. *Proceedings of the Royal Society of ...* 177, pp. 157–234.

Roelands, C. J. A. 1966. Correlation aspects of the viscosity-temperature-pressure relationship of lubricating oils. PhD PhD, Technical University Delft.

Sharif, K.J. et al. 2012. Modelling of elastohydrodynamic lubrication and fatigue of rough surfaces: The effect of lambda ratio. *Proceedings of the Institution of Mechanical Engineers, Part J: Journal of Engineering Tribology* 226(12), pp. 1039–1050. doi: 10.1177/1350650112458220.

Sherrington, I., University of Central Lancashire, 2009. Lubrication control system. U.S. Patent 7,552,799.

Sharif, K. J., Kong, S., Evans, H. P. & Snidle, R. W. 2001. Contact and elastohydrodynamic analysis of worm gears Part 1: Theoretical formulation. *Proceedings of the Institution of Mechanical Engineers, Part C: Journal of Mechanical Engineering Science*, 215, 817-830.

Singer, C., Holmyard, E.J., Hall, A.R. (eds), 1954. *A History of Technology. Vol I: From Ancient times to Fall of Ancient Empires.* Oxford: Oxford U.P.

Sjöberg, S. et al. 2016. Analysis of efficiency of spur ground gears and the in fluency of running-in. 93, pp. 172–181. doi: 10.1016/j.triboint.2015.08.045.

Snidle, R.W. et al. 2008. Scuffing Performance of a Hard Coating Under EHL Conditions at Sliding Speeds up to 16 m/s and Contact Pressures up to 2.0 GPa. *Journal of Tribology* 130(2), p. 021301. Available at: <http://www.scopus.com/inward/record.url?eid=2-s2.0-46049119692&partnerID=tZOtx3y1>.

Snidle, R.W. and Zhang, J. 2013. Analysis of Micro- Elastohydrodynamic Lubrication and Prediction of Surface Fatigue Damage in Micropitting Tests on Helical Gears. 135(January), pp. 1–9. doi: 10.1115/1.4007693.

Snidle, R. W., Evans, H. P., Alanou, M. P. and Holmes, M. J. A. 2004. Understanding scuffing and micropitting of gears. Presented at: Paper presented at NATO Research and Technology Organisation Specialists' Meeting on The Control and Reduction of Wear in Military Platforms, Virginia, USA, vol. RTO-MP. NATO Publication.

Sosa, M. et al. 2017. In situ running-in analysis of ground gears. *Wear* 352–353, pp. 122–129. doi: 10.1016/j.wear.2016.01.021.

Spikes, H.A. et al. 1986. Wear in rolling contacts. *Wear* 112(2), pp. 121–144. Available at: <https://www.sciencedirect.com/science/article/abs/pii/004316488690236X> [Accessed: 12 June 2018].

Stadtfeld, H.J. and Saewe, J.K. 2015. Non-Involute Gearing, Function and Manufacturing Compared to Established Gear Designs. *Gear Technology* (February), pp. 42–51.

Stanley, H.M. et al. 1990. Adhesion of Contacting Rough Surfaces in the Presence of Sub- Boundary Lubrication. *Transactions of the ASME* 112(January), pp. 98–104.

Stachowiak, G. and Batchelor, A.W., 2013. *Engineering tribology*. Butterworth-Heinemann.

Suresh, S., 1998. *Fatigue of materials*. Cambridge university press.

Tabor, D. 1951. *The Hardness of Metals*, Oxford, UK, Clarendon Press.

Tao, J. et al. 2003. Elastohydrodynamic Lubrication Analysis of Gear Tooth Surfaces from Micropitting Tests. *Journal of Tribology* 125(2), p. 267. Available at: http://orca.cf.ac.uk/2099/1/Elastohydrodynamic_Lubrication.pdf [Accessed: 12 June 2018].

Tallian TE. 1967 On competing failure modes in rolling contact. *ASLE Trans.* 10, 418-439. (doi:10.1080/05698196708972201).

Teer, D.G. and Arnell, R.D. 1975. Friction Theories. In: Halling, J. ed. *Principles of Tribology*. London and Basingstoke: The Macmillan Press Ltd., pp. 72–93.

Timoshenko, S., and Goodier, J.N. 1973. *Theory of Elasticity*, 3rd Edn. New York, London et al.: McGraw-Hill.

Tokuda, R. 1982. Observations of the Peeling of Failure and Surface-Originated Flaking from a Ring-to-Ring Rolling Contact Fatigue Test Rig. (511), pp. 150–165.

Tripathi, K. et al. 2017. Synergy Effect of Ultrasonic Nanocrystalline Surface Modification and Laser Surface Texturing on Friction and Wear Behavior of Graphite Cast Iron Synergy Effect of Ultrasonic Nanocrystalline Surface Modification and

Laser Surface. *Tribology Transactions* 60(2), pp. 226–237. Available at: <http://dx.doi.org/10.1080/10402004.2016.1158339>.

Turteltaub, S.Ã. and Suiker, A.S.J. 2005. Transformation-induced plasticity in ferrous alloys. *Journal of the Mechanics and Physics of Solids* 53, pp. 1747–1788. doi: 10.1016/j.jmps.2005.03.004.

Tudor, G. K. 1948. An Electrical Method of Investigating the Lubrication in a Journal Bearing. *Journal of C.S.I.R.*, 21, 202-209.

Vrček, A. et al. 2019. Micro-pitting Damage of Bearing Steel Surfaces under Mixed Lubrication Conditions: Effects of Roughness, Hardness and ZDDP Additive. *Tribology International* 138(April), pp. 239–249. Available at: <https://linkinghub.elsevier.com/retrieve/pii/S0301679X1930297X>.

Wagner, J.J. et al. 2017. The effect of contact pressure and surface texture on running-in behavior of case carburized steel under boundary lubrication. *Wear* 376–377, pp. 851–857. Available at: <http://dx.doi.org/10.1016/j.wear.2017.02.016>.

Wang, W. et al. 2000. Experimental study of the real time changes in surface roughness during running-in for PEHL contacts. *Wear* 244, pp. 140–146.

Way, S. 1935. Pitting Due to Rolling Contact. *ASME J. of Applied Mecanics* 2, pp. A49–A58. Available at: <https://ci.nii.ac.jp/naid/10016694142/> [Accessed: 12 June 2018].

Webster, M.N. and Norbart, C.J.J. 1995. An Experimental Investigation of Micropitting Using a Roller Disk Machine. *Tribology Transactions* 38(4), pp. 883–893. Available at: <http://www.tandfonline.com/doi/abs/10.1080/10402009508983485> [Accessed: 12 June 2018].

Webster, M.N. and Norbart, C.J.J. 2008. An Experimental Investigation of Micropitting Using a Roller Disk Machine. *Tribology Transactions* 38(4), pp. 883–893. Available at: <http://www.tandfonline.com/doi/abs/10.1080/10402009508983485> [Accessed: 12 June 2018].

Weeks, I. 2015. An Experimental Investigation into the Mixed Lubrication of Steel Surfaces. Cardiff University.

Whitehouse, D.J. and Archard, J.F. 1970. The properties of random surfaces of significance in their contact. *Roy. Soc. Lond* 316, pp. 97–121.

Winter, P.H. and Oster, D.P. 1990. Influence of Lubrication on Pitting and Micropitting Resistance of Gears. *Gear Technology*, pp. 16–23. doi: 10.1016/0142-1123(91)90105-8.

Williams, P. A., Finnis, M. P. & Kelly, D. A. 1988. History Dependence in 2-Disc Scuffing Tests. *Proceedings of the Institution of Mechanical Engineers Part C-Journal of Mechanical Engineering Science*, 202, 211-218.

Williams, J. 1994. *Engineering tribology*, Cambridge University Press.

Xiao, L. et al. 2003. A study on the effect of surface topography on rough friction in roller contact. *Wear* 254, pp. 1162–1169. doi: 10.1016/S0043-1648(03)00329-6.

Zahavi, E., Torbilo, V. and Press, S., 1996. *Fatigue design: life expectancy of machine parts*. CRC press.

Zhang, Y. et al. 2018. Numerical Prediction of Surface Wear and Roughness Parameters During Running-In for Line Contacts Under Mixed Lubrication. *Transactions of the ASME* 140(November), pp. 1–13. doi: 10.1115/1.4039867.

Zhou, R.S. et al. 1989. Micropitting in Rolling and Sliding Contact Under Mixed Lubrication. *Journal of Tribology* 111(4), p. 605. Available at: <http://tribology.asmedigitalcollection.asme.org/article.aspx?articleid=1459551>.

Zhu, D. et al. 2009. Pitting Life Prediction Based on a 3D Line Contact Mixed EHL Analysis and Subsurface von Mises Stress Calculation. *Journal of Tribology* 131(4), p. 041501. Available at: <http://tribology.asmedigitalcollection.asme.org/article.aspx?articleid=1468342>.

Zhu, H. et al. 2007. The changes of fractal dimensions of frictional signals in the running-in wear process. *Wear* 263, pp. 1502–1507. doi: 10.1016/j.wear.2007.02.011.

Zhu, D. & WANG, Q. 2013. Effect of Roughness Orientation on the Elastohydrodynamic Lubrication Film Thickness. *Journal of Tribology*, 135, 031501-031501.

Zhuravlev, V.A. 1940. On the question of theoretical justification of the Amontons – Coulomb law for friction of unlubricated surfaces. Journal of Technical Physics 10(17), pp. 1447–1452. doi: 10.1243/13506501JET176.

Appendix

Theory of changing the radius of curvature and the governing equations

$$h_m = \sum \frac{h(i)}{n}$$

Where h_m is a mean height, $h(i)$ is the height of the i th point, n is a number of peaks.

$$std.deviation = \sqrt{\sum (h(i) - h_m)^2}$$

Three point asperities:

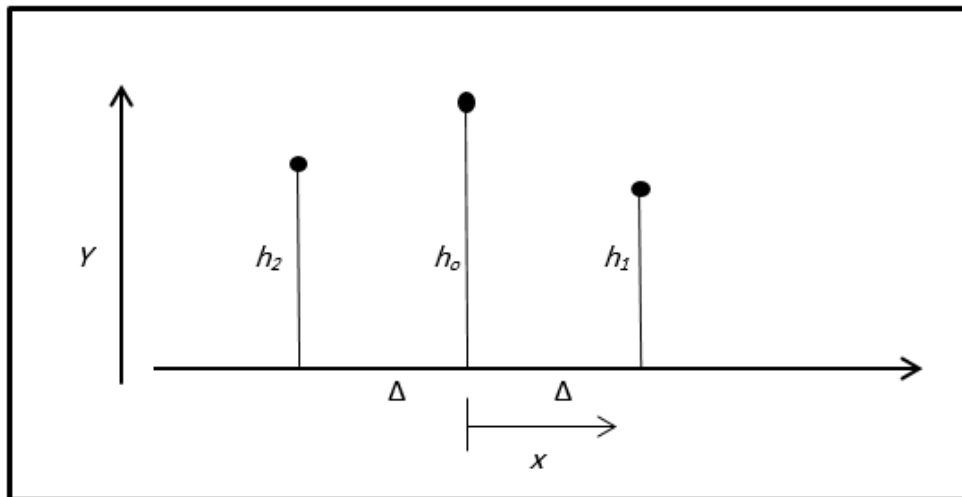


Figure 1 Shows three point asperities

$$R = \frac{-\left(1 + \left(\frac{dy}{dx}\right)^2\right)^{\frac{3}{2}}}{\left(\frac{d^2y}{dx^2}\right)}$$

Where R is Radius of curvature of $y=f(x)$. The minus sign is so that the surface in Figure 1 has opposite (convex) radius of curvature.

The equation of the parabola through these points is

$$y = h_o + \left(\frac{h_1 - h_2}{2\Delta} \right) x + \left(\frac{h_1 + h_2 - 2h_o}{2\Delta^2} \right) x^2 \quad (1)$$

$$\frac{dy}{dx} = \left(\frac{h_1 - h_2}{2\Delta} \right) + \left(\frac{h_1 + h_2 - 2h_o}{\Delta^2} \right) x \quad (2)$$

$$\frac{d^2 y}{dx^2} = \frac{h_1 + h_2 - 2h_o}{\Delta^2} \quad (3)$$

$$R = \frac{- \left[1 + \left\{ \left(\frac{h_1 - h_2}{2\Delta} \right) + 2 \left(\frac{h_1 + h_2 - 2h_o}{2\Delta^2} \right) x \right\}^2 \right]^{\frac{3}{2}}}{\frac{h_1 + h_2 - 2h_o}{\Delta^2}} \quad (4)$$

At $x=0$ the radius of curvature is

$$R_3 = \frac{- \Delta^2 \left(1 + \left(\frac{h_1 - h_2}{2\Delta} \right)^2 \right)^{\frac{3}{2}}}{h_1 + h_2 - 2h_o} \quad (5)$$

This gives current R_3 value at the peak point where suffix 3 denotes the radius of curvature based on three points (see Figure 1).

Consider that the reduction in height of h_o is Δh

Model for change

$$R_{\text{new}} = (1 + \gamma)R$$

Where γ is a parameter to be specified.

$$R_{\text{new}} = R + \Delta R$$

$$R_{new} = \frac{-\Delta^2 \left[1 + \left\{ \frac{h_1 - h_2}{2\Delta} \right\}^2 \right]^{\frac{3}{2}}}{h_1 + h_2 - 2(h_o - \Delta h)}$$

$$h_1 + h_2 - 2(h_o - \Delta h) = \frac{-\Delta^2 \left[1 + \left\{ \frac{h_1 - h_2}{2\Delta} \right\}^2 \right]^{\frac{3}{2}}}{R_{new}}$$

$$\Delta h = \frac{2h_o - h_1 - h_2}{2} - \frac{\Delta^2 \left[1 + \left\{ \frac{h_1 - h_2}{2\Delta} \right\}^2 \right]^{\frac{3}{2}}}{2R_{new}} \quad (6)$$

Four point asperities:

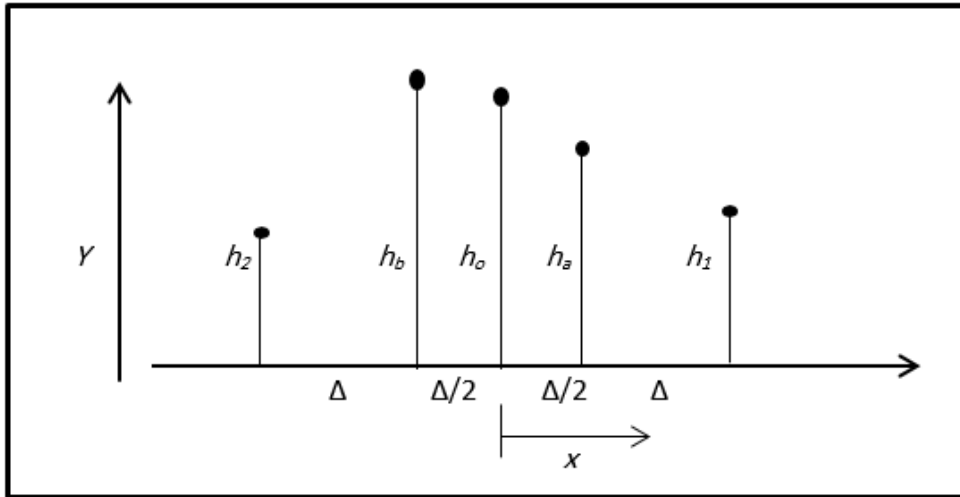


Figure 2 Shows four point asperities.

For the situation where one of the neighbours of the point under consideration is of similar height an alternative approach is to consider four points as defining the asperity shape. This is shown in Figure 2 where the neighbouring local high points are h_a and h_b , and h_o is a fictitious point midway between h_a and h_b . The parabola passing through h_1 , h_o and h_2 is

$$y = h_o + \left(\frac{h_1 - h_2}{2(1.5\Delta)} \right) x + \left(\frac{h_1 + h_2 - 2h_o}{2(1.5\Delta)^2} \right) x^2 \quad (7)$$

At $x = \Delta/2$

$$h_a = h_o + \left(\frac{h_1 - h_2}{3\Delta} \right) \frac{\Delta}{2} + \left(\frac{h_1 + h_2 - 2h_o}{4.5\Delta^2} \right) \left(\frac{\Delta}{2} \right)^2$$

$$h_a = h_o + \frac{h_1 - h_2}{6} + \frac{h_1 + h_2 - 2h_o}{18} = f_1(h_o) \quad (8)$$

At $x = -\Delta/2$

$$h_b = h_o - \frac{h_1 - h_2}{6} + \frac{h_1 + h_2 - 2h_o}{18} = f_2(h_o) \quad (9)$$

To obtain the best fit curve and make error equal zero

$$h_a - f_1(h_o) = f_2(h_o) - h_b$$

$$h_a - h_o - \frac{h_1 - h_2}{6} - \frac{h_1 + h_2 - 2h_o}{18} = h_o - \frac{h_1 - h_2}{6} + \frac{h_1 + h_2 - 2h_o}{18} - h_b$$

$$h_a + h_b = 2h_o + \frac{h_1 + h_2 - 2h_o}{9}$$

$$h_o = \frac{9(h_a + h_b) - h_1 - h_2}{16} \quad (10)$$

At $x=0$, the Radius of curvature for four point asperities is found by differentiating equation (7) gives

$$\frac{dy}{dx} = \left(\frac{h_1 - h_2}{3\Delta} \right) + \left(\frac{h_1 + h_2 - 2h_o}{2.25\Delta^2} \right) x \quad (11)$$

$$\frac{d^2 y}{dx^2} = \frac{h_1 + h_2 - 2h_o}{2.25\Delta^2} \quad (12)$$

And this is regarded as the radius of curvature of the asperity.

$$R_4 = \frac{-\left(1 + \left(\frac{h_1 - h_2}{3\Delta}\right)^2\right)^{\frac{3}{2}}}{\frac{h_1 + h_2 - 2h_o}{2.25\Delta^2}}$$

$$R_4 = \frac{-2\Delta^2 \left(1 + \left(\frac{h_1 - h_2}{3\Delta}\right)^2\right)^{\frac{3}{2}}}{h_1 + h_2 - h_a - h_b} \quad (13)$$

If radius is to change to R_{new}

$$R_{new} = R + \Delta R$$

$$h_1 + h_2 - 2(h_o - \Delta h_o) = -2.25\Delta^2 \frac{\left(1 + \left(\frac{h_1 - h_2}{3\Delta}\right)^2\right)^{\frac{3}{2}}}{R_{new}}$$

$$\Delta h_o = \frac{2h_o - h_1 - h_2}{2} - 1.125\Delta^2 \frac{\left(1 + \left(\frac{h_1 - h_2}{3\Delta}\right)^2\right)^{\frac{3}{2}}}{R_{new}} \quad (14)$$

New asperity shape has h_a and h_b modified to

$$h_{a_new} = h_o - \Delta h_o + \frac{h_1 - h_2}{6} + \frac{h_1 + h_2 - 2(h_o - \Delta h_o)}{18}$$

$$h_{a_new} = \frac{16h_o + 4h_1 - 2h_2}{18} - \frac{8\Delta h_o}{9}$$

$$h_{a_new} = \frac{9(h_a + h_b) - h_1 - h_2 + 4h_1 - 2h_2}{18} - \frac{8\Delta h_0}{9}$$

$$h_{a_new} = \frac{3(h_a + h_b) + h_1 - h_2}{6} - \frac{8\Delta h_0}{9} \quad (15)$$

$$h_{b_new} = h_o - \Delta h_0 - \frac{h_1 - h_2}{6} + \frac{h_1 + h_2 - 2(h_o - \Delta h_0)}{18}$$

$$h_{b_new} = \frac{16h_o - 2h_1 + 4h_2}{18} - \frac{8\Delta h_0}{9}$$

$$h_{b_new} = \frac{3(h_a + h_b) - h_1 + h_2}{6} - \frac{8\Delta h_0}{9} \quad (16)$$

Least squares Curve Fitting

Principle of least squares provides a unique set of values to the constants and hence suggests a curve of best fit to the given data. The method of least squares is probably the most systematic procedure to fit a unique curve through the given data points.

Fitting of Parabola

The general parabola equation is

$$y = a + bx + cx^2$$

$$\varepsilon = \sum_{i=1}^n (d_i)^2$$

Where d is the vertical distance between the known data and the fit function. Moreover, it represents the residual for the data pair (x_i, y_i) .

$$\varepsilon = \sum_{i=1}^n (y_i - (a_i + bx_i + cx_i^2))^2$$

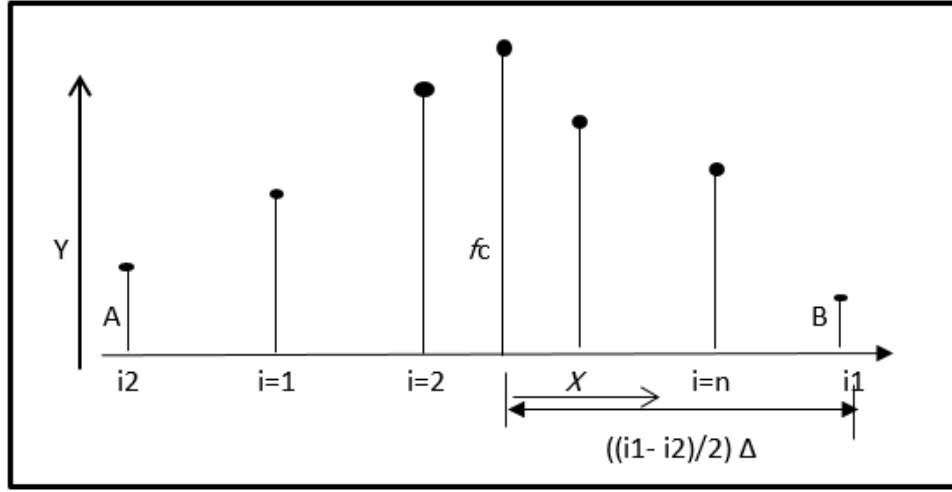


Figure 3 Shows (n) number of point asperities with fixed the end points.

Let the parabola that passes through points A and B be (see Figure 3).

$$f = f_c + \left(\frac{h_{i1} - h_{i2}}{(i1 - i2)\Delta} \right) x + \frac{2(h_{i2} + h_{i1} - 2f_c)}{(i1 - i2)^2 \Delta^2} x^2$$

$$f = f_c + F_1 x + [F_2 + F_3 f_c] x^2 \quad (17)$$

$$F_1 = \left(\frac{h_{i1} - h_{i2}}{(i1 - i2)\Delta} \right), \quad F_2 = \frac{2(h_{i1} + h_{i2})}{(i1 - i2)^2 \Delta^2}, \quad F_3 = \frac{-4}{(i1 - i2)^2 \Delta^2} \quad (18)$$

At $x=0$

$$f = f_c + F_1 * (0) + [F_2 + F_3 f_c] (0)^2$$

$$f = f_c$$

$$\text{At } x = \frac{+}{-} \left(\frac{i1 - i2}{2} \right) \Delta$$

$$f = f_c + \left(\frac{h_{i1} - h_{i2}}{2} \right) + \frac{2(h_{i2} + h_{i1} - 2f_c)}{(i1 - i2)^2 \Delta^2} * \frac{(i1 - i2)^2}{4} \Delta^2$$

$$f = f_c + \left(\frac{h_{i1} - h_{i2}}{2} \right) + \frac{(h_{i2} + h_{i1} - 2f_c)}{2}$$

$$f = f_c + \left(\frac{h_{i1} - h_{i2}}{2} \right) + \frac{(h_{i2} + h_{i1})}{2} - f_c$$

$$f = + \left(\frac{h_{i1} - h_{i2}}{2} \right) + \frac{(h_{i2} + h_{i1})}{2}$$

$$\text{At } x = + \left(\frac{i1 - i2}{2} \right) \Delta$$

$$f = h_{i1}$$

$$\text{At } x = - \left(\frac{i1 - i2}{2} \right) \Delta$$

$$f = h_{i2}$$

Error with data points $(x_i, y_i) \quad i = 1, n$

$$\varepsilon = \sum_{i=1}^n (h_i - f_i)^2$$

$$\varepsilon = \sum_{i=1}^n (h_i - F_1 x_i - F_2 x_i^2 - f_c - F_3 x_i^2 f_c)^2$$

Minimum error is when $\frac{\partial \varepsilon}{\partial f_c} = 0$

$$0 = 2 \sum_{i=1}^n (h_i - F_1 x_i - F_2 x_i^2 - f_c - F_3 x_i^2 f_c) * (-1 - F_3 x_i^2)$$

$$0 = 2 \sum_{i=1}^n (h_i - F_1 x_i - F_2 x_i^2 - f_c (1 + F_3 x_i^2)) * -(1 + F_3 x_i^2)$$

$$0 = -2 \sum_{i=1}^n (h_i - F_1 x_i - F_2 x_i^2 - f_c (1 + F_3 x_i^2)) * (1 + F_3 x_i^2)$$

$$0 = \sum_{i=1}^n (h_i - F_1 x_i - F_2 x_i^2 - f_c (1 + F_3 x_i^2)) * (1 + F_3 x_i^2)$$

$$0 = \sum_{i=1}^n (h_i - F_1 x_i - F_2 x_i^2) * (1 + F_3 x_i^2) - \sum_{i=1}^n f_c (1 + F_3 x_i^2)^2$$

$$f_c = \frac{\sum_{i=1}^n (h_i - F_1 x_i - F_2 x_i^2) * (1 + F_3 x_i^2)}{\sum_{i=1}^n (1 + F_3 x_i^2)^2}$$

$$f_c = \frac{\sum_{i=1}^n (h_i - F_1 x_i - F_2 x_i^2 + F_3 h_i x_i^2 - F_1 F_3 x_i^3 - F_2 F_3 x_i^4)}{\sum_{i=1}^n (1 + 2F_3 x_i^2 + F_3^2 x_i^4)}$$

$$f_c = \frac{\sum_{i=1}^n h_i - F_1 \sum_{i=1}^n x_i - F_2 \sum_{i=1}^n x_i^2 + F_3 \sum_{i=1}^n h_i x_i^2 - F_1 F_3 \sum_{i=1}^n x_i^3 - F_2 F_3 \sum_{i=1}^n x_i^4}{n + 2F_3 \sum_{i=1}^n x_i^2 + F_3^2 \sum_{i=1}^n x_i^4} \quad (19)$$

Moreover, calculate R from least-squares equation for n number of asperity points.

$$f = f_c + F_1 x + [F_2 + F_3 f_c] x^2 \quad i = 1, n$$

$$R = \frac{-\left(1 + \left(\frac{df}{dx}\right)^2\right)^{\frac{3}{2}}}{\left(\frac{d^2 f}{dx^2}\right)}$$

$$\frac{df}{dx} = F_1 + 2[F_2 + F_3 f_c] x$$

$$\frac{d^2 f}{dx^2} = 2[F_2 + F_3 f_c]$$

$$R = \frac{-\left(1 + (F_1 + 2[F_2 + F_3 f_c] x)^2\right)^{\frac{3}{2}}}{2[F_2 + F_3 f_c]}$$

At $x=0$ the radius of curvature is

$$R = \frac{-\left(1+(F_1)^2\right)^{\frac{3}{2}}}{2[F_2 + F_3 f_c]} \quad (20)$$

And if radius is to change to R_{new}

$$R_{new} = (1 + \gamma)R$$

$$R_{new} = \frac{-\left(1+(F_1)^2\right)^{\frac{3}{2}}}{2[F_2 + F_3(f_c - \Delta h)]}$$

$$2F_2 + 2F_3 f_c - 2F_3 \Delta h = \frac{-\left(1+(F_1)^2\right)^{\frac{3}{2}}}{R_{new}}$$

$$\Delta h = f_c + \frac{F_2}{F_3} + \frac{\left(1+F_1^2\right)^{\frac{3}{2}}}{2F_3 R_{new}} \quad (21)$$

New asperity shape for each point has modified to

$$f_{new} = f_c - \Delta h + F_1 x + [F_2 + F_3(f_c - \Delta h)]x^2 \quad (22)$$

When n=1 (3 point asperities)

$$F_1 = \left(\frac{h_{i1} - h_{i2}}{2\Delta}\right), \quad F_2 = \frac{2(h_{i1} + h_{i2})}{4\Delta^2}, \quad F_3 = \frac{-4}{4\Delta^2}$$

$$x_0 = 0$$

$$f_c = \frac{\sum_{i=1}^1 (h_0 - 0 - 0)}{\sum_{i=1}^1 (1 + 0)} = h_0$$

When n=2 (4 point asperities)

$$x_a = \Delta/2, \quad x_b = -\Delta/2$$

$$F_1 = \left(\frac{h_{i1} - h_{i2}}{3\Delta}\right), \quad F_2 = \frac{2(h_{i1} + h_{i2})}{9\Delta^2} = \frac{2(h_{i1} + h_{i2})}{9\Delta^2}, \quad F_3 = \frac{-4}{9\Delta^2}$$

$$f_c = \frac{\sum_{i=1}^2 (h_i - F_1 x_i - F_2 x_i^2) * (1 + F_3 x_i^2)}{\sum_{i=1}^2 (1 + F_3 x_i^2)^2}$$

$$f_c = \frac{(h_a - F_1 \frac{\Delta}{2} - F_2 \frac{\Delta^2}{4}) * (1 + F_3 \frac{\Delta^2}{4}) + (h_b + F_1 \frac{\Delta}{2} - F_2 \frac{\Delta^2}{4}) * (1 + F_3 \frac{\Delta^2}{4})}{2(1 + F_3 \frac{\Delta^2}{4})^2}$$

$$f_c = \frac{(h_a + h_b - F_2 \frac{\Delta^2}{2})}{2(1 + F_3 \frac{\Delta^2}{4})}$$

$$f_c = \frac{(h_a + h_b - \frac{2(h_{i2} + h_{i1}) \Delta^2}{(3)^2 \Delta^2} \frac{\Delta^2}{2})}{2(1 + (\frac{-4}{(3)^2 \Delta^2}) \frac{\Delta^2}{4})} = \frac{h_a + h_b - \frac{(h_{i2} + h_{i1})}{9}}{2(1 - \frac{1}{9})}$$

$$f_c = \frac{\frac{9(h_a + h_b) - h_{i2} - h_{i1}}{9}}{\frac{16}{9}} = \frac{9(h_a + h_b) - h_{i2} - h_{i1}}{16}$$

When n=3 (5 point asperities)

$$x_0=0, x_1= \Delta, x_2= -\Delta$$

$$F_1 = \left(\frac{h_{i1} - h_{i2}}{4\Delta} \right), \quad F_2 = \frac{2(h_{i1} + h_{i2})}{16\Delta^2}, \quad F_3 = \frac{-4}{16\Delta^2}$$

$$f_c = \frac{\sum_{i=1}^3 (h_i - F_1 x_i - F_2 x_i^2)}{\sum_{i=1}^3 (1 + F_3 x_i^2)}$$

$$f_c = \frac{h_o + (h_1 - F_1 \Delta - F_2 \Delta^2) + (h_2 + F_1 \Delta - F_2 \Delta^2)}{1 + (1 + F_3 \Delta^2) + (1 + F_3 \Delta^2)}$$

$$f_c = \frac{h_o + h_1 + h_2 - 2\Delta^2 F_2}{3 + 2\Delta^2 F} \quad (23)$$

When n=4 (6 point asperities)

$x_a = \Delta/2$, $x_b = -\Delta/2$, $x_1 = 3\Delta/2$, $x_2 = -3\Delta/2$ (see Figure 4)

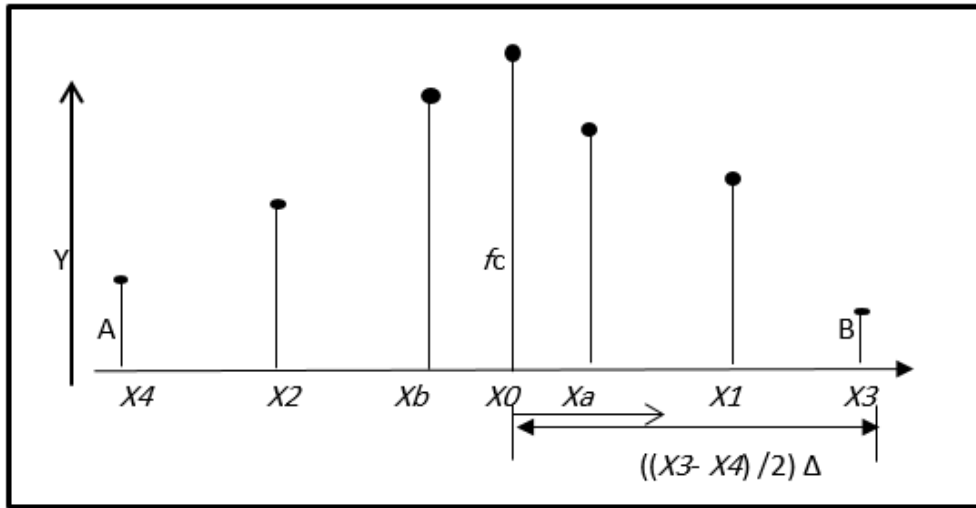


Figure 4 Shows six point asperities.

$$f_c = \frac{\sum_{i=1}^4 (h_i - F_1 x_i - F_2 x_i^2)}{\sum_{i=1}^4 (1 + F_3 x_i^2)}$$

$$F_1 = \left(\frac{h_{i1} - h_{i2}}{5\Delta} \right), \quad F_2 = \frac{2(h_{i1} + h_{i2})}{25\Delta^2}, \quad F_3 = \frac{-4}{25\Delta^2}$$

$$f_c = \frac{(h_a - F_1 \frac{\Delta}{2} - F_2 \frac{\Delta^2}{4}) + (h_1 - F_1 \frac{3\Delta}{2} - F_2 \frac{9\Delta^2}{4}) + (h_b + F_1 \frac{\Delta}{2} - F_2 \frac{\Delta^2}{4}) + (h_2 + F_1 \frac{3\Delta}{2} - F_2 \frac{9\Delta^2}{4})}{(1 + F_3 \frac{\Delta^2}{4}) + (1 + F_3 \frac{9\Delta^2}{4}) + (1 + F_3 \frac{\Delta^2}{4}) + (1 + F_3 \frac{9\Delta^2}{4})}$$

$$f_c = \frac{(h_a + h_b + h_1 + h_2 - F_2 \frac{\Delta^2}{2} - F_2 \frac{9\Delta^2}{2})}{4 + F_3 \frac{\Delta^2}{2} + F_3 \frac{9\Delta^2}{2}}$$

$$f_c = \frac{(h_a + h_b + h_1 + h_2 - 5\Delta^2 F_2)}{4 + 5\Delta^2 F_3} \quad (24)$$

When n=5 (7 point asperities)

$$x_o=0, \quad x_1=\Delta, \quad x_3=2\Delta, \quad x_2=-\Delta, \quad x_4=-2\Delta$$

$$F_1 = \left(\frac{h_{i1} - h_{i2}}{6\Delta} \right), \quad F_2 = \frac{2(h_{i1} + h_{i2})}{36\Delta^2}, \quad F_3 = \frac{-4}{36\Delta^2}$$

$$f_c = \frac{\sum_{i=1}^5 (h_i - F_1 x_i - F_2 x_i^2)}{\sum_{i=1}^5 (1 + F_3 x_i^2)}$$

$$f_c = \frac{h_o + (h_1 - F_1 \Delta - F_2 \Delta^2) + (h_3 - 2F_1 \Delta - 4F_2 \Delta^2) + (h_2 - F_1 \Delta - F_2 \Delta^2) + (h_4 + 2F_1 \Delta - 4F_2 \Delta^2)}{1 + (1 + F_3 \Delta^2) + (1 + F_3 \Delta^2) + (1 + 4F_3 \Delta^2) + (1 + 4F_3 \Delta^2)}$$

$$f_c = \frac{h_o + h_1 + h_2 + h_3 + h_4 - 10F_2 \Delta^2}{5 + 10F_2 \Delta^2} \quad (25)$$

When n=6 (8 point asperities)

$$x_a=\Delta/2, \quad x_b=-\Delta/2, \quad x_1=3\Delta/2, \quad x_3=5\Delta/2, \quad x_2=-3\Delta/2, \quad x_4=-5\Delta/2$$

$$F_1 = \left(\frac{h_{i1} - h_{i2}}{7\Delta} \right), \quad F_2 = \frac{2(h_{i1} + h_{i2})}{49\Delta^2}, \quad F_3 = \frac{-4}{49\Delta^2}$$

$$f_c = \frac{\sum_{i=1}^6 (h_i - F_1 x_i - F_2 x_i^2)}{\sum_{i=1}^6 (1 + F_3 x_i^2)}$$

$$\begin{aligned}
f_c &= \frac{(h_a - F_2 \frac{\Delta^2}{4}) + (h_1 - F_2 \frac{9\Delta^2}{4}) + (h_3 - F_2 \frac{25\Delta^2}{4}) + (h_b - F_2 \frac{\Delta^2}{4}) + (h_2 - F_2 \frac{9\Delta^2}{4}) + (h_4 - F_2 \frac{25\Delta^2}{4})}{(1 + F_3 \frac{\Delta^2}{4}) + (1 + F_3 \frac{9\Delta^2}{4}) + (1 + F_3 \frac{25\Delta^2}{4}) + (1 + F_3 \frac{\Delta^2}{4}) + (1 + F_3 \frac{9\Delta^2}{4}) + (1 + F_3 \frac{25\Delta^2}{4})} \\
f_c &= \frac{h_a + h_b + h_1 + h_2 + h_3 + h_4 - F_2 \frac{\Delta^2}{2} - F_2 \frac{9\Delta^2}{2} - F_2 \frac{25\Delta^2}{2}}{6 + F_3 \frac{\Delta^2}{2} + F_3 \frac{9\Delta^2}{2} + F_3 \frac{25\Delta^2}{2}} \\
f_c &= \frac{h_a + h_b + h_1 + h_2 + h_3 + h_4 - \frac{35\Delta^2}{2} F_2}{6 + \frac{35\Delta^2}{2} F_2} \tag{26}
\end{aligned}$$

When n=7 (9 point asperities)

$$x_o=0, \quad x_1=\Delta, \quad x_3=2\Delta, \quad x_5=3\Delta, \quad x_2=-\Delta, \quad x_4=-2\Delta, \quad x_6=-3\Delta$$

$$F_1 = \left(\frac{h_{i1} - h_{i2}}{8\Delta} \right), \quad F_2 = \frac{2(h_{i1} + h_{i2})}{64\Delta^2}, \quad F_3 = \frac{-4}{64\Delta^2}$$

$$f_c = \frac{\sum_{i=1}^7 (h_i - F_1 x_i - F_2 x_i^2)}{\sum_{i=1}^7 (1 + F_3 x_i^2)}$$

$$f_c = \frac{h_o + (h_1 - F_2 \Delta^2) + (h_3 - 4F_2 \Delta^2) + (h_5 - 9F_2 \Delta^2) + (h_2 - F_2 \Delta^2) + (h_4 - 4F_2 \Delta^2) + (h_6 - 9F_2 \Delta^2)}{1 + (1 + F_3 \Delta^2) + (1 + F_3 \Delta^2) + (1 + 4F_3 \Delta^2) + (1 + 4F_3 \Delta^2) + (1 + 9F_3 \Delta^2) + (1 + 9F_3 \Delta^2)}$$

$$f_c = \frac{h_o + h_1 + h_2 + h_3 + h_4 + h_5 + h_6 - 28\Delta^2 F_3}{7 + 28\Delta^2 F_3} \tag{27}$$

When n=8 (10 point asperities)

$$x_a=\Delta/2, \quad x_b=-\Delta/2, \quad x_1=3\Delta/2, \quad x_3=5\Delta/2, \quad x_5=7\Delta/2, \quad x_2=-3\Delta/2, \quad x_4=-5\Delta/2,$$

$$x_6=-7\Delta/2$$

$$F_1 = \left(\frac{h_{i1} - h_{i2}}{9\Delta} \right), \quad F_2 = \frac{2(h_{i1} + h_{i2})}{81\Delta^2}, \quad F_3 = \frac{-4}{81\Delta^2}$$

$$f_c = \frac{\sum_{i=1}^8 (h_i - F_1 x_i - F_2 x_i^2)}{\sum_{i=1}^8 (1 + F_3 x_i^2)}$$

$$f_c = \frac{h_a + h_b + h_1 + h_2 + h_3 + h_4 + h_5 + h_6 - 2(F_2 \frac{\Delta^2}{4} - F_2 \frac{9\Delta^2}{4} - F_2 \frac{25\Delta^2}{4} - F_2 \frac{49\Delta^2}{4})}{8 + F_3 \frac{\Delta^2}{2} + F_3 \frac{9\Delta^2}{2} + F_3 \frac{25\Delta^2}{2} + F_3 \frac{49\Delta^2}{2}}$$

$$f_c = \frac{h_a + h_b + h_1 + h_2 + h_3 + h_4 + h_5 + h_6 - 42\Delta^2 F_2}{8 + 42\Delta^2 F_2} \quad (28)$$